Universidade do Minho
Escola de Engenharia

Tiago André Rodrigues de Matos

Sediment circulation and accumulation sensors for *in situ* continuous monitoring

Dezembro de 2023

Universidade do Minho
Escola de Engenharia

Tiago André Rodrigues de Matos

Sediment circulation and accumulation sensors for *in situ* continuous monitoring

DIREITOS DE AUTOR E CONDIÇÕES DE UTILIZAÇÃO DO TRABALHO POR TERCEIROS

AGRADECIMENTOS

A colaboração entre membros de equipa, cooperação entre instituições, e demais sinergias envolvidas no contexto de um projeto de investigação são inegáveis, representando a espinha dorsal que sustenta o progresso e a qualidade dos resultados alcançados. A natureza multidisciplinar e complexa da investigação científica, que impõe uma convergência de conhecimento, experiência e habilidades, exige um ambiente colaborativo por forma a atingir os seus objetivos. Como tal, o mérito desta dissertação deve ser repartido por todos aqueles que, de alguma forma, ofereceram o seu contributo.

Em primeiro lugar, um profundo agradecimento aos orientadores professor Luís Miguel Valente Gonçalves, professor Marcos Silva Martins e professor Renato Filipe Faria Henriques. Pela orientação perspicaz, sabedoria e apoio incansável ao longo deste percurso académico, que foram fundamentais para moldar este trabalho. Agradeço pelo labor, dedicação e inspiração.

Aos diversos colegas de laboratório, colegas de investigação, colegas de projetos e técnicos, pelo companheirismo, suporte e entreajuda. Pelas discussões e colaborações que foram cruciais para o enriquecimento deste percurso. Agradeço por partilharem as vossas ideias e experiências, contribuindo assim para um ambiente académico estimulante.

Uma palavra às instituições TRATAVE, Camara Municipal de Esposende, Socorro a Náufragos de Esposende, Museu Marítimo de Esposende e ECIMAT – Universidade de Vigo, entre outros, pela cooperação, apoio e condições de trabalho fornecidas para a realização dos diversos trabalhos de campo.

À Fundação para a Ciência e a Tecnologia, que financiou este Programa Doutoral (SFRH/BD/145070/2019), o meu sincero reconhecimento pela oportunidade concedida e pelo investimento no avanço do conhecimento científico.

Por último, mas não menos importante, agradeço à minha família e amigos pela constante fonte de apoio e compreensão ao longo não só deste percurso académico, mas também do percurso da vida, contribuindo de maneira fundamental para o alcance dos marcos pessoais e profissionais.

Por fim, agradeço a todos aqueles que, de uma forma ou de outra, tornaram esta jornada possível. Que este trabalho possa contribuir, de alguma forma, para o avanço do conhecimento na respetiva área de estudo envolvente.

A todos, o meu muito obrigado!

STATEMENT OF INTEGRITY

I hereby declare having conducted this academic work with integrity. I confirm that I have not used plagiarism or any form of undue use of information or falsification of results along the process leading to its elaboration.

I further declare that I have fully acknowledged the Code of Ethical Conduct of the University of Minho.

RESUMO

A zona costeira é uma região complexa em termos de dinâmica hidráulica, geológica e ambiental. A compreensão dos processos sedimentares é essencial para validar modelos e garantir a gestão e proteção de infraestruturas e populações. Contudo, a correlação entre as projeções e as medições feitas em campo nem sempre são satisfatórias. A medição contínua em campo torna-se assim essencial para um estudo eficaz de cada processo ou ação.

Esta dissertação apresenta o desenvolvimento de instrumentos para medir processos sedimentares em campo. Estes processos são analisados e decompostos em dois ramos de estudo: deposição e erosão de sedimentos e transporte sedimentar. O transporte sedimentar, por sua vez, é decomposto em duas variáveis: concentração de sedimentos em suspensão e velocidade da água. Diferentes sensores foram desenvolvidos para medir temperatura da água, profundidade, turbidez, concentração de sedimentos em suspensão, velocidade da água e deposição e erosão sedimentar do leito aquático. Cada um dos dispositivos foi construído com alta eficiência energética para aumentar o tempo de vida útil das baterias, custos de fabricação reduzidos para permitir fabricação em massa, e tamanhos e pesos reduzidos para facilitar a instalação e manutenção. Os desenhos eletrónicos, mecânicos e de fabricação, bem como as metodologias de calibração, são apresentados para que os instrumentos possam ser replicados pela comunidade científica.

Uma estação de monitorização foi instalada no estuário do Rio Cávado (Esposende - Portugal) para testar e validar os instrumentos desenvolvidos. As medições de cada instrumento são discutidas e correlacionadas com outras variáveis ambientais para interpretar as dinâmicas no estuário. O objetivo de medir processos sedimentares foi alcançado, sendo possível observar a dinâmica da deposição e erosão sedimentar, a concentração do sedimento suspenso na coluna de água e a inversão de corrente durante os ciclos de maré. Foi também possível estimar a descarga de água, volume total de água, taxas de transporte sedimentar e quantidade total de sedimentos no estuário. Outros eventos como inundações e erosão do leito durante dias de precipitação, ou altas taxas de deposição sedimentar e aumento de sedimentos em suspensão na água durante eventos de floração de algas são discutidos e analisados. O problema da incrustação biológica é também estudado com o desenvolvimento e validação de técnicas para aumentar a longevidade dos sensores em campo sem necessidade de limpeza e manutenção.

Palavras-Chave: transporte sedimentar, deposição e erosão sedimentar, sensores, monitorização contínua

ABSTRACT

The coastal zone is a complex region in terms of hydraulic, geologic, and environmental dynamics. Understanding its sedimentary processes is essential to validate models and ensure the management and protection of infrastructures and populations. However, the correlation between projections and field measurements is not always satisfactory. Thus, continuous monitoring becomes essential for an effective study of each process and action.

This dissertation presents the development of new tools to continuously monitor sedimentary processes *in situ*. The sedimentary processes that take place in the watersheds are analysed and decomposed in two branches of study: sediment deposition and erosion of the streambed and sediment transport. The sediment transport is in turn decomposed into the two most important variables for the process: suspended sediment concentration and water velocity. Different individual sensors were developed to measure a set of water parameters: water temperature, depth, turbidity, suspended sediment concentration, water velocity and streambed height. Each one of the devices was built with high energy efficiency to extend the lifetime of batteries, reduced costs to allow massive replication, and reduced size and weight for ease of deployment and maintenance. The electronic, mechanical and manufacturing designs and calibration methodologies are disclosed so the instruments can be replicated by others.

A monitoring station was installed in the estuary of Cávado River (Esposende – Portugal) to test and validate the developed instruments in a real scenario. The monitoring results of each instrument are discussed and correlated with other environmental variables to interpret and analyse the dynamics in the estuary. The objective of measuring the different sedimentary processes *in situ* was accomplished. The developed instruments made it possible to understand the dynamics of sediment displacement in the streambed, suspended sediment concentration in the water column and inversion of stream flow during the tidal cycles. It was also possible to estimate the water discharge, total volume of water, sediment transport rates and total amount of sediment in the estuary. Other abnormal events such as floods and streambed erosion during precipitation days or high sediment deposition rates and increase of suspended sediment in the water during algae blooms are discussed. The problem of biofouling, which precludes long-time continuous monitoring, is also addressed with the development and validation of anti-fouling techniques to extend the monitoring time without the need for cleaning and maintenance.

KEYWORDS: sediment transport, sediment deposition and erosion, sensors, continuous monitoring *in situ*

INDEX

FIGURES

TABLES

ABBREVIATIONS AND ACRONYMS

A

ABS	Acoustic Backscatter Sensor
ABS	Acrylonitrile Butadiene Styrene
ADC	Analog to Digital Converter
ADCP	Acoustic Doppler Current Profiler
APHA	American Public Health Association
ASTM	American Society for Testing Materials
AUV	Autonomous Underwater Vehicle

B

C

CTD	Conductivity – Temperature - Depth

D

DAC	Digital to Analog Converter

E

EPA	U.S. Environmental Protection Agency
ETH	Ethernet

F

FFT	Fast Fourier Transform
FTU	Formazin Turbidity Units
FNMU	Formazin Nephelometric Multibeam Unit
FNU	Formazin Nephelometric Units
FNRU	Formazin Nephelometric Ratio Unit
FTO	Fluorine Tin Oxide

G

GLI	Great Lakes Instrument
GPS	Global Position System

GSM	Global System for Mobile Communications
H	
HAB	High-Altitude Balloon
HTML	Hypertext Markup Language
I	
I2C	Inter-Integrated Circuit
IC	Integrated Circuit
ICNF	Instituto da Conservação da Natureza e das Florestas
IMU	Inertial Measurement Unit
IoT	Internet of Things
IPMA	Instituto Português do Mar e da Atmosfera
IR	Infrared
ISO	International Organization for Standardization
J	
JTU	Jackson Turbidity Units
K	
L	
LAN	Local Area Network
LASER	Light Amplification by Stimulated Emission of Radiation
LED	Light-Emitting Diode
LiPo	Lithium Polymer
M	
MEMS	Microelectromechanical Systems
MOSFET	Metal Oxide Semiconductor Field Effect Transistor
N	
NTU	Nephelometric Turbidity Units
O	

P

P2P   Peer-to-peer

PBTs   Persistent Bio-accumulative Toxic Substances

PCB   Printed Circuit Board

PDMS   Polydimethylsiloxane

PEEP   Photo-Electronic Erosion Pin

PLA   Polylactic Acid

PMMA   Poly Methyl Methacrylate

PMT   Photomultiplier Tube

PHP   Hypertext Preprocessor

Q

R

RF   Radio Frequency

RTC   Real Time Clock

RVT   Room-Temperature-Vulcanizing

S

SD   Secure Digital

SDDIO   Secure Digital Input Output

SED   Surface Elevation Dynamics

SPI   Serial Peripheral Interface

SPM   Suspended Particulate Matter

SMD   Surface Mounted Device

T

TBT   Tributyltin

TCT   Thermal Consonance Timing

TMDL   Total Maximum Daily Load

ToF   Time-of-flight

TSS   Total Suspended Solids

TTN   The Things Network

TVP   Turbidity Vertical Profiler

U

UART   Universal Asynchronous Receiver/Transmitter

USGS   United States Geological Survey

UV   Ultraviolet

V

W

WWTP   Wastewater Treatment Plant

WRWA   Westport River Watershed Alliance

X

Z

1 INTRODUCTION

The seaside area is constantly changing due to the continuous action of wind and sea currents, which cause sediment displacement. The monitoring of sediment transport in the coastal zone is essential to validate coastal dynamics models and to support the project, management and protection of infrastructures and populations.

The quantification of sediment transport in the seaside zone is essential to understanding the evolution of the littoral coast [1-2]. However, the correlation between the prospected data and events and the measurements made in the field is not always satisfactory. One of the reasons that justify the observed difference is the great variability and complexity of sedimentary processes along the watersheds, which have different natural conditions, and limit the existing mathematical models. Therefore, continuous monitoring becomes essential for an effective study in each area of action.

1.1 An overview of sediment and sedimentary processes

Sediment is the conglomerate of materials, organic or inorganic, and is a naturally occurring matter that is broken down from rocks by processes of weathering and erosion, and is subsequently transported by the action of wind, water, ice, or by the force of gravity acting on these particles [3-4]. While the term is often used to indicate soil-based, mineral matter (e.g. clay, silt or sand), decomposing organic substances and inorganic biogenic material are also considered sediment [5]. While most minerals, also referred to as inorganic sediments, come from rock erosion and weathering, the organic ones are typically detritus and decomposing material such as shells of organisms or algae.

Sediment material is typically small, with clay defined as particles less than 2 μm in diameter, and coarse sand reaching up to 2 mm in diameter [6]. However, during floods or other high-flow events, even large rocks can be classified as sediment when carried downstream.

Sediment comes from geologic, geomorphic, and organic factors [7]. Sediment transported in rivers with headwaters from a mountain range often includes glacial silt. A body of water surrounded by swampland will be inundated with decomposing organic material [8]. The amount, material and size of the transported sediment is a sum of these influences in any waterway. In the natural cycle of sediment, its destination is the estuaries, where the material is subject to the dynamics of the river and maritime currents.

In aquatic environments, sediment can either be suspended (floating in the water column) or bedded (settled on the bottom of a body of water, also commonly referred to as accumulated or deposited). Suspended sediment is typically small, and it is carried along the water flow. Oppositely, larger and heavier particles will settle and accumulate on the seabed.

1.1.1 Sediment and geology

Typically, sediment particles are mineral-based and their nature is dependent on their location and geology. Glacial-type sediment is common in mountain ranges, while low-lying rivers are rich in soil-based sediment [7]. In high-flow waterways, sediment transport includes gravel, pebbles and small rocks. Rocks less prone to weathering are less likely to become sediment, while soft rocks erode more quickly and are easily carried away by the flow. The characteristics of the transported sediment are strongly influenced by the geology of the surrounding environment [9].

Specific geologic elements, such as basalt near volcanic plate boundaries or limestone, are typically localized in historically shallow marine regions [10]. Sediment transport is often responsible for intermixing these geologic materials by carrying mineral particles far away from their origin [7]. For example, mountain streams typically transport glacial silt to the estuary. In the same way, rivers that run through agricultural regions can carry fertilized soil into the oceans [11].

For millions of years, sediment deposition helped to form many of these geologic features. Sediment rocks such as sandstone and limestone are created by sediment deposits, which eventually become pressurized into stone. Once these rocks become re-exposed to water and air, the sediment transport process re-begins [12].

1.1.2 Sediment and geomorphology

Geomorphology refers to both the surface of the Earth (soil/terrain) and the processes acting on it, such as wind or rain. As explained before, sediments can come from the weathering of rocks and the erosion of surface materials. When wind, rain, glaciers and other elements or processes scour a rock surface, the particles are carried away as sediments.

In addition to the influence of wind and rain, sediment transport is also affected by the local topography [13]. The amount of sediment that flows in the water and the distance that it travels have a direct influence on the shape of the terrain where the waterway runs [9]. For example, bedrock streams are less likely to

contribute to the sediment load, as the channel is resistant to quick erosion. These rivers are considered non-alluvial channels (as well as man-made channels with no sediment).

Most rivers are alluvial, or self-formed, this is, they have created their path by carrying sediment away. In an alluvial stream, the depth and breadth of the waterway will depend on the strength of the water flow, as well as the material that makes-up the channel boundaries [9]. Rivers that run through soft soil typically have higher sediment transport rates than rivers that run over exposed bedrock. For bedrock streams, its sediment load is mostly taken from the sides and bottom of the channel. Oppositely, non-erodible bedrock terrains and highly vegetated areas are less subject to runoff erosion during flood events, as the roots of the plants hold the soil in place [13].

In addition to the effects that geomorphology has on sediment transport rates, the transport process itself plays a part in the outline of the terrain. As sediment is transported downstream, the water flow helps to shape the surface of the planet by carrying the eroded material away from some regions and depositing it in others.

1.1.3 Sediment and organic factors

In addition to the mineral aspect, sediment can also be of organic origin. Most sediment of organic origin comes from the inorganic or mineralised portions of some organisms, such as shells and exoskeletons or endoskeletons. These structures tend to fracture and form particles that contribute to the sedimentary flow. Other organic sediment comes from decaying algae, plants, and other organic material that falls into the water, such as leaves. Bacteria attached to this detritus or other inorganic matter are also categorized as organic [14]. Organic sediment transport varies by location and season. For example, Keith R. Dyer *et al.* reported in previous work an organic suspended load decrease in sediment transport from 85% to 18%, from February to November, due to seasonal effects [15].

Phytoplankton can also produce an important contribution to sediment load. In addition to the organic factor they provide, specific phytoplankton, such as diatoms, contribute to the inorganic component as well [5]. This inorganic material comes from diatom frustules and calcium carbonate detritus. While it is not specifically organic, it is organic in origin.

1.1.4 Sedimentary processes

There are two main processes of sediment behaviour in aquatic environments: its transport throughout the waterway, and its deposition, or accumulation, in the streambed. The sediment transport is directly influenced by the strength of the water body, which allows suspension and resuspension of the particles. When there is not enough water current to move the suspended material, it will fall and accumulate at the bottom of the stream (see Figure 1). Besides the natural sediment dynamics of the watersheds, other external factors can lead to severe consequences in the aquatic environment. They can be by natural events (e.g., weather, seasons) or anthropogenic ones (e.g., dams, ports, seawalls).
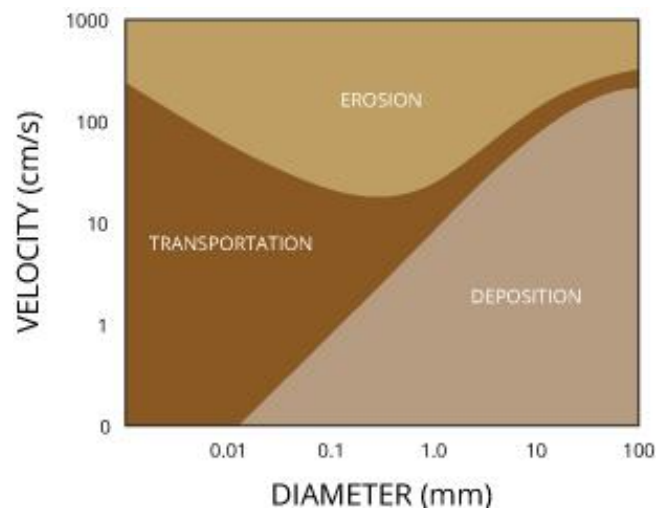
Figure 1. Hjulström curve, illustrating the influence of particle size and watercourse flow rate on sediment erosion, transportation, and deposition [16].

1.1.4.1 Sediment transport

Sediment transport, or sediment load, is the movement of organic and inorganic particles in water. In general, the higher the flow rate, the more sediment will be transported. Water flow can be strong enough to suspend particles in the water column, as they move downstream, or simply push them along the bottom of the waterway. Transported sediment may include mineral matter, chemicals, pollutants and organic material, and it can be divided into three different processes: bed load, suspended load and wash load [17].

Bed load is the portion of sediment transport that rolls, slides or bounces along the bottom of the waterway. This sediment is not considered suspended, as it is in constant contact with the streambed, and its movement is neither uniform nor continuous. Bed load occurs when the force of the water flow is strong enough to overcome the weight and cohesion of the sediment, making it move. While the particles

are pushed along, they typically do not move as fast as the water around them, as the flow rate is not high enough to fully suspend them. Approximately 5-20% of total sediment transport is bed load [7].

In situations where the flow rate is strong enough, some of the smaller and lighter bed load particles can be pushed up into the water column and become suspended. The size of the particles that can be carried as suspended load is dependent on the flow rate. Unless the flow rate increases, larger and heavier particles are more likely to fall through the upward currents to the bottom, increasing the turbulence at the streambed. In addition, suspended sediment will not necessarily remain suspended if the flow rate slows.
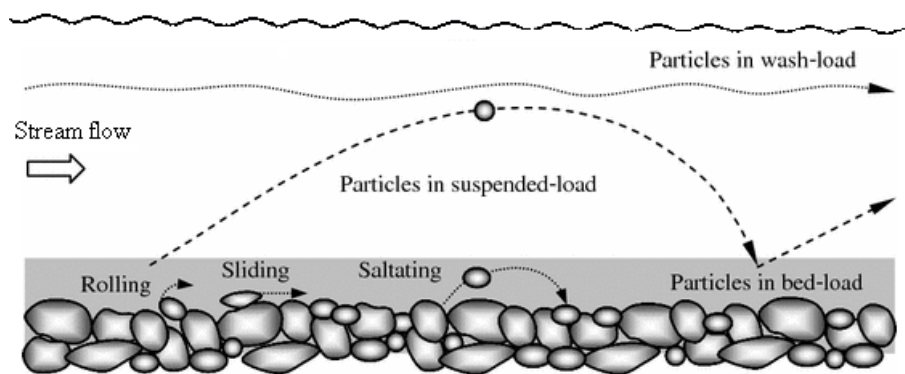
Figure 2. Classification of sediment transport in stream flow into three types—bed load, suspended load, and wash load [17].

It is important to notice that suspended load and suspended sediment are not the same, even if is often overlap. Suspended sediment is composed of any particles found in the water column, whether the water is flowing or not. On the other hand, suspended load is the amount of sediment carried downstream within the water column by the water flow. Suspended loads require moving water, as the water flow creates small upward currents (turbulence) that keep the particles above the streambed [9].

The wash load is a subset of the suspended load. It comprises the finest suspended sediment (typically less than 2 μm in diameter) [9]. The wash load differentiates from the suspended load because it will not settle to the bottom of the waterway during a low or no-flow period. Instead, these particles remain in permanent suspension as they are small enough to bounce on water molecules and stay afloat. This is the particular case of lakes and other small water movement waterways. In streams with constant water flow, the suspended sediment is the sum of wash and suspended loads.

Wash load reveals high importance in some watersheds since it is directly connected to the turbidity of lakes or slow-moving rivers [5]: when the flow rate increases (increasing the suspended load and overall

sediment transport), turbidity also increases. While turbidity cannot be used to estimate sediment transport, it can be used to evaluate suspended sediment concentration at specific locations [18].

1.1.4.2 Sediment deposition

Sediment deposition happens when the water flow slows down or stops, and heavy particles can no longer be supported by the bed turbulence, which makes them settle down to the streambed. Sediment deposition can be found anywhere in a water system, from high mountain streams to rivers, lakes, deltas and floodplains.

The suspended particles that fall to the bottom of a water body are called settleable solids [19]. As they are found in streambeds, these settled solids are also known as bedded sediment. The size of settleable solids will vary in different water systems. In high-flow areas, larger and heavier gravel-sized sediment will settle out first. Finer particles, including silt and clay, will be carried away to the estuarine where will settle or remain in circulation due to the action of seawater currents.

In marine environments, nearly all suspended sediment will settle due to the presence of salt ions. Salt ions bond to the suspended particles, attaching them to other particles in the water [20]. As the collective weight increases, the sediment begins to sink to the seafloor, and this is the reason why oceans and other marine ecosystems usually have lower turbidity levels (higher water clarity) than freshwater environments [20].

However, while estuaries and other tidal areas may be considered marine, they are not necessarily clearer than freshwater. Estuaries are the collection point for suspended sediment coming down the rivers. Furthermore, in a tidal area, the constant water movement causes the bottom sediment to continually resuspend, preventing high water clarity during tidal periods. Besides the quantity of sediment, the clarity of an estuarine is also influenced by its salinity level, which leads to an increase in sediment deposition [15].

1.1.4.3 Factors that influence sedimentary processes

Sedimentary processes are constantly subject to change. In addition to the changes in sediment load due to geology, geomorphology and organic elements, sediment transport and deposition can be altered by other external factors, namely due to alteration in the normal water flow by changes in the water level, weather events and human influence.

Water flow, also referred to as water discharge, is the most important element for sediment transport. The flow of the water body is responsible for picking up, moving and depositing sediments in the watercourse [21]. Without flow, sediment transport does not exist, as particles remain suspended or settle out without downstream movement. Water flow is variable, affected not only by the local terrain (e.g. slope), but also by the water level, which is typically influenced by precipitation or lack thereof.

Most changes in water level are due to weather events such as rainfall. Precipitation causes water levels to initially rise, and then return to the previous base flow level over the course of hours or days. Rainfall, whether slight or heavy, can affect water flow and sediment transport. The extent to which a weather event will influence sediment transport is dependent on the amount of sediment available. Snowmelt in a glaciated area will result in a high sediment load due to glacial silt [7]. Heavy rainfall over an area of loose soil and minimal vegetation will create runoff, carrying loose particles into the waterway [22]. Likewise, flooding will also pick up sediment from the area.

Seasonal effects are also responsible for changes in water level and flow [23]. Most seasonal changes are due to precipitation levels and events such as snowmelt. During low precipitation and low flow periods, sediment transport falls. During the peak of snowmelt, the sediment load can increase by a factor of 15 or more [9]. Climate change can also play a role in sediment transport, as it affects both the timing and magnitude of floods and other weather events [7].

Human land use, such as urban areas, agricultural farms and construction sites will also affect the sediment load. These effects are indirect, as they require heavy rainfall or flooding to carry their sediment into the waterway. However, anthropogenic land use is one of the leading contributors to excessive sedimentation due to erosion and runoff [24]. This increase occurs because disturbed areas (such as logging, mining, construction or farm sites) often expose or loosen topsoil, by removing native vegetation, that is easily carried into a nearby river or stream by rainfall and runoff.

Other anthropogenic factors also have an important influence on sediment transport and accumulation. Infrastructures such as dams and other human-made barriers affect the natural water flow through complete detention or restricted channels [25]. The restricted flow can cause the channel downstream of the infrastructure to become sediment-starved, while the sediment accumulation amount builds up. A sediment-starved river will not be able to provide habitats for benthic organisms or spawning fish. A highly silted reservoir behind the dam may face issues of too much sediment, including changes in aquatic life and the potential for algae blooms. On the other hand, when a dam release occurs, the flow rate

downstream can dramatically increase and, if it is controlled, it can be an important tool to refresh the bed material, and build sediment bars and other habitat areas [26].

Fluvial infrastructures play a role in sediment natural flow, but there are other anthropic causes. When looking at the human influence on sediment, it is impossible to neglect the coastal area. All over the seashore, seawalls are used to protect harbours, beaches and prevent erosion of urban areas. These structures are barriers to the sediment flow that shape the normal accumulation of sediments on the coast [27]. In the same way, dredging is a common technique that is used worldwide to collect construction material and remove and relocate deposited sediment on the littoral with the main purpose of cleaning navigation channels, harbours and beaches [28].

1.1.5 Sediment importance and consequences

Many ecosystems benefit from sediment transport and deposition, whether directly or indirectly. Sediment builds aquatic habitats for spawning and benthic organisms and is also responsible for providing nutrients to aquatic plants and vegetation in nearshore ecosystems such as floodplains and marshes [7]. Without sediment deposition, coastal zones would become eroded or non-existent [29].

Sediment deposition creates habitats for aquatic life. While too much sediment can be detrimental, too little sediment can also diminish ecosystem quality. Some aquatic habitats are even grain-size specific since many spawning habitats require a specific sediment size (e.g. gravel) and too fine sediment can end up smothering eggs and other benthic creatures [30].

While sediment is needed to build aquatic habitats and reintroduce nutrients for submerged vegetation, too much or too little sediment can easily cause ecological and safety issues. Whether the concerns are caused by scour, erosion, build-up or excessive turbidity, the sediment transport rate is an important environmental factor. In addition to the problems caused by load quantity, sediment can easily introduce pollution, microplastics, and other contaminants into the waterway, spreading the pollutants downstream [31].

1.1.5.1 Excessive sediment

High sediment load is the most common natural issue with sediment transport rates. Too much sediment can bury habitats, cause poor water quality, algae blooms and deposition build-up that may lead to the

physical alteration of the waterway. For aquatic life, excessive suspended sediment can disrupt natural aquatic migrations, and damage gills and other fish organs [32].

Diminished water quality occurs with unusually high sediment transport rates. Turbidity can cause water temperatures to rise (sediment absorbs more solar heat than water does) which will cause dissolved oxygen levels to drop, as warm water cannot hold as much oxygen as cold one [5]. In addition, suspended sediment blocks sunlight from reaching submerged vegetation, decreasing photosynthesis rates and lowering dissolved oxygen levels still further.

A continuous and anomalous increase of turbidity in an aquatic ecosystem may origin a big impact on its fauna and flora. The shortage of natural light might encourage more sensitive species to leave the area, while silt-tolerant organisms move in [33]. If the increase in the sediment load is due to agricultural and urban runoff, algae blooms can occur from the increased nutrient load carried into the water body [34].

Regular sediment deposition can build sediment bars, creating new aquatic habitats, but increased sedimentation can destroy more habitats than it creates. Siltation, the name for fine sediment deposition, occurs when water flow rates decrease dramatically. This fine sediment can smother insect larvae, fish eggs and other benthic organisms as it settles out of the water column [33]. Deposited matter can also modify the waterway banks and direction as an unusually high sediment load settles out. Sediment deposition is responsible for creating alluvial fans and deltas, but excessive accumulation of sediment can build up channel plugs and levees. These deposits can block the river from reaching other stream threads or floodplains and are a common estuarine problem for maritime navigation.

Increased sedimentation is considered one of the primary causes of habitat degradation. Depending on the local geology and terrain, sediment build-up can damage aquatic ecosystems not only in downstream areas but also in upstream headwaters as the deposits grow.

Sediment deposition is considered extreme when it exceeds the recommended or established total maximum daily load (TMDL). A TMDL establishes a limit for measurable pollutants and parameters for a body of water. That means that TMDLs can be created for several different elements of the sediment load, including total suspended solids, nutrient impairment, pathogens and siltation [35]. When developing a TMDL report, it is important to consider whether or not the waterway itself is generating the sediment load naturally, as an unstable stream channel [36].

1.1.5.2 Sediment starvation

Although too much sediment is a common concern, the lack of sediment in the waterway may also lead to environmental issues. Sediment starvation is often caused by man-made structures such as dams or by natural barriers that limit sediment transport. Without sediment transport and deposition, new habitats cannot be formed since it would lead to nutrient depletion in floodplains and marshes, and submerged vegetation could not grow [37]. Also, while water clarity is often heralded as a benchmark of water quality, low amounts of turbidity can protect aquatic species from predation [15]. Too little sediment can alter an ecosystem to the point that native species cannot survive.

In addition to the effect on aquatic life, the loss of sediment transport and deposition can cause physical changes in the terrain. It is common to see receding riparian zones and wetlands downstream of dammed rivers due to the loss of transported sediment [38]. Erosion is common downstream of a barrier, as is coastline erosion when there is no sediment carried by the rivers [39]. The flowing water will pick up new sediment from the bottom and banks of the waterway (eroding instead of refreshing habitats), as it attempts to adjust to a uniform flow rate. Too little sediment deposition can lead to the erosion of riverbanks and coastal areas, causing land loss and destroying the nearshore habitats [7].

1.1.5.3 Contaminated sediment and pollutants

Contaminated sediment is the accumulated riverbed materials that contain toxic or hazardous substances that are detrimental to aquatic, human or environmental health. These contaminants often come from point-source pollution such as industrial wastewater or other effluent sources. Though, they can also enter the water through runoff over contaminated soils (e.g., mine waste, landfills or urban areas), chemical spills, or deposits from air pollution [40].

As contaminants do not degrade or degrade very slowly, they can be a source of environmental issues for long periods, even if they are not frequently resuspended. The most problematic contaminants in both bedded and suspended sediment are metals and persistent bio-accumulative toxic substances (PBTs), such as pesticides and methylmercury. Respawning these sedimentary areas may involve dredging to remove the contaminated sediment from the waterway [41].

1.1.5.4 Scour

Scour is the erosion process when sediment transport removes material from a streambed or bank. It can occur anywhere where there is water flowing and erodible material. Local scour is the engineering term for the isolated removal of sediment at one location, such as the base of underwater structures, including bridge piers and abutments [42]. This localized erosion can cause structural failure, as bridges and overwater constructions rely on the bed sediment to support them.

While scour can occur anywhere, it is more likely to occur in alluvial waterways (erodible beds and banks), as opposed to bedrock-based (nonalluvial) channels. As water flow is responsible for conducting sediment transport, scour can occur even during low flow conditions. However, critical bridge scour typically occurs during periods of high flow, such as during a flood event [43]. Higher flow rates pick up more sediment. In consequence, turbulence occurs at the base of the piers as they interrupt and accelerate the flow. This turbulence in turn will increase the forces acting on the streambed, suspending additional particles and initiating higher sediment transport. Higher streambed rugosity and higher water depths create higher kinetic energy and turbulence. If too much sediment is removed, the structure can collapse. Scour due to flood-initiated sediment transport is the most common cause of bridge failure in the United States [43].

1.2 Objectives

As demonstrated, sedimentary processes play a major role in any aquatic environment. In the last decades, several computational models have been presented to predict sediment dynamics [44–48]. These models are accurate to a certain point [49]. The high complexity of real scenarios makes it a very difficult task to produce results with detail. The complexity of sediment transport rates is affected by innumerable variables such as bed geometry, particle size, shape and concentration, and the multiple forces acting upon the sediment as relative inertia, turbulent eddies or velocity fluctuations in speed and direction [50]. Most flow rate and sediment transport rate equations attempt to simplify the scenario by ignoring the effects of channel width, shape and curvature of a channel, sediment cohesion and non-uniform flows.

The use of monitoring data is usually referenced as one of the most important methods to improve the accuracy of said models. These data, provided by sensors deployed *in situ*, can be used both as input for the models and to validate their results. However, as will be demonstrated in the next chapter, the current state of the art of monitoring instruments for sedimentary processes has limitations.

The purpose of this dissertation is the development of automatic technology able to provide monitoring information about the sedimentary processes in the coastal area. However, these natural processes entail profound complexity. Along the presented work, the sedimentary process will be divided into sediment deposition and sediment transport, which in turn is divided into the sum of the different physical variables that compose them.

Several technologies and techniques are presented to achieve the final objective. The developed knowledge (be they sensors, systems, methods or methodologies) is confronted with the current state of the art of commercial instrumentation and scientific development to pursue innovation and take the available expertise a step forward.

2 STATE OF THE ART

The sedimentary processes can be narrowed into two different spectrums: sediment transport and sediment deposition and erosion. While it can be argued that the two processes are directly entwined by the bed load transport (the moment when the deposited sediment becomes suspended and vice-versa), the requirements and constraints to measure them are different. Thus, henceforward, they will be treated separately. This section presents the state of the art of the existing methods, methodologies, techniques and apparatus to monitor sediment transport and sediment deposition and erosion. It covers both the commercial and scientific know-how, from their historical background to the innovative cutting-edge tools of the present day.

Even if it is not directly linked to the sedimentary processes, the last subsection of this chapter reports on biofouling, how it affects the instrumentation tools for *in situ* monitoring, and the existing anti-biofouling techniques in use. The work presented in this dissertation will show that reliable continuous monitoring in the field is not possible if additional measures are not considered against this natural process. Thereby, this topic had to be addressed to accomplish the purposed objectives.

2.1 A theoretical approach

Sediment transport is constantly subject to change. Water flow, or water discharge, is the most important variable for sediment transport. The flow of water is responsible for picking up, moving and depositing sediment throughout the waterway.

There are two basic ways to calculate flow. It can be simplified as area (cross-section of the waterway) multiplied by velocity, or as a volume of water moved over time.

$$flow \: [m^3/s] = \: area \: [m^2] * velocity \: [m/s] \qquad (1)$$

or

$$flow \: [m^3/s] = \: volume \: [m^3] \: / \: time \: [s] \qquad (2)$$

The equations describing the water flow are simple, however, its interaction with sediments is more complex. The complexity of the sediment transport rate is affected by innumerable variables such as the bed geometry, particle size, shape and concentration, and the multiple forces acting upon the sediment as relative inertia, turbulent eddies or velocity fluctuations in speed and direction [50]. In particular, the

13

sediment transport rate is difficult to measure, as any measurement method disturbs the flow and affects the readings. Most flow rate and sediment transport rate equations attempt to simplify the scenario by ignoring the effects of channel width, shape and curvature, sediment cohesion and non-uniform flows.

The two main flow factors in sediment transport are the settling rate and the boundary layer shear stress [51]. The settling rate, also called Stokes settling or settling velocity, is derived from Stokes' Law and is related to the rate at which sediment falls through a liquid due to the action of the gravitational action and the drag force that keeps the particles suspended, as stated in the following equation [52]:

$$v_{settling} = \frac{g * (\rho_{particle} - \rho_{fluid}) * d_p^2}{18\mu} \tag{3}$$

$v_{settling} =$ settling velocity (m/s)

$g =$ gravitational constant (m/s²)

$\rho_{particle} =$ particle density (kg/m³)

$\rho_{fluid} =$ fluid density (kg/m³)

$d_p =$ particle diameter (m)

$\mu =$ fluid viscosity (Pa*s)

Understanding this relationship helps to define some of the forces that sediment transport must overcome relative to particle size.

The other factor, the shear stresses in the boundary layer of a sediment bed, explains how much force is required for water flow to overcome relative inertia and begin sediment transport (through bed load or suspended load).

$$\tau = \rho_{fluid} * v_{shear}^2 \tag{4}$$

$\tau =$ shear stress (Pa)

$v_{shear} =$ shear velocity (characteristic velocity of a turbulent flow) (m/s)

In a basic river system (like freshwater rivers), v_{shear} can be calculated as [53]:

$$v_{shear} = \sqrt{g * h * S} \tag{5}$$

$h =$ river depth (m)

$S =$ river slope (m/m)

In more complex water systems (like estuaries and oceans) this equation becomes inadequate. Instead, the Von Karman-Prandlt equation can be used, where the shear stress is influenced not only by the

viscosity of the liquid but also by the roughness of the sediment. The turbulent eddies created at the bottom by the water flow are also accounted for. This is also known as the Law of the Wall [54].

$$\frac{v_{avg}}{v_{shear}} = \frac{1}{k} * \ln\left(\frac{z}{z_0}\right)$$

(6)

$v_{avg} =$ averaged flow velocity (m/s)

$k =$ Von Karman's constant

$z =$ roughness above the bed (μm)

$z_0 =$ roughness as flow velocity approaches zero (μm)

The above equations give a basic understanding of some of the forces acting on sediment in the water. To further understand the conditions required for sediment transport, the shield stress equation can also be used. The shield parameter, along with the particle Reynolds number, predicts how much flow is required for sediment transport to exist [55].

The Reynolds number demonstrates if a flow is viscous enough to overcome the relative inertia of sediment. For sediment transport, the Reynolds number for flow through a sediment bed can be calculated from the boundary layer shear stress equation:

$$Re = \frac{v_{shear} * d_p * \rho_{fluid}}{\mu}$$

(7)

$Re =$ Reynolds number of the particle

The point at which water flow begins to transport sediment is called the critical Shields parameter (nondimensional number). This creates an empirical curve to approximate at what flow rate a sediment particle will move based on the particle size.

$$\tau_{shield} = \frac{\tau}{g * (\rho_{particle} - \rho_{fluid}) * d_p}$$

(8)

$\tau_{shield} =$ Shield parameter

While these equations help to define the minimum flow rate for sediment transport, they do not determine sediment load.

One sediment transport rate equation (in the form of bed load shield stress) was developed by van Rijn for the bed load transport of particles between 0.2-2 mm [56]:

$$tns_{bed} = 0.053 * ((\rho_{ss} - 1) * g)^{0.5} * d_{50}^{1.5} * \frac{tns_{st}^{2.1}}{d_g^{0.3}} \qquad (9)$$

$tns_{bed} = $ bed load shield stress (N/m²)

$\rho_{ss} = $ specific density of sediment (kg/m³)

$d_{50} = $ median particle diameter (m)

$tns_{st} = $ transport stage parameter (dimensionless)

$d_g = $ dimensionless grain size (m)

For the same sediment size, the suspended load transport rate (in the form of total non-settling suspended sediment transport concentration) is even more complicated [57]:

$$tns_{sus} = v_{avg} * h_{avg} * c_{ref} * \frac{(a/h)^z - (a/h)^{1.2}}{(1 - a/h)^z * (1.2 - z)} \qquad (10)$$

$tns_{sus} = $ total non-settling suspended sediment transport concentration (g/L)

$h_{avg} = $ average flow depth (m)

$c_{ref} = $ reference concentration (dimensionless)

$a = $ height above the bed, relative to particle size (m)

$z = $ suspension number

While van Rijn equations are the most popular to estimate sediment load, other curves have been developed, but all of them lack accuracy for different water bodies. Different water systems have different characteristics and properties. It is impossible to develop a global equation that will prevail in every watershed. If we stick to the most important properties, seven main variables influence sediment transport rate:

$$tns_{sediment\ rate} = f(\tau, h, d_p, \rho_{particle}, \rho_{fluid}, \mu, g) \qquad (11)$$

The sediment transport rate ($tns_{sediment\ rate}$) is a function of seven variables (shear stress, river depth, particle diameter, particle density, fluid density, fluid viscosity and gravitational constant), as well as the size-shape-density distribution (often assumed as a standard deviation of the particle diameter) of the suspended particles. In addition, a higher river discharge does not automatically mean that a river will have a higher sediment load. The quantity and material of the sediment particles, as well as the geography of the local terrain, will still play a contributing role in the sediment load.

The sediment load itself is calculated as a depth-integrated sediment mass above a unit area. It is variable for multiple reasons but can be estimated with a time-average collected sediment concentration. While it

is dependent on flow to initiate and continue transport, it is not usually calculated from flow rates, as the main variables in sediment load come from environmental factors.

2.2 Sediment transport

As seen before, calculating sediment transport rates is complex. The complexity of variables on stage (suspended materials properties such as colour, size, heavy and shape, and the characteristics of the fluid such as refraction index, colour, viscosity and velocity) makes the measurement methods properties very specific for each area of action. Because of that, there is no available instrument in the market that claims to measure suspended load.

At the current time, the *in situ* monitoring of sediment is performed by the estimation of single-point suspended sediment concentration (in g/L), or most commonly by the measurement of turbidity. However, suspended sediment concentration is not suspended load since it lacks the water discharge component. Thus, the measurement of sediment transport must be divided into two independent branches: (i) turbidity, or suspended sediment concentration, and (ii) water velocity.

2.2.1 Turbidity

Turbidity is a physical property of fluids that translates into reduced optical transparency due to the presence of suspended material that blocks the transmission of light. This material can be of organic or inorganic origin, varying in colour, matter and size, ranging from macroscopic to colloidal particles. Turbidity is not a physical quantity, so it is not directly measurable. The complexity of interactions between the optical properties of suspended material, the characteristics of the fluid, and the wavelength and intensity of the incident light turn turbidity into a visual property quite complex. Therefore, turbidity as an optical property of water becomes a complex parameter to standardize.

Total suspended solids (TSS) are the main cause of turbidity. The most common method of measuring suspended solids is by weight. To measure TSS, the water sample is filtered and dried, and the collected solids are weighed. This method is the most accurate technique for measuring total suspended solids. However, it is also more time-consuming and impractical for *in situ* monitoring [58].

The first practical attempt to measure turbidity in the laboratory was through the Jackson candle method [59]. Developed over a century ago, this instrument consists of a lighted candle, placed under a glass

tube with a flat bottom, as Figure 3 shows. The fluid, in which the turbidity is to be measured, is slowly poured into the tube until the flame image is no longer visible from a top point of view (the light does not disappear completely, just the image of the flame). This phenomenon occurs when the light is completely dispersed by the suspended particles in the liquid.

Eye

Scattered Light is as Intense as Transmitted Light — Image of Flame Disappears at this Depth

Scattered Light

Scattered Light Weak — Transmitted Light Strong

Length of Arrow Proportional to Intensity of Beam of Light
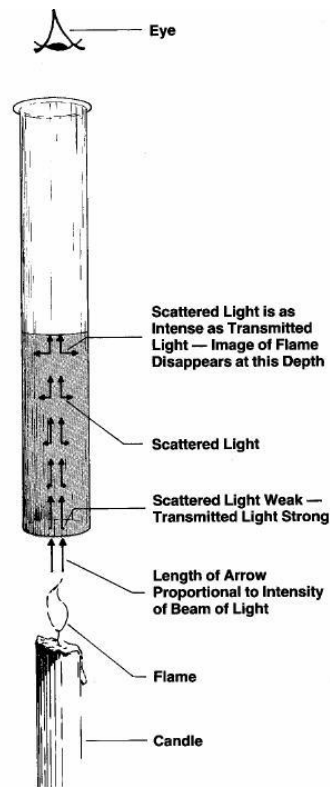
Flame

Candle

Figure 3. Illustration of the Jackson Candle method for turbidity measurement. The liquid is slowly poured into the tube until the image of the flame of the candle is no longer visible. Turbidity is quantitatively related to the volume of liquid in the tube at the point when the flame becomes indiscernible [60].

The tube contains a graduation that allows relating the volume of the liquid to its transparency and consequent turbidity. To standardize the instrument, the initial grading used was ppm (parts per million) of silicon dioxide (SiO_2, or commonly silica), called Jackson Turbidity Units (JTU). After the invention of formazin in 1926, a new degree was adopted: Formazin Turbidity Units (FTU). Formazin is currently the most popular turbidity standard solution used to calibrate turbidity devices.

Even with some improvements over time, this method always had limitations. The Jackson Candle has a limited dynamic range, and samples below 25 JTU are not possible to read. Also, the readings are subjective as they are based on human observation.

Other turbidimeters based on the extinction of light were developed. Among these, the most recognized is the Secchi Disk, created in 1865 by Pietro Angelo Secchi. Due to its simplicity, low cost, portability and ease of handling, it is still used in naval instrumentation.

The Secchi disk consists of a flat circular disk with a diameter between 16 cm and 40 cm, usually divided into four equivalent parts, with the contrasts of black and white or, in some cases, completely black or completely white [61]. The disc, attached by a rope, is slowly submerged in the water until it is no longer visible, finding the Secchi depth (see Figure 4). High depths are related to high clarity of water and low levels of turbidity. On the opposite, low depths indicate high levels of turbidity.
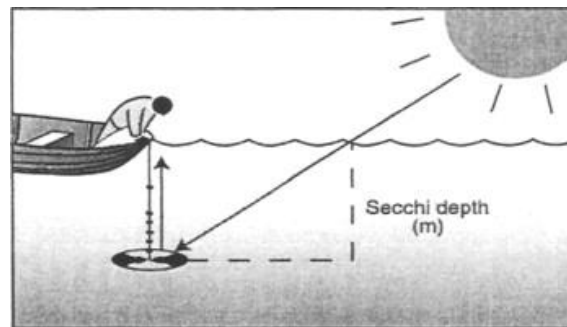
Figure 4. Illustration of using the Secchi Disk to measure turbidity. The disk is slowly submerged until it disappears, determining the Secchi depth that is correlated with a turbidity value [62].

The readings using this instrument depend on the attenuation of light in water, this is, the ability of light to penetrate the medium. When the disc is underwater and the light is reflected from it, the disc is visible to the observer. When the disc is obscured by suspended sediment, the light is scattered and diffused through the medium.

Although it is a widely used instrument, it is also unreliable. Readings are affected by changes in sunlight conditions, water shaking, time of day and human error [63]. Currently, these types of light-extinction methods are considered obsolete, in favour of electronic instruments that offer greater dynamic range and accuracy.

2.2.1.1 Standard optical methods

The optical turbidimeters have solved the problem of susceptibility to human error presented by previous methods while increasing their dynamic range and precision. These electronic devices use a light source and one or more optical receivers. When the light passes through the medium it is scattered, dispersed

and absorbed by the existing suspended particles, varying the electrical signal of the light detectors. This electrical value is then correlated to a turbidity value.

There are standardized methods for measuring turbidity, however, each measurement method uses a different unit. A multiplicity of turbidity units has been introduced because a change in the design, type of light source, detector and measuring angle will change the reading of the instrument. Thus, different turbidity instruments can produce different measurements in the same sample.

There are different standard water quality methods in use. The U.S. Environmental Protection Agency (EPA) has approved eight methods for drinking water monitoring. Until 2009, only four methods were accepted: EPA Method 180.1, Standard Method 2130B, Great Lakes Instrument Method 2 (GLI 2) and Hach Method. In 2009, the EPA approved four new methods: Mitchell Methods M527 and M5331, Orion AQ4500, and AMI Turbiwell. In addition to these, the United States Geological Survey (USGS) also uses other methods, such as the International Organization for Standardization (ISO) 7027. All these methods are used in water treatment plants for human consumption, offering high accuracy for low turbidity values.

For marine or river environments, where turbidity can have higher values, these devices become dysfunctional, not only because of their low dynamic range, but also because most are laboratory devices, making them large, expensive, and dependent on the electrical grid. Even though these instruments are not suited for *in situ* monitoring, their measuring methodology is the base for the following generation of *in situ* optical sensors.

EPA 180.1 is a turbidity measurement method approved to monitor the quality of water for human consumption [64]. This method uses nephelometric technology that measures diffused light at 90°, this is, the photodetector is positioned at 90° (±30°) to the light source (see Figure 5). To minimize differences in light scattering measurements, the light path from the light source to the photodetector is constricted to 10 cm. Additional receivers are allowed if the 90° angle prevails the most relevant. The light source used is a tungsten lamp with a colour temperature between 2200 and 3000 Kelvin. This means that the output is polychromatic (broadband spectrum).

The photodetector receives light with a wavelength of 400 to 600 nm. The broadband spectrum allows the instrument to be sensitive to smaller particles. This sensitivity means that a tungsten lamp source will provide a more accurate response than a monochromatic light source when measuring small suspended particles. However, it also makes the device more susceptible to coloured elements. If too much matter is absorbing different wavelengths, the accuracy of the sensor will decrease. Also, the use of the tungsten

lamp requires a daily calibration check and frequent recalibration due to the incandescent decomposition inherent to the lamp (as the lamp burns slowly, the light output decreases, changing the reading of the measurements).
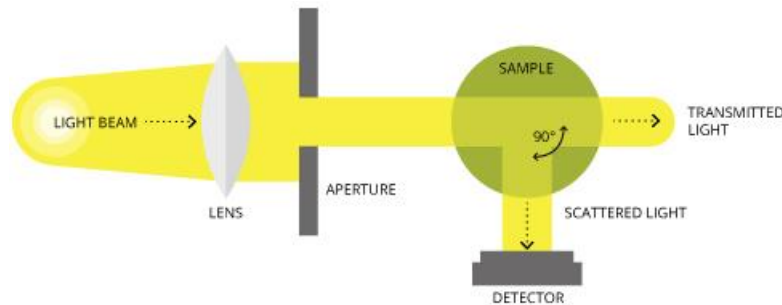
Figure 5. Illustration of the EPA 180.1 Method. A tungsten lamp with a colour temperature between 2000 and 3000 K illuminates the sample and a photodetector, placed at 90 ° to the light source, senses diffused light [65].

The EPA 180.1 Method uses nephelometric technology calibrated with a formazin standard. Thus, its units come in Nephelometric Turbidity Units (NTU). Instruments ruled by this standard are suitable for measuring turbidity levels between 0 and 40 NTU. At higher levels, the relationship between light scattering and turbidity becomes nonlinear. This means that the amount of stray light that can reach the photodetector decreases, limiting the capability of the instrument. The optimal condition for using this method is in samples without colour interference and low turbidity. However, if high turbidity samples need to be measured, the dilution of the sample is possible using the following equation [65]:

$$NTU = \frac{A * (B + C)}{C}$$ (12)

$NTU =$ turbidity value of the original sample (NTU)
$A =$ turbidity measured in the diluted sample (NTU)
$B =$ volume of dilution water (mL)
$C =$ volume of the sample taken for dilution (mL)

Standard Method 2130B was established by the American Public Health Association (APHA) for water and wastewater quality monitoring [66]. This method has only a few slight differences from EPA 180.1, so they are often confused. The components used and the design rules of the instrument are the same as the EPA 180.1. The differences relate to the definition of the primary calibration standard and the measuring range of the methods.

According to Standard Methods for Examination of Water and Wastewater, the only acceptable primary calibration standard is formazin, made from scratch by the user, following the specific instructions

described [67]. However, Method 2130B states that user-prepared formazin should be used as a last resource due to the use of carcinogenic compounds. Instead, they recommend the use of commercial or manufacturer-supplied calibration solutions, which are considered secondary standards. On the opposite, EPA 180.1 considers both user-prepared formazin and commercial formazin as primary standards and does not differentiate.

The second difference is the dynamic measuring range of the devices. EPA 180.1 sets the maximum measurement limited at 40 NTU, and for higher value measurements the sample must be diluted. Standard Method 2130B claims that its range extends to 1000 NTU and sample dilution should be avoided whenever possible as the composition of the sample may change, resulting in less accurate measurements.

The International Organization for Standardization has developed its nephelometric method known as ISO 7027 [68]. This standard attempt to ensure that turbidity devices have good repeatability and comparability. Although quite common throughout Europe, this method is not approved by EPA for drinking water regulations.

As with previous methods, turbidity is measured by diffuse light at 90°, and the difference relates to the spectral band of the light source. This method specifically requires a monochromatic light source, with a wavelength of 860 nm, and a spectral bandwidth of 60 nm. In most cases, instruments using this method use an 860 nm light-emitting diode (LED).

For the light detector, a 90° primary angle is required. Additional detection angles are also allowed, but the 90-degree nephelometric detector is the primary source of measurement. As for EPA 180.1, the light path distance is limited to 10 cm.

For turbidity levels between 0 and 40 NTU, the recommended unit for this method is the Formazin Nephelometric Unit (FNU). The USGS suggests that this method can be used up to 1000 NTU with a single photodetector, or up to 4000 NTU if additional detectors are used. For the last case, the used unit is the Formazin Nephelometric Ratio Unit (FNRU).

Both EPA 180.1 and ISO 7027 use nephelometric technology calibrated with the formazin standard. However, differences in the light source and slight differences in design create distinct measurement results. ISO 7027 has the advantage of using near-infrared light, which is less absorbed by coloured particles, thus reducing the error that a broadband light source has. In addition, LEDs are more stable over time than tungsten lamps. However, since longer wavelengths are less sensitive to small particle

sizes, this method produces turbidity readings slightly lower than the EPA 180.1 method for low turbidity values.

The GLI Method 2 doubles the number of light sources and photodetectors used in the previous methods, doubling the number of measurements and using it to cancel errors [69]. This method, also known as four-beam modulated turbidimetry, uses, for each measurement, an emitting source and two receivers positioned at angles of 180° and 90°. Alternating between active emitters changes the significance of each one in turn. It uses two 860 nm LEDs that alternate the pulses of light every half second. The photodetectors take simultaneous readings providing an active signal and a reference signal. The detector placed directly in front of the active LED is considered the reference signal, while the detector at a 90-degree angle is considered the active signal. Every half second, the active and reference signals alternate when the other LED pulses (see Figure 6).
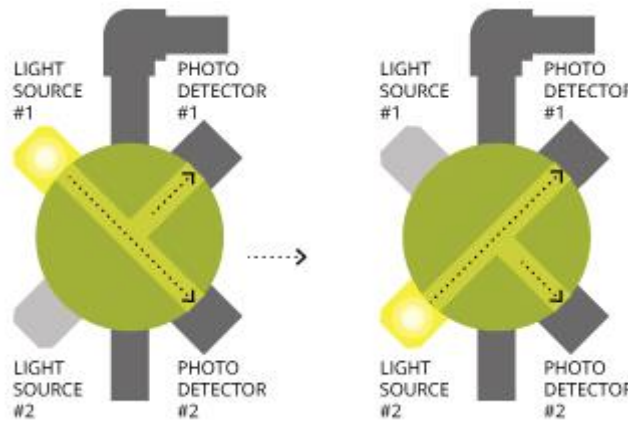
Figure 6. Illustration of GLI Method 2. When one of the LEDs is active, the leading receiver reads the reference signal, while the other captures the active signal. Upon turning off this LED and activating the other, measurements are repeated with the receivers assuming opposite roles [65].

Thus, GLI Method 2 provides two active and two reference measurements to determine each reading. Due to these differential measurements, errors that may appear are mathematically cancelled. The turbidity measured is calculated by the following expression:

$$NTU = Cal_0 * \sqrt{\frac{Ative_1 * Ative_2}{Reference_1 * Reference_2} - Cal_1}$$

(13)

NTU = turbidity value of the sample (NTU)

Cal_0 = calibration coefficient 0

Cal_1 = calibration coefficient 1

$Ative_1$ = 90 Degree Detector Current (Light Source 1 ON, Light Source 2 OFF)

$Ative_2$ = 90 Degree Detector Current (Light Source 1 OFF, Light Source 2 ON)

$Reference_1$ = Transmitted Detector Current (Light Source 1 ON, Light Source 2 OFF)

$Reference_2$ = Transmitted Detector Current (Light Source 1 OFF, Light Source 2 ON)

The GLI Method 2 allows higher sensitivity and error cancellation for turbidity levels between 0 and 100 NTU. However, its accuracy decreases as turbidity levels rise above 40 NTU due to the increase of scattered light. GLI 2 instruments are ideal for low turbidity ranges. When used on samples with turbidity levels between 0 and 1 NTU, they are extremely accurate.

Due to the multibeam design, the USGS recommend using Formazin Nephelometric Multibeam Unit (FNMU) instead of NTU. Instruments with this design are still classified as nephelometric technology due to the use of photodetectors at 90° angles.

Hach 10133 is a measurement method approved by the U.S. Environmental Protection Agency [70]. Based on nephelometric technology, this method uses light amplification by stimulated emission of radiation (LASER) as a light source, opposing to the tungsten lamp or infrared LED used by EPA 180.1 and ISO 7027, respectively.

The LASER emits red light with a wavelength between 630 and 690 nm, and the light path is limited to 10 cm. The photodetector is placed at 90° from the light source and is connected to a photomultiplier tube (PMT) through a fibre optic cable (Figure 7). The PMT is used to increase the sensitivity of the photodetector.
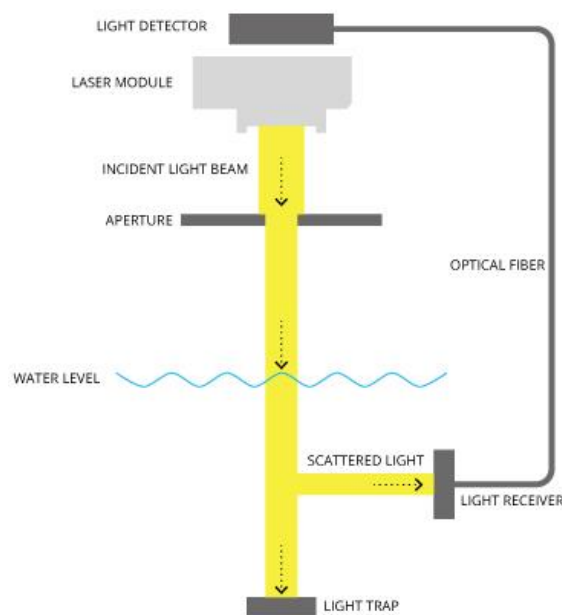
Figure 7. Illustration of Hach Method 10133, employing nephelometric technology for in-line monitoring. The detector is connected to a fibre optic cable to enhance instrument sensitivity.

This configuration allows the detection of very low turbidity levels. Due to the high resolution, its units are commonly expressed in milli Nephelometric Turbidity Units (mNTU). Thus, the recommended range for the instruments is 0 to 5000 mNTU (0 to 5 NTU). Unlike previous methods, the Hach Method 101033 was designed for in-line, or in-process, monitoring. Instruments following this method are ideal for fluids with very low turbidity such as drinking water or effluent in wastewater treatment plants.

Mitchell's methods are alternative testing procedures, approved by EPA in 2009, to measure drinking water turbidity. The term alternative test procedure refers to the use of EPA-approved nephelometric techniques without resulting in a completely new method. Thus, Mitchell's methods produce comparative results relative to the EPA 180.1 method. As Hach 10133, these technologies aim to be used for in-line monitoring.

For method M5271, the light source used is a LASER with a wavelength between 620 and 680 nm [71]. The M5331 uses a LED with a wavelength between 510 and 540 nm [71]. For both, the photodetector is placed at 90° with a margin of 30°, and the light path is limited to 10 cm. The major differences between these methods in comparison with the previous ones are the introduction of water bubble retention mechanisms and an anti-condensation window. Instruments conformed to these methods must be able to withstand up to 30 psi. Like the EPA 180.1 method, its measurement range is limited from 0 to 40 NTU.

The Orion AQ4500 method [72], developed by Thermo Fisher Scientific, is based on the use of the Thermo Orion AQUAfast turbidimeter model AQ4500 and is also an alternative test procedure for the EPA 180.1. This method uses one emitter and two spectrum receivers between 400 and 600 nm. The light source is a blue LED coated with phosphor. This configuration allows extending the 450 nm spectral band (blue) to "white" light. Thus, it has the same effect as the tungsten lamp of the EPA 180.1 method. The reason for using the LED instead of the lamp is the possibility of pulsating the emitting source at a high frequency, allowing synchronous detection. In this way, scattered light and inducted electronic errors can be corrected.

Two receivers sense the light: a nephelometric detector to measure turbidity and a transmitted light detector, placed at 0° from the emitting source, used as a reference for colour compensation (see Figure 8). The ratio between the two measurements results in the final turbidity value. Although the manual of this instrument claims that its measurement ranges from 0 to 4000 NTU, EPA only recognizes this

method for measurements up to 40 NTU. For turbidity values above this value, the sample must be diluted.
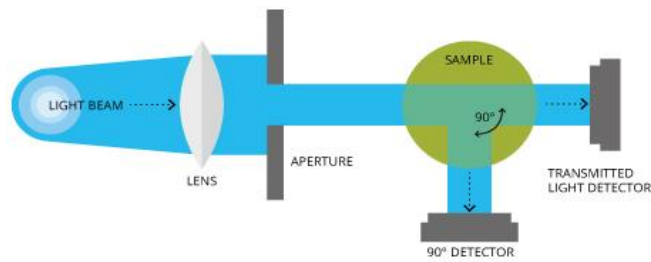
Figure 8. Illustration of the Orion AQ4500 method. A white LED emits light to the sample and the combination of values from the 90º and 0º receivers determines the final turbidity value [65].

The AMI Turbiwell, developed by SWAN Analytic Instruments, is also an alternative EPA-approved test procedure for continuous monitoring [73]. This turbidimeter has a unique property since it does not have direct contact with the fluid to perform the measurement. Also known as surface scatter, this method uses a reservoir, through which the liquid flows, with a thin glass opening that is exposed to a light source placed outside the tube (Figure 9). The emitted light is reflected by the particles in the liquid and sensed by a nephelometric receiver.
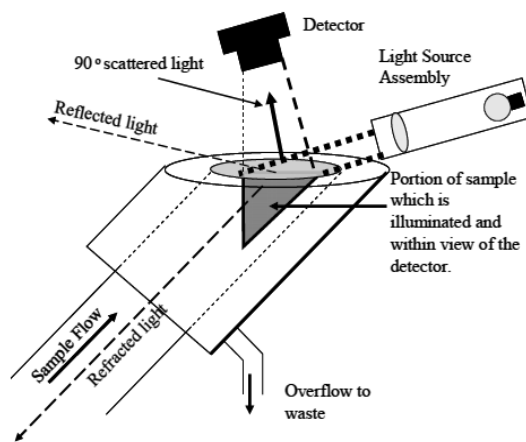
Figure 9. Illustration of a cross-section of an instrument following the AMI Turbiwell method. Water flows into an opening glass tube where measurements are made. A light source and nephelometric detector, placed outside the tube, are used to measure the turbidity [65].

The light-emitting source used is an LED with a spectral band of 400 to 600 nm and placed at 45° to the surface of the liquid. The photodetector is placed at 90° to the emitter and has the same wavelength sensibility. To be in accordance with the method, the sensed light cannot travel more than 10 cm. Although the method states that this system can be used for measurements up to 200 NTU, EPA limits it to 40 NTU.

2.2.1.2 Turbidity sensors for in situ monitoring

In the last decades, standardized turbidimeters have been optimized to increase their performance. However, when projected for *in situ* monitoring, they present some problems. First, most of the standardized methods are limited to 40 NTU. Rivers, coastal areas and estuaries can have high concentrations of suspended sediment in the water, so this range is not sufficient. Also, the standard methods are expected to be used for laboratory analysis or in-line measurements, which means that they are dependent on the electric grid, need human operation, are not suited for submersion, and, in many cases, are large, heavy and expensive. Nevertheless, they are the technological base used in the available optical turbidity sensors for *in situ* monitoring.

Due to the short dynamic range of the previous apparatus, a new light detection technique was introduced for *in situ* optical turbidimeters: the optical backscatter technology. Backscattering is the measurement of reflected light (scattered) by suspended sediment in the water. Opposite to the nephelometric technique, the light detector is placed at 135° related to the light source. This combination allows the measuring of higher turbidity levels, which is suited for environmental monitoring. To perform longstanding measurements in the field, other capabilities were optimized for these instruments: internal batteries, internal storage, electronic watertight, and, in some cases, biofouling protection.

Seabirds Scientific, Valeport and Seapoint Sensors are some of the most popular brands for oceanographic instruments, including optical backscatters. Hach and Hanna Instruments, are also recognized brands in this market. However, they primarily target wastewater treatment plants and other water treatment facilities. The commercial offer provided by these brands is wide, with different series of *in situ* turbidimeters with measuring ranges up to 4000 NTU and precision of 0.01 NTU.

Figure 10. Valeport Hyperion-T. Standalone commercial turbidity sensor that uses nephelometry technology for lower turbidity levels (0 to 1000 NTU) with a minimum detection level of 0.03NTU, and backscattering technique for higher values (1000 to 6000 NTU). The sensor is built in titanium housing and can be submerged up to 6000 m.

Although these devices are technologically suitable for *in situ* monitoring, they present a problem regarding their cost. Depending on the extras desired (battery, wipers, complementary sensors, etc.) its price typically ranges from 2000 € to 30.000 €, which is unpractical for massive deployments. Besides the price of these instruments, the difficulty of maintenance, installation, replacement and calibrations are pointed as some of the concerns of its users [74–75].

At the current time, the available *in situ* turbidimeters already offer the necessary measuring range, precision and speed for environmental monitoring. The technology based on transmitted light, nephelometry and backscattering detection has not changed. However, with the emergence of the Internet of Things (IoT) and smart sensors, the scientific community has gathered efforts to apply the available technology in the development of low-cost instruments [67–74]. These instruments usually measure turbidity using backscattering or nephelometry, are calibrated with standard formazin, have their unit in NTU, and cost less than 100 € in raw materials. However, most of the work presented in the literature presents devices confined to the laboratory and without field results. In many cases, the concerns about watertight or energy consumption, which are a requirement for *in situ* monitoring, are not even addressed. Additionally, there is a lack of comparison of these new devices with their commercial peers.

2.2.1.3 Acoustic turbidimeters

Besides the optical instruments, another technology can be used to estimate suspended sediment in the water: the acoustic turbidimeters, also known as Acoustic Backscatter Sensors (ABS).

Opposed to their optical peers, these sensors do not directly measure turbidity. The objective is to continuously measure the amount and size of suspended sediment in the medium, this is, to measure the total suspended solids in the water [84]. To do so, an emitter and an acoustic receiver are placed in the same plane and with the same orientation. The emitter generates acoustic waves that are reflected by the suspended particles flowing on the water. The reflected echoes are sensed by the receiver transducer (Figure 11). Acoustic turbidimeters process the power magnitude of the received echoes, estimating the amount and size of the particulate matter in the water [85]. Also, with the time of flight of the acoustic waves, it is possible to determine the distance to which the sediments are, thus obtaining a stratified measurement in depth.

The ABS technology presents significant advantages compared with optical turbidimeters: (i) it measures TSS instead of turbidity, which is a better estimation of suspended sediment concentration; (ii) it can

differentiate particulate size; (iii) decoding the frequency shift of the echoes it is possible to estimate water velocity, that correlated with the measurement of sediment concentration would provide data about sediment transport [86] (the acoustic sensors that measure water velocity are named ADCP and are presented in the next subsection). However, suspended sediment can take the most varied shapes, sizes and matter constitutions, resulting in different acoustic responses. The interpretation of echoes becomes difficult to decode, even with good calibrations [87–89]. Because of their low accuracy, ABSs have low acceptance when compared to optical technologies.
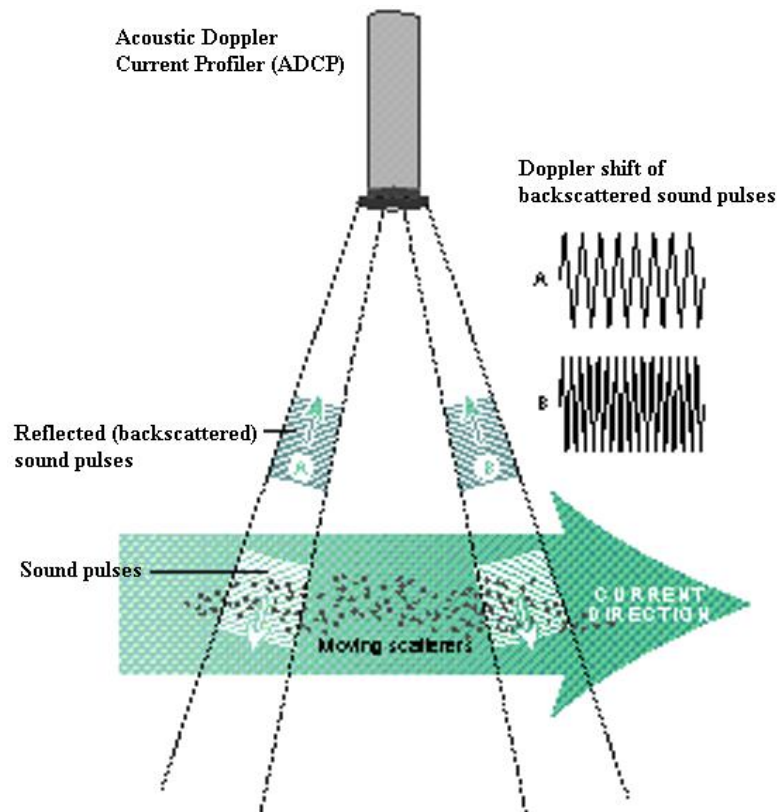
Figure 11. Illustration of the principle of operation of an acoustic backscatter. The instrument uses an acoustic emitter and receiver piezoelectric transducer. Upon actuation of the actuating transducer, the receiver will sense the acoustic echoes reflected by the surrounding sediment [90].

2.2.2 Water velocity

The water velocity, or flow velocity, is the second major component of sediment transport. It does not provide information about the sediment itself, but about how fast it moves and in which direction.

Supposing a turbidimeter taking records *in situ* measuring high turbidity values, it is not necessarily related to high sediment transport rates. High turbidity values are related to high concentrations of suspended sediment, but without water movement, there is no sediment transport. Similarly, lower

turbidity values can be related to high sediment transport rates and high water discharges. Sediment transport is the amount of sediment that passes through, and the water is the agent that makes it move.

The most basic sensor to measure water velocity is the mechanic anemometer. Historically used to measure wind, the same principle was adopted to measure liquids. The sensor consists of a rotating turbine in which the water flows. The higher the flux (or velocity), the faster it rotates. Typically, the turbine is ferromagnetic and generates electric impulses. The electric impulses are proportional to the rotating velocity of the turbine and so to the velocity of the fluid. While these instruments are commonly used in pipeline installations (in the water grid for example), their application for environmental purposes is difficult [91]. A sensor for continuous *in situ* monitoring needs to be submersible, and the watertight is complex when having moving parts such as the turbine. Also, the water of watersheds is not clean and the attachment of micro-organisms or mud on the turbine surface yields drifts in the measurements. Macro-biofouling is even more problematic since algae can attach to the device and completely stop the movement of the turbine.

2.2.2.1 Acoustic flow meters

The current standard technology used to measure water velocity *in situ* is by acoustic vibrations (ultrasound). Two working principles can be used: acoustic time-of-flight (ToF) sensors and Acoustic Doppler Current Profilers (ADCP) [92]. Both technologies use a piezoelectric emitter to generate acoustic waves (the piezoelectric material produces a mechanical vibration when excited with an electrical signal) and a piezoelectric receiver to sense the waves emitted (the piezoelectric material produces an electric signal when excited by a mechanical vibration).

The acoustic time-of-flight sensor is usually designed to have the emitter and receiver in parallel planes, with the fluid passing in between them. In other designs, both transducers can be confined in the same plane, and the plane parallel to the one the piezoelectric reflects the acoustic beam from the emitter to the receiver, as Figure 12 shows (direct transmission is not allowed for this typology) [91]. The velocity of the fluid is calculated using the time that the acoustic beam takes to reach the receiver. Since the acoustic waves propagate through the medium (in this case the fluid), the velocity of the beam changes with the velocity of the stream and is reflected in the measured time (time-of-flight).

The main disadvantage of the time-of-flight principle is that the velocity of sound is affected by the characteristics of the medium such as density, viscosity, temperature or pressure [93]. However, this

interference can be overcome using both transducers as emitter and receiver in turns (piezo 1 emits to piezo 2 and then piezo 2 emits to piezo 1). In this configuration, two times-of-flight are measured, and their subtraction cancels the effects of the medium (note that the time-of-flight decreases in the downstream direction and increases in the upstream).
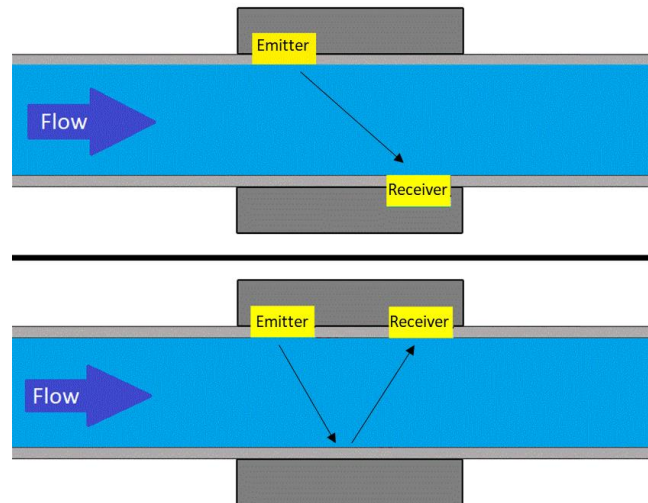
Figure 12. Illustration of two different designs of an acoustic time-of-flight current meter. In the image on the top, the emitter and receiver are in different planes and the fluid flows through them. In the image on the bottom, the emitter and receiver are in the same plane and a surface is used to reflect the acoustic beam.

The ADCP operates on the principle of the doppler effect (frequency shift) [94]. The piezoelectric emitter and receiver are in the same plane with the same orientation (same as the Acoustic backscatters, Figure 11). The emitter generates an ultrasonic beam into the stream flowing through the sensing area. The motion of the particles in the water causes a frequency shift in the beam, which is scattered to the second transducer. For a correct operation, there must be particulates in the stream, such as sediment or air bubbles, to reflect the ultrasonic beam [94]. The shift in the frequency of the echoes is proportional to the velocity of the fluid.

The design of the ADCP technology is more complex than the time of flight. Measuring frequency shift is more difficult than measuring time. Also, the ADCP relies on the echoes from small particles, so the frequency used for the piezoelectric is higher than for ToF meters (which requires more expensive transducers, more energy, and more sensitivity in the instrumentation circuit). However, because the ToF meters require a confined structure for the flux, the ADCPs have higher acceptance for environmental monitoring. Still, the major disadvantage of both technologies is their price, accuracy, and calibration in the case of doppler instruments.

2.2.2.2 MEMS flow meters

Over the past few decades, microelectromechanical systems (MEMS) have been demonstrating their potential in several areas. This technology offers small size, low cost and scalability that are not achievable using traditional engineering methods. Flow meters are an active topic of research with a focus on the areas of healthcare, physical activities, safety, medical, quality control and industrial applications.

The recent contributions of MEMS sensors to measure fluid velocities are usually in the size of the micro-scale. Nevertheless, it is possible to adapt the technology employed in these devices to bigger scales, suiting it for environmental monitoring purposes. The most important MEMS technologies in use for flow measurement are based on thermal, piezoresistive and piezoelectric principles [95].

Thermal flow sensors use heat transfer intensity to determine flow velocity. Three different sensing mechanisms can be used: hot-wire anemometry, calorimetry and thermal time-of-flight [96].

The hot-wire principle uses a heater (wire/resistor) supplied at constant power, or temperature, and measures its heat loss (left image in Figure 13). The heat loss has a direct relationship with the flow rate due to the thermal convection generated by the fluid. One of the challenges of this measurement is maintaining the temperature on the sensing element accurately [97]. Also, it allows measuring flow intensity but not direction.

Calorimetric flow sensors use two or more thermal sensors placed around a heater and measure the temperature asymmetry caused by the passing fluid (middle image in Figure 13). Therefore, this method measures the velocity of fluid indirectly. Unlike hot-wire sensors, calorimetric flow sensors have good performance in low flow rate measurement, but they saturate at high flow rates, which limits their dynamic range [98]. However, besides its intensity, calorimetric devices can also measure flow direction in both directions [99].
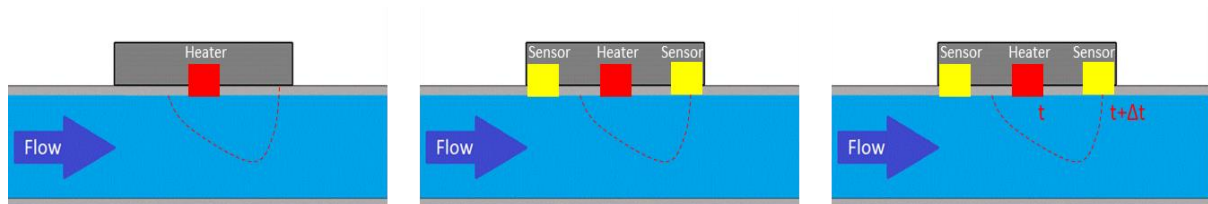
Figure 13. Illustration of the three configurations of thermal flow sensors. In the image at left, the hot-wire configuration: the heater is supplied at a constant power or temperature and the temperature loss is measured. In the image in the middle, the calorimetric configuration: thermal sensors placed around the heater measure the temperature variation. In the image at right, the heater is pulsed and the sensors measure the thermal time-of-flight.

Thermal ToF measurement uses the same principle as acoustic ToF but uses temperature instead of acoustic waves. The sensing element, placed at a defined position from the heater, measures the time that the temperature gradient takes to flow from the heater (right image in Figure 13). The temperature is transported by the fluid, so the flow velocity is directly related to the time measured [100]. This measuring principle allows measuring flow direction in different axes if multiple sensing elements are placed around the heater.

In general, thermal flow sensors are considered the most popular MEMS technology to measure fluid velocity due to their low cost, reliability, and accuracy. In addition, such sensors feature the advantage of being able to sense without the need for any mechanically moving components. However, sensing elements in traditional thermal sensors have a high specific heat capacity, making it hard to follow the weak heat convection transfer. This results in poor frequency response and difficult measuring of low flow rates. Also, MEMS-thermal flow sensor applications are often limited to a non-corrosive environment to prevent them from degradation and avoid irreversible damage, which limits their use in environmental monitoring.

Piezoresistive materials are also used in MEMS flow sensors. These materials exhibit a change in resistivity when subjected to external stress or strain [101]. This stress-resistance transduction makes the principle attractive to measure fluid velocity. In a piezoresistive flow sensor configuration, the drag and lift caused by the fluid bend a flexible surface (Figure 14). This surface comprises the piezoresistive material that changes its resistivity proportionately to the bending, which is indirectly related to the fluid velocity [102]. The higher the velocity, the higher the bending and the higher the resistive change.

The configurations of piezoresistive flow sensors have been evolving in the last decades from simple cantilevers [103–105] to bio-mimetic structures [106–108]. The scientific community have been making considerable attempts to use nature as a model for innovation and problem-solving. In the last few years, systematic studies have been conducted to understand various sensing mechanisms found in nature and to introduce increasingly sophisticated capabilities to artificial sensors and MEMS technology.

In particular for flow sensors, the lateral lines of blind cavefish have been a focus of study. With awareness of surrounding flow velocities, pressure, and its variations, the blind cavefish can perform rheotaxis, determine predator from prey, swim in groups, and navigate with high energy efficiency [109–110]. Several biomimetic lateral-line structures have employed an array of artificial piezoresistive hair sensors mounted on a substrate to improve the efficiency of water flow measurement by detecting underwater

pressure fluctuation [102–107]. In most bio-inspired sensors developed in the past, flow is measured by transferring the momentum induced by the water flow on a hair cell, which causes a deflection in the sensing membrane. This configuration makes it possible to build a densely distributed array of flow sensors with minimal intrusion to the flow field, which distinguishes them from other non-biomimetic MEMS flow sensors. These structures are intended to be robust to the harsh underwater environment while being sensitive to the flow around them. The major problem associated with this technology is the susceptibility that the piezoresistive material shows to changes in temperature and pressure.
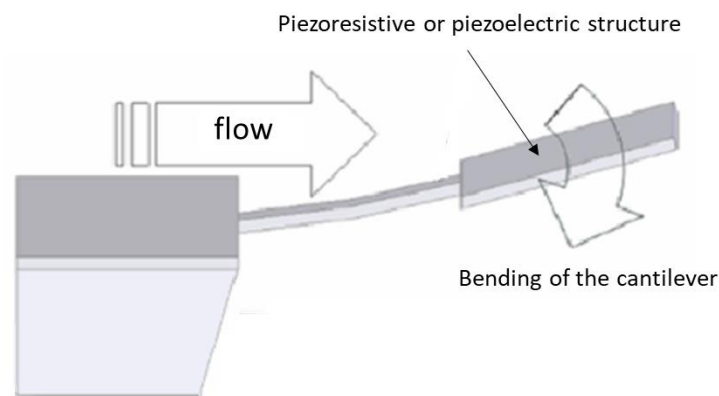
Figure 14. Illustration of a MEMS flow sensor based on cantilever structures. The flow induces a bending in the piezoresistive or piezoelectric structure that can be correlated with the flow velocity.

Finally, the piezoelectric flow sensors have similarities with the configurations of bio-mimetic piezoresistive devices but use piezoelectric material instead of piezoresistive [117–120]. As explained before, piezoelectricity is the property exhibited by dielectric materials, which develop surface distributions of electric charges when subjected to mechanical vibrations. Thus, the movement of the fluid causes a bend in the subtract, or hair cell, that produces an electric signal in the piezoelectric material [121–122]. Piezoelectric flow sensors are self-powered and hence, do not require a power supply to obtain the transduction output [123]. However, piezoelectricity needs mechanical movement to produce the electrical system. This means that this typology is ideal for sensing dynamic flow rather than static flow. Such sensors fail to detect static flow since they rely on the vibration of the fluid to generate the mechanical strain needed to produce a piezoelectric response.

2.3 Sediment deposition

Sediment deposition is the accumulation of sediment in the streambed that can no longer stay afloat. This sedimentary process has high relevance in estuarine areas, where the sediment tends to accumulate and have some residence time. Also, sediment deposition is enhanced with scour (re-suspension of deposited sediment) which is of great importance for river and marine-based structures. The monitoring of sediment deposition is essential, not only to support the project and management of maritime and fluvial infrastructures but also to protect aquatic life and safeguard its water quality [124]. Continuous monitoring is crucial for the quantification of sediment in the seaside zone and for understanding the evolution of the littoral.

Even though deposited sediment monitoring is an important variable in sedimentary studies, the current state of the art still relies on collecting field samples with mechanical systems such as bottles, traps, pump samplers or sample dredgers for posterior laboratory analysis [125–126]. These devices are simple containers that are placed in the streambed for a certain period. After the deployment, they are collected for posterior analysis of the sediment that was deposited during the test. In the case of the sample dredgers and pumps, the deposited sediment is collected from the streambed in real-time.

These techniques allow a full laboratory study of the sediment material and its characteristics. However, it is a time-consuming task that requires specialized equipment and staff, and it does not allow sedimentary processes to be observed with continuity, thus limiting their understanding. Also, the structural housing of the sediment bottles and traps causes hydrodynamic disturbance in the normal flow of the waterway, which difficult the natural sediment resuspension. Therefore, it provides a gross estimate of sedimentary rates. This problem opened space for new and automated instruments that aim to perform continuous monitoring of bedform evolution *in situ*.

The scientific community has been trying to overcome the lack of commercial instruments to continuously measure the accumulation of sediment on the streambed. Conductivity, optical and acoustic technologies have been employed to design new instruments and methods.

The measurement of deposited sediment by electric conductivity was first reported by P. V. Ridd in 1992 [127]. The sensor consists of a vertical array of ring electrodes along its length that measures conductivity, and it is intended to be buried in the streambed. The working operation of the instrument is based on the differences in conductivity of water and sediment. Later, a device was developed using a settling plate with two electrodes that change the electric conduction depending on the thickness of the accumulated

sediment [128]. In 2009, a new vertical array of electrodes was proposed using the electrical response of the sediment-water interface to find the sediment-water boundary [129]. Although these techniques are accurate, all of them require precise calibration and the sensor output is highly dependent on variables such as water depth, the conductivity of the medium and the sediment characteristics. Slight fluctuations of any of these parameters can significantly affect the accuracy of the readings.

An optical sensor to measure the thickness of sediment accumulation was presented using the backscattering technique to measure the amount of sediment that settles in a deposition plate [130–131]. The backscattered light power is used to estimate the amount of sediment accumulated over the plate. One of the limitations of the apparatus was the smoothness of the deposition plate, which resulted in rapid resuspension and made it difficult to make accurate measurements during high flows. An improvement of the instrument was presented in 2017, with a surface more closely approximated to the complex and typically rugose microtopography of coral surfaces [132]. The main problem associated with these instruments is that they can only measure the settled sediment and do not provide any information about resuspension rates or erosion.

Similar to the conductivity sensors, vertical optical arrays were also proposed to measure deposited sediment. First, in 1991, the Photo-Electronic Erosion Pin (PEEP) was presented [133]. Later, in 2015, the Surface Elevation Dynamics (SED) sensor was also proposed [134]. Both these two instruments use a vertical array of optical receivers to detect the boundary where the receivers can no longer detect natural light (the detectors that do not sense light are buried in sediment). Both sensors can continuously measure deposited sediment and erosion rates with a resolution of 2 mm. These instruments are dependent on natural light and cannot take measurements during the night, at high depths, or in water with high turbidity where the natural light cannot reach. Still, the PEEP, SED and SediMeter (a commercial optical sensor from Lincon, Inc. that uses the same technology) are the instruments used to assess bedform dynamics in the sedimentary studies presented at the current time.

In 2008, the PEEP-3T system was presented as an improvement of the original PEEP [135]. This new sensor has the same capabilities as the original PEEP but intends to measure bed erosion during the night using the thermal consonance timing (TCT) method. The basis of TCT is that near-surface vertical temperature gradients in sediment are normally more extreme than in the overlying water. Therefore, if a given space is occupied by sediment, strong temperature gradients, orthogonal to the surface, are developed across it. However, if erosion then removes that sediment and replaces it with water, temperature gradients across the same space reduce substantially. Consequently, the time of the switch

from strong to weak temperature gradients represents the time of the erosion event [136]. The PEEP-3T kept the same light-sensing design of PEEP and added two thermistors to measure the TCT, as Figure 15 shows.
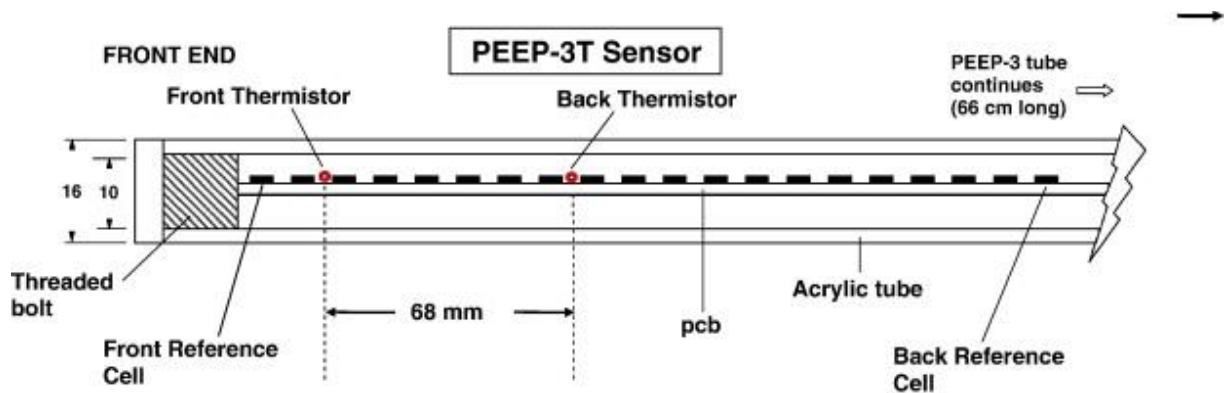
Figure 15. Illustration of the PEEP sensor, which consists of a vertical array of photodetectors (reference cells) to measure daylight. If the detectors do not measure light, it indicates that it is buried in sediment. The new version PEEP-3T added two thermistors to measure the thermal consonance timing and can detect erosion during the night when sunlight does not exist [135].

The use of TCT to detect streambed erosion was successfully validated with the PEEP-3T sensor. However, the data provided is rather qualitative than quantitative. The thermal sensing design of the sensor allows it to detect if erosion happened, but it does not provide a real measure as it does during the day. The need for daylight to have significant sediment deposition measurements was not overcome and the sensor did not have better acceptance than the original PEEP.

Acoustic technology has also been used to monitor bed elevation using underwater acoustic altimetry principles [137–138]. This technology is widely used in underwater remote-operated vehicles (ROVs) and autonomous underwater vehicles (AUVs) for seafloor mapping and underwater 3D reconstruction and was successfully applied to measure streambed elevation [139–141]. As seen before for turbidity sensors based on acoustics, this technology implies high costs and complexity. This technology usually requires an infrastructure to fix the sensor, so it is traditionally used to monitor scour in bridge piers and other fluvial and maritime infrastructures, but not usually employed in sedimentary assessments.

2.4 Anti-biofouling techniques

This subsection was published in "Design and *In situ* Validation of Low-Cost and Easy to Apply Anti-Biofouling Techniques for Oceanographic Continuous Monitoring with Optical Instruments", Sensors MDPI [142].

Biofouling, or biological fouling, is the accumulation of biological material from molecules to metazoans on surfaces. Soon after a structure is immersed in water (fresh or salty) it is gradually covered by organisms which may compromise the operation of the devices. In some cases, the biofouling formation is virtually instantaneous [143]. These organisms can be divided according to their size, into primary film (biofouling), micro-organisms (also called micro-fouling), and macro-fouling [144]. The succession of the fouling states can be divided into five main events [145]:

1. Absorption of organic and inorganic macromolecules immediately after immersion, forming the primary film.
2. Transport of microbial cells to the surface and the immobilization of bacteria on the surface.
3. Bacterial attachment to the substratum through extracellular polymer production, forming a microbial film on the surface.
4. Development of a more complex community with the presence of multicellular species, microalgae, debris, sediments, etc., on the surface.
5. Attachment of macroalgae and marine invertebrates such as barnacles or mussels.

The fouling formation is not standard, but a combination of different physical, chemical, and biological factors. The water properties (pH, salinity, temperature, conductivity, dissolved oxygen, etc.), hydraulic conditions, depth, season, and local fauna and flora species composition play a major role in the fouling development. Thus, while the formation of biofouling in the surfaces is certain, its development is difficult to predict [146].

Biofouling is of extreme importance for monitoring instruments. Even a small amount of biofilm in the sensing area can produce undesired interferences in the readings of the sensor, which can no longer provide reliable information. These interferences can result from the clogging of sections, membranes, or filters in mechanical sensors (as well as changes in the normal mechanical properties of MEMs sensors); contamination in chemical sensors (for example, macro-fouling in dissolved oxygen sensors); increasing resistance to heat exchange in thermal sensors; increasing of acoustic absorption and

consequent decrease in receiving power in acoustic sensors; and increasing of optical absorption and consequent decrease in receiving power in optical sensors [146–152].

Additional problems associated with biofouling emerge in the case of marine optical sensors where high optical transparency is required. Before deployment, calibrations are needed for the good operation of most monitoring instruments. Long-term monitoring can result in biological attachments in the surface of the sensor that may require hard mechanical cleaning methods, such as high-pressure water jets, brushes or chemical methods. These methods can modify the initial status of the sensitive area of the sensor, and consequently, make the comparison of the metrological responses of the sensor before and after the deployment difficult. Moreover, bad cleaning will have the same result [154].

Some commercial anti-fouling techniques are available and applied to oceanographic instruments. The most known are the biocide generation systems based on copper corrosion mechanisms or tributyltin (TBT) leaching [155]. Even though the use of TBT leaching has proven to be efficient, it presents adverse environmental effects and was banned for antifouling paints and ships' hulls [156]. Thus, protections based on TBT leaching cannot be considered a solution for biofouling protection.

Nevertheless, copper biocide properties can still be used to protect monitoring instruments. This protection, usually called "copper shutter", uses a copper housing with a mechanism with a motor driver and a shutter that only opens to take measurements. The sensor is kept inside the copper shutter, which remains closed while the sensor is not taking measurements, in the darkness, and allows biocide concentration to increase, thus preventing biofilm formation [157].

Another mechanical anti-fouling technique, and the most common in use for commercial instruments, is the use of wipers or scrapers in the sensing area [157–158]. This technique is effective if the wipers or scrapers are in proper condition and the sensor head is suited for the cleaning process. The major disadvantage of these mechanical systems is the complexity of the watertight needs of the mechanical moving parts. This technique must be implemented in the early stages of the sensor development and cannot be adapted to old ones. Additionally, the motor used to move the mechanical gears needs energy from the batteries, which decreases the operation time of the instrument.

New technologies have been presented in the recent literature to reduce the impact of biofilm, as well as ways of controlling its presence on the surface of sensors. Different active techniques based on ultraviolet [159–161], laser [162–163], direct electrification [164–165], bubbles [167], or acoustics [167–169]

were demonstrated to be effective but presented high energy requirements for continuous and long-term monitoring.

Another active technique is based on the use of chlorine, both by *in situ* production by salty water electrolysis and by bleach injection [170–171]. Primarily used in industrial applications, chlorine techniques have recently migrated to oceanographic instruments, as is the case of Wet Labs/Sea-Bird WQM (the device uses a reservoir for the chlorine solution and a pump to inject it into the surface of the sensor), or electrolysis chlorination systems in monitoring stations [173]. Other techniques based on chlorine production, that focused on protecting only the sensing area of the instrument, have been presented [174]. These techniques have less energy needs and are more compliant with long-term monitoring power requirements.

Finally, nano-coatings of the glass surface, coatings of the sensing area of the sensors or bio-mimetics shapes and materials are emerging techniques that have shown their potential mostly in laboratory experiments [174–178].

Even though biofouling is far from being a problem solved, many techniques have been presented in the last decades to extend the deployment time of monitoring instruments. However, many of them are also still restricted to laboratory conditions and sea truth validation of their reliability is still needed.

3 TECHNOLOGY DEVELOPMENT

As explained in the previous chapters, there is a need for automatic instruments to monitor the sedimentary dynamics *in situ*. The sedimentary processes were divided into sediment transport and sediment deposition and erosion. As explained before, three variables must be measured to provide a full study of these processes: turbidity (or suspended sediment concentration), water velocity and sediment accumulation and erosion on the streambed. An additional variable, the water depth, was taken into account to monitor tidal cycles, which are one of the agents for sediment circulation in estuarine areas.

This chapter reports the technological development of new and innovative apparatus and methods to measure these variables. The development from scratch of these sensors is disclosed, presenting the mechanical and electronic designs, laboratory and principle of operation experiments, and the decision-making during the process. During the engineering development stage, and aiming for the *in situ* operations, the new instruments were idealized to have the following characteristics:

- Reliability: the most important characteristic of the developed sensors is to provide reliable and consistent data of their measurements, with the appropriate measuring range and resolution for their application.

- Watertight: to perform continuous monitoring *in situ*, the sensors must be able to operate underwater for days. Thus, the watertight of the electronics is necessary.

- Energy-efficiency: the lifetime of the sensors, without the need to change batteries, is essential for long-time monitoring and reducing maintenance costs.

- Cost-efficiency: one of the problems of the available commercial sensors is their cost. The new sensors must be concerned with providing similar results to their commercial peers while reducing their material costs to allow massive replication.

- Reduced size and weight: the sensors must be small and light to be easy to transport and install, reducing logistics complexity and costs.

Besides the sensors, the development of anti-biofouling techniques for optical sensors and data loggers are also presented. The data loggers were essential during field experiments to host multiple sensors, process and save data with time and date and, in some cases, send data in real-time to an online platform.

3.1 Water depth and temperature sensors

While it is not one of the variables selected to evaluate sedimentary processes, the water depth, or water level, is an important measurement for field experiments conducted in estuaries and other areas where sediment is exposed to tidal cycles.

The MS5837-30BA is an I2C digital integrated circuit (IC) that measures temperature and absolute pressure with an operating range of -20 to +85 °C and 0 to 30 bar, and resolution of 0.008 °C and 0.2 mbar, respectively. It is a low-power (3 V, 0.6 µA) and small-size device (3.3 x 3.3 x 2.75 mm) that costs less than 8 €. The integrated circuit itself is not suited to be submerged, but its fabricant (TE Connectivity) states that the *"sensor is optimized for water depth measurement systems with a resolution of 0.2 cm"*. The adaption of the IC to work underwater is possible, and it was done by BlueRobotics, which sells its *Bar30 High-Resolution 300m Depth/Pressure Sensor* that uses the MS5837-30BA (Figure 16).

Due to these characteristics, the MS5837-30BA was adapted for water submersion and integrated into the developed sensors. It provides data about water temperature and depth (calculated using the measured pressure).

Figure 16. From the left to the right, the figure presented the MS5837-30BA IC and the depth sensor from BlueRobotics.

3.2 SPM Sensor – turbidity and suspended particulate matter

Parts of this subsection were published in "Development of a Cost-Effective Optical Sensor for Continuous Monitoring of Turbidity and Suspended Particulate Matter in Marine Environment", Sensors MDPI [180] and "Optical device for *in situ* monitoring of suspended particulate matter and organic/inorganic distinguish", IEEE/MTS OCEANS Marseille 2019 [181].

The SPM sensor aims to continuously monitor turbidity and suspended particulate matter *in situ*. Illuminating an aqueous sample containing undissolved matter, the emitted light is subjected to attenuation, diffraction and reflection caused by the particles that obstruct the passage of light. Using

optical transducers (light-emitting source as actuator and photodetectors as receivers), a correlation can be established between the electric value sensed by the optical receivers and the turbidity or concentration of suspended sediments in the sample.

The selection of the transducers is crucial for the correct operation of the sensor. The infrared (IR) wavelength was selected (940 nm) due to its lower susceptibility to the colouration of the particles. This wavelength is also outside the optical absorption range of organic matter (typically ultraviolet, green and blue). Moreover, it is expected less ambient light interference due to the higher light absorbance from water in this wavelength when compared to the visible spectrum.

LEDs were selected to use as light-emitting sources due to their low cost and wide commercial offer. In addition, LEDs present a faster response than lamps, allowing light to be pulsed at high frequencies. Also, compared to LASERs, LEDs require less maintenance and present fewer calibration problems. As optical receivers, and to implement the light-electric transduction, three phototransistors in different positions related to the emitting source were used, providing backscattering, nephelometric and transmitted light detections. The optical transducers were positioned in a radial configuration with a 3 cm diameter, as demonstrated in Figure 17.
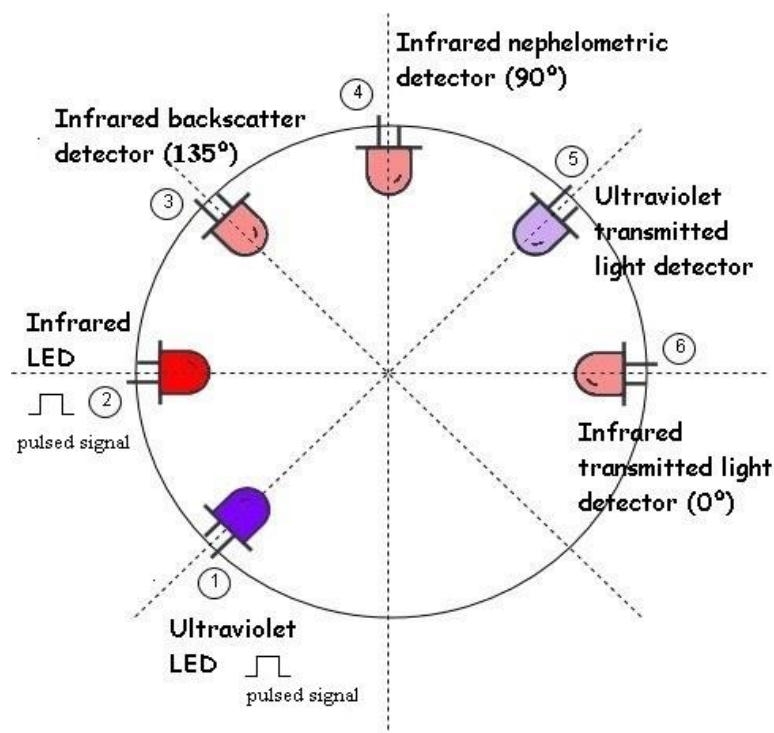
Figure 17. Illustration of the design schematic of the positions of the optical transducers. It showcases the IR LED (2) and three types of detection: backscatter (3), nephelometric (4) and transmitted light (6). Additionally, the UV emitter (1) and wideband receiver (5) are presented. Different receptor positions relative to the light source result in distinct electrical responses.

43

For the backscattering light detection technique, a photodetector (Figure 17 (3)), is placed at 135° to the light source (Figure 17 (2)), to sense the light scattered from the suspended sediment in the fluid. For distilled water, this type of detection has a zero-optical sensing value (there are no obstacles reflecting the light). With the increase of turbidity and consequent increase of suspended sediments and reflections, the detected light output increases. The advantage of this type of detection is the wide measuring range and accuracy for high turbidity values. On the other hand, for low turbidity values, backscattering is not as accurate as nephelometric detection. The backscatter detection strongly depends on the size, composition and shape of the suspended particles [182].

The nephelometric detection measures the diffracted light at 90° (Figure 17 (4) and (2)). As for the backscatter technique, for distilled water, the absence of optical obstacles results in a null optical value, which will increase with the increase of suspended particles. However, for high turbidity values, the reflected light is absorbed by the materials and the output decreases. The nephelometric detection is particularly accurate for low turbidity and depends mostly on the size and number of particles in suspension [183].

The transmitted light detection is the measurement related to the absorbance of light and uses an optical detector at 0° in relation to the light source (Figure 17 (6) and (2)). For distilled water, the detector has a maximum output value, that will decrease with the increase of turbidity (particles will absorb and scatter the light on its path). This technique presents higher sensibility, offering a wide dynamic range. On the other hand, it is vulnerable to colouration and particle size, which results in lower precision [184].

Finally, an ultraviolet (UV) emitter and wideband receiver (Figure 17 (1) and (5)) are used to distinguish organic from inorganic matter. These two types of matter present different behaviours to different wavelengths. Compared to inorganic matter, organic compounds have a higher ultraviolet/infrared absorption ratio [185]. Considering this, discrimination between different types of matter may be possible using the absorption values of infrared and ultraviolet transmitted light detectors. Instead of UV, other wavelengths could be used. However, since most marine phytoplankton and chlorophyll have fluorescence in green, blue and yellow, it could produce associated errors in the measurements [186].

3.2.1 Hardware design

A small-size PCB (Supplementary Material II 1) with the electronics was designed to be assembled inside the sensor housing. The PCB comprises the power circuit, low-power microprocessor, actuation circuit

for the LEDs, instrumentation circuit for the photodetectors and RS485 communications. Figure 18 shows a scheme of the electronic circuits and the complete schematics can be consulted in Supplementary Material I 1.
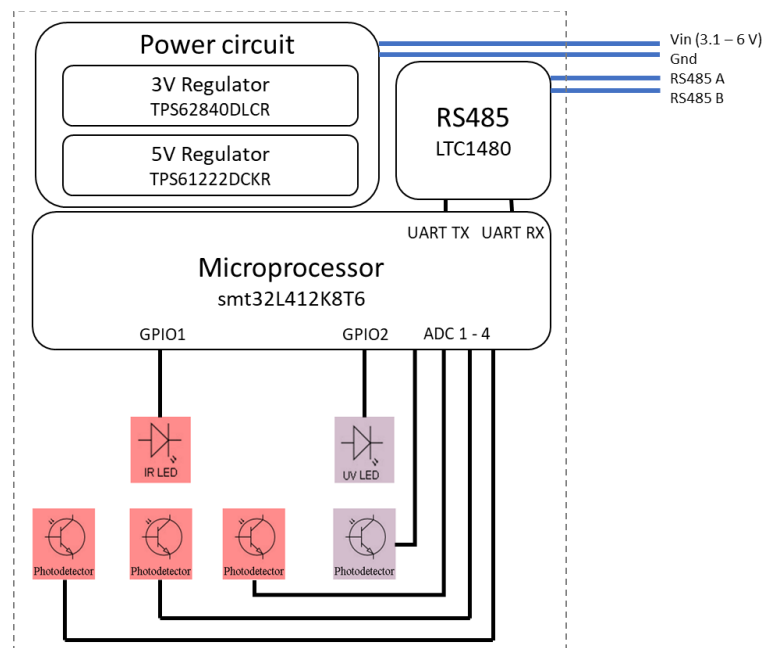
Figure 18. Illustration of the electronic scheme of the sensor. The sensor is powered by an external source and uses an RS485 bus for data transmission (complete electronic schematic in Supplementary Material I 1).

The sensor uses one VSLY5940 infrared LED with 940 nm wavelength, 600 mW/sr radiant intensity at 100 mA and ±3° emitting angle, and one VAOL-5GUV8T4 ultraviolet LED with 385 nm wavelength, 80 mcd luminous intensity at 20 mA and 30° emitting angle. Since LEDs are in contact with water, instead of air, different refraction can occur. The emitting angles tend to be larger than expected since water has a higher refractive index.

To match the IR light source, three W53P3C phototransistors are used as IR photodetectors (central wavelength of 940 nm, 20° view angle and 100 nA dark current). To match the ultraviolet light source is used one TEPT5700 phototransistor with a wavelength peak of 540 nm (a UV optical filter can be used for better selectivity), 50° view angle and 3 nA dark current.

Each phototransistor uses a serial resistor as a current-to-voltage converter (the value of the resistor depends on the desired electronic gain). The four analog signals provided by the photodetectors are read by the microprocessor that also turns the LEDs on and OFF using a DMG6968U-7 Metal Oxide Semiconductor Field Effect Transistor (MOSFET). The STM32L412K8T6 microprocessor was selected due to its cost, low power in standby mode (32 nA) and accurate 12-bit channel analog-to-digital converter

(ADC). The ADC of the microprocessor is used to measure the phototransistors' outputs with the LEDS ON and OFF. The OFF readings are used to correct the measurements to external light sources.

The sensor is powered by an external source, such as a 3.7 V lithium polymer (LiPo) battery, and uses two DC-DC converters to regulate the input voltage to 3 V and 5 V. The maximum input voltage of the developed sensor is 5.5 V. The boost-converter TPS61222DCKR (0.7 to 5.5 V input voltage and 0.2 µA shutdown current) regulates the 5 V and supplies the UV LED that has a 3.6 V forward voltage. The remaining electronic is supplied with 3 V regulated by the step-down converter TPS62840DLCR (6.5 V maximum input voltage, 750 mA maximum current and 60 nA quiescent current). The sensor transmits data using an RS485 bus. The low-power transceiver LTC1480 provides the UART - RS485 interface. The RS485 protocol theoretically allows up to 32 drivers in one system, supporting communications over distances of up to 1200 meters, and can keep baud rates from 110 to 115200 bps.

With this configuration, the SPM sensor presents a power consumption of 400 mW when taking measurements (5 ms active time) and 60 µW in sleep mode.

The structural housing of the sensor is 3D printed in polylactic acid (PLA) or acrylonitrile butadiene styrene (ABS) materials and comprises the LEDs and photodetectors presented in Figure 17 and the printed circuit board. A U-shape housing was first designed and later it was changed to an L-shape for less interference with the natural stream flow during the field experiments. Photographs of the two types of the SPM Sensor are presented in Figure 19. The corresponding mechanical drawings can be consulted in Supplementary Material III 1 and Supplementary Material III 2.

Figure 19. The top images showcase U-shape SPM Sensors and the bottom image displays a set of L-shape SPM Sensors.

The interior of the housing is filled with epoxy resin (HB EPOSURF2—HBQUIMICA) or polyurethane material (HB R 16/25—HBQUIMICA) to be watertight and protect the electronics from water infiltration. Both materials demonstrated good performance for waterproof needs. A four-core electric cable is used with the power and RS485 communication lines to be connected to an external data logger.

The SPM sensor has a production cost below 20€ including hardware components and structural materials.

3.2.2 In-lab calibration

Different laboratory calibrations were conducted to prepare the sensor for the *in situ* measurements. The mathematical correlation between turbidity or SPM and the electrical output of each photodetector is presented, as well as the methodology for distinguishing organic from inorganic matter. The calibration procedure to eliminate the external light influence, that affects the measurements, is also demonstrated. Tests for different water temperatures (5 to 35 °C) and salt concentrations (0 to 60 g/L) were also conducted to assess possible interferences with the output of the sensor, but no changes were registered.

The following subsections describe the methodologies for the different calibrations of the SPM Sensor. The data presented are representative of a single calibration. This means that new replicas and new calibrations before and after *in situ* experiments may produce different results.

3.2.2.1 Suspended sediment concentration (inorganic matter)

This calibration is conducted to match the output of the photodetectors to the concentration of suspended sediments, in g/L, as recommended by Gibbs [187], Downing [188], Zaneveld et al. [188] and Boss et al. [189], among others. Seashore sand collected from the field was used. A calibration for two different sizes of sand (180 μm and 350 μm) is presented to understand the differences in the responses of the photodetectors.

A 3 L volume of distilled water was used as the first sample and measurements were made with increments of 30 g (10 g/L) of sand, up to a maximum of 420 g. For each concentration, 20 measurements were recorded to calculate its mean and standard deviation. The test setup included an opaque container to eliminate the external light effects and a mechanical mixer to keep the particles suspended and generate a homogeneous mixture (Figure 20).

Mechanical mixer

sensor
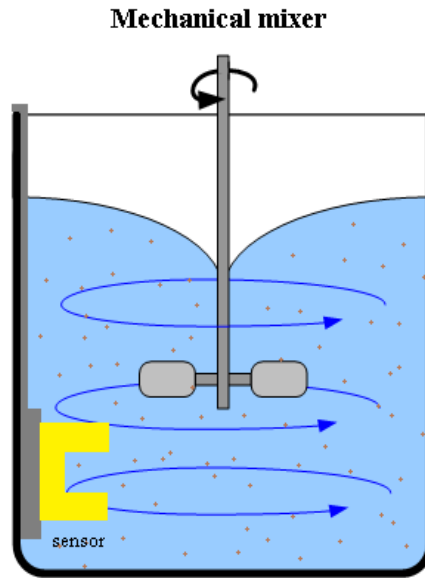
Figure 20. Illustration of the calibration setup using seashore sand. The measurements were taken in an opaque container to eliminate the external light. The mechanical mixer was used to keep the particles in suspension throughout the process.

The calibration results for 180 μm and 350 μm seashore sand are shown in Table 1 and Table 2, respectively.

Table 1. Mean and standard deviation results for the calibration with 180 μm sand. For each concentration, 20 measurements were recorded for statistical analysis.

	IR backscatter (V)		IR nephelometric (V)		IR transmitted (V)		UV transmitted (V)	
g/L	mean	σ	mean	σ	mean	σ	mean	σ
0	0,186	0,020	0,41	0,012	2,046	0,016	2,075	0,018
10	0,234	0,082	0,527	0,035	1,553	0,215	1,382	0,185
20	0,327	0,023	0,61	0,109	1,235	0,119	0,649	0,153
30	0,352	0,026	0,635	0,046	0,952	0,102	0,356	0,083
40	0,361	0,029	0,664	0,042	0,889	0,092	0,254	0,051
50	0,396	0,093	0,654	0,087	0,659	0,093	0,122	0,033
60	0,425	0,034	0,654	0,101	0,576	0,091	0,015	0,027
70	0,42	0,080	0,635	0,081	0,444	0,081	0	0,012
80	0,469	0,037	0,566	0,053	0,474	0,073	0,01	0,007
90	0,483	0,034	0,527	0,084	0,405	0,084	0,02	0,011
100	0,493	0,056	0,503	0,039	0,381	0,105	0	0,007
110	0,493	0,043	0,464	0,119	0,288	0,046	0,005	0,011
120	0,522	0,090	0,435	0,056	0,264	0,059	0	0
130	0,483	0,057	0,415	0,110	0,225	0,049	0	0
140	0,503	0,039	0,396	0,058	0,19	0,058	0	0

Table 2. Mean and standard deviation results for the calibration with 350 μm sand. For each concentration, 20 measurements were recorded for statistical analysis.

	IR backscatter (V)		IR nephelometric (V)		IR transmitted (V)		UV transmitted (V)	
g/L	mean	σ	mean	σ	mean	σ	mean	σ
0	0,205	0,019	0,464	0,027	2,144	0,028	2,051	0,022
10	0,229	0,036	0,61	0,072	1,724	0,174	1,675	0,278
20	0,269	0,065	0,698	0,065	1,494	0,200	1,235	0,249
30	0,288	0,072	0,757	0,061	1,265	0,189	0,752	0,236
40	0,366	0,084	0,825	0,078	1,079	0,133	0,547	0,142
50	0,366	0,098	0,791	0,050	0,918	0,060	0,4	0,138
60	0,425	0,043	0,84	0,087	0,718	0,199	0,137	0,180
70	0,41	0,041	0,801	0,056	0,562	0,085	0,107	0,166
80	0,449	0,051	0,854	0,049	0,498	0,101	0,059	0,141
90	0,469	0,099	0,869	0,083	0,396	0,204	0,039	0,049
100	0,508	0,093	0,894	0,066	0,293	0,058	0,015	0,079
110	0,498	0,088	0,903	0,052	0,273	0,045	0,029	0,026
120	0,444	0,044	0,84	0,087	0,237	0,055	0	0,014
130	0,415	0,039	0,859	0,071	0,225	0,052	0	0,007
140	0,444	0,051	0,762	0,052	0,215	0,035	0	0,007

The mean values of the electric output of the four light detections are rearranged in the graphs of Figure 21 for easier visualization. All the techniques present the expected theoretical behaviour described before: with the increment of the suspended particles in the sample, the electric output of the transmitted light techniques decreases and the electric outputs of the nephelometric and backscattering increase. For the nephelometric technique is also possible to observe the decrease of the electric output due to the light absorption at high sediment concentrations.

The fluctuations in the measurements are originated by the movement of the particles due to the mechanical mixer and the fact that the sample is not homogeneous. It is also important to notice different particle sizes produce different responses in the output of the sensor, which means that the characteristics of sediment must be considered for every course of action. This is an ideal example of why is difficult to standardize the turbidity parameter and compare measurements from different turbidity units and different sensors.

A mathematical expression based on the calibration results was developed for each detection to correlate the SPM, expressed in g/L (*pm*), as a function of the electrical value output of the receptors in Volt (*v*), for 180μm and 350μm sand. These equations are introduced in the firmware of the sensor to estimate suspended sediment concentration *in situ*.

Figure 21. Output voltages of the photodetectors for different concentrations of 180 and 350 μm seashore sand. The three IR techniques are presented (backscattering, nephelometry and transmitted light) as well the UV transmitted light detection. The mathematical fitting of the curves of interest is presented.

Different methodologies can be adopted to estimate sediment concentration *in situ*. Each one of the detection techniques can be used as a standalone or a combination of two or more techniques can be employed. For the combination methodologies, it can be used the mean or weighted sum of the different techniques, or it can be predefined by the use of a specific detector for different levels of sediment concentration (for example, nephelometry for low concentrations and backscattering for high concentrations).

3.2.2.2 Organic matter

The SPM sensor was designed with IR and UV transmitted light channels to distinguish organic from the inorganic matter due to the different responses of matter to infrared and ultraviolet wavelengths. A generic calibration becomes impractical due to the great variability of absorption properties of the organic matter

that may exist [183]. Therefore, a proof of concept is presented to show that distinguishing organic and inorganic matter is possible.

The sensor was submerged in 400 mL of distilled water and a solution of phytoplankton was used to increase the organic matter in the sample. This phytoplankton solution had its origin in an *in vitro* culture and its concentration is unknown. The objective of the experiment was to prove that the IR/UV ratio changes with the increase of organic matter.
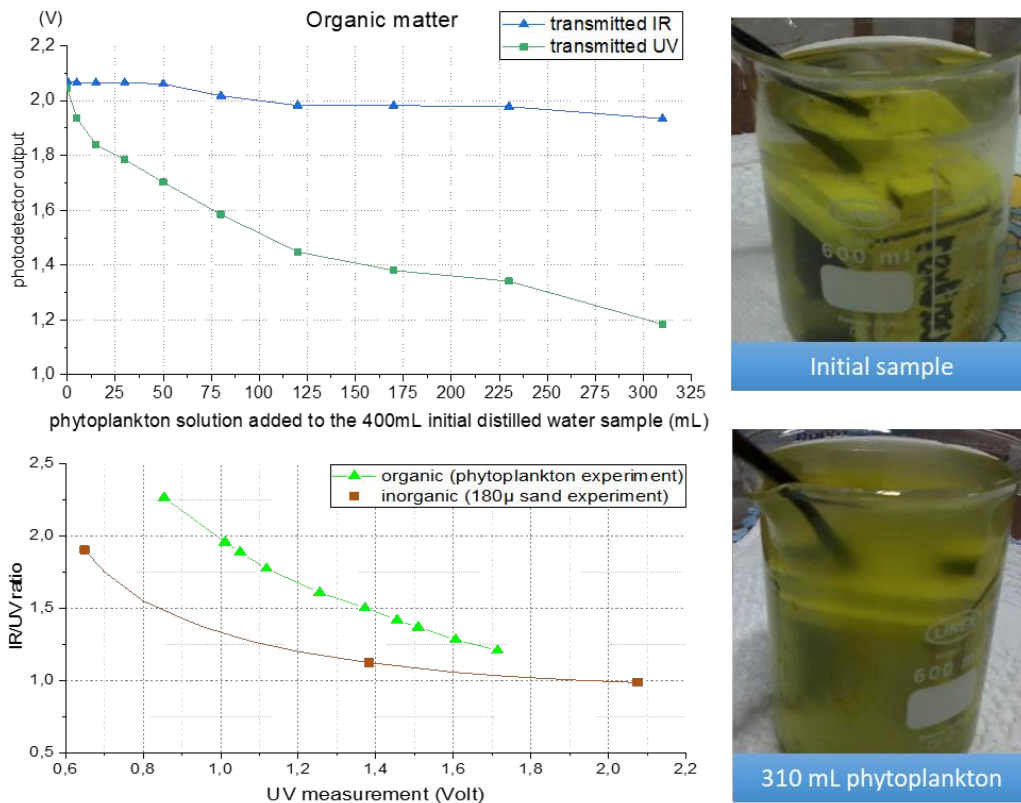
Figure 22. Top Graph: Transmitted IR and UV outputs with the addition of organic matter (phytoplankton) to the sample. Bottom Graph: Comparison of IR/UV ratios for the phytoplankton experiment (absorption ratio with organic matter) and the experiment with 180 μm sand presented in Figure 21 (absorption ratio with inorganic matter). Right Images: Visualization of the solution with distilled water and after adding 310 mL of phytoplankton solution.

The top graph of Figure 22 shows that, for the organic matter, the light absorption in the UV range is higher than in the IR wavelength. The ultraviolet transmitted light detector presents a higher voltage drop compared to the infrared one, which shows a slow decrease due to the reduction of the sample transparency. Analysing the bottom graph of Figure 22, it is observed that the UV light attenuation is higher with organic matter (data from the phytoplankton experiment) than with inorganic matter (data from the calibration with 180 μm sand presented in Figure 21). Thus, the IR/UV ratio can be calculated and used to estimate the amount of organic matter in the concentration of suspended sediment.

The overall concept of the IR/UV ratios works. However, the practical estimation *in situ* is more complex. This methodology is a good tool for qualitative analysis of the suspended sediment composition. To target quantitative estimations, it is necessary to know the characteristics of the organic compounds expected and perform a similar calibration with that matter. Nonetheless, it is important to understand that a slight difference in the organic compounds used during the calibrations and found in the field can produce errors in the IR/UV ratio.

3.2.2.3 Turbidity

The SPM Sensor was calibrated with formazin to enable the comparison with commercial instruments. A 4000 NTU Turbidity Formazin Standard was used to calibrate the sensor to Nephelometric Turbidity Units (NTU). The initial 4000 NTU solution was diluted with deionized water to make samples with lower turbidity. The dilution followed the methods and procedures of the Hach Water Analysis Guide [190]:

$$Dilution_{factor} = \frac{volume_{total}}{volume_{sample}} = \frac{volume_{deionized\_water} + volume_{NTU\_sample}}{volume_{NTU\_sample}} \qquad (14)$$

For this calibration, a new methodology is demonstrated. Unlike the calibration with suspended sediment, where each detection was treated individually, for the turbidity calibration an algorithm was developed to combine the four photodetector outputs. It is important to note that both data processing can be.

The turbidity output ("calculated turbidity" in Figure 23) was calculated using the mean value of the four photodetectors' outputs. Each output was first scaled to a 0 – 100 % reading. The reading from transmission IR and UV detectors was inverted, due to the decrease of voltage with the increase of turbidity: 0% was calculated with a 100% voltage reading and vice-versa (the voltage output of the backscatter and nephelometric detectors increases with the increase of turbidity but decreases for the transmitted techniques). The mean of the four detecting technologies was then applied.

Turbidity was calculated with a linear regression in the logarithmic scale, i.e., using the logarithm of the sensor output to calculate the logarithm of turbidity (NTU). The dashed line in Figure 23 presents the ideal calibration. The calibration results show that the maximum voltage reading value of the sensor has not been reached with the 4000 NTU sample, so even higher values could be measured. For the lower part of the dynamic range the sensor theoretically measured 0.1 NTU. However, the results also show an uncertainty from 1 to 2.5 NTU.
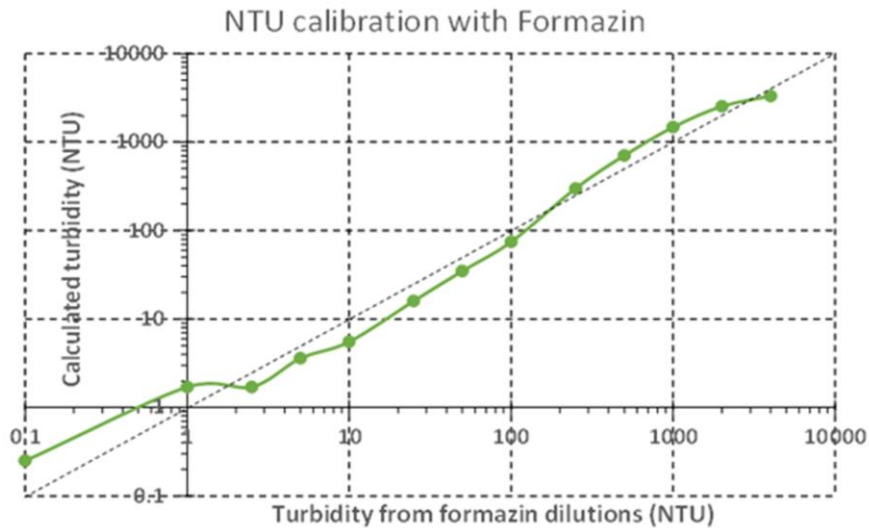
Figure 23. Results for the calibration with formazin with samples from 0.1 to 4000 NTU combining the three different light detections.

3.2.2.4 External light

Since the SPM sensor uses optical technology, the external light, such as daylight, has a clear influence on the measurements. Despite using pulsed light and the output differences with LEDs ON and OFF, if an external light reaches the photodetector, it produces a voltage offset. This happens due to the non-linearity of light versus output of the detectors. This effect is important for *in situ* measurements, where daylight or other natural or unnatural light sources can interfere with the measurements of the instrument.

The sensor was submerged in water with a white light source illuminating the sample at an increasing power (the offset produced by the external light was increased while the turbidity of the sample remained the same). The measurements of each photodetector with the corresponding LED ON and OFF were recorded.

Figure 24 presents the infrared transmitted light detector output, with the infrared LED ON and OFF, as a function of the external light. The value 0 % corresponds to the dark current of the phototransistor and 100 % when it is saturated.

The results show that the difference between the turbidity value (LED ON) and the offset produced by the external light source (LED OFF) is not constant. Thus, the sensibility of the turbidity sensor decreases with the increase of the external light.
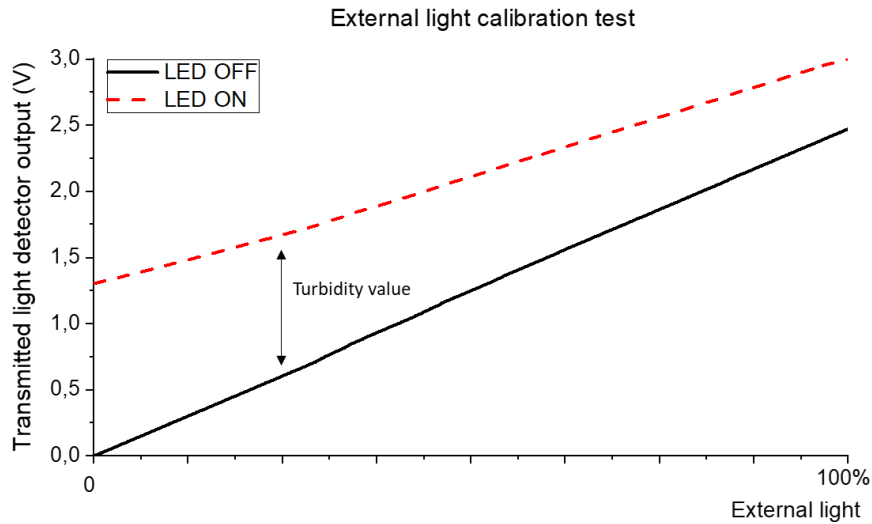
Figure 24. Results of the external light calibration for the IR transmitted light detector output. A sample with constant turbidity was illuminated by an external light source at increasing power. The detector output voltage with the IR LEDs ON (turbidity measurement) and OFF (external light influence) were recorded. The value 0 % corresponds to the dark current of the phototransistor and 100 % when it is saturated.

A mathematical expression was calculated for each photodetector to eliminate the external light effect. The first step is to draw the ON-OFF variation (measurement with LED ON minus measurement with LED OFF) as a function of the external light and divide it by the measurement value when the external light is zero (measurement that corresponds to the real turbidity value).

$$f_{on-off}(external\ light) = \frac{f_{LED\ on}(external\ light) - f_{LED\ off}(external\ light)}{f_{LED\ on}(0)} \qquad (15)$$

The result of Equation (15) translates into a function of coefficients to be applied to the ON-OFF measurements of the sensor:

$$measurement = \frac{measurement_{LED\ on} - measurement_{LED\ off}}{f_{on-off}(measurement_{LED\ on})} \qquad (16)$$

These equations are used to process the *in situ* data and eliminate the offset caused by any kind of external light. The final measurement value (in Volt) can be then correlated to a turbidity or suspended sediment concentration value using the respective calibration equations.

Figure 25 shows the results of using a simple ON-OFF calibration versus the developed calibration equation using the data presented in Figure 24. Since the turbidity of the sample did not change, the correct measurement of the sensor must be a constant voltage value. As observed, the ON-OFF technique does not provide good results. On the opposite, the developed calibration eliminates the effect of the external light.
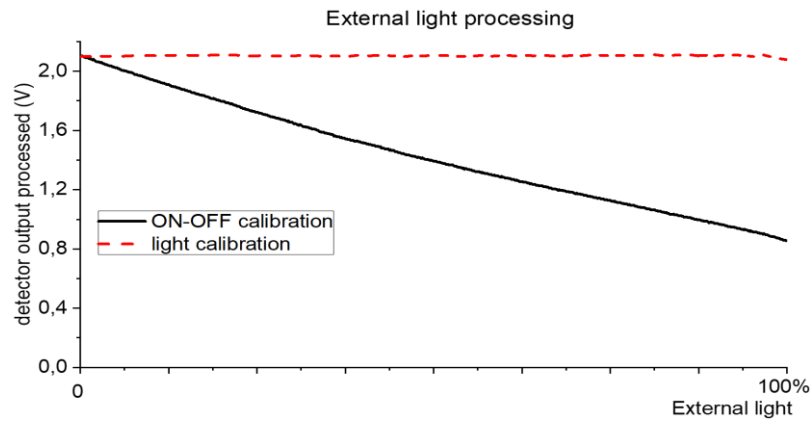
Figure 25. Results of the different calibration methodologies to eliminate the external light. The ON-OFF calibration in displayed in a continuous black line and the developed calibration in a red dashed line.

3.2.3 Preliminary tests

The SPM sensor was subject to two different tests to validate its operation. The first experiment was conducted in the wastewater treatment plant Tratamento De Águas Residuais Do Ave – TRATAVE, Guimarães, Portugal. The sensor was installed for 24 hours in a wastewater tank with a Solitax sc probe from Hach (0.001 - 4000 NTU, calibrated with formazin). Both sensors measured turbidity with a sample period of 3 minutes. Before the experiment, the SPM sensor was calibrated with formazin and to the external light correction. Figure 26 shows the results of the test.
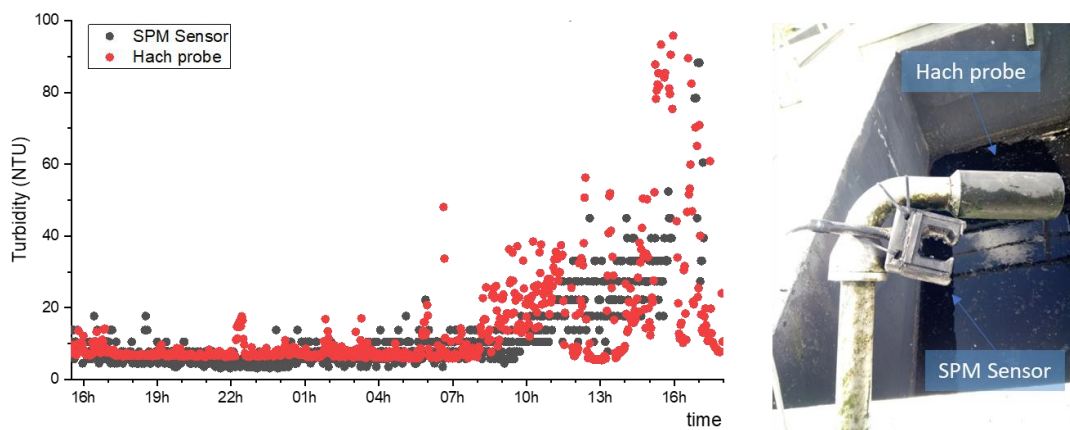
Figure 26. Recorded data from Hach and SPM sensors in TRATAVE. Grey circles present data from the SPM sensor and red circles from the Hach probe. The right image provides a visual overview of the installation setup featuring both sensors.

The sensors recorded similar values at the beginning of the experiment. At 8h both sensors started to drift due to the fouling on the surface of the instruments. This is a normal event, the Hach probe is cleaned at least one time a day for proper operation. This experiment showed that the calibrations for external light and turbidity work, and that the developed sensor can deliver similar results as the

commercial one. However, the SPM sensor does not match the resolution of its commercial peer. The resolution discrepancies are highlighted during the drifting phase. The SPM sensor data are presented in steps, which is related to the resolution of the ADC. On the other hand, the measurements of the Hach probe are smooth and without the existence of step lines.

The second experiment was conducted on a river to validate the suspended sediment concentration calibration. The device was installed in Este River (Braga, Portugal, 41°31'37.9" N 8°26'07.3" W) during a day when it was expected to rain. The place of the test was strategically chosen on the way out of the city and in a muddy area. An increase in sediment load due to the surrounding mud and dirt of the city was expected with the increase in precipitation.

Figure 27 shows the results of sediment concentration during the experiment. The calibrations for external light and 180 μm seashore sand were used to convert the output of the sensor to values of suspended sediment concentration.
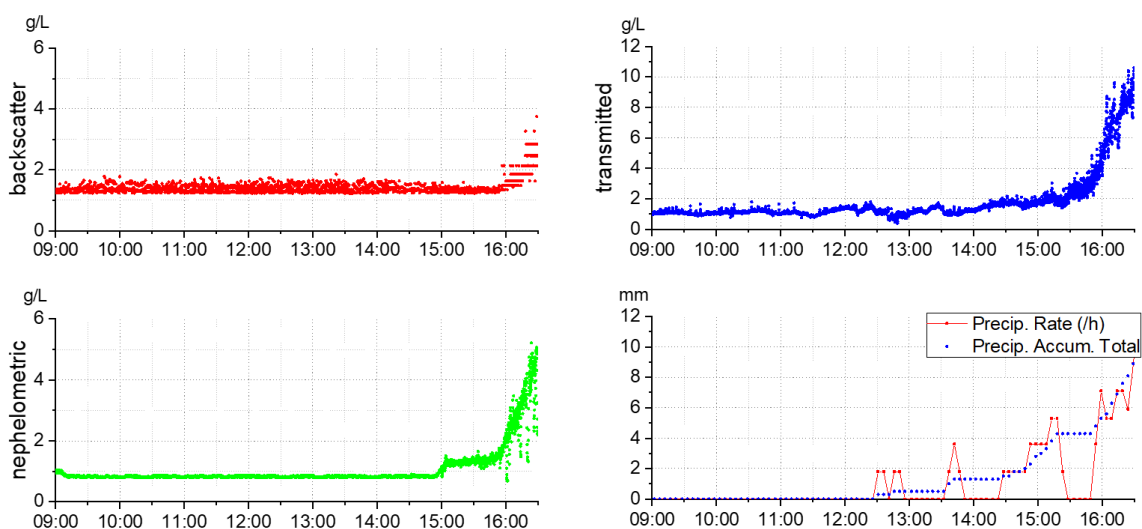
Figure 27. Results of the test in Este River. The graphs show the SPM readings for backscatter, nephelometric and transmitted IR techniques and the total precipitation accumulation and precipitation rate (precipitation data from Instituto Português do Mar e da Atmosfera – IPMA).

As expected, the sensor registered an increase in the suspended sediment with the precipitation. The transmitted sensor revealed a higher sensibility, detecting up to 10g/L, compared to 5g/L and 4g/L of nephelometric and backscatter, respectively. Results may be affected since the river is polluted. There are several particles with the potential to affect the sense of each phototransistor (colour, size and different matter have different results for the different detections). Also, the sensor was calibrated with 180 μm seashore sand, which does not correspond to the expected sediment in the river. No variation was detected before the rain, from 9h to 12h, confirming again the calibration regarding external light.

3.3 TVP Sensor – turbidity vertical profiler

This subsection was published in "Design of a Multipoint Cost-Effective Optical Instrument for Continuous *In situ* Monitoring of Turbidity and Sediment", Sensors MDPI [191].

The Turbidity Vertical Profiler (TVP) is an adaptation of the technology developed for the SPM Sensor to monitor turbidity and suspended particulate matter in the vertical profile of the water column. One obvious solution for multiple monitoring in depth would be the replication of several SPM Sensors to be deployed. The TVP Sensor is intended to provide a modular instrument for this effect, reducing cost and power consumption, and increasing scalability and ease of use.

The SPM Sensor used IR backscattering, nephelometric and transmitted light detection, and a UV transmitted channel. The ultraviolet and infrared transmitted light channels were maintained to distinguish organic from inorganic matter. For turbidity and sediment concentration, the new device only uses the backscatter technique. Since the nephelometric technique has high performance for low turbidity values, which are not expected in coastal areas, this light detection technique was discarded to reduce costs.

The developed instrument integrates several sensing nodes along a one-body and compact structure, controlled by a single microprocessor. The TVP Sensor is a 645 x 55 x 15 mm bar with 8 measuring nodes displaced 70 mm vertically from each other (see Figure 28). Each node has a 30 mm diameter and comprises the optical transducers.

Figure 28. Image of the TVP Sensor. The instrument comprises 8 monitoring nodes with the backscatter and transmitted light channels along a 645 mm bar and it is intended to be placed vertically in the water column to measure the vertical turbidity profile.

The instrument was built with a scalable and modular philosophy so that similar bars can be fixed on the top of the previous one (from the stream bottom to the surface) and increase the number of nodes and monitoring points along the water column. Each bar has an underwater connector on its top and another on its bottom to connect the previous and following bars. The connectors share power and data bus and

allow the use of the bars as a single instrument. Figure 28 shows the bar of the bottom end. It has a connector on its top to connect to the next bar and it is intended to be buried vertically in the streambed.

3.3.1 Hardware design

The hardware was slightly changed in relation to the SPM Sensor. T1-3/4 (5 mm) packages were used previously for the optical transducers. In the new device, the package was changed to T1 (3 mm) to reduce the size of the measuring nodes. The light-emitting-diode TSUS4300 (950 nm, 16° emitting angle and 18 mW/sr radiant intensity at 100 mA) was selected as the IR source. The phototransistors TEFT4300 (950 nm, 30° view angle and 1 nA dark current) complete the IR pair for the backscattering and transmitted light channels. The UV channel uses one UV3TZ-390-30 (390 nm, 15° emitting angle and 10 mW emitting power at 15 mA) as the light source and one wideband phototransistor SFH 3310 (spectral range from 350 to 900 nm, view angle of 75° and 3 nA dark current). Notice that the use of LEDs instead of LASERs was kept due to their good performance in SPM Sensor, wide commercial offer and lower price.

A microprocessor was carefully chosen to manage and control the eight nodes and their respective optical emitters and receivers. The STM32L496ZG microprocessor was used due to its low power, 24x12-bit ADC channels (3 photodetector analog signals x 8 measuring nodes requires 24 ADC channels) and several GPIOs (8 IR LEDs and 8 UV LEDs to be controlled). Alternatively, a simpler microprocessor and multiplexer could be used. However, the sensitivity of the measurements could be affected due to the internal resistance of the multiplexer, and it would increase the cost and power consumption of the sensor.

The rest of the electronics is similar to the SPM Sensor. The TPS62840DLCR regulates the voltage of the system to 3 V and supplies the electronic circuits. The TPS61222DCKR regulates the voltage to 5 V that is needed for the UV LED (3.4 V maximum forward voltage). The 16 LEDs (8 IR and 8 UV) are controlled by the microprocessor that turns them ON and OFF using the respective DMG6968U-7 MOSFET. The 24 photodetectors use a resistor as a current-to-voltage converter that is read by the 24 ADC channels. Two LTC1480 are used for two RS485 buses (one for the top connector and the other for the bottom connector) that are connected by two independent UARTs of the microprocessor. The complete electronic schematic of the TVP Sensor is presented in Supplementary Material I 2 and the printed circuit board is in Supplementary Material II 2.

The structural housing of the sensor was manufactured with epoxy resin that comprises the electronics to meet the watertight needs for submersion. Each TVP Sensor has a production cost of 38 € without the underwater connectors (the connector price can vary from 40 € to 80 € depending on the brand) and replicates eight SPM Sensors. The instrument has a power consumption of 500 mW when taking measurements (25 ms active time) and 150 µW in sleep mode.

3.3.2   In-lab calibration and comparison with the SPM Sensor

As for the SPM Sensor, the TVP must be calibrated before deployment. Since the technology and variables to measure are the same, the developed device needs to be calibrated for turbidity, suspended sediment concentration, organic matter and external light, depending on the objective of the field tests. The calibration procedures are the same as presented before (but this time for each one of the eight nodes of the TVP Sensor).

Different formazin solutions were diluted from an initial standard sample of 4000 NTU, following the procedure of Equation (14). For each sample, the sensor recorded 20 measurements for each photodetector (backscatter, IR transmitted and UV transmitted) of each one of the 8 nodes, at a sampling period of 0.5 seconds.

Figure 29 shows the calibration with formazin for the TVP and SPM sensors. The output voltages obtained in the three measuring techniques (IR backscattering, IR transmission, and UV transmission) are presented in three separated graphs. Each graph presents the output voltage of the 8 nodes of the TVP Sensor and the measurement of the SPM Sensor for the corresponding detection technique.

For the backscattering technique, the higher voltage output was achieved with the sample with 4000 NTU. This is the sample in which is expected more optical scattering due to the higher number of suspended particles. As the sample is diluted, the number of suspended particles decreases, as do the optical scattering and electrical output of the photodetector.

For the transmitted light techniques, both infrared and ultraviolet, the opposite happens. For the 4000 NTU solution, the emitting light is reflected and absorbed in its direct path, and the photodetector senses a minimum amount of light. As the turbidity decreases, the passage of light increases and so does the electric output of the photodetector.
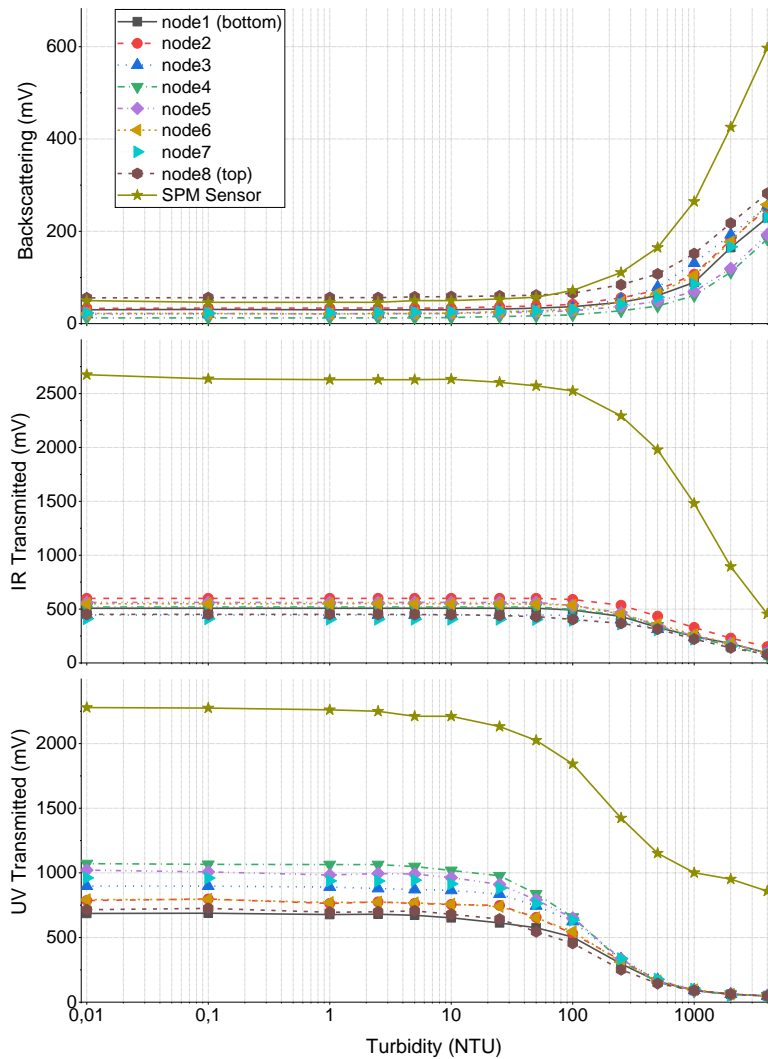
Figure 29. Results of the calibration with formazin for the three light detection techniques of each 8 nodes of the TVP Sensor and comparison with the SPM Sensor.

Comparing the curves of the TVP with the SPM Sensor, the new device presents lower sensitivity, mainly in IR and UV-transmitted channels. This happened due to the use of different transducers (3 mm instead of the 5 mm used in the SPM Sensor). The new LEDs have less radiant power and the photodetectors have less sensitivity. In this case, and to have a good comparison, both sensors had the same resistor gain (1 MΩ for the backscattering, 80 kΩ for the IR transmitted and 220 kΩ for the UV transmitted). These values can be changed to increase the sensitivity of the sensor.

With this configuration, the TVP did not show good sensitivity to turbidity values under 10 NTU, which underperforms against the SPM Sensor. Still, the achieved range is adequate to monitor coastal areas where higher turbidity values are expected. At the upper limit of the scale, while the IR and UV transmitted channels were already within their limit, the backscattering detector was able to measure turbidity values above 4000 NTU.

3.3.3 In-lab experiment with seashore sand

A laboratory experiment was conducted to replicate the sedimentary processes that might happen in the field and to evaluate the behaviour of the TVP Sensor. The instrument was submerged in a container with distilled water (minimum turbidity value) and seashore sand was gradually released from its top until the sediment settled on its bottom. This event was repeated until the container became saturated with sand (as demonstrated in Figure 30).
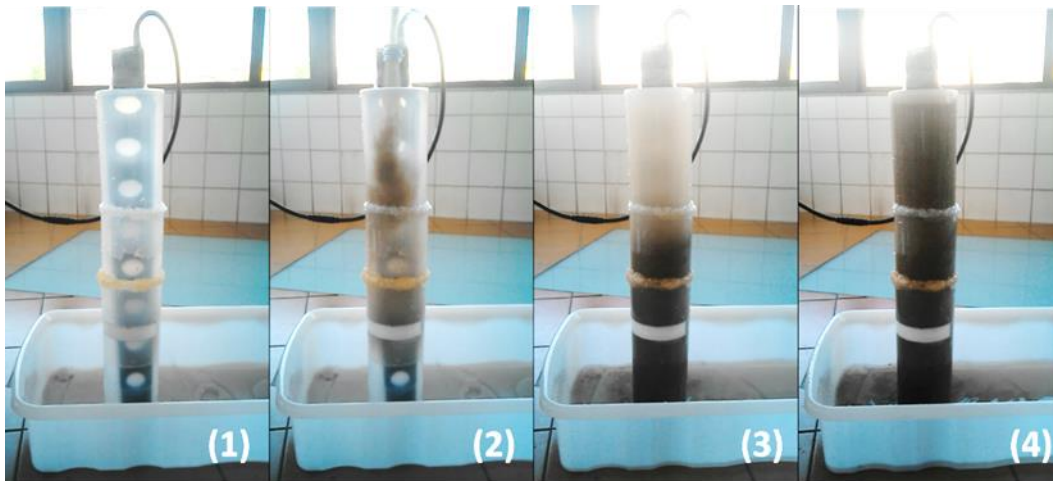
Figure 30. In-lab experiment with the TVP Sensor. The sensor was submerged in a container with distilled water (1) and seashore sand was released from its top (2). The release of sand was repeated (3) until the container became saturated with sand (4).

During the experiment, the electrical outputs of the photodetectors of all nodes were recorded with a sample period of 200 ms. Figure 31 shows the measurement of the backscatter photodetectors of the eight nodes of the TVP sensor.

At the beginning of the experiment (time (1)), the photodetectors presented an electrical output corresponding to low turbidity. Whenever the sand was released (e.g., time (2)), all nodes presented a peak in their output and then decreased to a value slightly above the previous value. This happens because of the passage of the particles that settle to the bottom of the container and create a momentaneous increase of scattered light when passing by the respective node. While this does not faithfully simulate the transport load *in situ*, it shows that the sensor can measure abrupt changes in turbidity due to sediment transport.

As the sand was released, the heavier particles settled in the bottom and the smaller and lighter ones remained suspended, bouncing in the water (wash load) and increasing the turbidity (e.g., compare the value difference of time (1) and (3)). This behaviour was detected by the photodetectors and reflected in

the progressive increase of their electrical output (the mean value is continuously increasing during the test).
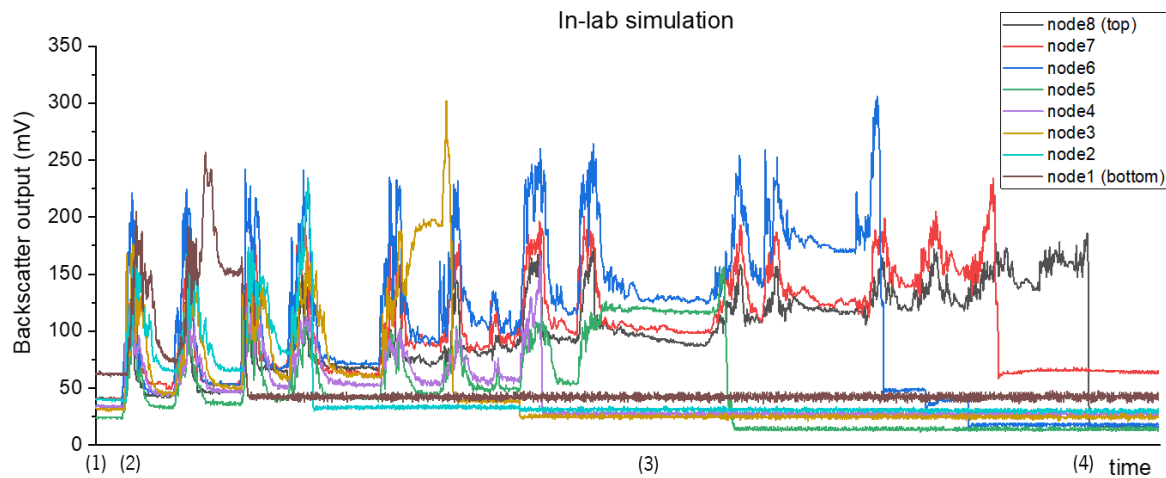
Figure 31. The electrical outputs of the backscatter channels of the 8 nodes were recorded during the in-lab simulation with seashore sand. The time labels (1) to (4) are related to the same moment in the photographs in Figure 30.

Although it was not the main purpose, the device showed the potential to monitor sediment accumulation. One by one, the nodes became buried in sand with the deposition of the released sand to the bottom of the container. The graph shows that the backscatter photodetector of node1 was the first to abruptly change its output to a low value, followed by nodes 2 to 8. This event occurs when the node is completely buried in sand and the photodetector can no longer receive light from the LED since the sediments act as an opaque wall.

It is important to notice that the electrical output of each photodetector for the lowest turbidity value is higher than when the node is buried (dark current of the photodetector), so a low turbidity value is not mistaken with a buried node. In the same way, if the top node of the instrument is out of the water, the measurement will not be confused with low turbidity levels. For this case, and since the light attenuation in the water is higher than in the air, the sensor would deliver high electrical output values, corresponding to negative turbidity values.

The insight of the TVP Sensor to measure deposited sediment was the basis for the development of a new sensor dedicated to measuring this sedimentary process.

3.4 SDE Sensor – sediment deposition and erosion

This subsection was published in "Development of an automated sensor for *in situ* continuous monitoring of streambed sediment height of a waterway", Science of The Total Environment, Elsevier [192].

The sediment deposition and erosion (SDE) sensor was developed to monitor the processes of sediment deposition *in situ*. The instrument is intended to be buried in the streambed of the waterway and uses 32 IR emitter-receiver pairs along its body, with 5 mm displacement, and a total measuring length of 160 mm. As Figure 32 shows, the optical transducers are separated into two printed circuit board arrays, one for the IR emitters and the other for the IR receivers. The PCBs are placed in front of each other, displaced by 15 mm, and with the emitter-receiver pairs aligned (principle of transmitted light detection).
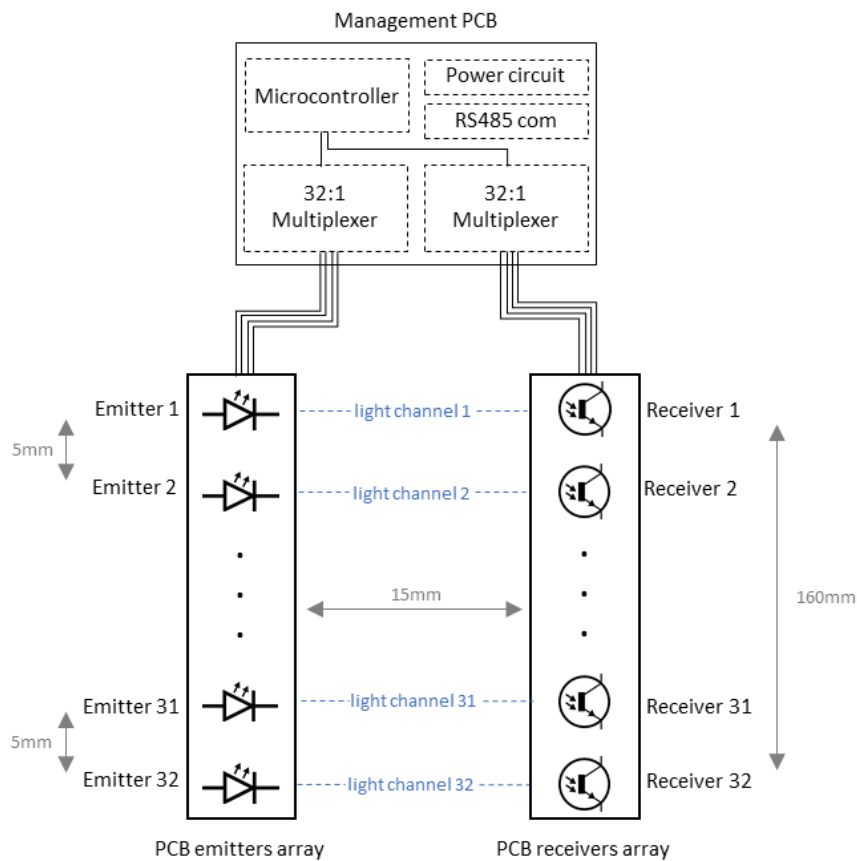
Figure 32. Illustration of the design scheme of the 32 light channels of the SDE sensor. The instrument uses two aligned printed circuit boards, displaced by 15 mm, with arrays of 32 light emitters and 32 light receivers. Each one of the nodes is displaced 5 mm from the adjacent, resulting in a maximum sediment accumulation length of 160 mm. A third printed circuit board is used with the power, instrumentation and processing circuits.

The instrument is intended to be buried in the streambed. This configuration allows measuring the height of the streambed and analysing the deposition of suspended sediment and sediment resuspension and

erosion. One at a time, each one of the 32 nodes emits light from the emitter to the receiver. The channel is clear if the receiver senses the light emitted by its pair. Otherwise, the channel is obstructed with sediments and the light cannot reach the detector. Analysing the electrical output of each receiver, the sediment height is estimated based on the number of detectors that can no longer detect light. The sensitivity of the emitter-receiver pairs was designed so that in water with 4000NTU the light sensed by the receivers is higher than zero. This means that the sensor can properly work in high-turbidity waters.

3.4.1 Hardware design

Small surface-mounted device (SMD) packages were used for the light emitters and receivers to achieve the 5 mm resolution. The light-emitting diodes APT2012F3C (940 nm, 120° emitting angle and 1.2 mW/sr radiant intensity at 20 mA) and the phototransistor APT2012P3BT (940 nm, 160° view angle and 100 nA dark current) were used for the 32 channels. The optical arrays are switched by two ADG732BSUZ multiplexers (32-to-1 bidirectional channel, 4 Ω ON resistance, 30 mA maximum continuous current), one for the LEDs and the other for the photodetectors, that are controlled by an STM32L412K8T6 processor. As before, the photodetectors have a resistor gain in series with the phototransistor, and the electric output is read by the ADC of the microprocessor. The SDE Sensor uses the LTC1480 for the RS485 bus and the TPS62840DLCR regulator to supply the electronic circuits.

The complete electronic schematic of the management PCB can be consulted in Supplementary Material I 3 and the respective PCB in Supplementary Material II 3. The complete schematic of the array PCB can be consulted in Supplementary Material I 4 and the respective PCB in Supplementary Material II 4. The SDE sensor has a power consumption of 150 mW when taking measurements (35 ms active time) and 60 μW in sleep mode.

The structural housing of the sensor is formed by three bodies: the housing of the two PCB arrays with the photo transducers and the housing of the management PCB. The three bodies are filled with epoxy to meet the watertight needs and to fix the bodies in one single structure. Two vertical steel supports of 500 mm are fixed on the side of each array to increase the robustness of the sensor to the water flow and to make it easier to bury the sensor during its installation *in situ*.

Figure 33 shows the mechanical drawing of the SDE Sensor. The instrument has a manufacturing cost of 32 € in raw materials, including electronics and structural housing.
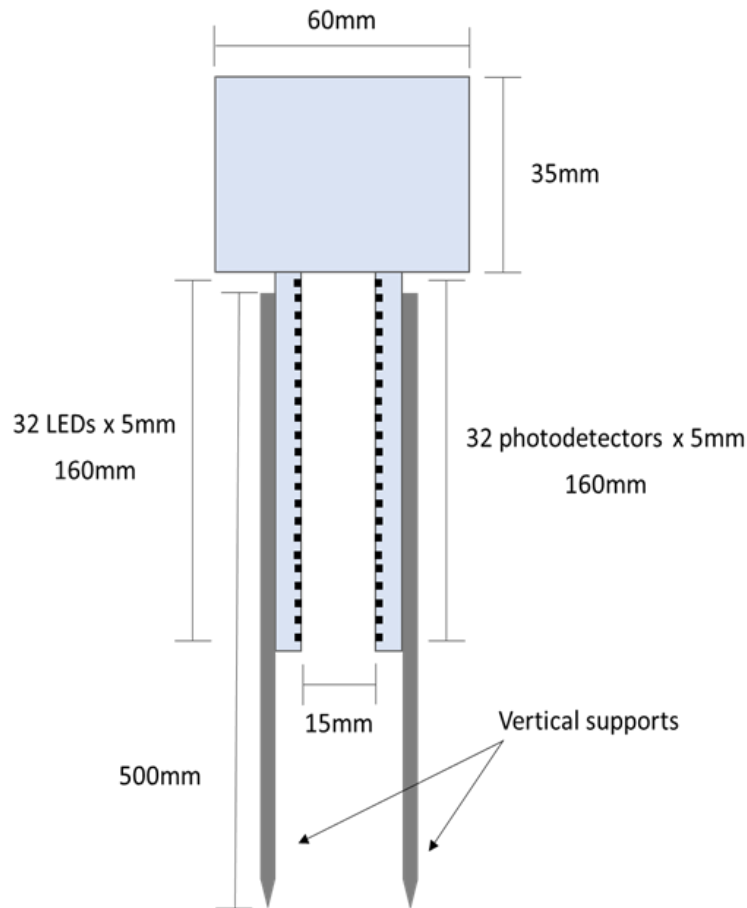
Figure 33. Illustration of the mechanical drawing of the SDE Sensor. The instrument is composed of two vertical arrays with the optical channels and the housing for the remaining electronics. Two vertical supports, one for each optical array, are used to be buried in the sand, allowing easy deployment and providing higher robustness to the water flow during the *in situ* experiments.

3.4.2 In-lab experiment

A laboratory experiment was conducted to evaluate the operation of the SDE Sensor. A similar procedure to the in-lab experiment with the TVP Sensor was designed to simulate the sediment deposition process that occurs *in situ*. The instrument was buried, with all the optical channels uncovered, in a cylindrical recipient with seashore sand and water. As Figure 34 shows, seashore sand was slowly added to the recipient to simulate the sediment deposition and gradually cover the optical channels of the instrument.

During the experiment, the instrument was taking records of each optical channel at a sampling frequency of 2 Hz. One at a time, each one of the 32 LEDs was turned ON and the electrical output of the corresponding optical receiver was recorded. Figure 35 shows the measurements taken from the top (further away from the sand) and bottom (closer to the sand) channels of the device. The time marks in the top horizontal axis correspond to the same labels in Figure 34.
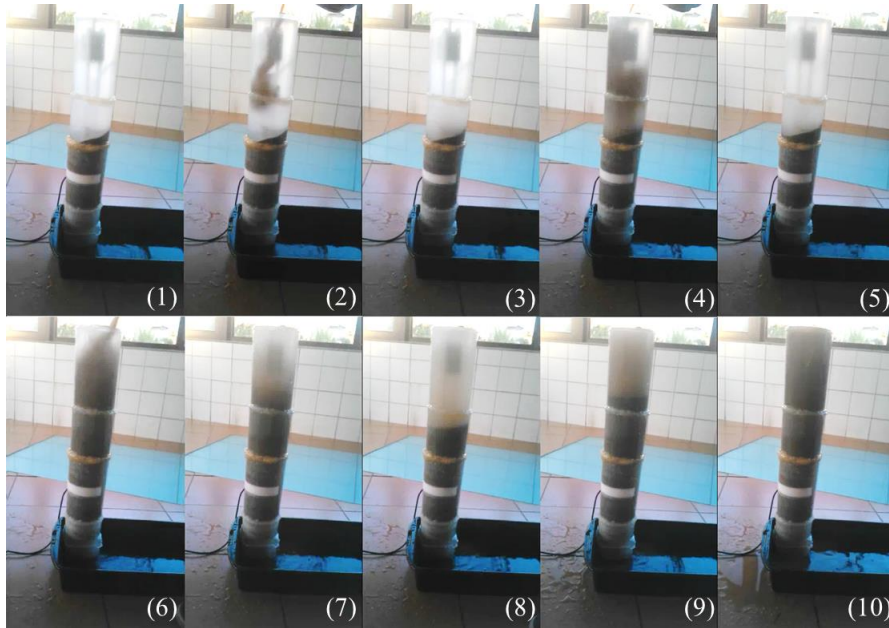
Figure 34. Photographs of the SDE Sensor at different stages of the laboratory experiment. The instrument was buried in a recipient with seashore sand and water (1). Seashore sand was slowly released to the recipient to increase the sediment deposition (2-9) until the instrument became covered with sand (10).

The experiment started with the sensor buried in the sand on the bottom of the recipient, with all the optical channels uncovered (time (1)). This time corresponds to the lower turbidity value during the experiment. For the transmitted light detection technique, high electrical outputs are related to low turbidity values, as Figure 35 shows.

In the first release of sand (time (2)), both channels measured an abrupt decrease in the electrical output caused by the settling of the heavier particles. While the remaining sediment was settling, the average value of turbidity decreased when compared to the period before the release of sand (compare the output value during the times (1) and (3)). This behaviour was repeated during the experiment with sand releases at (4) and (6) and settling periods at (5) and (7-9).

It is important to notice that the output decrease rate is higher for the bottom channel than for the top channel. This happens because the turbidity increases from the top of the container to its bottom while the sediment is settling (as is perceptible in Figure 34). Also, the turbidity value gets higher (output voltage gets lower) at each release of sand (see the difference between (1), (3), (5), (8) and (9)). This happens because the finer and lighter particles do not have time to settle and contribute to the increase of turbidity in the water. In Figure 34 it is possible to visually interpret the differences in the water clarity at the different periods of the experiment.
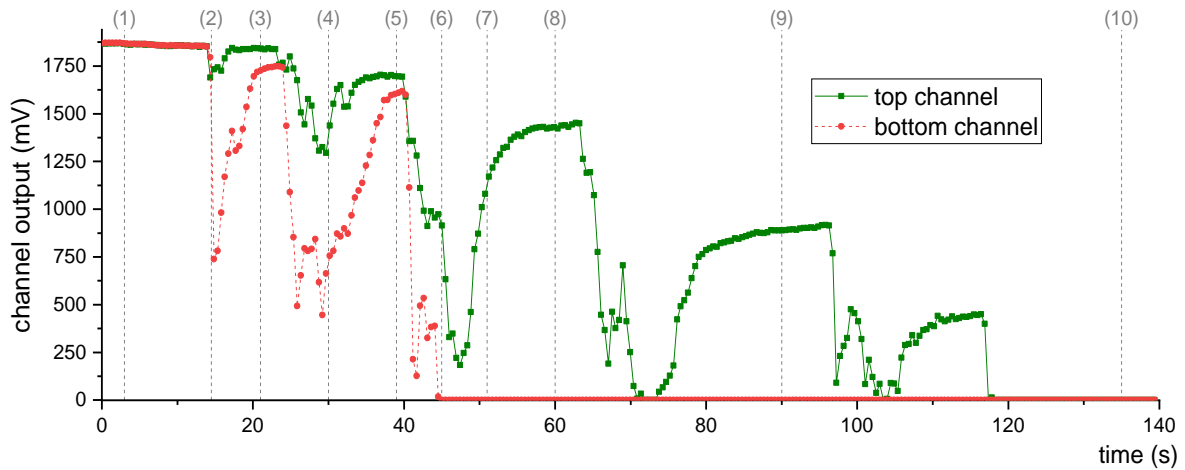
Figure 35. Results of the in-lab experiment with the SDE Sensor. The measurements of the top channel (green square and solid line) and bottom channel (red circle and dash line) were recorded while the device was being buried with seashore sand. The time marks in the top horizontal axis correspond to the same labels in Figure 34.

Even with high turbidity levels, the channels were still able to detect turbidity variations, at least until the channel output reached zero. When this happened, the light emitted could no longer reach the optical receiver, which meant that the channel was buried in the sand. The bottom channel was buried first (Figure 35 at 45 seconds) and then the top channel (Figure 35 at 119 seconds). The other 30 optical channels became buried in between this period. This is the principle that makes the SDE Sensor able to measure sediment accumulation in the streambed of a waterway.

Figure 36 shows the records of all 32 channels, as well as the calculated level of sediment accumulation that is the final output of the device. The output of the instrument is 0 mm when all channels are uncovered. However, whenever one of the bottom channels becomes buried, the sediment accumulation increases by 5 mm up to a maximum of 160 mm (32 channels with 5 mm resolution). While this experiment only demonstrates sediment accumulation, streambed erosion is also detected when the top-covered channels become uncovered.

The developed sensor does not need any calibration for proper operation. The photodetector output is zero when the channel is buried with sediment. While there is a need for most electronic sensors to correspond their electrical output to a physical variable, the measurement principle of the SDE Sensor is binary: the optical channel is completely blocked or not (covered with sediment or not). This means that each one of the optical channels has a binary output. The sediment height is computed based on the number of consecutive channels that cannot detect light (measured from the bottom to the top).
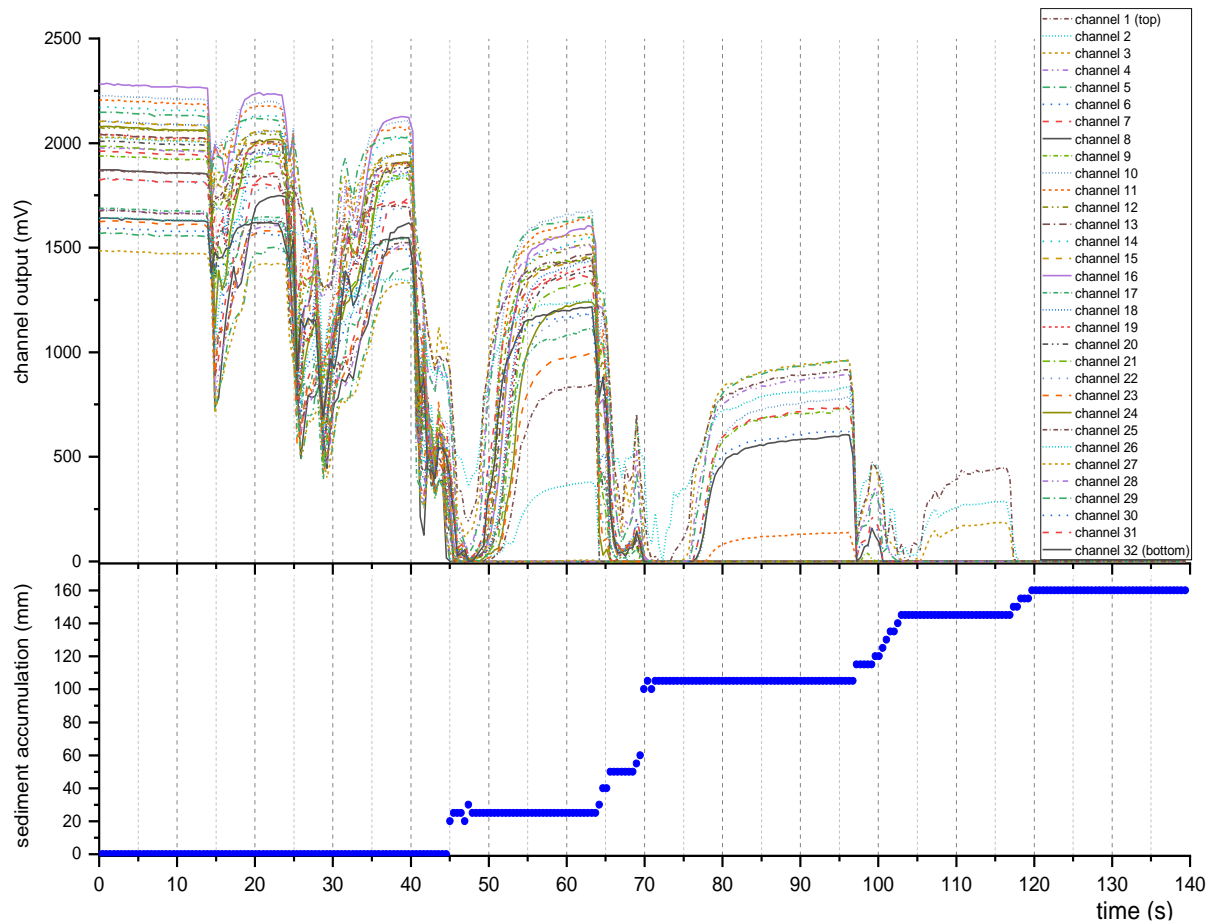
Figure 36. Results of the in-lab experiment with the SDE Sensor. The top graph presents the electrical output of the 32 optical channels. The bottom graph presents the calculation of sediment accumulation.

Note that in an ideal instrument, the output of all 32 channels should be the same for the same water sample and the output of all channels should have been the same before the sand was released. This did not happen because of the electronic component tolerances and differences in the alignment of the optical transducers. Nevertheless, the sediment height calculation is not affected because of the binary output of the optical channels.

This experiment was conducted to test the SDE Sensor in a simulation of a fast sediment deposition that would increase the sediment accumulation in the streambed. The behaviours demonstrated in this experiment, both for turbidity and sediment deposition, are phenomena that are expected to occur during *in situ* deployments at a lower deposition rate.

3.4.3 SDE Sensor – portable version

After the publication of "Development of an automated sensor for *in situ* continuous monitoring of streambed sediment height of a waterway" in Science of The Total Environment, Elsevier [192], an environmental American Association engaged contacts regarding the SDE Sensor.

The Westport River Watershed Alliance (WRWA), together with former scientists from the U.S. Environmental Protection Agency (EPA), was starting a project to rehabilitate the population of oysters in Hix Bridge, State of Massachusetts, United States (41°34'12.6" N 71°04'18.2" W). Among other water variables, one of the interests of the project was to study the sediment accumulation rates that have been burying the community of oysters in the estuary. To do so, a dedicated instrument to monitor sediment deposition and erosion was needed, and there was no commercial offer that met the criteria of the project. This was the start of a collaboration to use the SDE Sensor in the WRWA study.

The needs and constraints of the installation proposed by the WRWA were different from the original design of the SDE Sensor. The SDE Sensor was designed to be connected by a cable to a data logger that shares power and communications. However, the WRWA needed to install the instrument in the middle of the river, in depths up to 10 meters, and the use of a cable crossing the river up to the margin was not viable. Attending to these needs, a new version of the SDE Sensor was designed with an integrated data logger and power.

The features of the original SDE Sensor were maintained (type of measurement, resolution and measuring length), but the electronics were changed to incorporate data-logging features. Also, the new sensor needed a way to plug, unplug and charge the battery and download the monitoring data preserving the watertight needs.

The portable version of the SDE Sensor was designed with a watertight capsule (Figure 37 (2)) to access the battery plug, microSD card to store data and coin battery to power a real-time-clock (RTC) (Figure 37 (5), (4) and (3), respectively). A silicon cover, sealant o'ring and cap (Figure 37 (6), (7) and (8), respectively) were designed to close the capsule and prevent the water from reaching the electronics during deployments.

Regarding the electronics, the former microprocessor was replaced by an STM32L496ZGT that has an internal RTC (powered by the coin battery) and Secure Digital Input Output (SDDIO) to interface the microSD card. Since the monitoring data was stored in the SD card, the RS485 bus was not used in this version. The complete electronic schematic of the management PCB of the SDE Sensor – portable can

be consulted in Supplementary Material I 5 and the respective PCB in Supplementary Material II 5. The complete schematic and printed circuit board for the optical arrays are the same as the original sensor (Supplementary Material I 4 and Supplementary Material II 4).
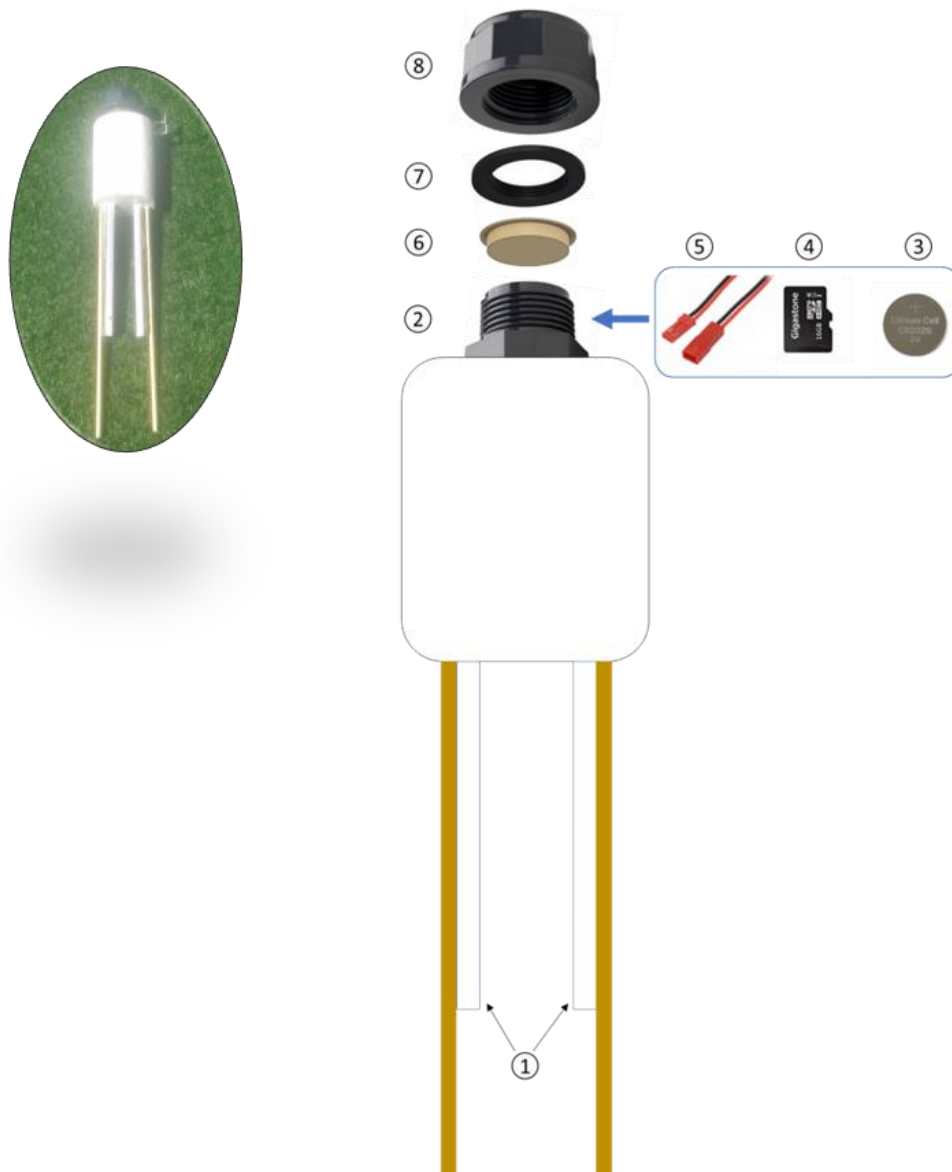
Figure 37. Illustration of the design of the portable version of the SDE Sensor. The new version comprises a watertight capsule with a battery and a microSD card to store the monitoring data.

Given that the sensor was built to be used by a third party, additional precautions were taken to make it user-friendly and simple to set its basic configurations such as changing the measuring sampling period or setting the date and time of the logger. The user manual of the portable version of the SDE Sensor, presented in Supplementary Material V – SDE Sensor User Manual (portable version), instructs how to set these configurations, deploy the sensor, process the monitoring data and do the maintenance of the instrument.

3.5 MEMS biomimetic current meter – water velocity

The set of instruments presented before provided the tools for sediment monitoring. However, the variable of water velocity is still missing to understand sediment transport. This subsection is under revision to be published in Conference Proceedings MTS / IEEE OCEANS Singapore 2024 with the title "Design, simulation and fabrication of a MEMS biomimetic current meter inspired by the lateral line of the blind cavefish to measure flow in 2 axes".

Considering the technologies available in the literature, acoustic devices are normally used for environmental monitoring. However, MEMS technology as gathered attention due to its success in other application fields. The low-cost, low-size and high scalability make this technology attractive to explore.

A MEMS structure inspired by the lateral line of blind cavefish was developed to measure water velocity Figure 38). The lateral line is made up of a series of neuromasts arranged in an interconnected network along the head and body. Neuromasts are made up of a cluster of sensorial cells encapsulated within a jellylike sheath called the cupula [193-194]. The cupula is a flexible organ that bends with the movement of the water (or the movement of the fish in the water). The sensorial system of the cupula allows the fish to sense water velocity and direction. The same principle of operation was replicated using MEMS technology. In other words, the objective was to design a flexible structure entwined with a sensing mechanism that would allow measuring water velocity and direction.
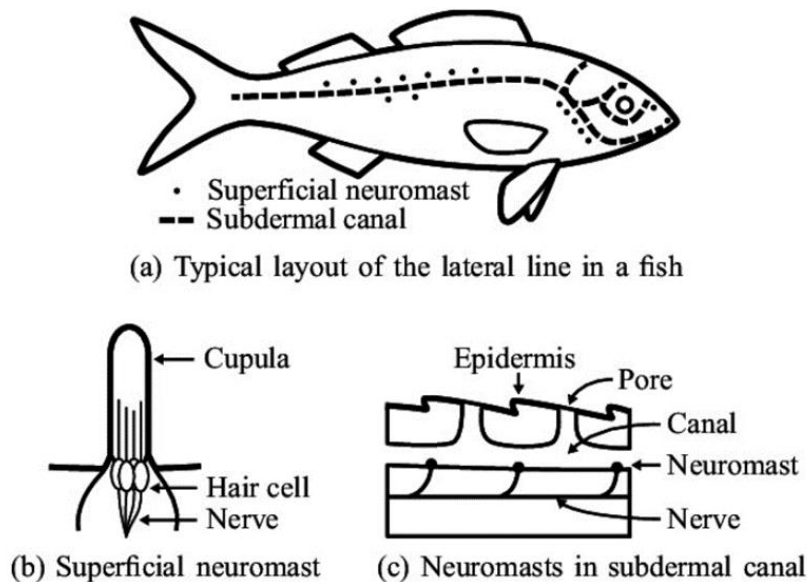
Figure 38. Illustration of the lateral line system of blind cavefish [195]. The cupula structure (b) was the base for the development of the sensor to measure water velocity.

3.5.1 Device simulation

The cupula structure was designed and tested using the software COMSOL Multiphysics. The mechanical stress resulting from the water flow was simulated for different cupula designs to study their deformation.

Initially, a 10 x 10 x 0.05 mm base of Polyimide tape (Kapton HN) was designed to support a cylinder (the cupula) with a 5 mm diameter and 10 mm height. The Kapton is a standard material used in MEMS technology to design sensing structures. The deformation of the structure was simulated for flow velocities of 0.01 m/s, 0.1 m/s and 1 m/s. Two types of materials for the cylinder were studied: Polydimethylsiloxane (PDMS) and Poly methyl methacrylate (PMMA). The Kapton base was anchored on its boundaries so that the remaining structure could move freely with the deformation of the cylinder.
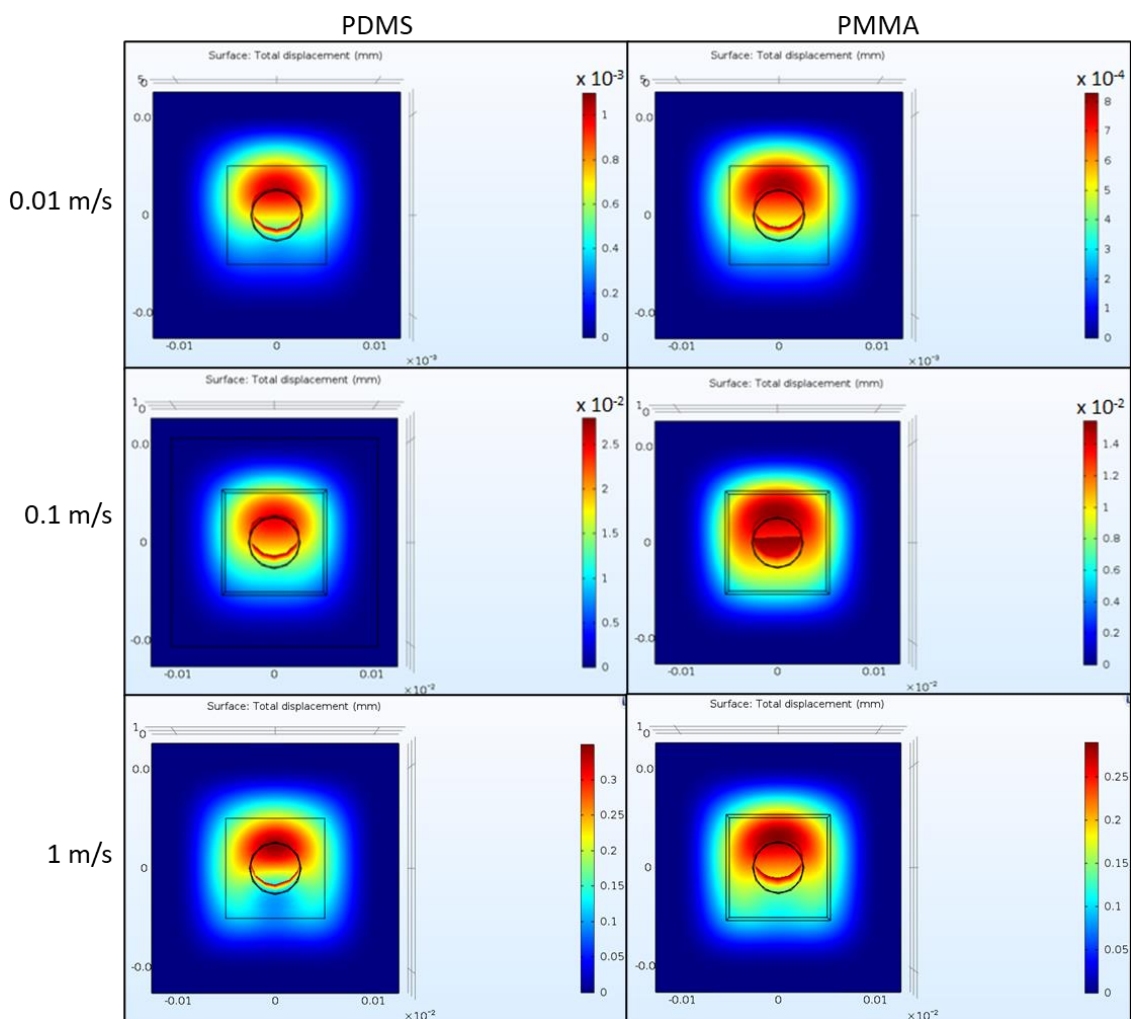
Figure 39. Simulation of the structure deformation to different water velocities and different structural materials. For all simulations, the cupula geometry was constrained to 10 mm height and 5 mm diameter. The images at left show the results for the cupula with PDMS material and the images at right for PMMA. Colour scale of the total displacement of the structure in mm (note that scales are all different). The images are presented from the top-view and the flow was applied from the top to the bottom and perpendicular to the length of the cylinder.

Figure 39 shows the total displacement of the Kapton base that is caused by the bending of the cupula to different flows. For all simulations, the flow was applied in the same direction, from the top to the bottom referenced as the top-view visualization shown in Figure 39, and perpendicular to the length of the cupula.

The simulations show that the higher the velocity of the fluid, the higher the bending of the cupula and consequently the higher the displacement of the base. This is the mechanism of interest that allows measuring water velocity: the displacement of the material of the base is correlated to the flow intensity.

The topic under study was the magnitude of the displacement using different materials for the cupula. As the simulations show, for the same flow velocity, a stiffer material (PMMA) bends less and causes less displacement on the base when compared to a more flexible material (PDMS).

Not only the material of the cupula is important, but also its geometry. A second round of simulations was made to study the displacement of the base for different sizes of the cupula. The dimensions of the Kapton base were increased to 25 x 25 x 0.05 mm and the flow velocity was fixed at 0.1 m/s. The simulations were computed for different combinations of height and diameter of the cupula. The simulations were run for all the possible combinations of 5, 10, 15 and 25 mm diameter with 1, 3, 5, 7.5, 10, 12.5 and 15 mm height.

Figure 40 shows the total displacement of the Kapton for different dimension combinations of the cupula diameter and height. The graphs show that for every fixed cupula diameter (every curve in the right graph of Figure 40), the total displacement of the base increases till a certain cupula height (around 5 to 7.5 mm) and then decreases. In physical terms, this means that the higher the area of contact between the fluid and the cupula (that in this case increases with the height), the higher the bending and consequently the higher the displacement of the Kapton base. The displacement starts to decrease when the structure of the cupula is too rigid to bend (the same happened before when the cupula was simulated with PDMS and PMMA).

It is important to notice that the maximum displacement of the base was achieved for 5 mm or 7.5 mm height. However, this is the optimal point for a flow velocity of 0.1 m/s. If the fluid velocity increases, the maximum of every curve will shift to the right (the height of the optimal point will increase). The opposite would happen for lower fluid velocities and the height of the optimal point would decrease.
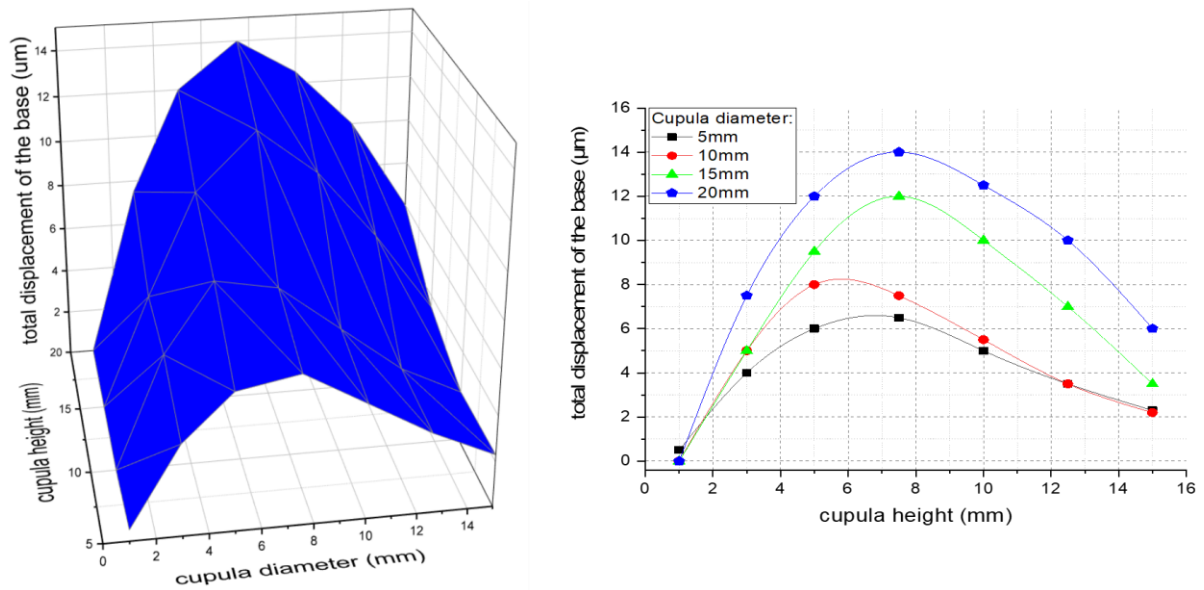
Figure 40. Results of the simulation of the total displacement of the base for a constant flow velocity and different cupula dimensions.

Although this explanation was made for a fixed cupula diameter and a variable cupula height, the same happens when the height is fixed and the diameter changes (easier to visualize on the left graph of Figure 40). The displacement of the base increases with the increase of the diameter of the cupula till the optimal point (the area of contact with the fluid increases) and then decreases due to the increase in the rigidity of the cupula.

The simulations were run to a maximum of 20 mm diameter. The results show that the cupula size can be increased to achieve higher displacement in the base (compare the maximum displacement accomplished with 5, 10, 15 and 20 mm of diameter). However, 20 mm is a big size for MEMS technology. The objective of the sensing device was to have a good trade-off between the MEMS technology and the capabilities needed to perform reliable monitoring *in situ*.

The second phase consisted of designing the transduction mechanism to convert the displacement of the base to an electric signal. A strain gauge, commonly used in MEMS technology, was used as a piezoresistive transductor (see Figure 41).

The strain gauge was placed at the bottom layer of the Kapton and 100 μm from the cupula boundary. As presented in Figure 39, the area of the base closest to the cupula is the zone where there is more deformation. This is the region of interest to achieve higher resistive variation with the deformation of the gauge structure.
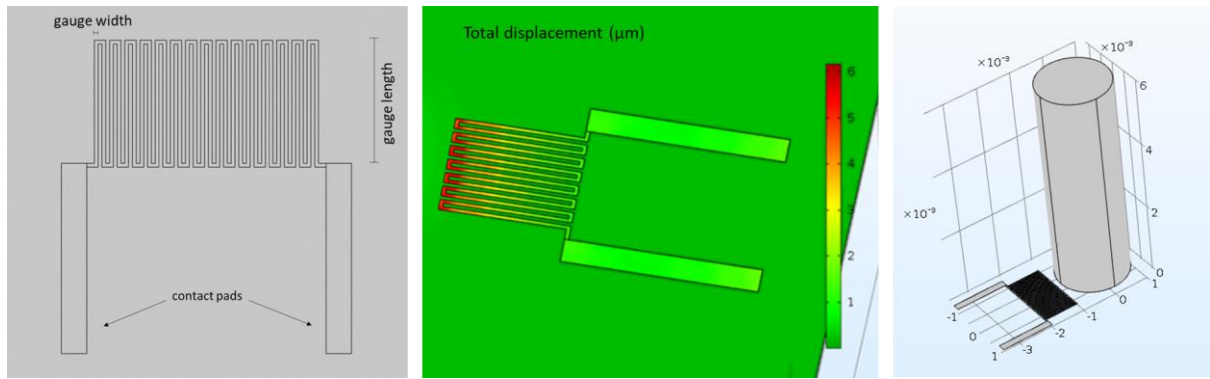
Figure 41. Illustrations of the strain gauge layout. The left image shows the design of the gauge. The middle image shows and example of its deformation. The right image shows its position regarding the cupula.

The behaviour of the strain gauge to the displacement of the base was simulated to understand how the resistance changes. The dimensions of the cupula were fixed to 10 mm height and 5 mm diameter, the Kapton base to 10 x 10 mm, and the strain gauge to 1 mm length, 30 μm width, 200 nm thickness and 15 turns/spirals. The material used for the strain gauge was aluminium.

Figure 42 shows the resistance variation of the strain gauge to flow velocities from -0.5 to 0.5 m/s in the y-axis, in 0.1 m/s steps. The results show that the structure has a nominal resistance of 141.32 Ω. This is the value for a null flow when there is no displacement of the base. When the flow increases, and consequently increases the displacement of the material, its resistance increases (flow in the positive y-direction, bottom-left image of Figure 42). When the flow is applied in the opposite direction (flow in the negative y-direction, top-left image of Figure 42) the resistance decreases.
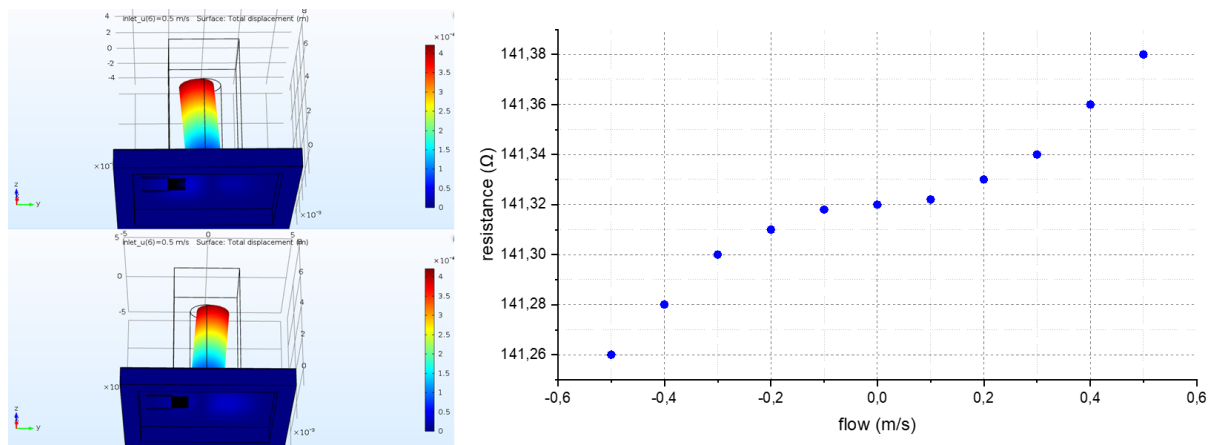
Figure 42. Simulation of the resistance variation of the strain gauge to different flow velocities. The flow was applied in the direction of the y-axis. The top-left image shows the total displacement for the vectorial flows of (0 , -0.5 , 0) m/s and the bottom-left image shows the total displacement for (0 , 0.5 , 0) m/s.

This happens because when the flow causes the cupula to bend, one of the sides of the base extends and the other compresses. For example, for a positive flow velocity (when the fluid is flowing in the y-axis, from left to right in the left images of Figure 42), the cupula bends in the same direction (from the left to the right), which causes an extension in one side of the base (at the left of the cupula, where the strain gauge is placed) and compression in the opposite side. If the strain gauge is extending (the total length of the piezoresistive material increases) the resistance increases. If the strain gauge compresses (the total length of the piezoresistive material decreases) the resistance decreases.

The resistance relation with the length, width, thickness and resistivity of the material is given by the following equation:

$$Resistance = \rho \frac{total\_length}{thickness * width}$$

(17)

Even though the extension/compression mechanism is only dependent on the dimensions of the cupula and flow, the proportions of the strain gauge combined with its placement on the base define the sensitivity and resistance variation of the piezoresistive material. Table 3 shows the simulation results for structures with different lengths to a flow velocity of -0.5 m/s. The dimensions of the cupula, Kapton base and thickness, width and turns of the gauge were preserved, only the length of the gauge was changed.

Table 3. Resistance variation of the strain gauge to a flow velocity of -0.5 m/s using different lengths.

Length (mm)	nominal (Ω)	-0.5 m/s (Ω)	Δ (Ω)	Δ (%)
0.3	42.824	42.789	0.035	0.081
0.5	71.000	70.961	0.039	0.055
0.75	106.210	106.160	0.050	0.047
1	141.320	141.260	0.060	0.042
1.5	211.750	211.680	0.060	0.028
2	282.160	282.110	0.050	0.017

The results show that the nominal resistance of the strain gauge increases with its length and according to Equation 17. For each length, the flow velocity of -0.5 m/s produces a variation in the piezoresistive material. While the resistance variation is lower for smaller lengths, its percentual variation is higher. This happens because, as seen before, the total displacement is higher the closer to the cupula (reassess the middle image of Figure 41). Hence, a piezoresistive structure with a small length will be predominantly in the area where the displacement is higher. On the opposite, greater lengths will be only partially in this region. The disadvantage of using small lengths is that the nominal resistance is lower, which makes it

harder to read by the electronic instrumentation. Nonetheless, the number of turns can be increased to increase the nominal resistance value.

A last set of simulations was conducted to understand how the resistance of the strain gauge changes to flow from different directions. As Figure 43 shows, a second structure was placed in the Kapton base, mirrored by the centre of the cupula and in front of the first strain gauge. A resistance-to-voltage circuit using a half-Wheatstone bridge was added to the model to compute the electrical output of the sensor.
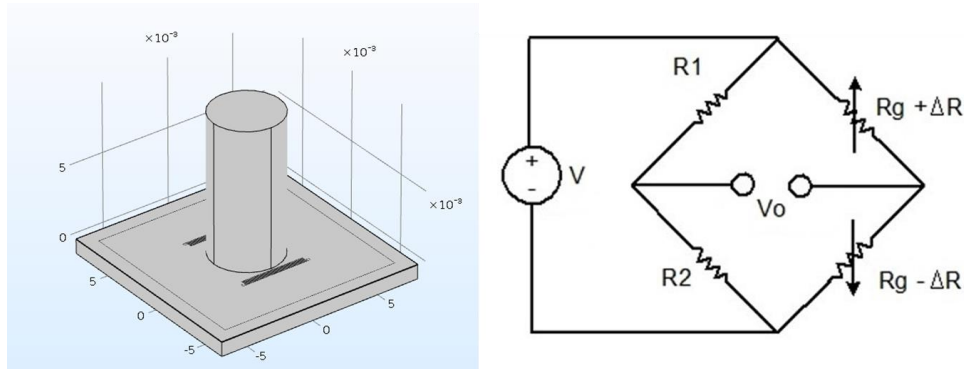
Figure 43. The left image shows the placement of a second strain gauge on the Kapton base. The right image shows the electric circuit of a half Wheatstone bridge, using both gauges as Rg and R1=R2=183.6324 Ω, that was used to compute the electrical output of the sensor.

The dimensions of the strain gauges were set to 0.3 mm length, 0.03 mm width, 0.2 nm thickness and 40 turns, which resulted in a nominal resistance of 183.6324 Ω. This was the value used for R1 and R2 of the Wheatstone bridge in Figure 43. The Rg $\pm$ ΔR are the resistance of the strain gauges (one compressing, - ΔR, and the other extending, + ΔR). The Wheatstone bridge was computed with a gain of 2000 and 5V supply.

A simulation was run to compute the output of the Wheatstone bridge to flow velocities from -1.5 to 1.5 m/s, in 0.25 m/s steps, at 0° (y-axis, top-right image of Figure 45) and 90° (x-axis, top-left image of Figure 45) to the direction of the piezoresistive structures.

The top graph of Figure 44 shows the electrical output of the sensor using both strain gauges in the Wheatstone bridge circuit. The curve of the output of the sensor for flows at 0° (blue circles and blue line) is similar to the one presented in Figure 42 but in Volt instead of Ω. For flow at 90° (red circles and red line), the output of the sensor would be ideally zero for any given velocity in the x-axis. However, since the strain gauges are 3D structures, they suffer extension and compression on their width (extension/compression on their length for flow in the y-axis and extension/compression on their width for flow in the x-axis). To reduce the interference to flow at 90°, the width of the gauge must be the

smallest possible (this dimension is limited by the fabrication rules and machinery used during the fabrication of the piezoresistive structures).
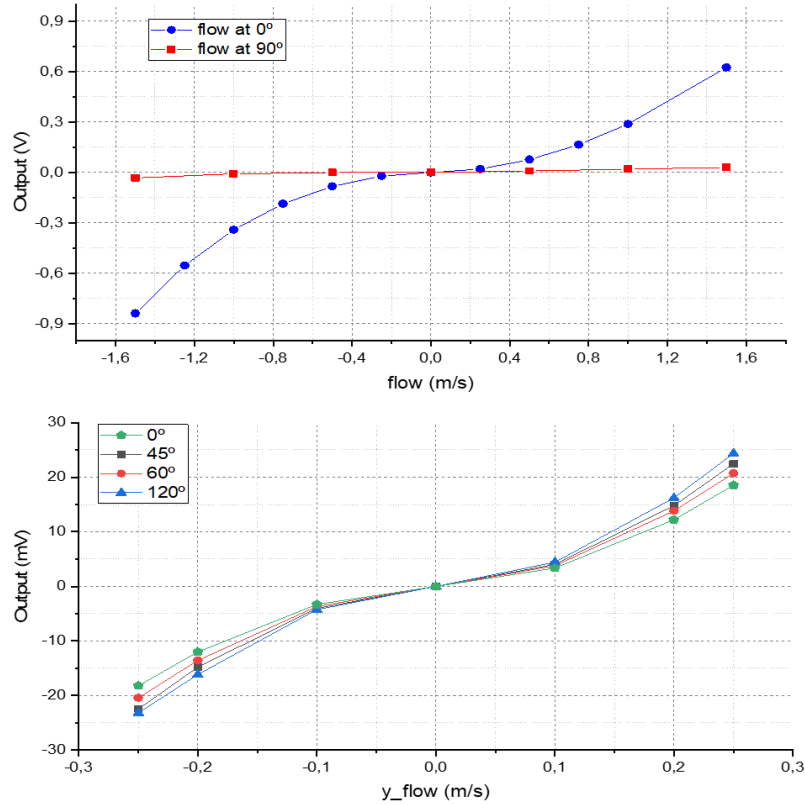
Figure 44. Results of the simulation of the MEMS sensor for flows at different angles of incidence. The top graph shows the simulation results for flow velocities from -1.5 to 1.5 m/s at 0º (blue circles and blue line) and 90º (red squares and red line). The bottom graph shows the simulation results for the vectorial flow velocities in the y-axis for flows at 0º, 45º, 60º and 120º.

The bottom graph of Figure 44 shows the vectorial flow in the y-axis (y_flow) produced by different magnitudes at 0°, 45°, 60° and 120°. Theoretically, the curves would be similar. However, some discrepancies are found due to the extension/compression of the width of the gauges (as demonstrated for flows at 90°).

The vectorial component of interest for any given flow in an α direction is given by the following equation:

$$flow_{vectorial} = flow * \cos \alpha$$

(18)

For the vectorial orientation of the 3D visualizations of Figure 45, a flow of 1 m/s at α=0° (y-axis) produces a vectorial flow in the y-axis of 1 m/s. For the same flow magnitude at α=90° (x-axis), the vectorial flow in the y-axis is 0 m/s. Likewise, the same flow at α=45° is composed of the vectorial sum of 0.5 m/s on the x-axis and 0.5 m/s on the y-axis. This is the principle that allows measuring the velocity and the direction of flow.

78
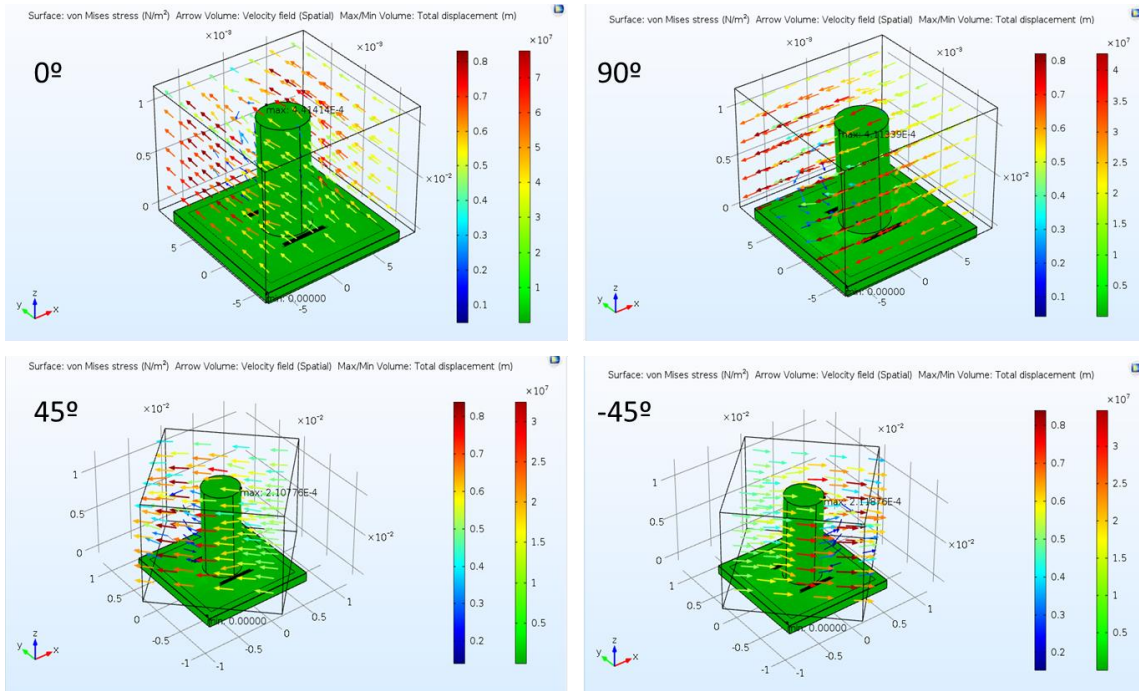
Figure 45. Illustration of COMSOL simulations for induced flows at 0º, 90º, -45º and 45º.

Another pair of strain gauges were replicated and added to the Kapton base to measure the fluid in the x-axis. Also, for each one, another piezoresistive structure was added parallel to the first and 2.5 mm distant from the boundary of the cupula.

As demonstrated before, the longer the distance to the cupula, the smaller the displacement of the material. The objective of the last four strain gauges is to complete two Wheatstone bridges to measure flow in 2 axes. The final design of the piezoresistive structures and intended instrumentation circuit is presented in Figure 46.
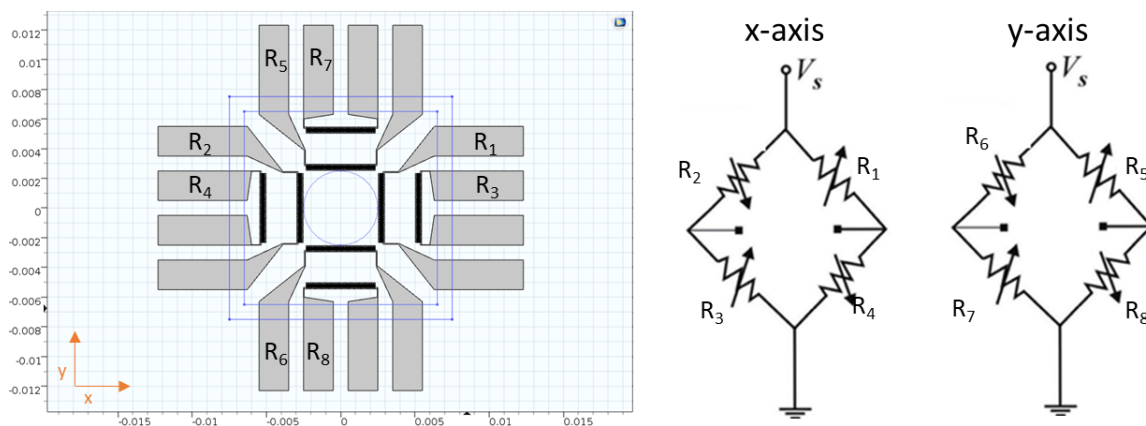
Figure 46. The left image displays the final design of the strain gauges and their positioning relative to the cupula. On the right, the image illustrates the complete Wheatstone bridge circuits used to measure fluid velocity in two axes.

3.5.2 MEMS fabrication and assembling

The dimensions of the MEMS components define the optimal sensitivity of the sensor for a given flow magnitude. This subsection presents the decisions for the definition of the structural dimensions considering the desired application and fabrication machinery constraints.

The first component developed was the thin-film aluminium strain gauges on a Kapton membrane fabricated using photolithography and standard microfabrication techniques (wet etching). The strain gauge dimensions were defined to be 50 µm width, 700 µm length and 200 nm thickness. The thickness and width were defined by the resolution of the fabrication machinery. The length was chosen to have a good trade-off between the desired nominal resistance (125 Ω) and the percentual variation when subject to mechanical deformation. The strain gauges were placed at 100 µm from an expected cupula of 5 mm diameter. Each one of the 8 structures was designed with 23 turns. Figure 47 shows the fabrication design of the thin-film material.
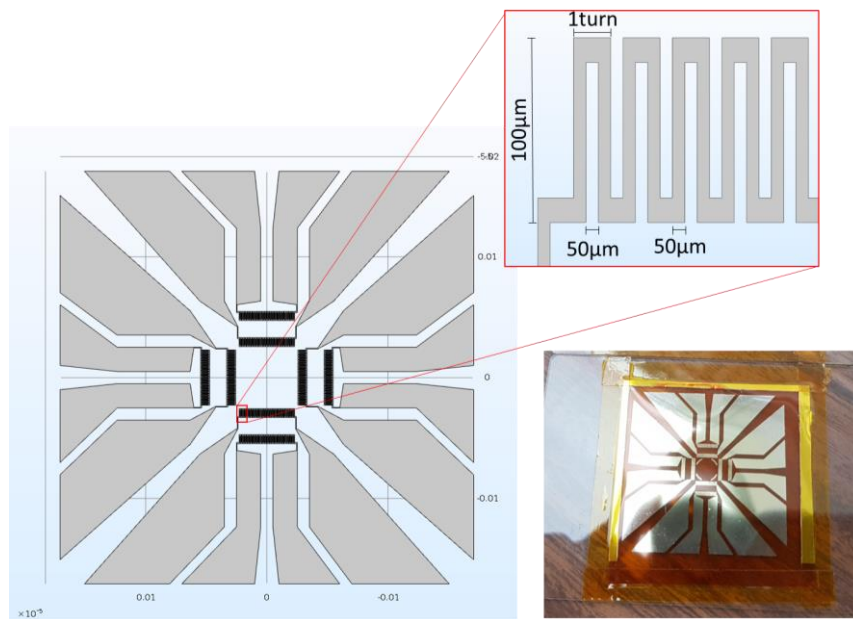
Figure 47. Illustration of the fabrication design of the thin-film aluminium strain gauges a Kapton membrane.

The second part of the fabrication was the design of the cupula and its assembly in the Kapton base (on the opposite side of the thin-film deposition). The cupula was designed with 5 mm diameter and 1 cm height. PDMS (standard material in MEMS fabrication) was chosen to build the cupula using a 3D printed mould and cured in an oven after the mixture of the PDMS base and the crosslinking agent.

The working principle of the developed sensor relies on the deformation of the Katon base resulting from the bending of the cupula. This means that the connection between the PDMS structure and the Kapton membrane is crucial for good operation. Even though the PDMS is a viscous material with good adhesion properties [196], the link between the PDMS and the Kapton must behave as a single material. There are different processes and technologies to bond PDMS with other materials [197]. Considering the intended application and the available machinery, the bonding of the PDMS with Kapton was attempted by using oxygen plasma treatment [198], but without success. Thus, the remaining available technique was the deposition of a thin membrane of PDMS in the Kapton membrane to act as glue between the base and the cupula, as demonstrated in the top-left image of Figure 48.

The final part of the structural fabrication was the electric connection to the pads of the gauges. Since it is not possible to solder on top of aluminium films, the contact between the pads and an electrical cable is rather difficult. The solution employed was to "glue" multifile flat cable to the pads with silver conductivity paint. After the paint dried, aluminium tape was applied to the contacts to increase its robustness (top-right image of Figure 48). With the connection validated, the pads were covered with polyurethane (bottom-left image of Figure 48). The final structure of the sensor is presented in the bottom-right image of Figure 48.
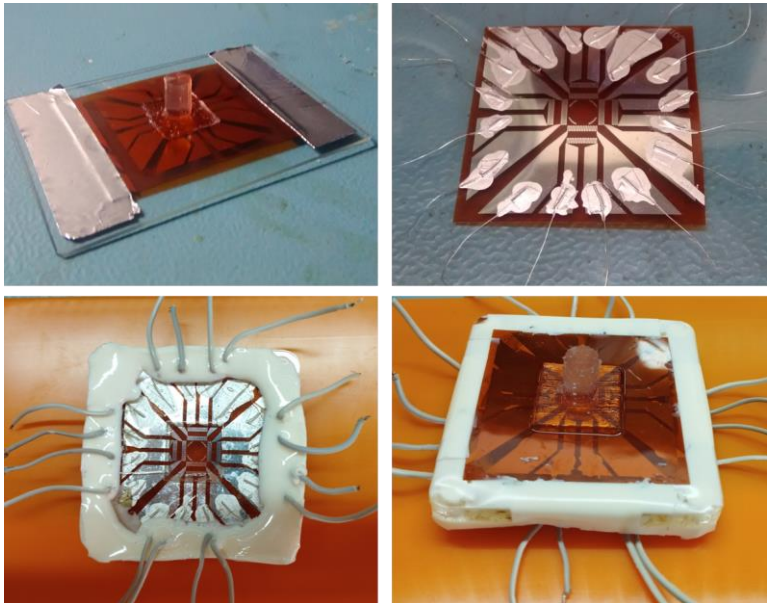
Figure 48. Illustrations of the fabrication and assembly process of the MEMS sensor. The top-left image demonstrates the bonding of the Kapton base to the cupula, while the top-right image shows the electrical connection of the aluminium thin film to a multifile electric cable. In the bottom-left image, the polyurethane deposition on the pads is depicted. The final MEMS structure is presented in the bottom-right image.

3.5.3 Hardware and testing

Once the fabrication and assembling were completed, the MEMS structure was tested with a 3-axe Manual Linear Stage. The structure was fixed on the base of the linear stage and the cupula was manually bent to simulate the flow (the contact with the precision arm was made on the top of the cupula). A high-precision multimeter (1 mΩ resolution) was used to measure the resistance variation of the strain gauges. Figure 49 shows the setup used for the test.
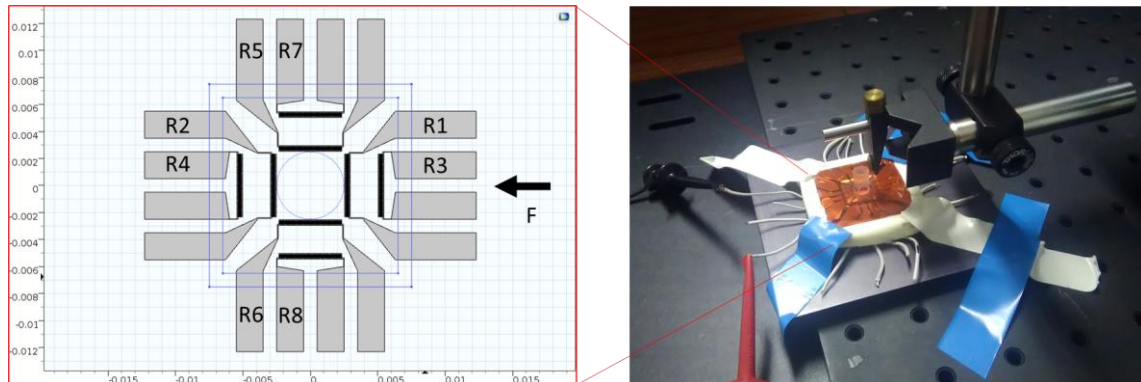
Figure 49. Test setup of the MEMS sensor with a 3-axe manual linear stage.

Figure 50 shows the results of a test with the setup presented in Figure 49. The arm of the linear stage was moved 5 mm in the horizontal axis, producing a bending on the cupula (flow increasing) and then returned to the initial position (flow decreasing). Each one of the strain gauges was measured individually and the percentual resistance variation was computed.

The left graph of Figure 50 shows the results for the gauges closer to the cupula (R1, R2, R5 and R5 referenced in Figure 49) and the right graph of Figure 50 shows the results for the strain gauges further away from the cupula (R3, R4, R7 and R8 referenced in Figure 49).
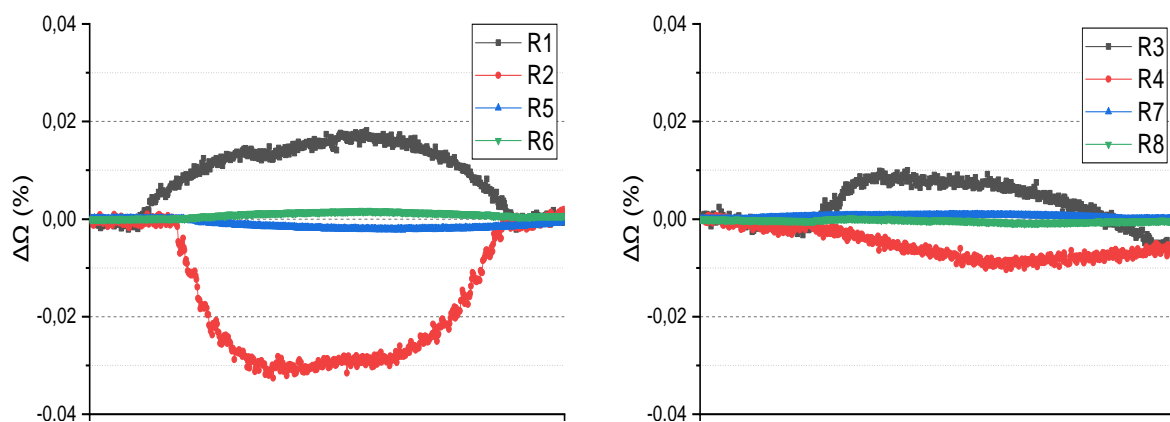
Figure 50. Results of the percentual resistance variation of the eight gauges of the MEMs sensor during the tests with the 3-axes manual linear stage (test setup of Figure 49).

The results show that the MEMS structure presented the predicted operation. When the linear stage is applying a force on the cupula, R1 and R3 are extending (resistance increases) and R2 and R4 are compressing (resistance decreases). The resistance variation is higher for R1 and R2 compared to R3 and R4. This happens because the gauges closer to the cupula have higher compression/extension. At the same time, the resistance of R5, R6, R7 and R8 are not expected to change. The slight resistance change that is observed in the graphs can be explained by the width of the gauges that are not null (the same happened in the COMSOL simulations) and by the fact that the sensor was assembled manually, so the placement of the cupula is not accurate. This can also be noticed in the maximum resistance variation discrepancy of R1 ($\approx$0.02 %) and R2 ($\approx$0.03 %) which infers that the cupula might be closer to R2.

It was noticed during similar tests with the manual linear stage that the strain gauges did not always respond as expected and several times the resistances did not return to their nominal value when there was no force being applied. This behaviour can be observed in the right graph of Figure 50. At the end of the experiment, when the arm of the linear stage returned to the initial position, R3 and R4 had a $\approx$0.005 % difference to its nominal resistance. Still, the hardware for the electronic instrumentation was designed to measure the two full-Wheatstone bridges. Figure 51 shows the electronic scheme of the reading electronic circuit.
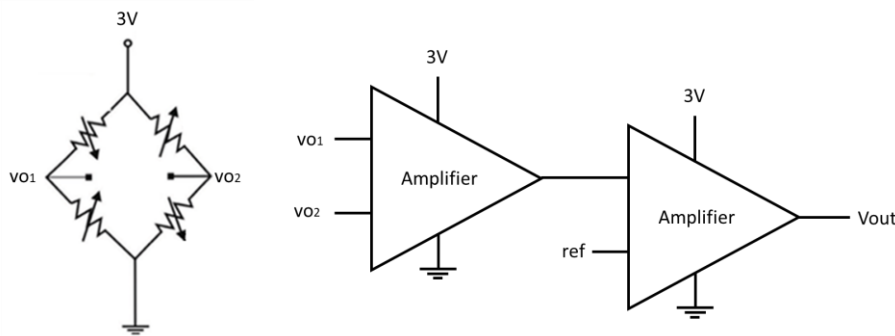
Figure 51. Illustration of the scheme of the electronic instrumentation used to read the two full-Wheatstone bridges.

As for the hardware developed for the previous sensors, the electronic system in use is supplied by 3V. The reading instrumentation was designed with two stages of instrument amplifier (to avoid electronic saturation due to the offset of the bridge) that amplifies the voltage signal from the Wheatstone bridge. The voltage of the second amplifier is read by the ADC of an STM microprocessor. A printed circuit board was designed with the instrumentation circuit, STM32L412C8T6 microprocessor, TPS62842DGRR

voltage regulator and LTC1480 RS485 transceiver. The complete electronic schematic can be consulted in Supplementary Material I 6 and the respective printed circuit board in Supplementary Material II 6.

The instrumentation circuit successfully amplified the signal of the Wheatstone bridges. However, over time and with the burden of tests with the 3-axes linear stage, the erroneous behaviour of the gauges increased to the point that the intended operation was no longer viable. Figure 52 shows the resistance variation of R2 of a later experiment using the same test setup presented in Figure 49.
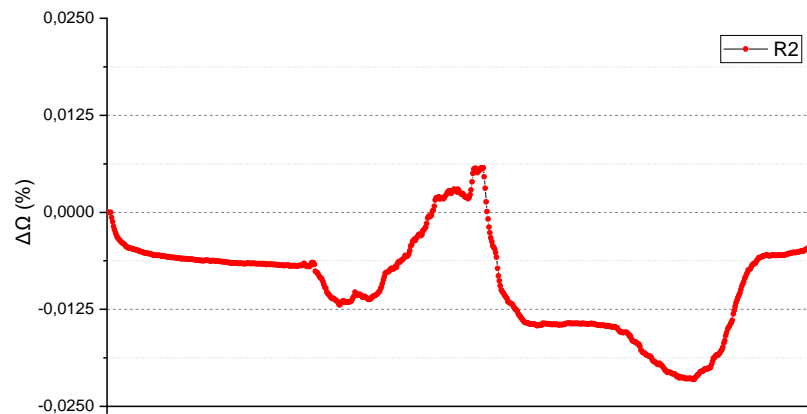
Figure 52. Results of the percentual resistance variation of R2 in a later test with the 3-axes manual linear stage (same test setup of Figure 49).

Even though the test setup is the same, the results of Figure 52 are significantly different from the ones of Figure 50. Remembering the fabrication process, the cupula was assembled to the Kapton base using a thin membrane of PDMS. With time, and with the bending of the cupula, the link between the PDMS and the Kapton became weaker, which resulted in an erroneous deformation of the thin-film substrates. This happened due to the overload of testing in the 3-axes linear stage, which means that the sensor does not have the necessary robustness to be deployed in more rigorous conditions like underwater.

Even though the principle of operation of the biomimetic MEMS sensor was validated, the developed instrument does not possess the necessary robustness and long-term stability for environmental monitoring. To carry on with this technology it is necessary a better technique to couple the cupula to the Kapton or use other materials for the base and/or cupula with better mechanical link properties. Since this problem was not overcome, it was chosen to pursue different technologies to measure water velocity.

3.6 Acoustic ToF current meter – water velocity

An acoustic ToF current meter was developed to measure water velocity. The technology employed on this instrument is the same used in other available acoustic meters, so it does not hand out innovation. The main objective of the development of this sensor was to replicate the existing technology while reducing costs.

The device uses two PZT-5H ceramic piezoelectric discs with 110 μm thickness and 1 cm diameter as acoustic piezoelectrics. The transducers were hand-built, with the piezoelectric element glued to a stainless-steel mass and isolated with a thin silicone layer to protect it from the water. The fabrication of the transducers followed the methodologies of Martins *et al.* [199] to be able to use frequencies up to 1 MHz.

The acoustic transducers were assembled in a stainless-steel plate, displaced 9 cm from each other, and mounted at a 45° angle (Figure 53). The acoustic beams are reflected in a secondary stainless-steel plate parallel to the plane of the transducers.
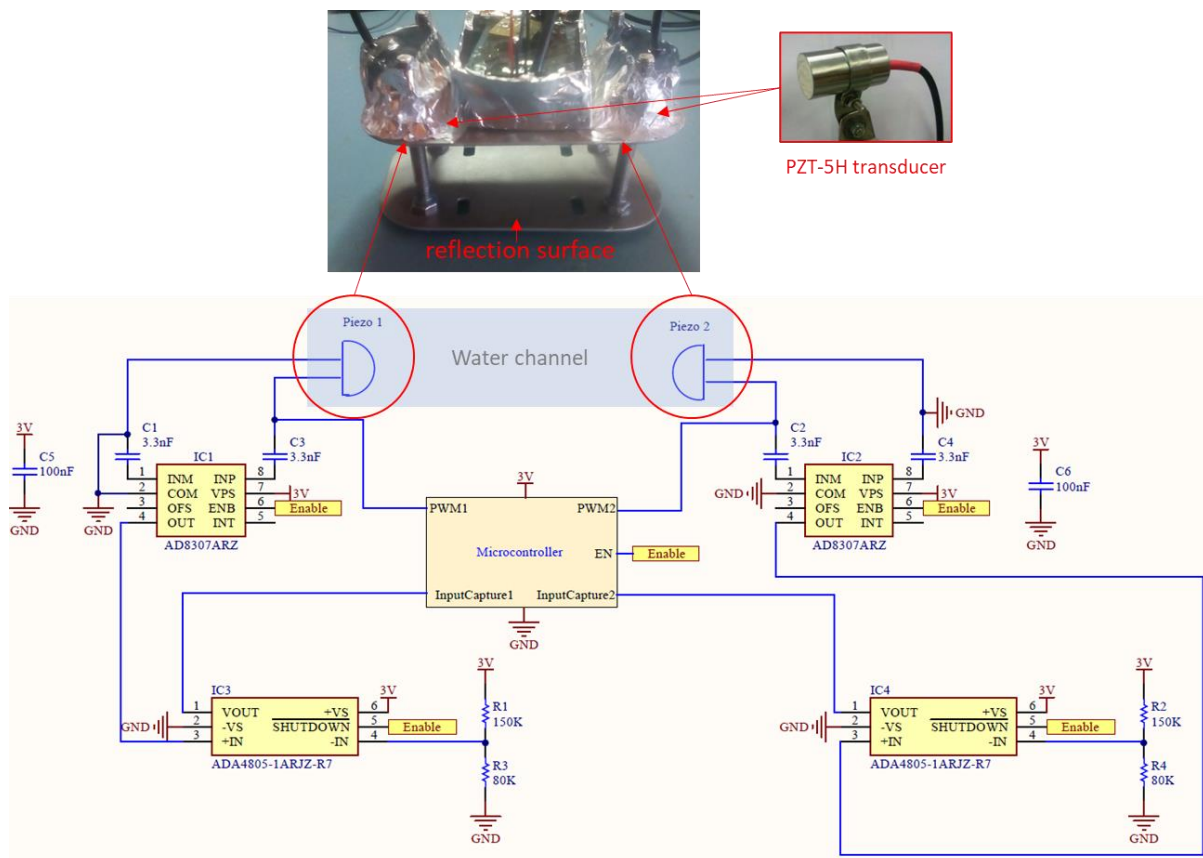
Figure 53. Illustration of the acoustic ToF current meter, electric scheme and PZT-H5 transducer.

An STM32L412K8T6 microprocessor generates a quadrangular signal with 1.5 V amplitude, 1.5 V offset, 1 MHz and 50% duty cycle. This signal is applied to the active emitter transducer that sends the acoustic beam. For better performance, a sinusoid signal can be used, but ceramic material also presents a good performance with quadrangular excitation.

The emitted beam is reflected in the mirror surface and sensed by the active piezoelectric receiver, which turns it into an electric signal. The signal is coupled using an AD8307ARZ logarithmic amplifier that converts the received signal into a DC output as a function of the input frequency (constant, 1MHz) and input power. The output of the logarithmic amplifier is used in an ADA4805 operational amplifier, designed as a comparator circuit, that defines a threshold and produces a binary signal. The output signal of the ADA4805 flags the time from the emission of the acoustic beam to its reception from the receiver, as Figure 54 shows. This time is measured by the microprocessor and used to calculate the water velocity.
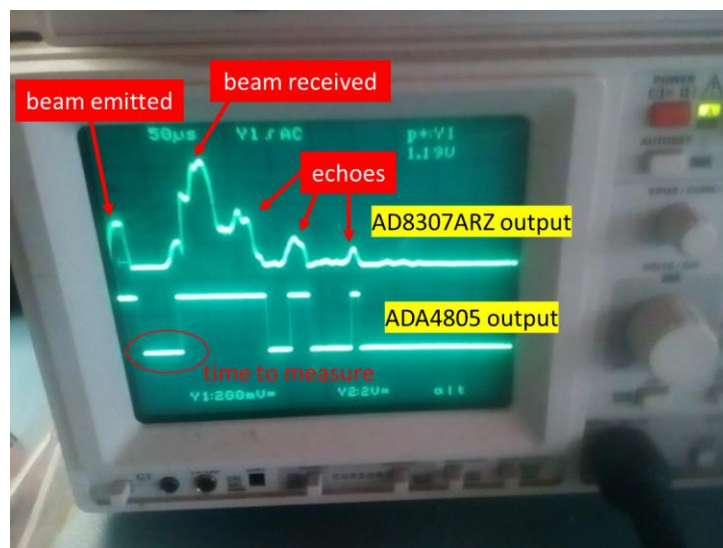
Figure 54. Oscilloscope caption that demonstrates the principle of operation of the acoustic ToF current meter. The oscilloscope shows the output signals of the AD8307ARZ logarithmic amplifier and the ADA4805 comparator after the emission of an acoustic beam. The pulse flagged "time to measure" is used to measure the water velocity.

As for the other developed sensors, the electronic circuits are supplied with 3 V using a TPS62840DLCR regulator and the sensor uses an RS485 bus to communicate. The complete electronic schematic can be consulted in Supplementary Material I 7 and the respective PCB in Supplementary Material II 7.

The electronics were designed to perform a bidirectional measurement, this is, both transducers emit acoustic waves to their pair in turns. As explained in the state of the art, the bidirectional measurement is needed to cancel the effects of depth, temperature and other characteristics of the medium.

To calculate the water (or other fluid) velocity, the sensor measures the time that the acoustic beams take to travel from piezo A to piezo B (hereinafter referred to as $time_1$) and the time that the acoustic beam takes to travel from piezo B to piezo A (hereinafter referred to as $time_2$). If the fluid is flowing from A to B, $time_1$ will be smaller than $time_2$.

Considering Newton's equation of motion, it is given the relationship between velocity, distance and time:

$$velocity = \frac{distance}{time} \tag{19}$$

Using the equation to describe the times measured by the sensor and the 9 cm distance between the acoustic transducers, it can be inferred:

$$time_1 = \frac{0.09}{velocity_1} \quad \wedge \quad time_2 = \frac{0.09}{velocity_2} \tag{20}$$

Note that the velocity for $time_1$ is necessarily different from $time_2$ for non-null water velocities. Otherwise, the times would be equal.

The *velocity* variable is a sum of the vectorial forces acting on the acoustic beams (the velocity of sound and the velocity of the medium). The two forces are additive for the downstream measurement. For the upstream measurement, the forces are subtractive:

$$velocity_1 = v_{sound} + v_{flow} \quad \wedge \quad velocity_2 = v_{sound} - v_{flow} \tag{21}$$

The angle of the transducers to the stream flow is 45° and the vectorial acoustic path is not 9 cm but $9 * \cos(45^\circ)^{-1}$ cm. Also, the velocity of sound must be decomposed in $v_x = v * \cos(45^\circ)$ and $v_y = v * \sin(45^\circ)$. This is true for the unidirectional measurement of time-of-flight technology. However, the objective of using bidirectional measurement is to cancel mathematical the properties of the medium. This means that the v_{sound} changes with the characteristics of the fluid.

Assuming the variables $velocity_1$ and $velocity_2$ of Equation (21) e Equation (20) and solving it for v_{sound}:

$$\begin{cases} v_{sound} = \dfrac{0.09 * \cos(45^\circ)^{-1}}{time_1} - v_{flow} \\ v_{sound} = \dfrac{0.09 * \cos(45^\circ)^{-1}}{time_2} + v_{flow} \end{cases} \tag{22}$$

v_{sound} can now be cancelled to get an equation with the variables of the measured time and the velocity of the fluid:

$$\frac{0.09 * \cos(45^\circ)^{-1}}{time_1} - v_{flow} = \frac{0.09 * \cos(45^\circ)^{-1}}{time_2} + v_{flow} \qquad (23)$$

Solving the Equation (23) for v_{flow}:

$$v_{flow} = \frac{0.09}{2 * \cos(45^\circ)} * \left(\frac{1}{time_1} - \frac{1}{time_2} \right) \qquad (24)$$

This is the equation that the sensor uses to calculate the velocity of water using the two times measured. Contrary to the sensors presented before, the physical equations of the principle of operation can be described, so the typical calibrations are not necessary.

The microprocessor used offers a time-measuring resolution of 11 ns, which means that the acoustic ToF current meter cannot measure velocities lower than 10 cm/s. For a better resolution, faster microprocessors with higher time resolution can be used. In addition, a different setup can also increase the distance between the transducers.

The developed sensor presents a power consumption of 50 mW when taking measurements (10 ms active time) and 60 µW in sleep mode. It had a cost of 53 € in raw materials, including the acoustic transducers, to be developed.

While the correct operation of the sensor was achieved, the 10 cm/s resolution of the sensor underperforms the capabilities of the available current meters. Also, as will be presented in the section on the *in situ* experiments, the structural design of the sensor was propitious to the attachment of algae which interfered with the measurements. The search for a better instrument was still in demand.

3.7 SeT Sensor – sediment transport

Parts of this subsection are under revision to be published in the Journal of Environmental Management, Elsevier, with the title "Design of a sensor to estimate sediment transport in situ using the measurements of water velocity, suspended sediment concentration and depth".

The last technology developed to measure water velocity was the use of a cantilever structure with piezoresistive transduction. Reminding, the cantilever is an elongated structure that is subject to the movement of the fluid. Due to the drag forces acting upon the structure, it will bend and cause compression or extension of the piezoresistive material and change its resistance (a similar mechanism to the cupula used for the MEMS sensor).

Two prototypes were developed before achieving the final design of the sensor. While the electronic instrumentation to read piezoresistive signals is well consolidated in the literature, the development of the mechanical parts of the cantilever, which needed to consider submersion needs, is rather complex.

The first developed prototype used a 55.37 mm Flex Sensor from Spectra Symbol. The Flex Sensor is a flexible strip, with 25 kΩ nominal resistance and a 45-125 kΩ bend resistance range, that was developed to sense the motion of fingers for the Nintendo Power Glove (Figure 55).

Figure 55. The Flex Sensor from Spectral Symbol (image at left) was developed to sense the finger motion for the Nintendo Power Glove (image at right).

The Flex Sensor has the advantage of comprising the cantilever structure and the piezoresistive material. For developing an instrument to measure water velocity, it needed to be integrated with the electronic instrumentation and be prepared for submersion.

To meet the watertight needs, the flexible strip was covered on both sides with a flexible silicon (Soudal T-Rex Flex) and its bottom extremity was anchored to the housing of the sensor. Regarding the electronic circuits, the piezoresistive transducer was coupled with a gain resistor and impedance buffer (as recommended in the datasheet of the Flex Sensor) and its output was read by the ADC of an STM32L412K8T6. The 3V TPS62840DLCR regulator and the LTC1480 RS485 transceiver were used for the voltage regulation. All the electronics were comprised in a 3D printed housing that was filled with polyurethane to protect it from the water. The complete electronic schematic is presented in Supplementary Material I 8, the printed circuit board in Supplementary Material II 8 and the 3D drawing of the housing of the sensor in Supplementary Material III 3.

This prototype with the Flex Sensor did not achieve the desired performance during the field tests. The device showed an abnormal variation in its output (at the time it was thought that it was related to the susceptibility of the piezoresistive material to temperature). Also, the Flex Sensor presented different sensitivity depending on the bending direction, which means that the resolution to measure upstream and downstream flow would be different. However, the major concern was about the silicon used to cover

the Flex Sensor that did not provide the necessary robustness to be deployed (the bottom right image of Figure 56 shows a cut in the silicon after the in situ test).
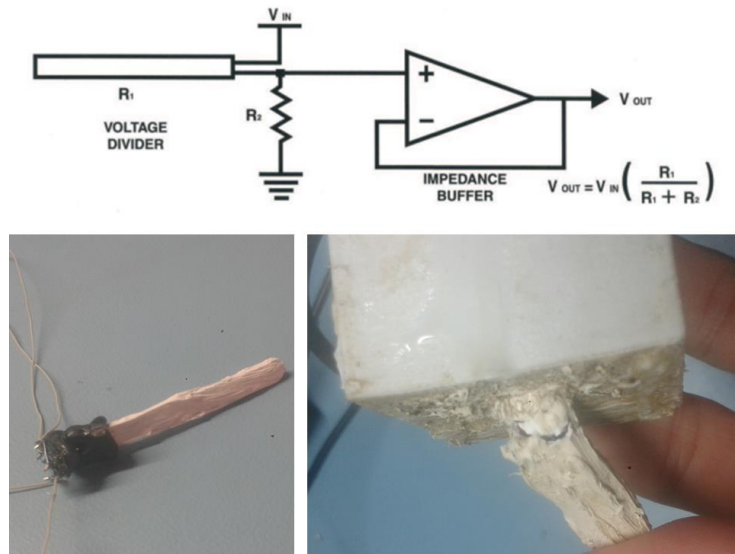
Figure 56. The top image shows the electric scheme to couple the Flex Sensor. The bottom-left image showcases the Flex Sensor after being coated with flexible silicon and the bottom-right image reveals the sensor after the *in situ* experiment, exhibiting the silicon cover torn.

A second prototype was built to refine and improve the problems presented by the previous device. The cantilever of the new instrument was re-designed with two Flex Sensors, placed back-to-back, to have a similar resolution in the upstream and downstream directions. The coupling of the piezoresistive material was changed to a half Wheatstone bridge and instrument amplifier to increase the sensitivity and reduce the temperature interference (image at left in Figure 57). The cover of the piezoresistive material was also changed to an RTV-2 elastomer silicon (HB Flex 901 – HB Quimica) that presented better properties in terms of flexibility, robustness, and ease of application.
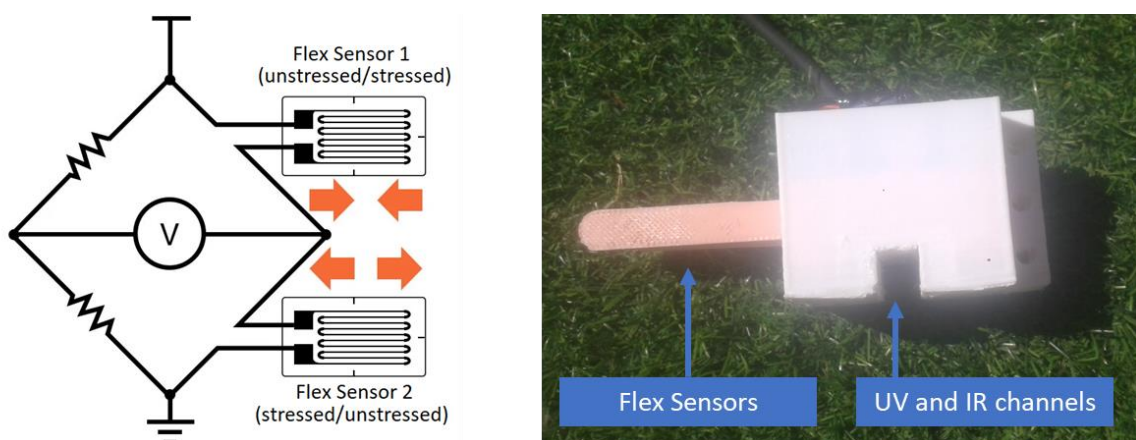
Figure 57. The left image shows the electric circuit of the Flex Sensors in a half Wheatstone bridge and the right image shows the second prototype of the sensor after fabrication.

Since the final objective of the sensor was to measure sediment transport, the new version was designed with infrared and ultraviolet transmitted light channels (1 cm of distance between the light source and the receiver).

The electronics for the optical channels were the same as applied before in the optical sensors. An STM32L412K8T6 controls the LEDs using the respective DMG6968U-7 and the photodetectors use a resistor gain so the output is read by the ADC (IR channel: VSLY5940 light source and W53P3C phototransistor; UV channel: VAOL-5GUV8T4 light source and TEPT5700 phototransistor). The sensor uses the voltage regulators TPS62840DLCR and TPS61222DCKR for 3 V and 5 V, respectively, and the RS485 transceiver LTC1480. An ADA4805 instrumentation amplifier and an AD8227 operational amplifier were used for the Wheatstone bridge instrumentation. The housing of the sensor was 3D printed to assemble the electronics, cantilever and optical channels (image at right in Figure 57). Polyurethane was used to protect the electronic from the water. The complete electronic schematic can be consulted in Supplementary Material I 9 and the respective PCB in Supplementary Material II 9. The 3D drawing is presented in Supplementary Material III 4.

The second prototype with the Flex Sensors was tested in the field and the abnormal output variation detected on the first prototype was still noticed. A deeper investigation of the Flex Sensor showed that similar problems have been found by others. Tiboni *et al.* presented mechanical tests with the Flex Sensor that resulted in 13% hysteresis and 93% repeatability when bending the sensor from 0° to 110° [200]. The use of the Flex Sensor was abandoned due to these characteristics.

A cantilever using four strain gauges TENMEX TF3/120-K (120 Ω nominal resistance, ±0.5% tolerance and 5 x 7.5 x 0.06 mm dimension) was used for the third prototype and final version of the SeT sensor. Due to the small size of the strain gauges, the cantilever was designed with two pairs of TF3/120-K placed back-to-back to perform a full-Wheatstone bridge. Two of the strain gauges were glued using cyanoacrylate on the top layer of a 20 mm x 80 mm x 200 μm acetate strip and the other two on the bottom layer and back-to-back to the front strain gauges. The acetate strip and strain gauges were embedded in room-temperature-vulcanizing (RVT) elastomer silicone (HB Flex 901 Silicone RTV-2, HBQuimica) to meet the water-tight needs. The fabrication process of the cantilever is presented in Figure 58.
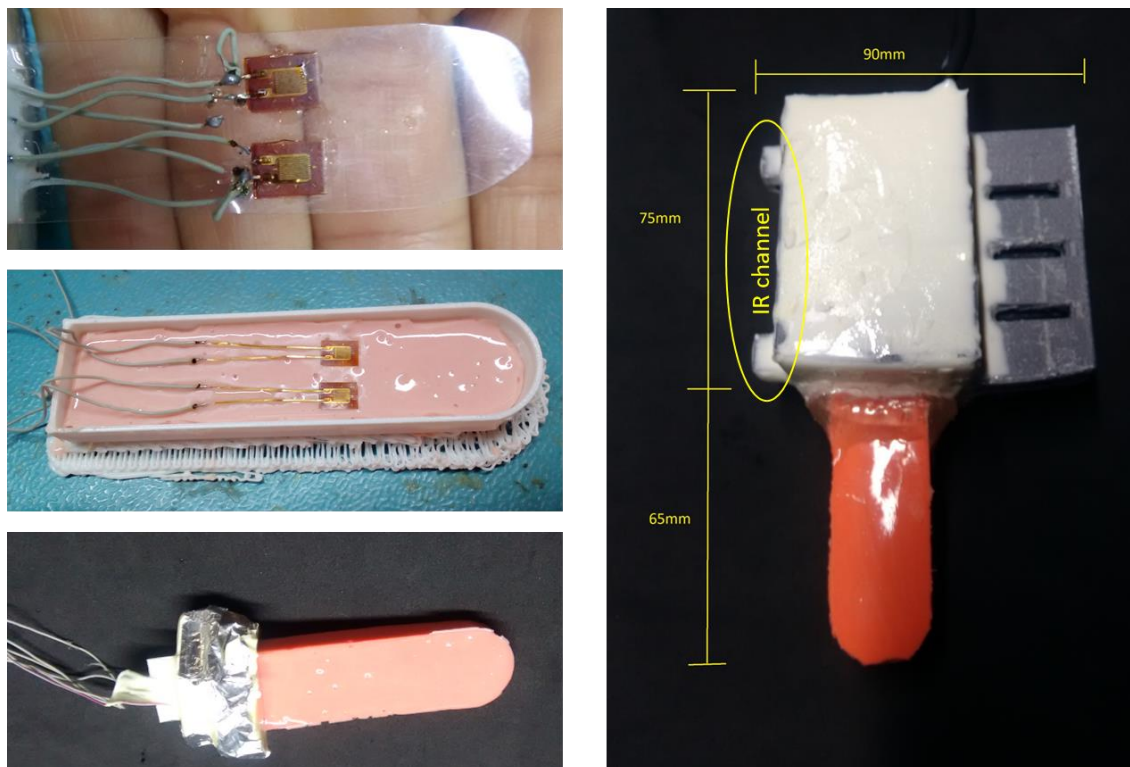
Figure 58. Fabrication process of the cantilever and SeT sensor. The top-left image presents the four strain gauges glued to the acetate strip with cyanoacrylate glue (two on the top layer and two on the bottom layer). The middle-left image presents the cantilever being covered with silicone. At the bottom-left image is the result of the cantilever. The right image presents the SeT sensor with the cantilever and the optical IR channel to measure suspended sediment concentration.

As for the second prototype, an IR channel with a 45 mm light path was added to the sensor to measure turbidity and/or suspended sediment concentration. The electronic used in this final instrument are the same as used in the second prototype but using the four strain gauges in a full-Wheatstone bridge and without the electronics for the UV channel. The MS5837-30BA pressure and temperature sensor was assembled into the sensor housing. The complete schematic of the SeT sensor can be consulted in Supplementary Material I 10 and the respective PCB in Supplementary Material II 10. The 3D drawing is presented in Supplementary Material III 5.

The SeT Sensor measures water velocity in 1-axis and two directions, and turbidity and/or sediment concentration to perform a complete monitoring of sediment transport. The instrument had a production cost of 70 € in raw materials and has a power consumption of 325 mW when taking measurements (3 ms active time) and 60 µW in sleep mode.

3.7.1 In-lab calibration

A set of laboratory experiments were conducted to calibrate the sensor to be able to estimate sediment transport *in situ*. Besides the water temperature and pressure from the MS5837-30BA, the other two variables that the sensor measures are the suspended sediment concentration (or turbidity) and the water velocity.

Setups of laboratory experiments were designed to correlate both the electrical output of the photodetector to different suspended sediment concentrations and the electrical output of the Wheatstone bridge to different fluid velocities in two directions. An additional test was conducted to mitigate the susceptibility of the strain gauges and remaining electronics to temperature variations.

3.7.1.1 Suspended sediment calibration

Since the objective of the developed sensor is to measure sediment transport and not turbidity, the sensor was calibrated with seashore sand instead of formazin. As presented before for the calibration of the turbidity optical meter, the use of different sizes of suspended sediment produces different output results (revise the results of Figure 21). Since sedimentary transport is highly influenced by the wash load, the sediment calibration of the sensor was conducted using small particle sizes.

Seashore from the place where the sensor was intended to be installed (estuary of Cávado River, Portugal) was collected, grinded and sieved using a 125 μm American Society for Testing Materials (ASTM) sieve. It was observed that with this particle size, the sediment remained in suspension on the water and took more than 30 seconds to settle after the agitation of the sample.

The sensor was submerged in a container with distilled water and the prepared seashore sand was gradually added. Before every measurement, a mechanical mixer was used to homogenize the sample and resuspend the settled sediment. Twenty measurements with a sampling period of 0.5 seconds were recorded for suspended sediment concentrations of 0, 0.1, 0.23, 0.35, 0.46, 0.59, 0.7, 0.88, 1.07, 1.22, 1.37, 1.66, 1.85, 2.33, 3.04, 4.05, 5.09, 6.62, 9.14 and 11.68 g/L (see Figure 59 for samples comparison).

Figure 60 shows a boxplot graph with the maximum, minimum, mean and outliers (red crosses) of the records during the calibration experiment. The results show the expected behaviour of a transmitted light detection technique. The sensor recorded maximum output values for the distilled water sample (0 g/L)

that decreases with the increment of sediment in the water that scatters and absorbs the transmitted light.

| 0,23 g/L | 0,7 g/L | 1,37 g/L | 3,04 g/L | 5,09 g/L | 11,68 g/L |
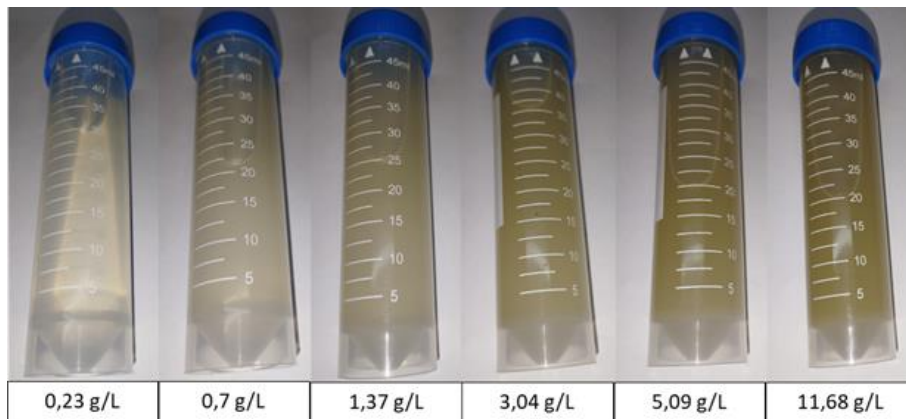
Figure 59. Sediment concentration comparison with samples used during the calibration of the sensor.

The data shows that the sensitivity of the sensor decreases from 656 to 9.3 mV/(g/L), in the range of 0 to 12 g/L. Considering the output voltage and the 12-bit ADC, the resolution of the sensor decreases from 0.001 g/L to 0.1 g/L in the same range. The higher resolution in the range of 0 to 4 g/L provides the necessary limit of detection for *in situ* monitoring.

The curve fitting of the correlation between the sensor output (mV) and the sediment concentration (g/L) was computed (cyan line in Figure 60) and embedded in the software of the sensor for the *in situ* phase. A calibration for the external light was also conducted as described in section 3.2.2.4.

Curve fitting:
ssc -> suspended sediment concentration (g/L)
out -> sensor output (mV)
$ssc = -1E\text{-}09out^3 + 5E\text{-}06out^2 - 0,0072out + 4,0315$
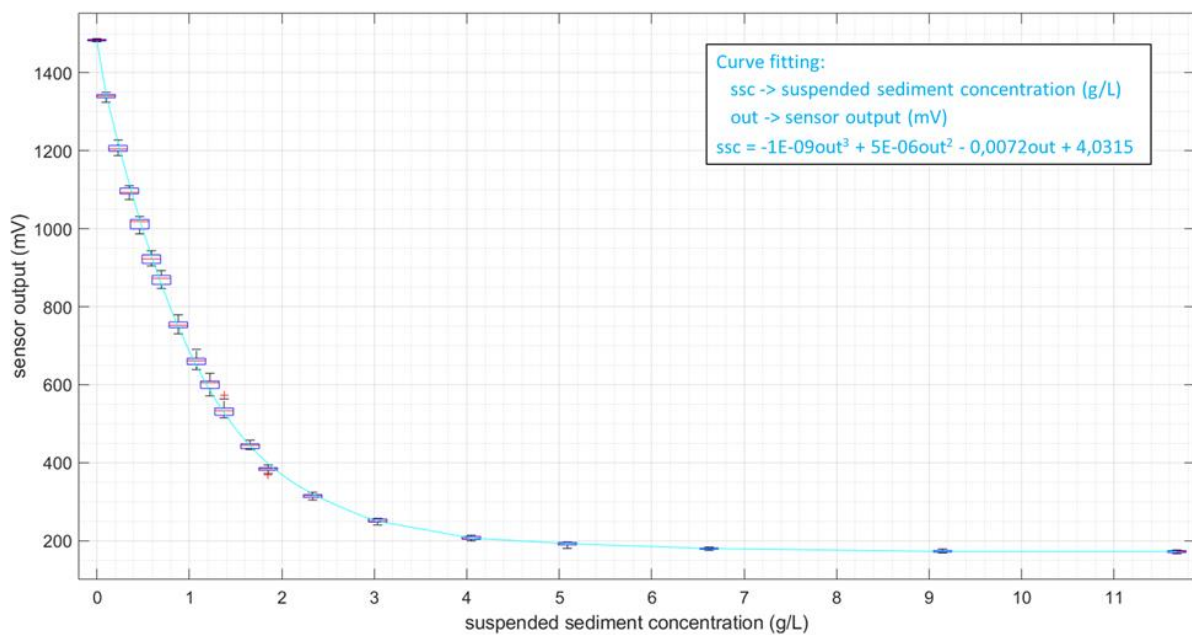
Figure 60. Boxplot graph of the calibration of the SeT Sensor with seashore sand for suspended sediment concentrations from 0 to 11.68 g/L.

3.7.1.2 Water velocity calibration

The second variable measured by the SeT sensor is the water velocity. A testing setup was prepared to calibrate the sensor for different flow magnitudes, which consisted of a water circuit composed of a water pump, a closed chamber with the sensor and water channels/connections (Figure 61). Two different water pumps were used to generate 18 flow intensities: Jebao DC-650 pump (8 intensity levels) and Jebao DC-4000 (10 intensity levels).
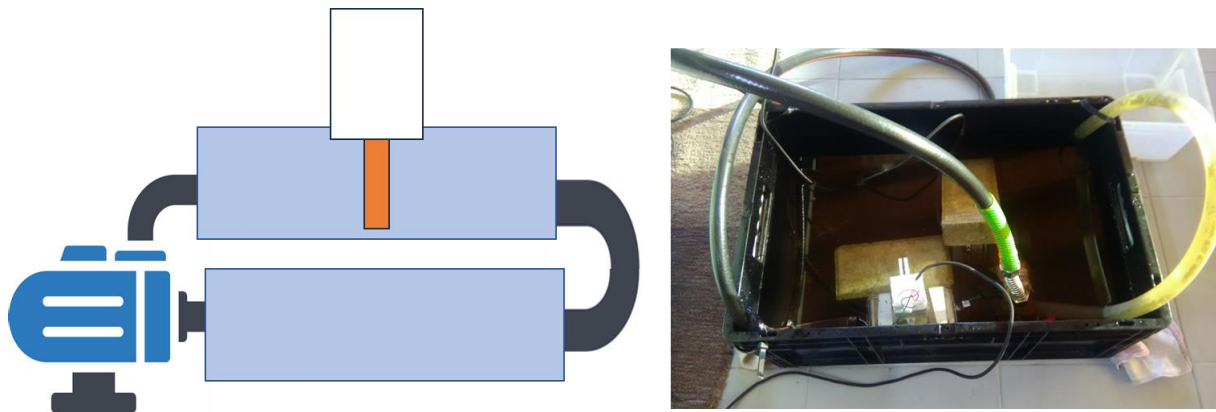
Figure 61. Test setup of the water velocity calibration with the SeT sensor. The left image shows the scheme of the water circuit. The right image shows a photograph of the system with the Jebao DC-4000 pump.

For each one of the 18 flow intensities, the water circuit was open to measure the time of discharge for 2 Litre (which gives the flow in m^3/s) and the corresponding water velocity was calculated using Equation (1) and using the section area of the sensor chamber. For each flow intensity, the sensor recorded 20 measurements with a sampling period of 1 second. After the experiment, the inlet and outlet of the chamber were inverted, and the test was executed again to measure the water velocity in the opposite direction.

Figure 62 shows the records of the calibration experiment with both water pumps in a boxplot graph (median, minimum, maximum and outliers). The results of the different pumps are coherent with each other. The records for 0 m/s and from 0.5 m/s to 0.752 m/s (common ranges for both pumps) are similar. The graph shows that the variance of the measurements increases for higher flow rates (and mostly for the Jebao DC-4000 pump). This behaviour happens because the turbulence inside the chamber of the sensor increases when the flow magnitude increases.
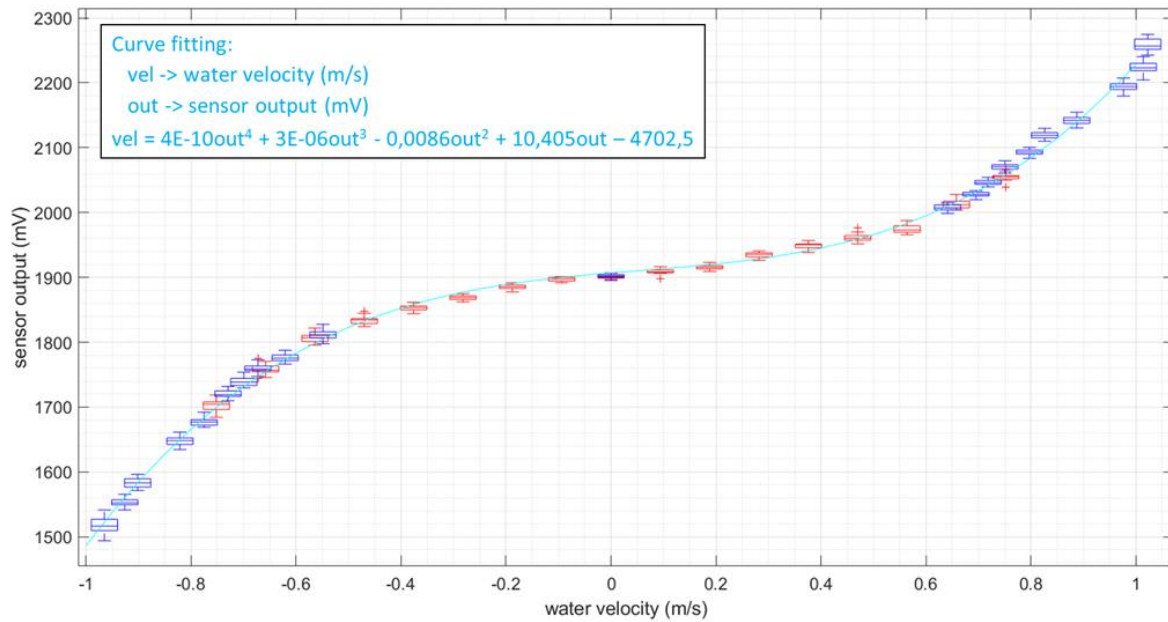
Figure 62. Results of the water velocity calibration with the SeT sensor. The boxplot graph shows in red boxes the records using the Jebao DC-650 pump and in blue boxes the records using the Jebao DC-4000. Outliers are shown in red crosses.

The sensor presented a sensitivity of ≈135.28 mV/(m/s) and maximum uncertainty of ±0.09 m/s in the range |velocity|< 0.5 m/s, and ≈578.17 mV/(m/s) and maximum uncertainty of ±0.03 m/s in the range 0.5 > |velocity| < 1 m/s.

The curve fitting of the data was computed using a 3-order polynomial curve (cyan line) to correlate the sensor output (mV) to values of water velocity (m/s). This curve was embedded in the software of the sensor for the *in situ* phase.

3.7.1.3 Temperature calibration

The major factor that can produce errors in the velocity measurements is the susceptibility of the strain gauges to temperature. Even though the full-Wheatstone bridge is used to reduce this error, an experiment was conducted to analyse the response of the sensor to different water temperatures.

The sensor was placed in a container with water at 25 °C and ice. The device took records with a sample period of 5 seconds till the water temperature reached 10 °C. Figure 63 shows the measurements recorded during the experiment.

Since there is no flow in the container, for a good operation the output of the sensor must be constant. However, the results show that the temperature affects the output, and it needs to be corrected. As for

the influence of the external light on the optical turbidity sensors demonstrated before, a similar mathematical calibration was calculated to correct the output as a function of the water temperature.
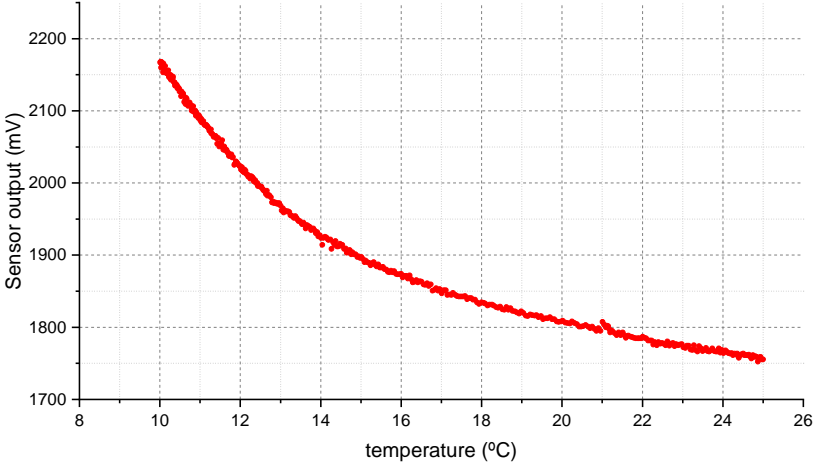
Figure 63. The graph shows the change in the sensor output for different water temperatures.

The first step is to divide the output measured by the corresponding output value for 0 m/s (there was no water flow in the container during the experiment). According to the calibration for water velocity presented in the previous subsection, the output value that corresponds to 0 m/s is 1901 mV (the calibration was performed with water at 15 °C).

Figure 64 shows the relative coefficient of this division (note that the coefficient value of 1 corresponds to the water temperature of 15 °C, as supposed).

$$y = -0,0001x^3 + 0,0069x^2 - 0,1481x + 2,0428$$
$$R^2 = 0,999$$
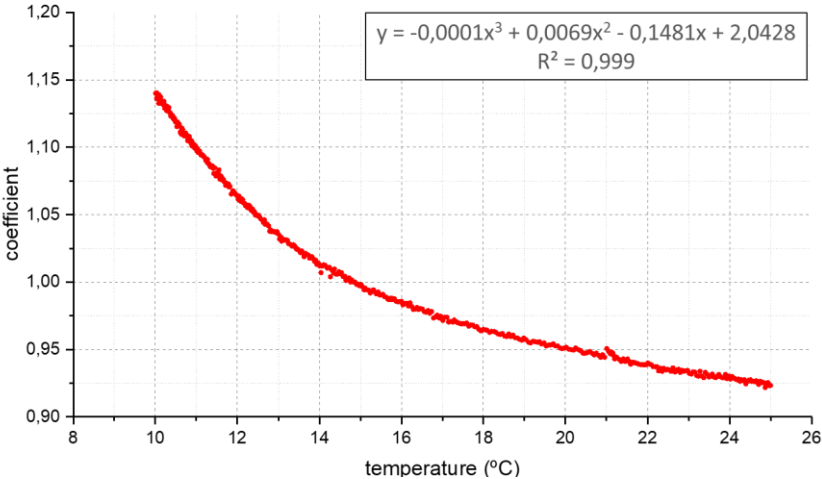
Figure 64. Results of the relative coefficients of the water temperature experiment using the sensor output corresponding to 0 m/s (1901 mV) as reference. The equation in the box label represents the fitting of the curve.

The coefficient function was fitted in a 3-order polynomial curve that is used to rectify the sensor output as a function of the water temperature according to the following equation:

$$output_{rectified} = \frac{output_{measured}}{f_{coefficient}(temperature)} \qquad (\,25\,)$$

Figure 65 shows the results of the presented calibration applied to the data of Figure 63. The results show that the algorithm developed to reduce the susceptibility of the sensor to the water temperature works, presenting a calibrated output with minimal variation.
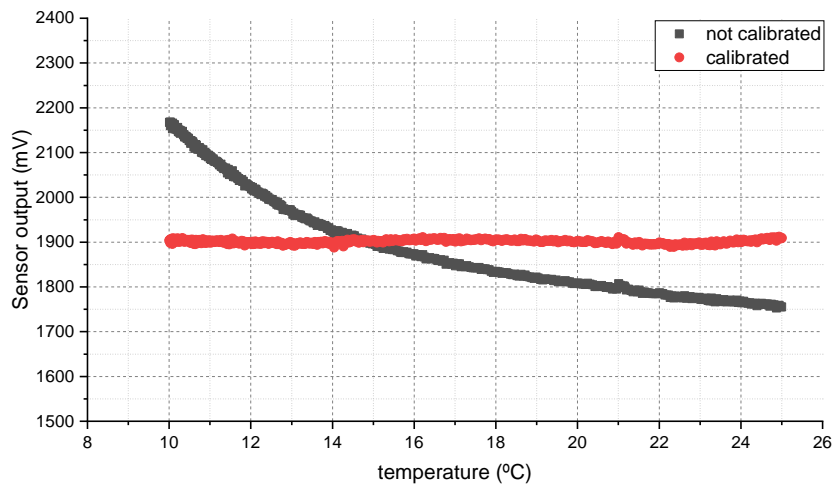
Figure 65. Comparison of the sensor output with the calibrated and not calibrated curves for the experiment with different water temperatures.

3.8 Anti-biofouling Techniques

This subsection was published in "Design and *In situ* Validation of Low-Cost and Easy to Apply Anti-Biofouling Techniques for Oceanographic Continuous Monitoring with Optical Instruments", Sensors MDPI [142].

Along this chapter, it was presented the design of sensors for continuous monitoring. The structural housing of these instruments was built using 3D printed materials such as PLA or ABS, which are less robust and more susceptible to biofouling when compared to materials used in commercial sensors (e.g., titanium and sapphire glass). For this reason, biofouling is a major concern, particularly when these cost-effective sensors are intended to match the performance of their commercial peers.

In particular, sensors that make use of optical techniques are more susceptible to biofouling, which decreases their sensitivity and reliable lifetime. Even a small amount of biofilm on the surface of the optical areas can produce interference in the measurements due to absorption and light scattering. Considering that biofouling starts its formation the moment the instrument is submerged, optical sensors can have a short period of operation.

The developed optical instruments use backscattering, nephelometry and transmitted light techniques. For the transmitted detection, both fouling on the surface of the optical transducers and the existence of macro-fouling in the sensor housing can block the passage of light and increase the turbidity values measured by the sensor. However, for the backscattering and nephelometric techniques, while the decrease in the optical signal results in lower turbidity values, macro-fouling can also generate undesired scattering that increases the turbidity measurements. This factor presents additional challenges when analysing the biofouling interference for the backscattering and nephelometric techniques. To reduce the complexity of the biofouling effects in the measurements, the problem was narrowed using only the transmitted light detection.

3.8.1 Hardware design

Six probes were built using different anti-biofouling techniques or housing materials: PLA housing, ABS housing, PLA with copper filament housing, epoxy coating, PDMS coating and chlorine production. The probes were designed in a tube shape with an optical measuring area in its inside. This shape was chosen to create a sensing area with low fluid flow and turbulence, so that some of the techniques (localized chlorine production and copper biocide) could be more effective than in an open design, unprotected from the normal stream flow.

Each one of the probes uses one infrared 980 nm (LED) and one infrared 980 nm phototransistor that measures light at 180° from the light source. The top image of Figure 66 shows the 3D design and schematic of the optical transducers. The sensor housing presented was slightly changed to adapt each one of the different anti-biofouling techniques in test. These techniques can be divided into four different groups: structural materials and copper biocide, transparent coating, and chlorine production (bottom image of Figure 66).

The electronics of the instrument were designed using similar circuits used in the developed optical sensors. An STM32L422RBT6P microprocessor was selected to turn the LEDs ON and OFF using a MOSFET. The photodetectors use a resistor gain for the current-to-voltage converter that is read by the ADC channels. The TPS62842DGRR regulates the 3 V that supplies the circuit and the LTC1480 interfaces the UART of the microprocessor with the RS485 bus. The complete schematic is presented in Supplementary Material I 17 and the respective PCB is in Supplementary Material II 17.
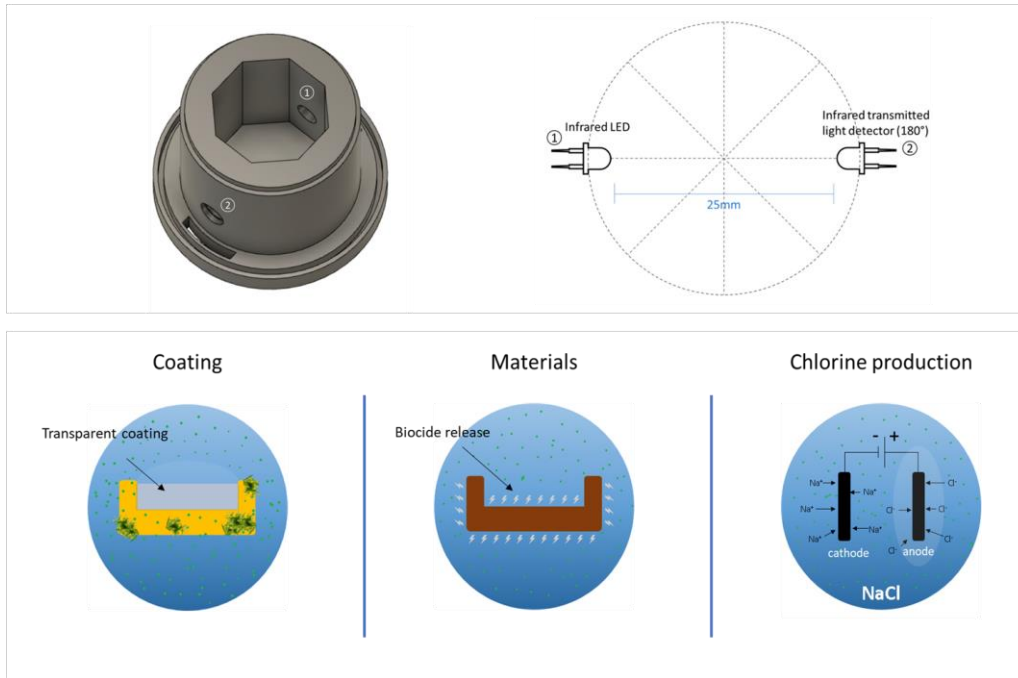
Figure 66. The top image shows the mechanical drawing of the probe comprising the optical transducers (left image) and the scheme of the positions of the LED (1) and the transmitted light detector (2) (right image). The bottom image shows a scheme of the anti-biofouling mechanisms using coatings, different materials (copper biocide) and chlorine production by the electrolysis of salty water.

The six probes were assembled on one board with a minimum distance of 1 cm from each other, as Figure 67 shows. Due to the confined shape of the probes, the techniques based on biocide production are not expected to affect the other probes through the spread of the biocides.

Figure 67. Anti-biofouling techniques probes. Probe 1: ABS material; Probe 2: PLA with copper filament; Probe 3: PDMS coating; Probe 4: PLA material; Probe 5: epoxy coating; Probe 6: chlorine production.

3.8.1.1 Structural materials

The characteristics of the housing of the sensor play a major role in the attachment of biofilm. Smooth surfaces are less susceptible to attaching biological organisms when compared to rough surfaces (in fact, rough surfaces are sought to design artificial reefs [201]). In addition, materials such as inox or titanium are known to be less propitious to biological film formation when compared to plastic ones.

The most effective materials against biofouling are also more expensive. Since one of the needs of this work is to test the application of anti-biofouling techniques in low-cost instruments, the two cheapest and wider in-use 3D printing materials were tested: PLA and ABS.

It is important to notice that the PLA and ABS probes are not anti-biofouling techniques but rather the use of different structural materials (these materials do not have intrinsic anti-biofouling characteristics). In both probes, the optical transducer surfaces are in contact with the water without any protection. However, both ABS and PLA materials are often catalysed with organotin which can leach out and act as an antifoulant [202-203].

The performance of ABS and PLA probes in the field is not expected to differ significantly, which would allow their use as control samples and to be compared with the other techniques.

The PLA and ABS probes are shown in Figure 67 as probes 4 and 1, respectively.

3.8.1.2 Copper biocide

The cooper technique was based on the use of 3D printed material PLA with copper filament (FlashForge PLA Copper 1.75 mm) for the structural housing of the probe. As for the PLA and ABS probes, the surfaces of the optical transducers are in contact with water. However, copper has biocide properties that prevent the formation of biofilms. Therefore, since the transducers are comprised inside the tube shape, it is expected that the release of biocide into the water extends the operation time of the sensor when compared to PLA and ABS.

The advantage of using this technique is that it is easy to apply (just the use of different materials in the 3D printer) and it is still a cost-effective material. The main disadvantages are that the copper protection has a limited time since it loses its biocide properties over time and, as stated before, the biocide is not environmentally friendly.

The structural housing of the PLA with copper filament probe was all built with that material, including the outside walls of the probe, which means that the release of copper biocide is not confined. Still, in open waters, the release of copper is not expected to be high enough to influence the biofouling protection of the other probes, and if it happens, it will only affect the outside walls and not the sensing areas.

The PLA with copper filament probe is presented in Figure 67 as probe 2.

3.8.1.3 Transparent coatings

In the previous techniques, the materials used are intended to protect the structural surfaces of the device and possibly the nearby optical parts where biofouling must be avoided. For this technique, transparent coatings are used to directly cover the optical parts and make use of their anti-biofouling properties.

The optical sensors present an enhanced challenge since the coatings must ensure the passage of light. Attending to this need, two easy-to-apply transparent materials were used: transparent epoxy resin (HB EPOSURF2—HBQUIMICA) and polydimethylsiloxane (PDMS—Sylgard® 184 Silicone Elastomer Kit). Both probes were built in ABS and the optical transducers were coated with the transparent materials. The idea of using both PDMS and epoxy as anti-biofouling coatings has been presented before [203–207].

Epoxy resin is an affordable and widely used material that is easy to apply. The resin takes about 7 days to cure before it is ready for immersion. If the coating is submerged earlier, the surface may become whitish and reduce the sensitivity of the optical channel.

The PDMS is an affordable material with wide use in MEMs fabrication and, although it needs dedicated machinery to cure, it is also easy to apply.

The main disadvantage of these techniques is that even though the materials are transparent they still cause light attenuation. If the sensor is built from scratch, this attenuation can be compensated with electronic instrumentation. If the sensor is already built and the coating is applied afterwards, new calibrations are required.

It is important to notice that, as for the structural materials, the effectiveness of the coatings depends on their anti-biofouling properties; in the case of PDMS the release of organotin and for the epoxy other toxic compounds.

The probes are presented in Figure 67 as probes 5 and 3, respectively.

3.8.1.4 Chlorine production

Chlorine is used worldwide for water disinfection. In the developed technique, the electrolysis of salty water is used to produce chlorine biocide. In this approach, the electrodes are usually based on platinum, dimensionally stable anodes of Ti-support coated by noble metal oxides such as ruthenium, iridium, tantalum, zirconium, and doped diamond electrodes. Although this technique is effective in producing chlorine biocide, the opacity of the electrodes has always been an obstacle to its application in optical instruments.

A new approach to producing chlorine biocide is presented. It combines the advantageous features of the platinum material with transparent conductive oxides [209-210]. In this technique, the anode electrode that produces chlorine is transparent and can be directly applied above the optical transducers (like the transparent coatings). This electrode is constituted by platinum nanoparticles coated with a transparent conductive fluorine tin oxide (FTO) thin film supported on a glass substrate. A stainless-steel electrode was used as a cathode for long durability in water without oxidation.

Considering the laboratory experiments of Pinto *et al.* [210], the electric power for the chlorine production in this probe was designed to be 1050 μW in a 2.5 cm^2 area. The production was set to be ON all the time and only turned OFF when the sensor takes measurements. With this configuration, the sensor achieves a production rate of approximately 4 mg of chlorine per hour.

The main disadvantage of this technique is the need for electric power which reduces the operation time of the sensor. However, it allows controlling the amount of chlorine biocide to the minimum required to avoid biofouling, maintaining the sensor area cleaned without negative impact on the marine environment. This technique is only suited for marine environments since it does not work in freshwater.

As demonstrated by Pinto et al. [210], chlorine production is a local process restricted to the surface of the glass substrate. Thus, as for copper biocide, chlorine production is not expected to affect the biofouling of the neighbouring probes.

The chlorine production sensor probe is presented in Figure 67 as probe 6.

3.8.2 In-lab calibration

Before deployment at the sea, the probes were calibrated to correlate the electrical output to the corresponding value of turbidity. The six probes were calibrated to NTU using the same methodology as for the SPM and TVP Sensors. An initial solution of 4000 NTU was diluted in distilled water following Equation (14). Different dilution factors were used to calibrate the sensors for 1000, 500, 250, 125, 62, 31, 15, 7.5, and 3.8 NTU.

Figure 68 shows the calibration of each probe with the turbidity solutions. During the development of the instrument, the electric gain of each technique was adjusted so that for diluted water (low turbidity values) the corresponding voltage outputs were similar. For high turbidity values, the sensitivity of the epoxy, PDMS, and chlorine techniques was lower compared to PLA, ABS, and copper (different slopes in the curves). This is a result of the coating of the optical transducers that attenuate light. Other differences in the values obtained from the different techniques are related to the alignment of the optical transducers, which were manually assembled.
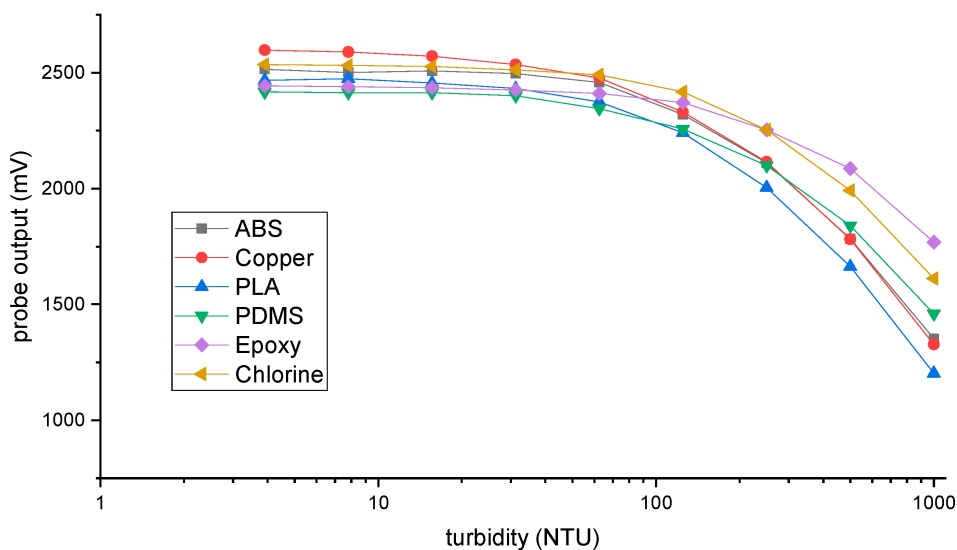
Figure 68. Results of the calibration with formazin of the six anti-biofouling probes. The electrical voltage output of each detector is correlated to the different turbidity solutions.

Each one of the curves was used to convert the electrical output of the probes to turbidity values during the *in situ* test. After the experiment and cleaning of the sensors, a new calibration was conducted to check if the probes kept the same output as before the experiment, or if there was a decrease in the signals, resulting from the biofouling.

3.9 Data logger

The data logger is a crucial part of every monitoring system. The sensors presented before are fully automatic and were developed to perform individual monitoring *in situ*. However, like most other sensors, they need additional systems to store and process data and host multiple monitoring devices if needed.

The scheme overview of the developed data loggers is presented in Figure 69. It is composed of the power circuit, microprocessor (to receive and process the data from the sensors), real-time clock (to keep date and time), storage unit (to save the data), RS485 bus (to communicate with the sensors) and external communications (to send data in real-time).
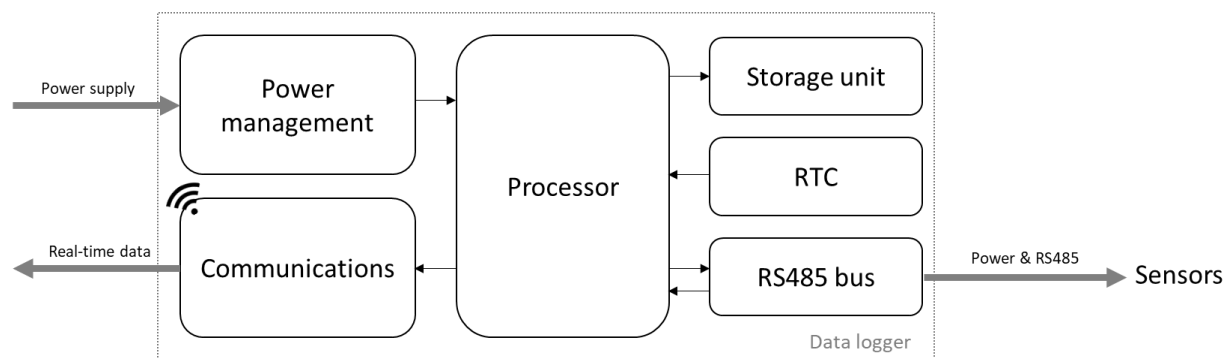
Figure 69. Illustration of the scheme overview of the data logger.

The first version of the data logger was designed using an STM32L496ZG microprocessor. This processor was chosen due to its multiple UART, I2C and SPI ports (that can be used to integrate other commercial sensors and electronic modules), internal RTC with independent power supply and internal SDMMC controller module (used to host SD cards). A printed circuit board was designed with the microprocessor, microSD card holder (storage unit), coin battery holder (to supply the RTC), LTC1480 transceiver for the RS485 communications and TPS62840DLCR voltage regulator to supply the electronics. The electronic schematics can be consulted in Supplementary Material I 11 and the respective PCB in Supplementary Material II 11.

The Covid-19 pandemic situation, followed by the Russia-Ukraine war, had a significant impact on the electronics market. The scarcity of primary materials for the manufacturing of semiconductors led to a shortage of electronics ICs, particularly in the sector of microprocessors which had a waiting line of more than 1 year. The STM32L496ZG soon disappeared from the market and new versions of the data logger were replicated with the similar STM32L552ZET6Q processor (electronic schematic in Supplementary Material I 12 and respective PCB in Supplementary Material II 12). However, this second microprocessor

also became out of stock. At a certain point, there were no microprocessors with SDMCC host controllers available to buy.

To overcome this problem, a set of data loggers for mainstream packages/pinouts was developed to use the microprocessors available on the market. The new data loggers used LQFP-64, LQFP-48 and LQFP-32 packages, which do not have the SDMCC host controller but can use the SPI protocol to communicate with an SD card. A TPS61222DCKR 5V regulator and MCP73831T-5ACI_OT battery charger were added to the new versions of the data loggers. The electronic schematics and respective PCBs of the three types of data logger can be consulted in Supplementary Material I 13-15 and Supplementary Material II 13-15.

3.9.1 External communications

While the main function of the data logger is to save the data from the monitoring sensors, there has always been a concern about providing this information in real-time. With the emergence of the IoT, storage systems such as SD cards are becoming obsolete as a primary source of information and losing space to online platforms. With that in mind, different technologies of wireless communications were prepared to be used in different monitoring applications and to have the capability to send the data in real-time to other access points. These technologies were based on the integration of commercial modules of radio frequency (RF), Wi-Fi, Global System for Mobile Communications (GSM) and Satellite.

For the RF communications, three commercial modules/transceivers were validated: E30-170T27D from EBYTE, RFM98 Lora transceiver and Xbee SX 868 from Digi. The main characteristics of each one of the modules are summarized in Table 4.

Table 4. Characteristics of the radio frequency modules.

RF Module	Frequency (MHz)	Receiver sensitivity	Transmit power	Transmit current	Price
E30-170T27D	170	-121 dBm	27 dBm	70 mA	10 – 15 €
RFM98 Lora	433 and 868	-148 dBm	20 dBm	28 mA	5 – 10 €
Xbee SX 868	868	-113 dBm	13 dBm	55 mA	40 – 50 €

All three modules claim communication transmission distances above 2 km with a clear line of sight. Theoretically, the lower the carrier frequency, the higher the distance that can be achieved for the same transmitting power. However, the antenna in use is also important, and lower frequencies need larger antennas.

A particularity in the comparison of the three modules is the higher price of the Xbee from Digi. However, while the E30-170T27D and RFM98 are limited to the use of the physical communication layer to transmit data between similar nodes in a Peer-to-peer (P2P) configuration, the module from Digi can create private mesh networks with application layers for control, security, redundancy and synchronism protocols.

The major disadvantage of the RF modules is that they can only be used to transmit data between nodes, and do not allow sending it to an online platform. If online data is needed, a possible solution with RF technology is using the MKR WAN 1300 microcontroller.

This module is based on the Atmel SAMD21 processor and the Murata CMWX1ZZABZ LoRa transceiver and has the particularity of using the LoRaWAN protocol to transmit data to a global collaborative IoT online platform: TTN – The Things Network (https://www.thethingsnetwork.org/).

This microcontroller has several GPIOs, ADCs, UART, I2C and SPI buses, so it can be used as a data logger by itself. Its major disadvantage is that it was not developed with low power concerns, so it is not the best option for autonomous continuous monitoring without the electrical grid. Also, the LoRaWAN needs LoraWAN routers in the range of the nodes to communicate with the TTN. Otherwise, it is only useful to use as P2P transmission as the other modules.

The ESP-12E ESP8266 was validated for Wi-Fi technology. This module can create private networks and establish LAN communications with other ESP nodes. Additionally, it can be connected to any Wi-Fi router and access the Internet. The ESP8266 is a microcontroller with several GPIOs, ADCs, UART, I2C and SPI buses, so it can also work as a data logger.

Since this module is suited for low-power applications and has a low price (5-10 €), a PCB was designed to integrate the ESP with commercial SD cards and RTC modules, and an RS485 bus to communicate with the developed sensors (electronic schematic in Supplementary Material I 16 and respective PCB in Supplementary Material II 16).

The disadvantages of the ESP8266 are the need for an available WiFi network to send data to the Internet and the maximum transmission distance is lower than the RF technologies (just a dozen of meters).

Figure 70 shows a range test comparison using an ESP8266 network and an RF Digi Xbee mesh.

Figure 70. Results of a communication range test in an urban area using a Digi Xbee mesh with transmission rates of 10 kbps (yellow line) and 80 kbps (orange line), and an ESP8266 network (blue line). The emitting module was placed in a location with a clear line of sight to the west.

If there is no Wi-Fi network available, and a connection to the Internet is necessary, the GSM, or similar technology, is a possible solution. The SIM7000E module was tested using its commercial expansion shield for Arduino. The SIM7000E works with AT commands and supports GSM, LTE CAT-M1(eMTC) and NB-IoT communications. The module can send data to the internet using the mobile data of a SIM card.

Dedicated IoT SIM cards from Things Mobile (https://www.thingsmobile.com/) were used for this purpose. The main advantage of the GSM modules is that they can access the internet anywhere the mobile signal is available. However, these modules are not low-power (a power supply of 7-12 V and 2 A is needed for proper operation) and the electrical grid is usually needed. Also, accessing the internet using GSM is a paid service.

Both the ESP8266 and the SIM7000E can connect to the internet. A website was created to complement these modules and present the data from the loggers online. The website was built in PHP and HTML language using the Local by Flywheel software and was hosted in the 000webhost domain of Hostinger servers (https://pt.000webhost.com/).

The website was developed to receive data from GET requests and to save it in text files (same as for the SD cards) that are stored in the server cloud. From the main user point of view, it shows the received data, in real-time, in customized charts and graphics powered by Google Charts (see Figure 71).
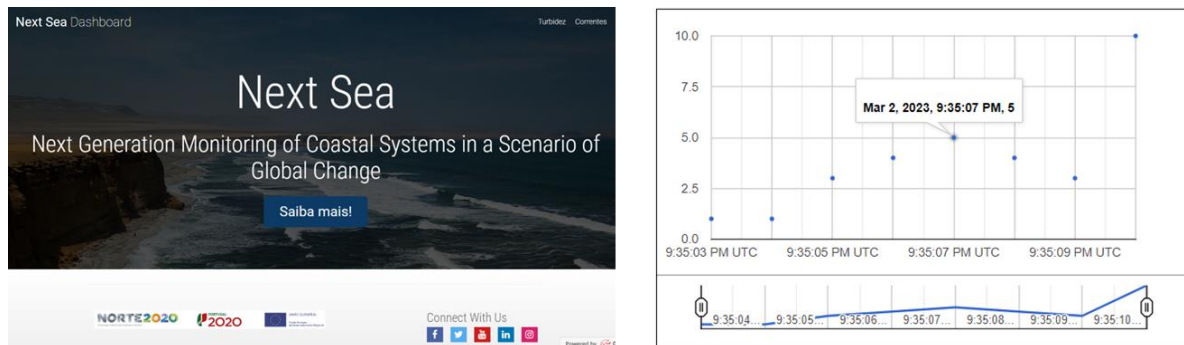
Figure 71. The left image shows the main page of the developed website. The right image shows a chart with data sent to the website.

The use of satellite communications using IRIDIUM was also validated for totally remote applications where the mobile network is not available. The RockBLOCK 9603 IRIDIUM module was chosen due to its compact size (45 x 45mm and 45 g), ease of integration (it is controlled by AT commands) and online platform to receive data (https://rockblock.rock7.com/Operations). The module has a typical transmit consumption of 50 mA (average over 60 second period) and a sleep mode of 73 µA. The main disadvantage of this technology is the price of the module (almost 300 €). Also, satellite communication is a paid service

4 IN SITU MONITORING EXPERIMENTS

This section was published in "A low-cost, low-power and low-size multi-parameter station for real-time and online monitoring of the coastal area", OCEANS Conference (IEEE), Hampton Roads 2022 [211].

The main purpose of the developed technologies was to perform continuous monitoring *in situ*. The laboratory and controlled environment tests showed that the sensors were suited to measure the intended variables. However, field tests present higher and different difficulties and are needed for the final evaluation of the performance, capabilities and disadvantages of said sensors.

The estuary of Cávado River (Esposende, Portugal) was chosen to test the instruments. The river mouth of Cávado is characterized by shallow waters and high sedimentary dynamics that cause several problems in the proper navigation of the estuary and are the major issue for the effective protection of the urbanized coastal line during storms. As Figure 72 shows, this coastal region has been suffering changes in its geomorphology during the last decades [212].

Figure 72. Satellite photographs that show the changes in the geomorphology of the estuary of Cávado River during the last decades. The inlet of the river mouth has been suffering several changes and shallow formations that are a constant problem for the navigation of the channel.

Several governmental actions took place to solve the problem but without success. The need for data about the sedimentary dynamics in this area, together with the characteristics of the estuary, provided an opportune environment to build a monitoring station for the evaluation of the developed technology.

The monitoring station was installed in a dock at 1100 meters from the estuary inlet (41°31'56.84'' N, 8°47'4.16'' W), as Figure 73 shows. The station was designed with a central unit with data logger capabilities (outside the water) and a set of sensors to perform continuous monitoring.

Figure 73. Installation of the monitoring station in the estuary of Cávado (41°31'56.84'' N, 8°47'4.16'' W). The first inset image shows the position of the central unit (outside the water) and the position of the sensors (underwater). The second inset image shows underwater photographs of some of the sensors installed: the SDE Sensor at the top left, a set of SPM Sensors at the top right, the acoustic ToF current meter at the bottom left, and the second prototype of the SeT sensor at the bottom right.

The central unit was installed outside the water to provide easy access to change batteries, download the data, and other maintenance purposes. It was designed in a centralized configuration to host multiple sensors and be responsible for managing the power of the station, accessing, processing, and storing the monitoring information and sending it, in real-time, to an online platform (electronic setup in Figure 74).
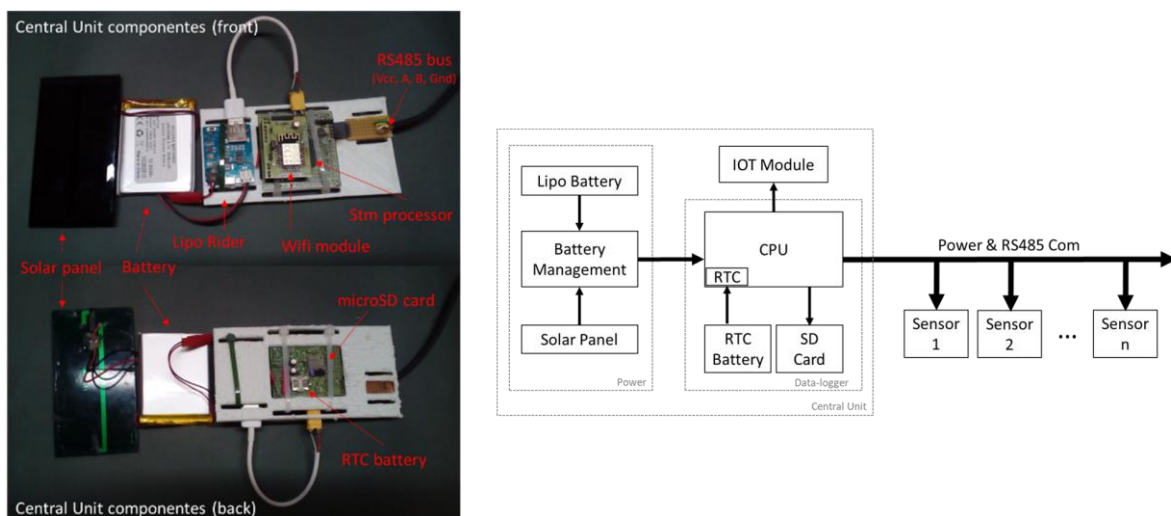
Figure 74. The left image shows the components used in the monitoring station. The right image shows the scheme of electronic modules used in the station.

The station was powered by a 3.7 V 4000 mAh LiPo battery, charged with a 250 mW 5 V solar panel and a LiPo Rider V1.3 battery manager. The LiPo Rider is a commercial module that can be used to charge the battery using a solar panel or a CA/CC 5 V transformer if an electrical grid is available. The 5 V output of the module powered the data logger and the sensors of the station.

The STM32L496ZGT data logger was used to control the sensors and receive their measurements. The data was saved on the microSD card and the internal real-time clock of the STM processor was powered by a coin battery to keep time and date when the station is not powered. The ESP8266 Wi-Fi module received the monitoring information and sent it to an online website using the city Wi-Fi. Figure 75 shows a print screen of the website with turbidity data.
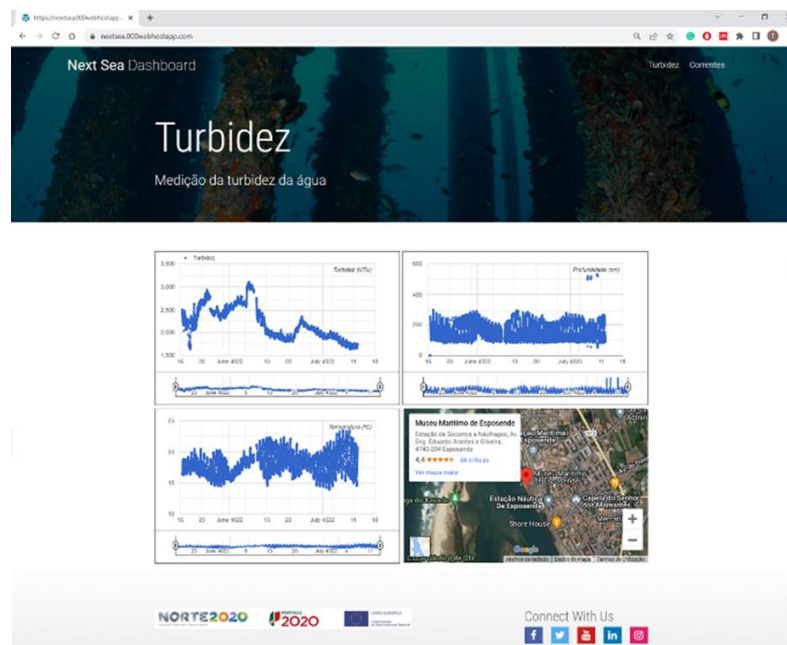
Figure 75. Website print-screen of the data sent by the station from 16th May to 12th July 2022. At the time, the station was hosting sensors to measure turbidity (top left graph), water depth (top right graph) and water temperature (bottom left graph).

The monitoring sensors were installed underwater and connected to the central unit by an electric cable. The electronic set presented in Figure 74 had a total cost of 55 € and power consumption of 15 mW in running mode and 300 mW when sending data using the Wi-Fi module (typically 3 seconds, maximum 15 seconds, depending on the Wi-Fi signal strength).

Since the station was installed inside a natural park, the monitoring experiments were conducted with the legal consent of Delegação Marítima de Esposende da Capitania do Porto de Viana do Castelo (Supplementary Material IV 1), Instituto da Conservação da Natureza e das Florestas – ICNF (Supplementary Material IV 2) and Câmara Municipal de Esposende.

4.1 Water depth and temperature sensors

One of the most important variables to measure in estuaries is the water level (calculated using the pressure measurements from the MS5837 sensor) which is influenced by the tidal cycles. Through this chapter, it will be shown that most of the patterns recorded in the dynamics of the estuary are correlated with the change of tides. Thereby, anytime a sensor was installed in the station, the MSB5837-30B was used to track the tidal changes.

The ocean tides are controlled by the gravitational pull of the moon and sun and are affected by the annual and monthly orbits of these bodies. A spring tide occurs when there is a new or full moon. Because it follows the lunar cycle, a spring tide happens twice a month. With the moon and sun roughly aligned, the tides are on average slightly larger than usual. On beaches, this can be seen when the water comes further up the shore than it usually does.

The neap tide follows seven days after a spring tide. Like the spring tide, it is connected to the lunar phases and takes place after the first and third quarters of the moon. It happens when the moon and sun are at right-angles to each other. The effect of this alignment is that there is less amplitude between high and low tides. This means that on a neap tide, the water does not rise or fall to its usual heights. A high tide will be less high, and a low tide will be less low, decreasing the difference between them.

Figure 76 shows an example of the water level data produced by the MS5837-30BA sensor. The graph shows that the water depth where the sensor was installed varies from 100 cm during the low tides, to almost 350 cm during the high tides. It shows a signal with a period of approximately 12 hours that is related to the change of tides (6 hours from low tide to high tide) and another with a period of 15 days related to the spring and neap tides. It is possible to observe the difference in the tide amplitude between the spring and neap tides.

In the same graph, it is also possible to observe that some of the low tides have higher water depth than expected (e.g., the 3rd of February to the 6th of February or the 10th of May to the 12th of May). This unusually high water level in the estuary happened due to the strong precipitation that caused floods.

These two phenomena, tides and floods, are the main contributions of water depth sensors in monitoring experiments conducted in estuarine areas.
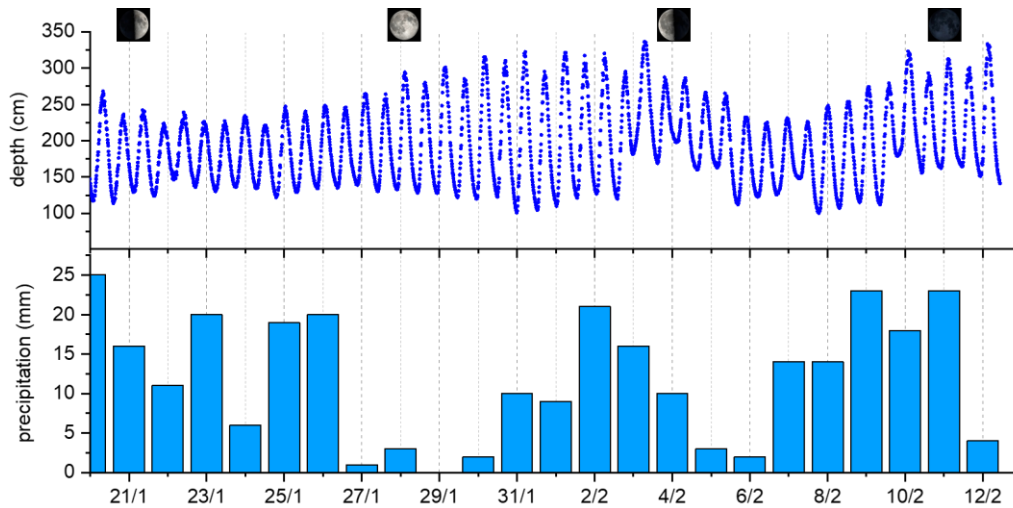
Figure 76. Monitoring results of water level produced by the MSB5837-30BA sensor from the 21st of January to the 12th of February 2021. The top graph shows the variation of water depth with the tidal cycles and the moon phase on its top. The bottom graph shows the daily accumulated precipitation (data from Instituto Português do Mar e da Atmosfera — IPMA).

The other variable measured by the MS5837-30BA sensor is the water temperature. Figure 77 shows the water level and water temperature recorded by the station from the 20th of January 2021 to the 3rd of February 2021 (top graph) and from the 1st to the 15th of April 2021 (bottom graph).
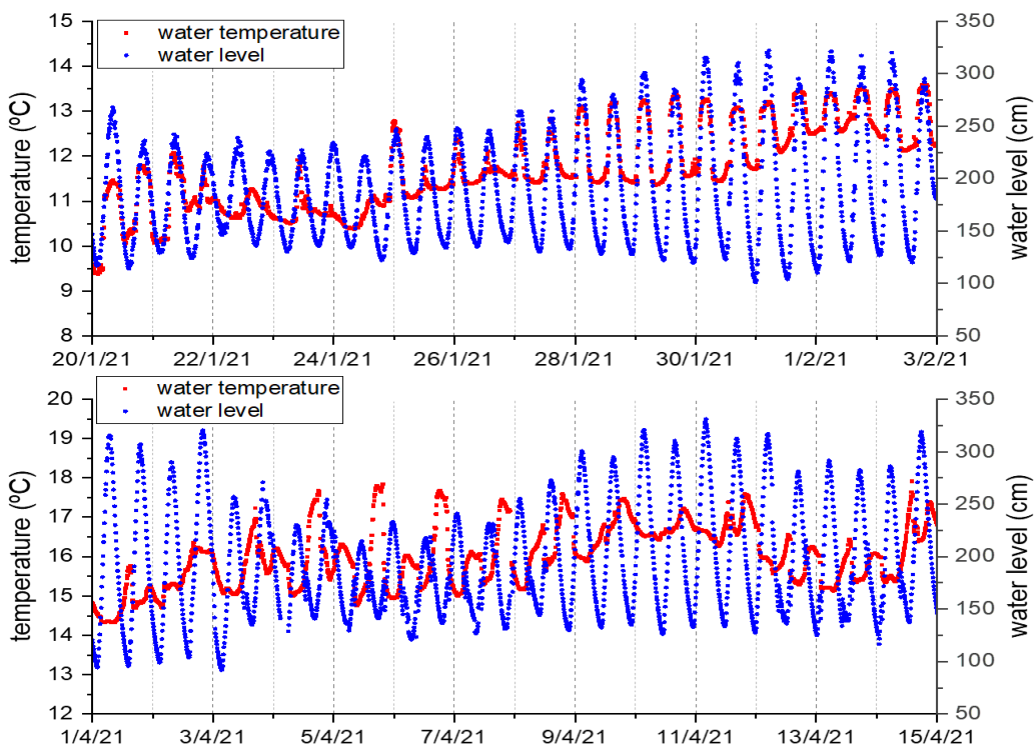
Figure 77. Monitoring results of water temperature and water level produced by the MS5837-30BA sensor. The top graph shows the data from the 20th of January 2021 to the 3rd of February 2021. The bottom graph presents the data from the 1st of April 2021 to the 15th of April 2021. The water temperature is presented in red squares and the water level is in blue circles for both graphs.

The top graph shows that the water temperature on the estuary is higher during the high tides than the low tides, with a temperature amplitude of about 1.5 °C in 6 hours (the time from a low tide to a high tide). This means that the water in the river stream is colder than the water coming from the ocean. Just two months later the pattern is inverted. The bottom graph shows that, in that time frame, the water from the ocean is cooling the estuary during the high tide, and during the low tide the water from the river is increasing its temperature. Moreover, the average temperature of the estuary has increased by about 3 °C when compared to the data from late January 2021.

This is a seasonal effect that affects the average water temperature in the estuary. While the ocean temperature does not change much, the water coming from the river has different temperature ranges during winter and summer. The station has recorded minimum water temperatures of 8 °C during winter and maximum water temperatures of 25 °C during summer.

4.2 SPM Sensor – turbidity and suspended particulate matter

The SPM Sensor was tested and validated several times in the station. This subsection describes one of those experiments and presents the major findings with this instrument.

The estuaries are the ending point of the sediment load that keeps settling and resuspending due to the forces of the river and the ocean. The Cávado River passes through urban and agricultural areas that cause significant runoff to the river during precipitation days. Additionally, there are three wastewater treatment plants (WWTP) upstream of the monitoring station. All these conditions combined make the turbidity, or suspended sediment concentration, a difficult parameter to interpret. The main objective of the experiments with the SPM Sensor was to find patterns and recurrent behaviours that could be explained by sedimentary dynamics.

A set of four SPM Sensors in an L-shape was installed, from the 20th of January 2021 to the 5th of May 2021, in an inox structure buried in the streambed of the estuary with an Archimedes' screw. The sensors were placed at 50 to 100 cm from the streambed and with the sensing area facing down to reduce daylight interferences. The sensors were set to take measurements with a sample period of 5 minutes. Figure 78 shows a scheme and photograph of the installation.
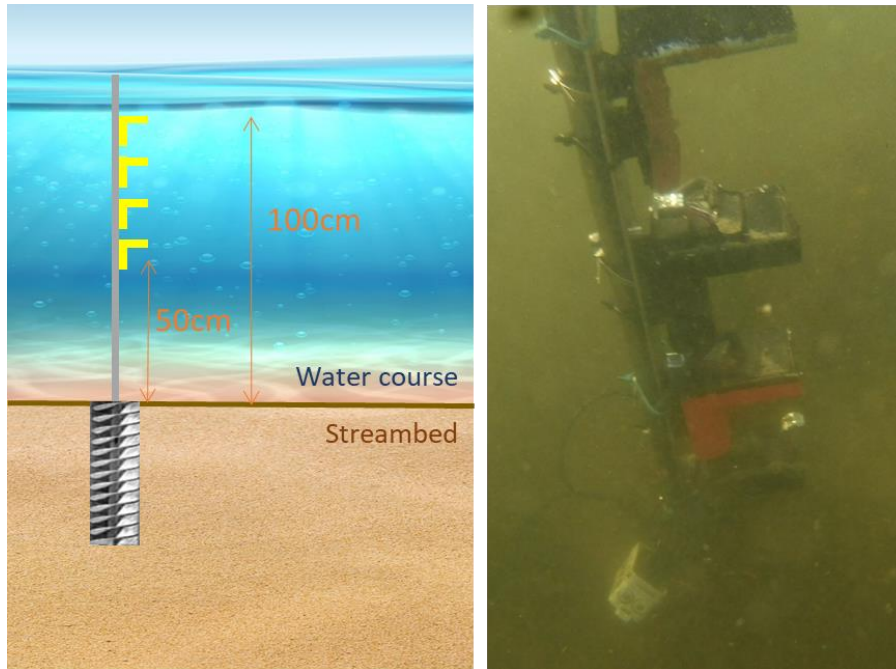
Figure 78. Illustration and underwater photograph of the installation of a set of SPM Sensors. The left image shows the scheme of the installation and the right image shows an underwater photograph of the sensors.

Figure 79 shows the results during the first 10 days of the experiment. The top graph presents the correlation of turbidity with the tidal cycles. It is possible to observe that during this period, the turbidity measurements had an average value of 125 NTU and that it increased during the high tides. Even though this increase in turbidity does not happen in every tidal cycle, it does in most of them, which makes it plausible to associate it with the sedimentary dynamic of the estuary.

The turbidity value of 125 NTU is not "clean" water, and it is consonant with the visually inspected during the field trips (and it is observable in the underwater photograph of Figure 78). Also, the high tides seem visually more turbid than the low tides, but the depth differences can easily mislead this perception. Another important factor is that the water in the estuary is more turbulent during the high tide, which is an agent of sediment transport and resuspension. The visual inspections taken along the experiment are in accordance with the monitoring results.

Another observable pattern during the experiment was that the increase of turbidity during the high tide is higher during the spring tides than during the neap tides (see the difference of magnitude in the turbidity peaks from the 22nd to the 27th of January with the 27th to the 30th of January). If the amount of suspended sediment in the estuary is higher during the high tide, it means that it is related to the action of the sea. So, it makes sense that during the spring tide, when the estuary is more affected by the ocean, the

turbidity Increases. Both the increase of turbidity during the high tide and the higher turbidity peaks during the spring tides are events that were systematically recorded along all the experiments conducted with the SPM Sensor.
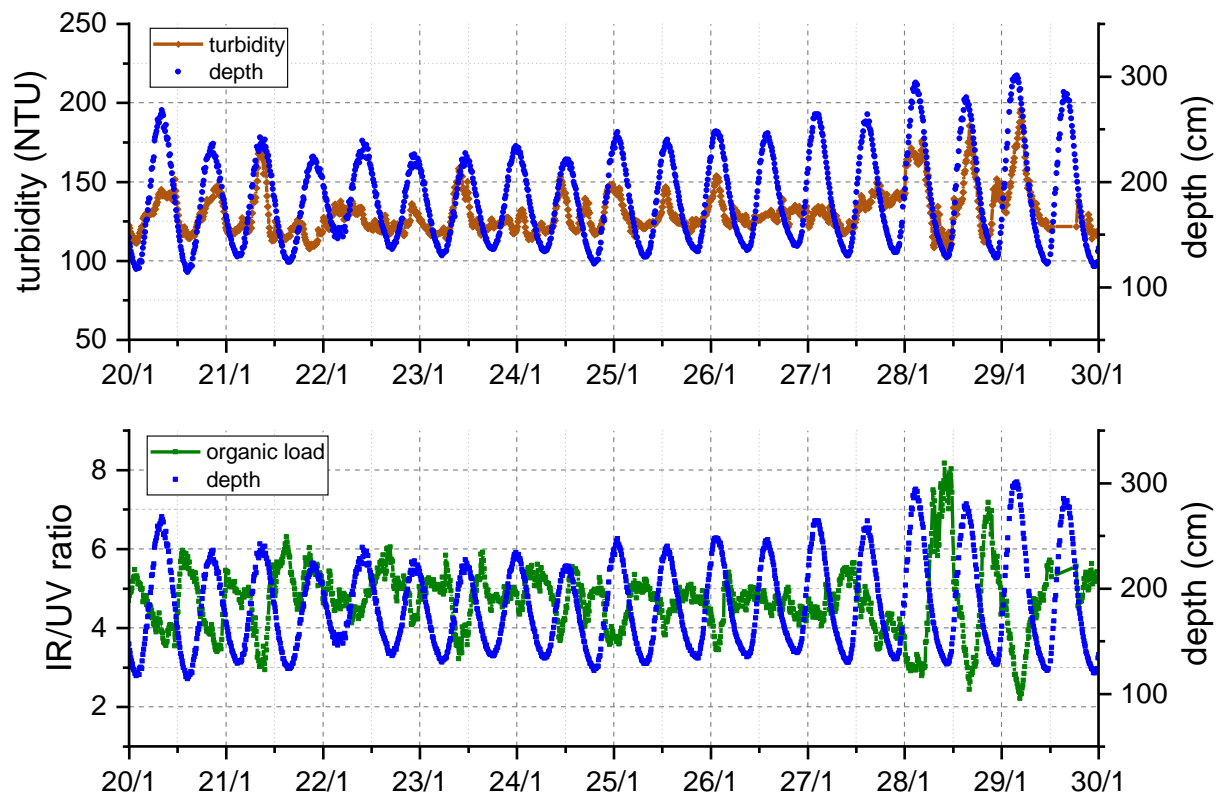
Figure 79. Monitoring results of SPM Sensor and depth from the 20th to the 30th of January 2021. The top graph presents the turbidity records in brown circles and brown line (left side y-axis). The bottom graph presents the IR/UV ratio, related to the organic load, in green circles and green line (left side y-axis). The blue circles represent the data from the depth sensor and show the tidal cycles (right side y-axis).

Even if the turbidity is higher during the high tide, the opposite happens for the UV measurement. The bottom graph of Figure 79 shows the IR/UV ratio that is used to evaluate the organic load. The results show that the amount of organic sediment is higher during the low tides. This is theoretically expected in coastal areas since rivers normally have higher organic loads compared with the sea.

Figure 80 shows the turbidity results of the whole experiment. It is observable that after one week of testing the measurements start to drift. This happens due to the formation of biofouling in the sensing areas of the sensor that gradually obstruct the optical channels.

Also, in this River, the macrofouling, such as algae from the ocean, and the mud of the estuary is an additional obstacle to getting reliable monitoring information. Biofouling formation is the current major problem associated with optical devices that limit observations in environmental studies.
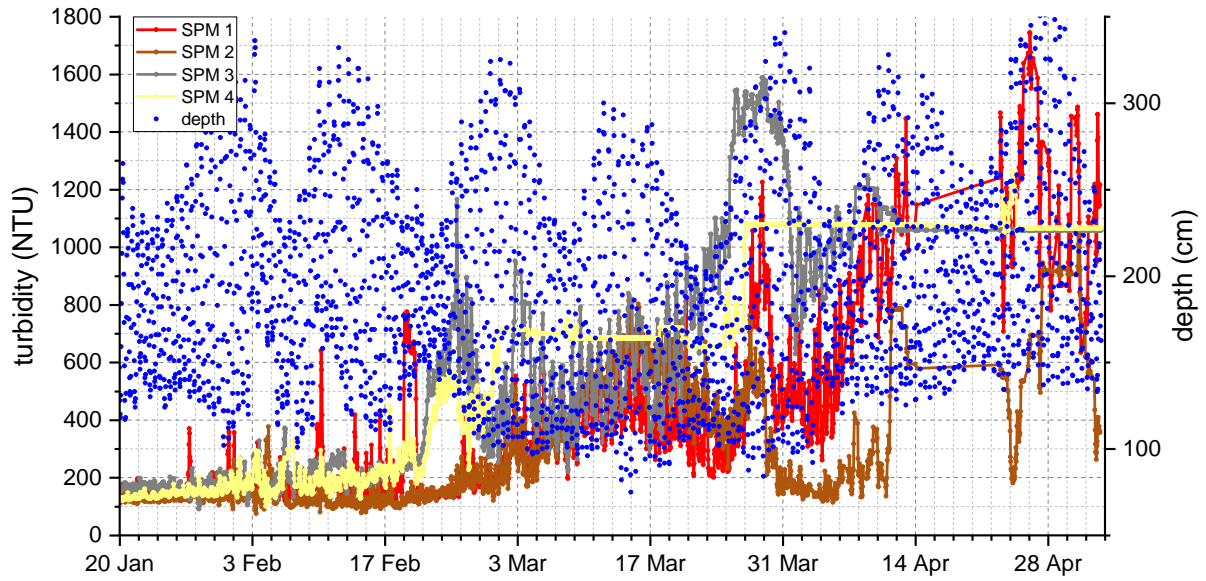
Figure 80. Monitoring results of the experiment with the four SPM Sensors (SPM 1 – 4) from the 20th of January to the 5th of May 2021. The data from the SPM sensors is presented in red circles and red line, brown circles and brown line, grey circles and grey line and yellow circles and yellow line (left y-axis) and the water depth in blue circles (right y-axis).

Figure 81 shows underwater photographs of the sensors during the experiments that show the evolution of the biofouling formation. Both the graph of Figure 80 and the images of Figure 81 show that this problem limits the time of experimentation without maintenance and cleaning actions.

Figure 81. Underwater photographs of the SPM sensors during the *in situ* experiment.

4.3 TVP Sensor – turbidity vertical profiler

This subsection was published in "Design of a Multipoint Cost-Effective Optical Instrument for Continuous *In situ* Monitoring of Turbidity and Sediment", Sensors MDPI [191]. It presents the monitoring experiment with the TVP Sensor from the 10th to the 16th of April 2019.

The instrument was connected to the data logger of the monitoring station that received and stored the monitoring information with a sample rate of 1 min. The developed device was buried in the streambed of the estuary, with nodes 8, 7 and 6 uncovered, and the remaining buried in the sand. Complementarily, the MS5837-30BA sensor was used to record the tidal cycles. The water depth sensor was attached to an infrastructure, in a fixed position, at the same water depth as the middle of nodes 5 and 6, as Figure 82 shows.

This configuration would allow measuring turbidity at three different depths (nodes 6, 7 and 8) and detect changes in the deposited sediment. If node 5 became uncovered, deposited material was resuspended (erosion). Otherwise, if node 6 became covered, sedimentary material was deposited in the streambed (sediment accumulation).
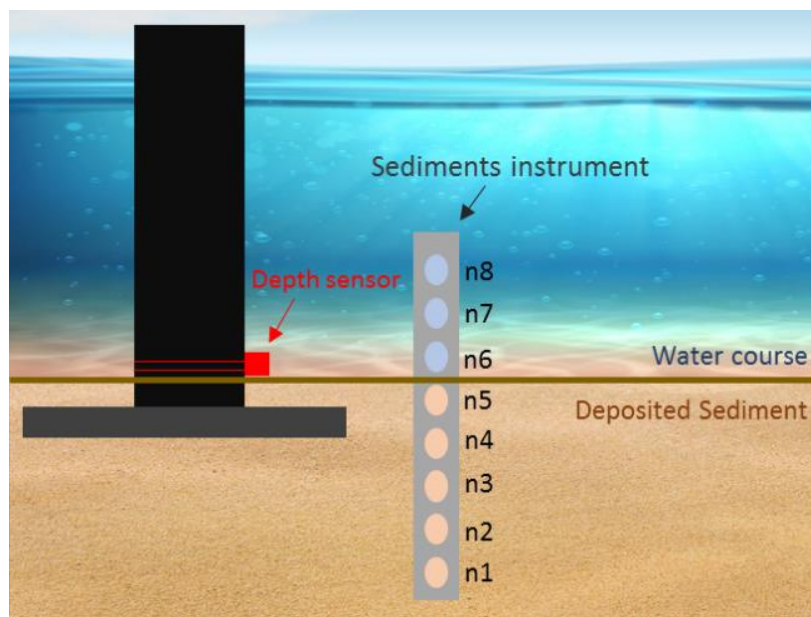
Figure 82. Illustration of the installation design of the TVP sensor. The depth sensor was installed at the bottom of the watercourse, at the same water depth as the middle of nodes 5 and 6 of the turbidity profiler.

Figure 83 shows the turbidity measured by the backscatter detectors from the three unburied nodes. The results show a pattern between the tidal cycles and the turbidity. Most of the low tide periods are marked by a peak of turbidity that disappears with the high tide. This behaviour is not in accordance with the

dynamics registered during the experiment with the SPM Sensors. However, these two experiments were conducted two years apart and, as explained before, the sedimentary dynamics in the estuary are constantly changing.
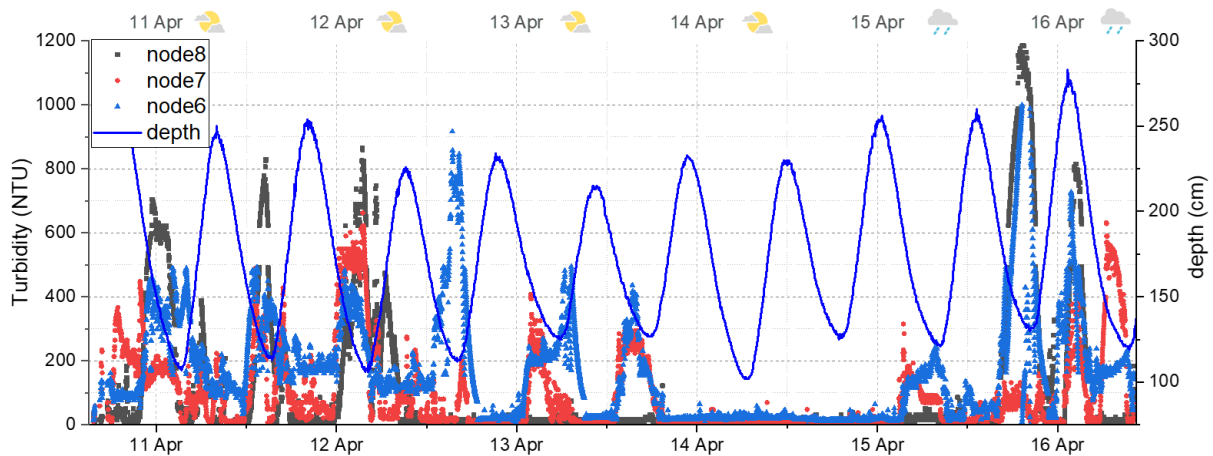
Figure 83. Monitoring results of turbidity produced by the TVP Sensor from the 10th to 16th of April 2019. The grey squares, red circles and blue triangles show the backscattering measurement data of nodes 8, 7 and 6, respectively. The blue line shows the measurement of the water level provided by the depth sensor.

A plausible explanation for the occurrence is that, while the SPM Sensors measured the sediment load in the water column, the TVP sensor was installed in the estuary bed, so its measurements are related to the bed load transport. Analysing the data from this point of view, it could mean that while the sea transports fine sediment to the estuary during the high tide, increasing the wash load and the suspended sediment, the sediment transported by the river is heavier and has a higher impact on the bed load.

What is in accordance with the experiments with the SPM sensors is the turbidity variation during spring and neap tides. The turbidity peaks during the low tides on the 13th of April are lower compared with the days before. On the 14th of April, no peaks were detected at all, and at the end of the 15th of April, the turbidity peaks appeared again. This event happened during the transition from the neap to the spring tide.

Analysing the data of the 14th of April, when there were no turbidity peaks, the TVP sensor measured average turbidity values of 27 NTU, 32 NTU and 35 NTU from nodes 8, 7 and 6, respectively. This slight difference in the turbidity values can be explained by the depth difference between the nodes (that would explain the discrepancies between the suspended and bed load measurements), by inaccuracies during the calibration (considering the turbidity steps used during the formazin calibration, a difference of 8 NTU is acceptable) or by biofouling interference in the readings.

For the attempt to measure sediment accumulation, the node 6 delivered turbidity measurements during the experiment, which means that it was uncovered all the time. Additionally, nodes 5 to 1 presented a constant value during the test, below the threshold value, which indicates that the photodetectors remained buried. This does not necessarily mean that there were no changes in the streambed height, but that the distance of 70 mm between the nodes was not sufficient to detect changes in the morphology of the streambed.

Finally, even though a calibration for the distinction between organic/inorganic material was not established for this sensor, a demonstration of the different responses of the matter to the ultraviolet and infrared light channels is presented. Figure 84 shows the measured data of ultraviolet and infrared transmitted light detectors of node 8.
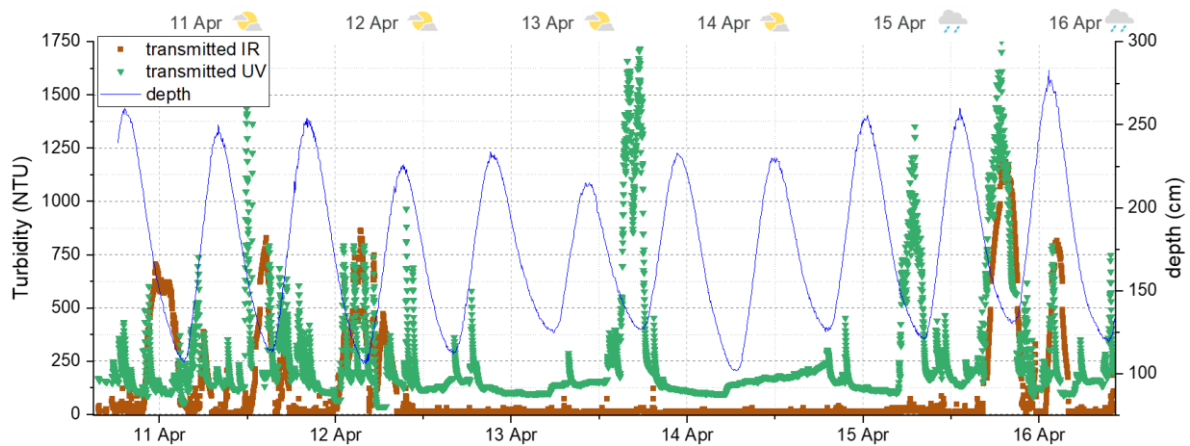
Figure 84. Monitoring results of the organic/inorganic distinguish produced by the TVP Sensor from the 10th to 16th of April 2019. The brown squares show the measurements of the IR transmitted channel and the green triangles are the measurements of the UV transmitted channel, both from node 8. The blue line shows the measurement of the water depth.

The data shows that the ultraviolet detector produced higher turbidity values compared to the infrared one. These results agree with the concept that organic matter has higher absorption to ultraviolet wavelength when compared to infrared, which results in lower luminosity sensed by the UV channel and higher turbidity output. The higher turbidity peaks of the UV channel were detected during the low tide, meaning that the organic load is carried by the river, and not by the ocean (the same behaviour detected by the SPM sensors).

The turbidity measurements of both IR and UV transmitted channels are compliant with the ones from the backscattering technique presented in Figure 83. However, there are turbidity peaks on the 13th and 15th of April, only detected by the UV channel. This behaviour can be explained by a high organic load

that did not produce changes in the turbidity measured by the IR channels such as algae blooms, anthropogenic contaminants like pesticides or water colouration.

Despite that these phenomena can be explained by the factors mentioned, it is important to notice that other events may have contributed to the occurrence. Weather events (on the 15th of April, the anomalous high turbidity peak was probably caused by the rainwater that dragged dirt from the urban area to the estuary), wastewater discharges (existence of wastewater pipelines upstream of the station) and attachment of undesired debris or biological material in the sensor sensing surfaces (biofouling) may have also influenced the results.

The TVP sensor was developed to be a scalable instrument to measure turbidity and suspended sediment concentration along the water column. It was designed to increase the measuring length by adding measuring bars on top of each other. For this purpose, a structure would be needed to support the vertical arrays. Also, the area of the monitoring station had minimum depths of 1 meter which did not justify the use of this instrument in this location. Thus, the use of the TVP in the monitoring station was discarded for the use of multiple SPM sensors that offered better accuracy and ease of installation.

4.4   SED Sensor – sediment deposition and erosion

This subsection was published in "Development of an automated sensor for *in situ* continuous monitoring of streambed sediment height of a waterway", Science of The Total Environment, Elsevier [192]. It presents the *in situ* experiment with the SDE Sensor to measure sediment displacement on the streambed, from the 5th of January to the 3rd of May 2021.

The developed device was buried in the streambed of the estuary, with channels 1 to 19 uncovered, and the remaining 13 nodes buried in the sand (installation setup presented in Figure 85). The channel 20 was set to correspond to 0 mm of streambed height. With this configuration, the instrument would be able to measure the periods when the suspended sediments were settling (accumulation would increase and more optical channels would be covered with sand) and when the deposited sediment resuspended due to the action of sea currents or the river flow (the streambed would erode and the more optical channels would become uncovered). The sensor was set to take measurements every 30 minutes.

Complementarily, the MS5837-30BA sensor was used to measure the tidal cycles. This data was used to correlate the accumulation measurements with the hydraulic dynamics. The depth sensor was attached to the top of the sediment accumulation sensor, in a fixed position, with the zero-depth arbitrarily defined

as the position of the sensor at the moment of the installation. This setup was used only for field test purposes, without aiming to obtain datum-based values of water or sedimentation depths.
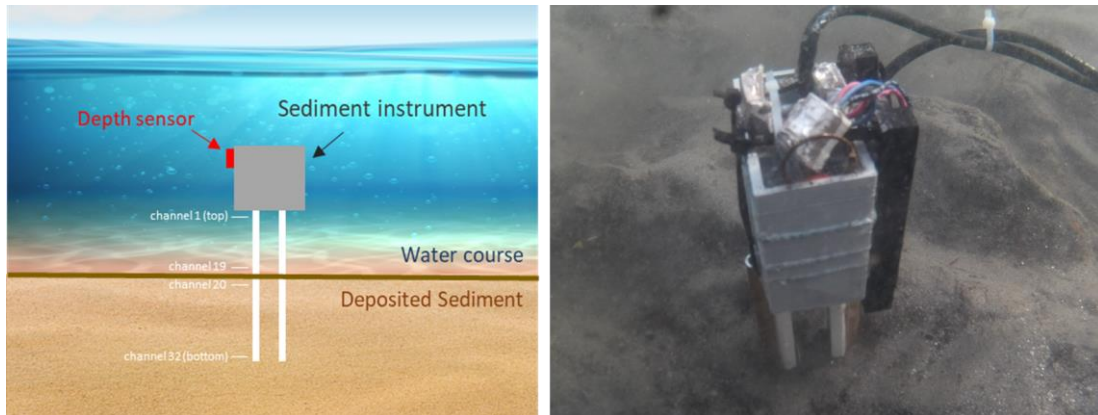
Figure 85. Illustration and underwater photograph of the installation of the SDE Sensor. The sensor was buried in the streambed of the estuary with nodes 1 to 19 uncovered and 20 to 32 covered with sediment. The depth was used to provide information about the water level and tidal cycles.

Figure 86 shows the measurements of the SDE Sensor and the water depth during the first week of deployment. The streambed height, starting at 0 mm and corresponding to the optical channel 20, is represented in the left-side y-axis with brown circles and a brown solid line. In the right-side axis is presented in blue circles the data of depth. Analysing the first days of the test, even if that did not happen during all the tidal cycles, the data shows a pattern of sediment deposition during the high tide (accumulation increased) and sediment resuspension during the low tide (accumulation decreased).
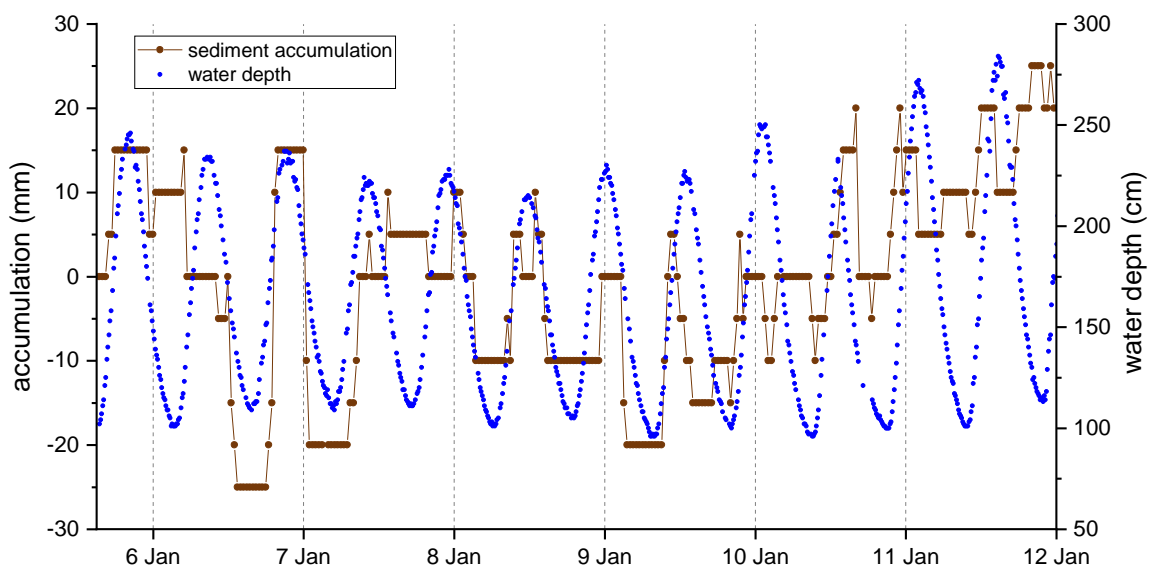
Figure 86. Monitoring results of sediment accumulation and water depth in the first week of deployment of the SDE sensor (5th of January to 12th of January 2021). The brown circles with the brown solid line are the data output of the sediment accumulation sensor (left side y-axis). The blue circles represent the data from the depth sensor and show the tidal cycles in the estuary (right side y-axis).

This behaviour matches with one of the phenomena expected in the estuarine areas. During the low tide, the sea currents have minimal or no effect at all on the normal flow of the river. However, when the tide increases, the normal flow strength is diminished by the sea entering the estuary, and it can be cancelled and even overcome. During the peak of the high tide, lower water flow strength is expected and the water in the estuary becomes saltier. Both these two conditions contributed to the settling of fine particles that are suspended in the water, which leads to an increment of the accumulated sediment in the streambed.

Once the tide starts to decrease, the river flow increases and its maximum strength happens during the low tide. At that time, the flow strength is higher than during the high tide, so the fine sediment that has settled before enters now in resuspension in the direction of the sea. This behaviour was recorded during the 119 days of the experiment.

The SDE sensor uses transmitted light IR channels to detect the existence of sand. Even if it is not the purpose of the instrument, if the channels are not obstructed, they can be used to estimate turbidity or suspended sediment concentration (it is the same technology employed in the SPM sensor for the transmitted light detection). Figure 87 shows the top channel output (further away from the streambed) from the 19th of January to the 1st of February.
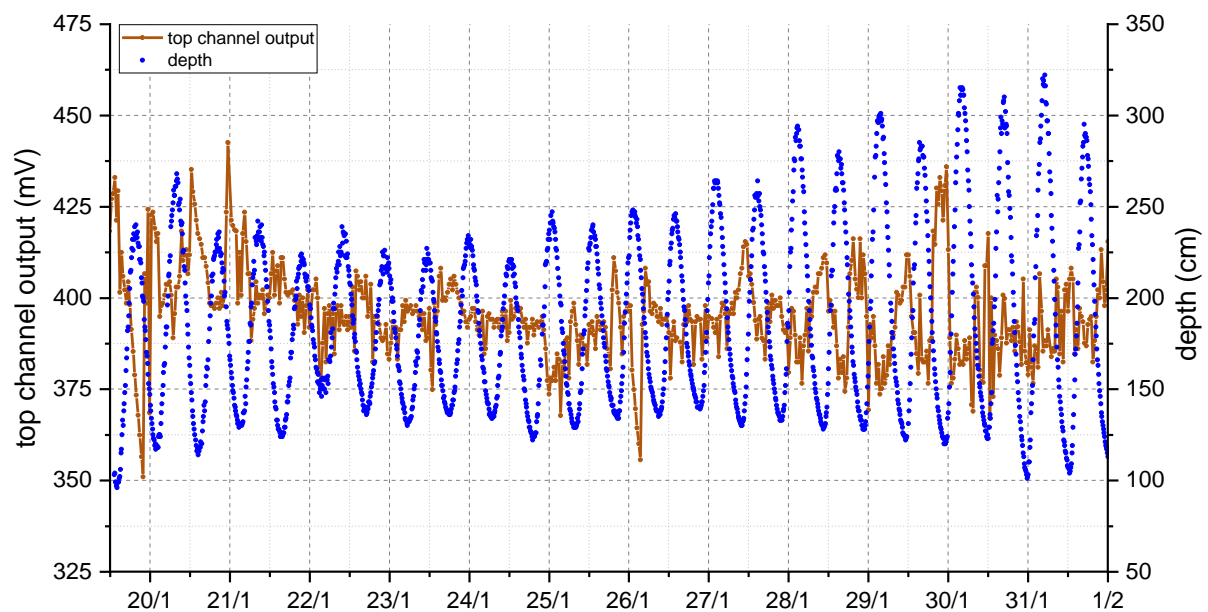
Figure 87. Monitoring results from the top channel of the SDE sensor and water depth from the 19th of January to the 1st of February 2021. The brown circles with the brown solid line are the output of the top channel of the SDE sensor (left side y-axis). The blue circles represent the data from the depth sensor and show the tidal cycles in the estuary (right side y-axis).

The graph shows that the optical channel presents an increase in its output during the low tides (that is translated into a decrease in turbidity) and a decrease during the high tides (an increase in turbidity). This

behaviour is in accordance with the increase of sediment deposition during the high tides, and corroborates the data recorded by the SPM sensors presented in the subsection before (both tests were conducted at the same location and time). Also, the pattern of high turbidity peaks during the spring tides detected by the SPM sensors was recorded by this instrument too. These results show that if a calibration with formazin is established, the SDE Sensor is also capable of measuring turbidity (or suspended sediment concentration if calibrated with sediment).

During the first fortnight of the tests, the sensor recorded an increase in the accumulated sediment in the streambed of the estuary, reaching a maximum of 70 mm on the 20th of January. This date marked the start of 4 weeks of intense precipitation, and the sensor detected an abrupt decrease in its measurements during the following days.

On rainy days, the volume of water in the river increases. As Figure 88 shows, the depth sensor recorded the river flow increasing from the 20th to 30th of January, the 3rd to 5th of February and from the 9th to 12th of February. On these days, the depth during the peak of the low tide is higher than expected, which means that the estuary had an abnormally higher water volume.

Figure 88. Monitoring results of sediment accumulation and water depth from the 5th of January to the 26th of February 2021. The top graph shows in brown circles and brown solid line (left-side y-axis) the data of sediment accumulation and in blue circles (right-side y-axis) the data of the water depth sensor. The bottom graph shows the daily accumulated precipitation (data from IPMA).

Particularly in rivers that pass by urban areas, as is the case of the Cávado River, not only additional water is added to the waterway, but also mud and dirt that run off from the riverbanks and are drained

from the surroundings. In these conditions, the river gains high kinetic energy that results in a higher water velocity and turbulent flow.

During these abnormal conditions, the sediment dynamics in the estuary did not follow the normal balance of sediment deposition and resuspension shown in Figure 86. The high strength of the river course resulted in the erosion of the streambed at an unusual rate. From the 20th of February, when the sensor registered a maximum of 70 mm of accumulated sediment, to the 10th of February, when the sensor was measuring –65 mm, the streambed of the estuary eroded 135 mm and all the 32 channels of the instrument became uncovered.

From 10th to 18th February some sediment deposition was recorded, as well as the resuspension of sediment. However, the device was on its measurement length limit (starting position of the deployment with 13 channels uncovered, and 5 mm resolution, resulting in an erosion measurement limit of 65 mm) and no other changes were recorded till the 26th of February since all channels were uncovered.

Figure 89 shows underwater photographs of the sensor at the beginning of the installation and on the 26th of February when the sensor had all channels uncovered and could not take measurements.

Figure 89. Underwater photographs of the SDE sensor at different times of the field experiment. The top-left image shows the moment when the sensor was deployed, with its measure corresponding to 0 mm. The top right image shows the sensor with all 32 optical channels completely uncovered (26th of February, measure corresponding to -65 mm). The bottom-left image, also on the 26th of February, shows the sensor buried again in the streambed (only the vertical position changed). The bottom-right image shows the repositioning of the sensor, on the 19th of April, after the sensor was buried in sand and algae.

Analysing the photographs, it is possible to notice differences in the type of sediment deposited in the estuary bed. In the top-left image (beginning of the installation) the streambed sand had ripple marks and its surface was uneven. However, this layer of thin sediment disappeared in the top-right and bottom-left images, and the streambed looks more swept due to the erosion caused by the days of strong precipitation.

On the 26th of February, the sensor was buried again in the sand in the same location as before (only its vertical position was changed), with nodes 1 to 14 uncovered, as shown in the bottom-left photograph of Figure 89. To continue the previous measurement the sensor output was "zeroed", with the optical channel 15 corresponding to -65 mm. Figure 90 shows the continuation of the experiment.
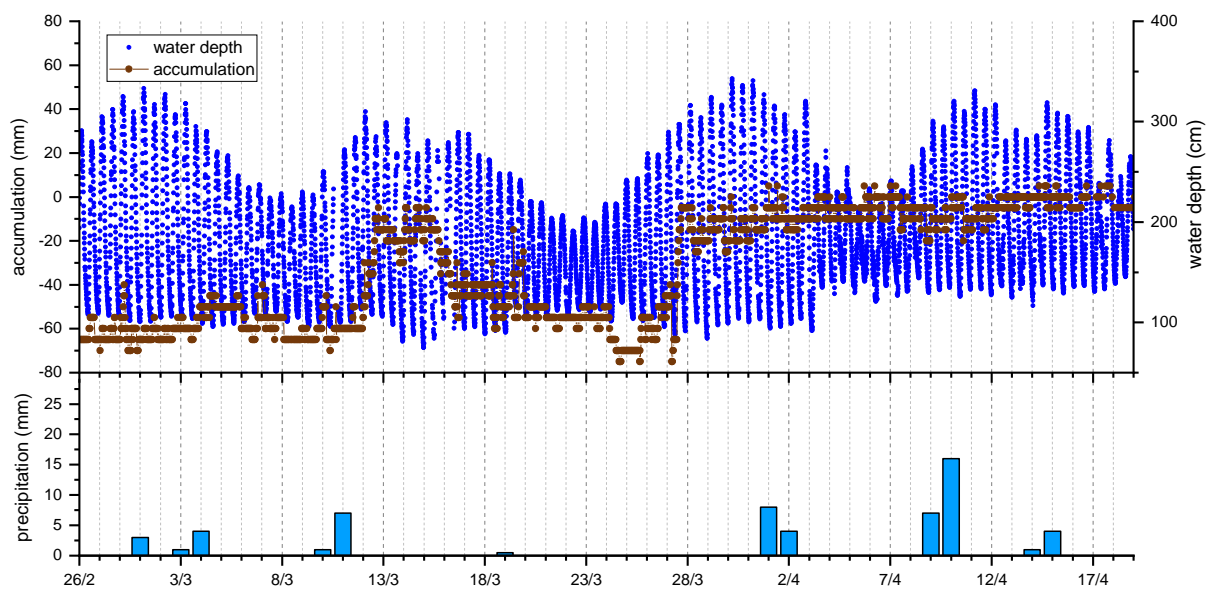
Figure 90. Monitoring results of sediment accumulation and water depth from the 26th of February to the 19th of April 2021. The top graph shows in brown circles and brown solid line (principal y-axis) the data of sediment accumulation and in blue circles (secondary y-axis) the data of water depth. The bottom graph shows the daily accumulated precipitation (data from IPMA).

After the rainy days, the accumulation of sediment in the streambed slowly returned to the initial values. The accumulation rates during the low and high tides shown in Figure 86 were recorded again, and a new pattern was observed. Analysing the data in Figure 90, it is possible to see a tendency for higher deposition rates during the spring tide. On the opposite, higher sediment resuspension and erosion were recorded during the neap tide.

The bulge of the ocean and its effects on the estuary during high tidal periods were observed in the data of the water level sensor, mostly in the average depth of the high tides. In the periods of the neap tides, the water level registered depth values between 200-250 cm during the peak of the high tide, while for

the spring tides, some of the high tide peaks almost reached 400 cm. This means that during the spring tides, the salinity level in the estuary is expected to be higher than during the neap tides, which is a possible cause for the higher sediment deposition rates recorded during this period.

After the 28th of March, the sensor was on its top measuring limit (all the nodes became buried). The reason for this high deposition rate is unknown. However, this period was marked by an increase of algae and high turbidity in the estuary. The phenomenon of algae bloom is a plausible explanation for the increase in sediment deposition.

The sensor registered sediment accumulation values in its top measuring limit until the 19th of April. At this date, the sensor was found in the estuary streambed buried with sand and algae. As before, the position of the sensor was adjusted so that sediment deposition and erosion were possible to monitor again. The sensor was buried with nodes 17 to 32 covered and 1 to 16 uncovered and its position was zeroed again.

Comparing the underwater photographs of Figure 89 it is possible to notice the increase of turbidity, as well as the green pigment in the water resulting from the presence of algae in the estuary (all photographs were taken with the same camera configurations, during the low tide and at similar weather conditions). In the bottom-right photograph, it is also possible to see macro fouling attached to the structural housing of the sensor. However, the monitoring nodes were clean (the sensor was not removed from the streambed and no cleaning was made).

After the repositioning of the sensor, the field experiment preceded an additional 10 days, ending on the 3rd of May, when the sensor was again close to its measuring limit. Once again, this period was marked by high turbidity in the estuary and the existence of algae bloom, and the sensor registered an increase in sediment accumulation in the streambed.

This high sediment deposition rate was only disrupted by the precipitation from the 21st to the 26th of April when bed erosion was registered. However, immediately after the precipitation days, the high deposition rates were recorded again.

Figure 91 shows all the monitoring records of the sediment accumulation and water level during the experiment.
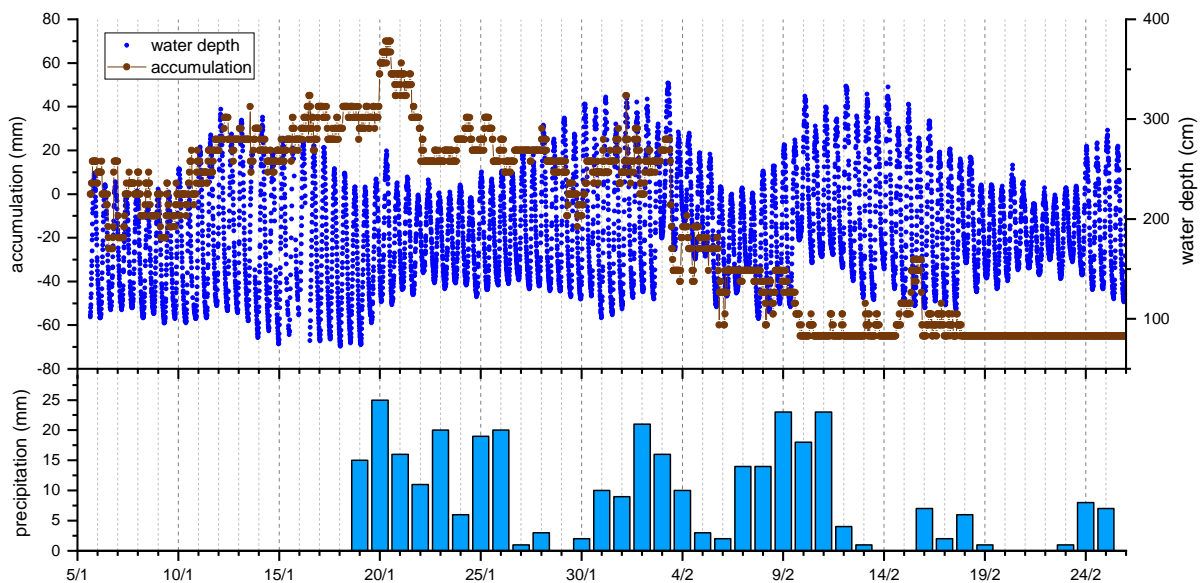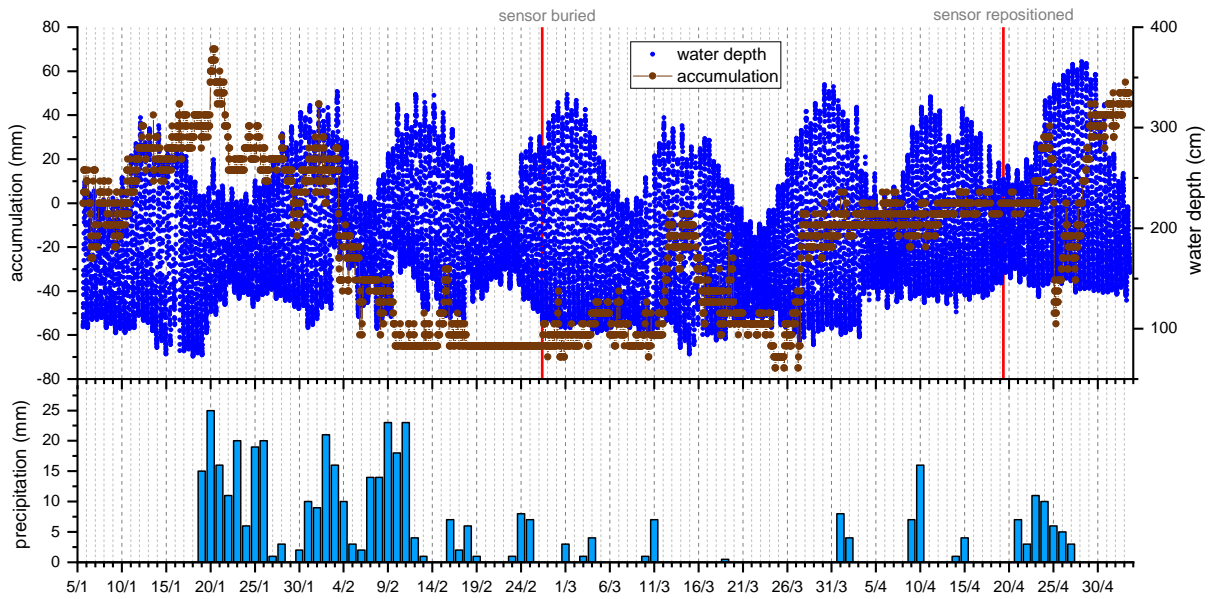
Figure 91. Monitoring results of sediment accumulation and water depth from the 5th of January to the 3rd of May 2021. The top graph shows in brown circles and brown solid line (principal y-axis) the data of sediment accumulation and in blue circles (secondary y-axis) the data of water depth. The red lines mark the moment when the device was vertically repositioned. The bottom graph shows the daily accumulated precipitation (data from IPMA).

4.5 Acoustic ToF current meter – water velocity

The acoustic ToF current meter was installed in the estuary of Cávado from the 16th to the 18th of March 2021. It was fixed on an inox structure, buried in the streambed with an Archimedes screw, as demonstrated in Figure 92. The sensor was placed in a position that would allow measuring water velocity in the downstream and upstream directions of the river.
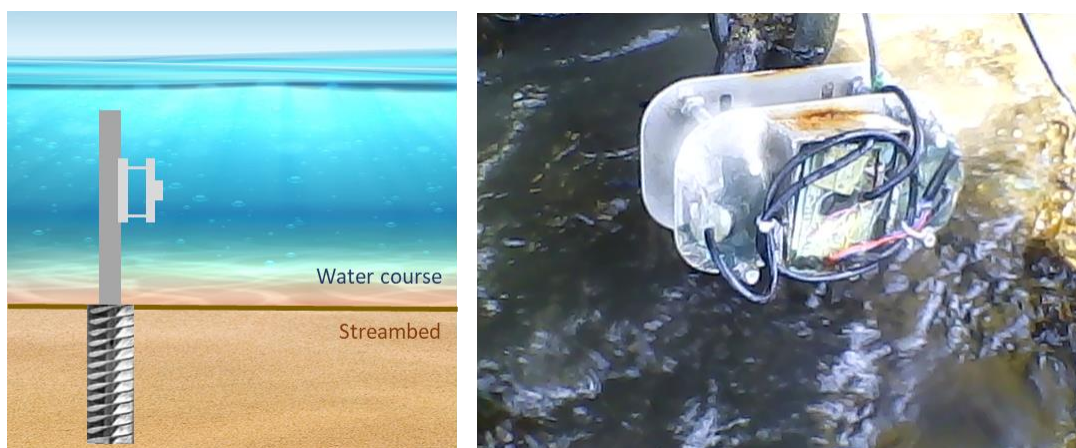
Figure 92. The left image shows an illustration of the installation setup of the acoustic ToF current meter. The right image shows a photograph of the sensor before being submerged in the water.

Figure 93 shows the records of the ToF current meter during the *in situ* experiment. The sensor was able to measure the water velocity both in the downstream and upstream directions. Note that the downstream direction is represented by positive water velocity values and the upstream by negative values. The results show that the maximum flow intensities for each direction occurred during the peak of the tides. During the flood tides (when the tide is coming in or rising, moving from low tide to high tide) and ebb tides (when a tide is receding or going out, moving from high tide to low tide), it is possible to observe the change of direction of the stream flow.

Figure 93. Monitoring results of water velocity from the 16th to the 18th of March 2021. The graph shows in orange circles the water velocity produced by the acoustic ToF current meter (left y-axis) and in blue circles the water depth produced by the depth sensor (right y-axis).

A curious behaviour can be observed in the data. During the flood tide, when the water velocity starts do decrease to change its direction, some measurements are missing. During these periods, the sensor struggled to take measurements because the emitted beam did not reach the acoustic receiver. This means that there was an obstruction of the acoustic channel. The cause pointed out for this behaviour was the settlement and attachment of algae to the sensor during periods of low flow. Once the flow increased, now in the upstream direction, the algae released from the structure of the sensor and the acoustic channel became clear to take measurements again. This was a recurring event during the whole experiment.

The susceptibility of the sensor to algae attachment inquired to pursue other techniques to measure water velocity. The acoustic ToF sensor was developed merely as a backup resource since the other technologies to measure water velocity were presenting additional challenges to be operated in the field.

4.6 SeT Sensor – sediment transport

This subsection is under revision to be published in the Journal of Environmental Management, Elsevier, with the title "Design of a sensor to estimate sediment transport in situ using the measurements of water velocity, suspended sediment concentration and depth".

Sediment transport can be estimated by correlating the suspended sediment concentration with the water velocity. The SeT sensor was developed for this purpose and its final version was installed in the estuary of Cávado from the 26th of May to the 1st of June of 2023. The device was fixed to an inox structure buried in the estuary bed, with the cantilever length and optical channel perpendicular to the streambed, as Figure 94 shows. The sensor was set to take measurements every 5 minutes.
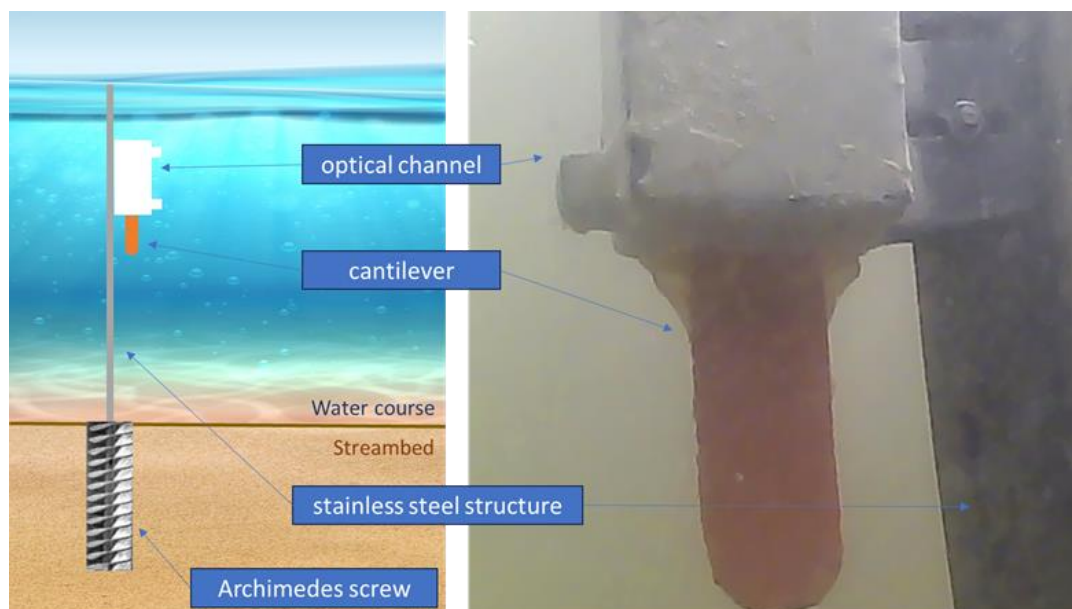
Figure 94. Illustration and underwater photograph of the installation setup of the SeT Sensor. The right image shows the sensor at the moment of installation.

Figure 95 shows the measurements of water velocity during the first 3 days of the experiment. Unlike prototype I and II (field experiments can be consulted in Supplementary Material VI – i) SeT Sensor – prototype I and ii) SeT Sensor – prototype II), the SeT Sensor presented a steady reference corresponding to the value of null velocity and turn of the flow direction.

The data shows that the water velocity intensifies during the peaks of low (downstream direction represented by positive water velocity values) and high (upstream direction represented by negative velocity values) tides. It is possible to observe the change of the stream direction during the rising and leaking of tides.
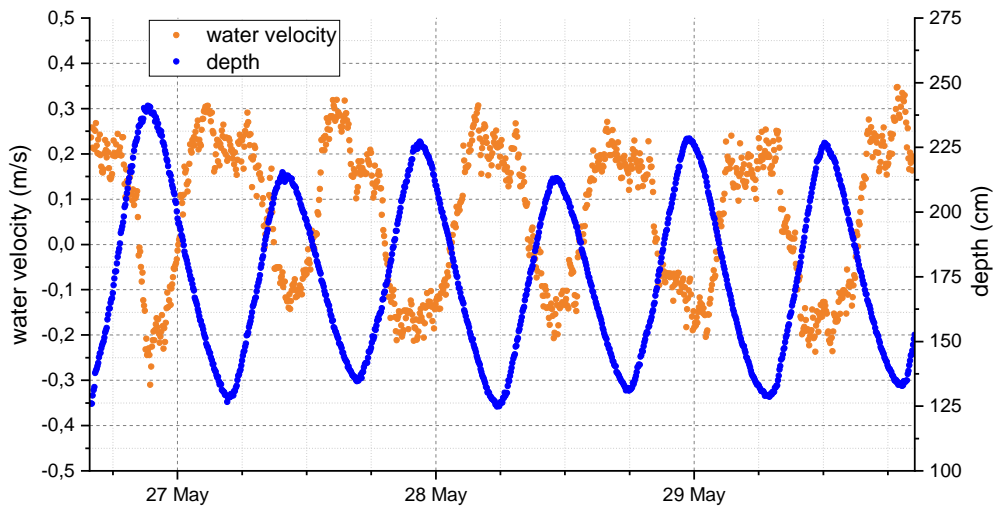
Figure 95. Monitoring results of water velocity from the 26th to the 29th of May 2023. The graph shows in orange circles the water velocity produced by the SeT Sensor (left y-axis and positive values for downstream direction) and in blue circles the water depth recorded by the depth sensor (right y-axis).

Comparing the data of the SeT Sensor experiment with the one from the acoustic ToF meter (data of Figure 93), it is observed that the correlation of the tidal cycles and water velocity signals are similar and the hydraulic dynamics recorded by both sensors are coherent. There is a difference in the magnitude of the water velocity during the peaks of tides (≈0.25 m/s for the SeT sensor and ≈0.75 m/s for the ToF sensor), but the experiments were conducted 2 years apart and the experiment with the ToF current meter was conducted during high precipitation days which as influence in the normal river flow. Also, the test with the ToF sensor was during a spring tide and the one with the Set sensor was during a neap tide.

The problem of algae clogging presented by the ToF sensor was not observed for the new instrument. During the first days of operation, the cantilever current meter presented reliable data, without outliers or other erroneous measurements. However, this field experiment was marked by extreme algae blooms phenomena and the estuary became full of floating macro flora. This event led the cantilever to get stuck in algae and stop producing consistent data.

Figure 96 shows the complete data of water velocity during the experiment and an underwater photograph of the sensor when it was recovered. After the 30th of May, there was an abrupt increase in the water velocity that was caused by the attached algae that were forcing the bending of the cantilever in the downstream direction. After this event, the sensor could no longer provide reliable measurements. The underwater photograph of Figure 96 shows the attachment of the algae to the cantilever, which was forcing it to the downstream direction. The sensor was fully functional after recovery and cleaning.
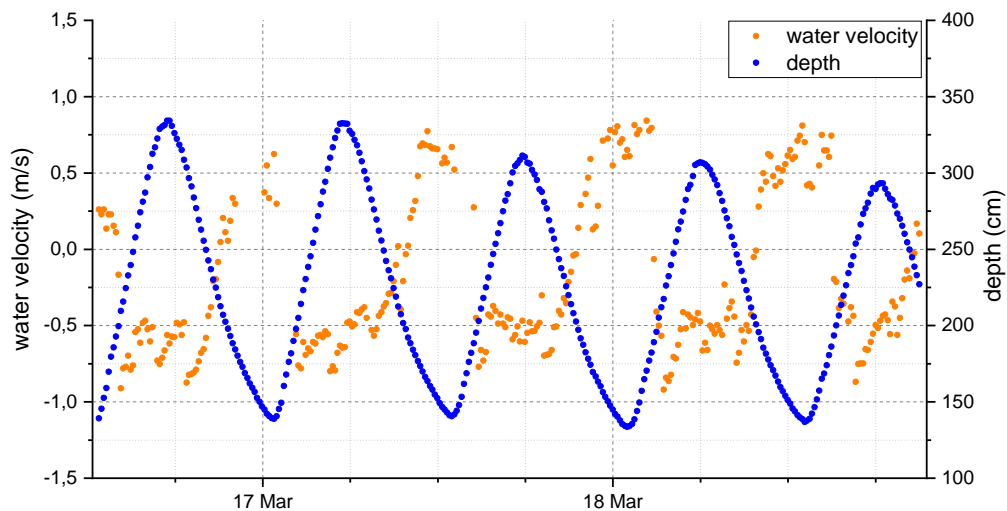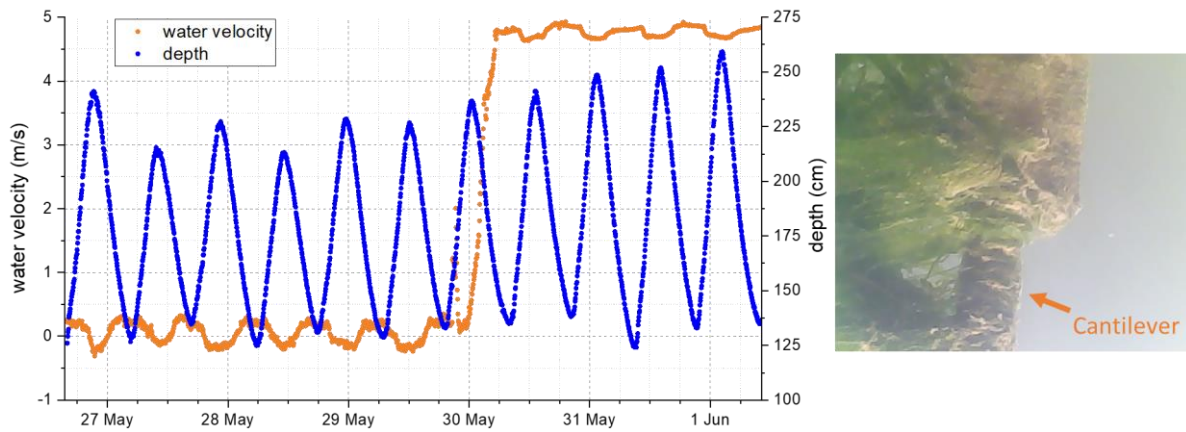
Figure 96 Monitoring results of water velocity from the 26th of May to the 3rd of June of 2023. The graph shows in orange circles the water velocity produced by the SeT Sensor (left y-axis and positive values for downstream direction) and in blue circles the water depth recorded by the depth sensor (right y-axis). The image at right shows an underwater photograph of the sensor with the cantilever stuck in algae.

The SeT sensor was also designed with an optical channel to measure suspended sediment concentration. The graph of Figure 97 shows the measurements of suspended sediment concentration recorded during the experiment.
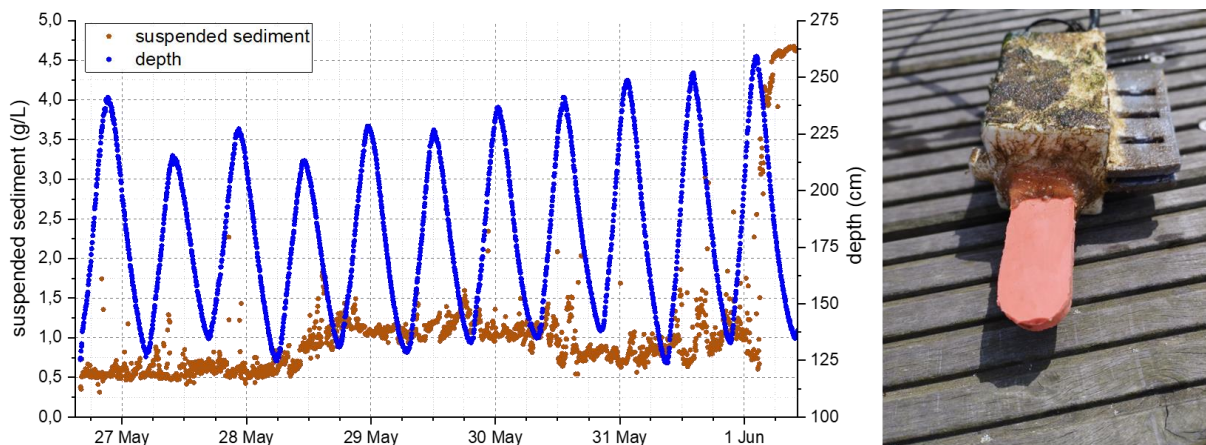
Figure 97. Monitoring results of suspended sediment concentration from the 26th of May to the 3rd of June of 2023. The graph shows in brown circles the suspended sediment concentration produced by the SeT Sensor (left y-axis) and in blue circles the water depth produced by the depth sensor (right y-axis). The photograph at right shows the state of the sensor after recovery.

The field test started on the 26th of May with a suspended sediment concentration of ≈0.6 g/L that gradually increased during the 28th of May. While this behaviour typically matches the beginning of biofouling attachment on the surface of the optical transducers, the sediment concentration decreased during the 30th of May. A possible explanation is that the 28th to the 30th of May were the days when the algae bloom appeared or intensified, increasing the suspended load in the estuary. Other events such as

discharges from the WWTP upstream of the sensor or an increase in the sediment load of the river can also be the cause of this event.

The experiment ended on the 1st of June when the optical channel of the sensor was obstructed with algae. It is possible to observe in the graph an abrupt increase in the suspended sediment concentration to 4.5 g/L. This sudden increment in the sediment concentration is a typical behaviour that happens when the channel is partially or totally obstructed. The natural increase and decrease of suspended sediment in the watersheds are expected to be smoother. When the sensor was recovered, it was confirmed optical channel was obstructed with algae.

After the recovery of the sensor and the macrofauna removed, the device did not present visual damages in the cantilever or optical channel. The structure had encrusted biological and geological residues, as the image of Figure 97 shows, but the surfaces of the cantilever and optical transducers were clean.

4.6.1 Sediment transport analysis

The SeT sensor successfully recorded data on suspended sediment concentration and water velocity. This subsection presents how these two variables can be correlated to analyze sediment transport. The data recorded from the 26th to the 29th of May (while the cantilever was producing reliable measurements of water velocity) is used for demonstration.

The first step is to calculate the function of water discharge using Equation (1). The values of water velocity are the measurements recorded by the sensor and presented in Figure 95. The values of the area are related to the cross-section of the river.

Even though the water height is not uniform along the river width, a practical estimation can be done using the water level values recorded by the depth sensor. Using the recorded data of water velocity and depth, and a river width of 385 meters (river width estimation of the cross section where the sensor was installed) a gross approximation of the water discharge can be calculated. Additionally, the total volume of water was estimated with an approximation of the integration of the water discharge function:

$$total\_volume(t) = \sum_{i=0}^{n-1} water\_discharge(t_i) * \Delta t \qquad (26)$$

The results for the water discharge and total volume of water are presented in Figure 98. Compared with the measurements of water velocity presented in Figure 95, some details must be noticed. The sensor

measured higher water velocity during the low tides (≈ 0.2 to 0.3 m/s) compared with the high tides (≈ 0.1 to 0.2 m/s). However, this difference is less evident in the water discharge data. The water discharge considers not only the water velocity but also depth. Thus, the low tides are marked by higher currents and lower depths (smaller cross-section area) and the high tides by lower currents but higher depths (larger cross-section area). This correlation between water velocity and depth balances the discharge intensity for the different tidal cycles.
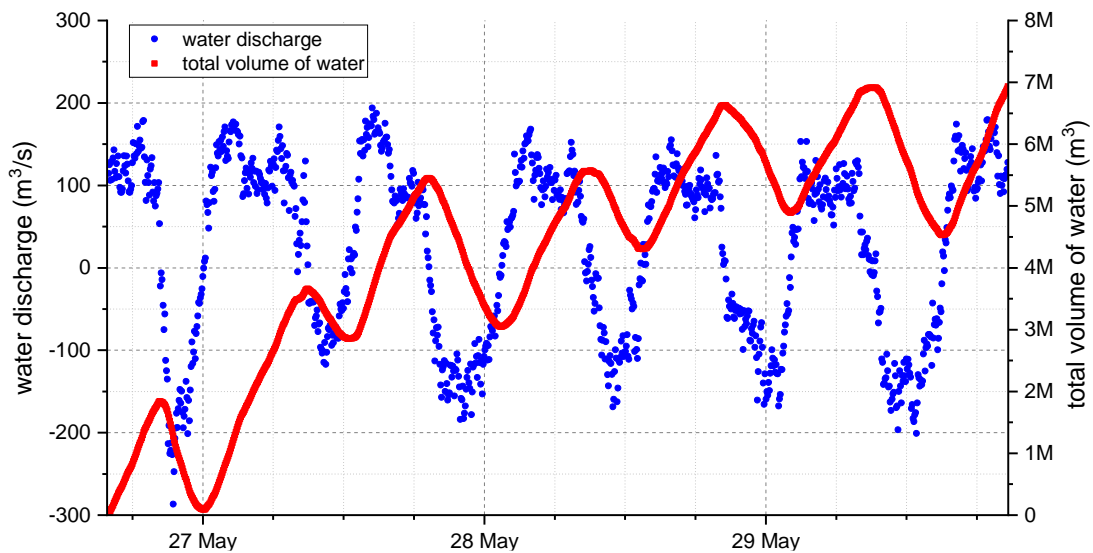
Figure 98. Estimation results of water discharge and total volume of water. The graph shows in blue circles the water discharge calculated using Equation (1) and the measurements of water velocity and depth in Figure 95. The red squares show the total volume of water calculated using the integration of the water discharge function, as shown in Equation (26).

During the low tide (normal flow of the river), the sensor estimated maximum water discharges of 100 to 200 m³/s. These values are in accordance with a monitoring station from Sistema Nacional de Informação de Recursos Hídricos (https://snirh.apambiente.pt/), installed 16 km upstream of the deployment of the sensor, that has measured water discharges from 30 to 250 m³/s from 1990 to 2017.

Even though the water discharge intensity is similar for the peak of low and high tides, their duration is rather different. In the graph of Figure 98, it is possible to observe that the time when the mass of water is flowing upstream (from the ocean to the river) is smaller than when flowing downstream (from the river to the ocean). This event has a direct impact on the total volume of water that infers the average flow direction by the accumulation of water discharge along the time.

The estimated data of the total volume of water shows that its average value is increasing. This means that, in the local installation of the sensor, the water is flowing predominantly in the downstream direction. Even though this is the normal behaviour of a river (water flowing downstream), it is important to

understand that the location of the test is close to the river mouth and is highly influenced by the ocean. The closer the point of collection is from the river mouth, the more influence of the ocean and less influence of the river are expected, decreasing the slope of the total volume of water function.

Considering the two complete days of monitoring (27th and 28th of May), the data presents an accumulative total volume of water flowing from the river to the ocean of ≈3M m³/day. The duration of the field experiment is small to draw conclusions, but the data available indicates that the amount of volume of water per day decreases from day to day. A plausible explanation for this event is that the test was conducted during the transition period from the neap to the spring tide. This means that from day to day the influence of the ocean intensifies, which may cause an increase in the intensity and duration time of the water discharge in the upstream direction.

Having the water discharge calculated, the final step is to calculate the sediment transport rate. The transport rate is defined by the amount of sediment flowing along the course of water and can be calculated by the following mathematical expression:

$$transport\_rate[kg/s] = water\_discharge[m^3/s] * suspended\_sediement[g/L]$$

(27)

As before, the total amount of sediment flowing in the estuary is calculated with an approximation of the integration of the transport rate function as follows:

$$total\_sediment(t) = \sum_{i=0}^{n-1} transport\_rate(t_i) * \Delta t$$

(28)

Figure 99 shows the sediment transport rate estimated using the data of water discharge and the measurements of suspended sediment concentration according to Equation (27). Additionally, the total amount of suspended sediment was calculated using Equation (28).

Since the suspended sediment concentration measured did not present significant variations (Figure 97), the resulting signal of the transport rate is modulated by the shape of the water discharge data. As before, positive values of transport rate mean that the sediment is flowing in the downstream direction and negative ones in the upstream direction.

The higher transport rates occur during the peak of the low and high tides derived from the higher discharge intensity registered during these periods. The graph shows maximum transport rates of 50 to 200 kg/s which are plausible values for small rivers such as the Cávado River, as demonstrated by the monitoring network of Sistema Nacional de Informação de Recursos Hídricos.
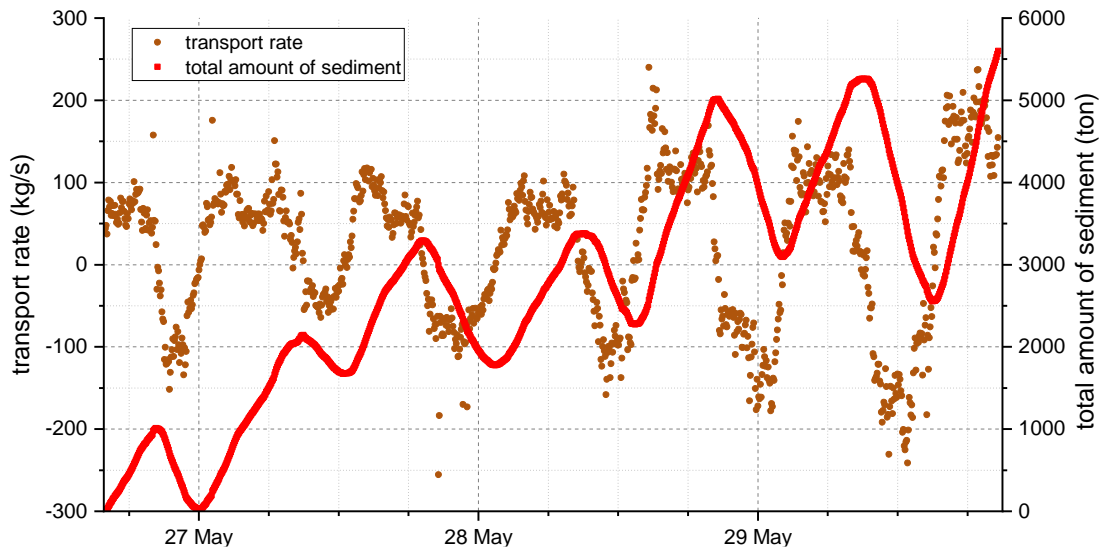
Figure 99. Estimation results of sediment transport rate and total amount of sediment flowing in the estuary. The graph shows in brown circles the sediment transport rate estimated using the data of water discharge from Figure 98 and the measurements of suspended sediment concentration presented in Figure 97, according to Equation (27). The red squares show the total amount of sediment calculated using the integration of the sediment transport rate function, as presented in Equation (28).

The total amount of sediment indicates that most of the sediment is flowing from the river to the ocean. However, it doesn't mean that all this sediment has its origin in the course of water upstream of the station. Since the local of the experiment is close to the river mouth, most of this sediment is expected to be a continuous suspension and resuspension of the same sediment circulating in the estuary. The data shows an accumulative of 2000 tonnes of sediment per day, flowing from the river to the ocean, during the two complete days of the experiment.

4.7 Anti-biofouling techniques

This subsection was published in "Design and *In situ* Validation of Low-Cost and Easy to Apply Anti-Biofouling Techniques for Oceanographic Continuous Monitoring with Optical Instruments", Sensors MDPI [142].

The anti-biofouling instrument was initially installed in the monitoring station of Cávado. However, the evaluation of the biological formation on the probes was a difficult task due to the high sedimentary dynamics and mud in the estuary (consult Supplementary Material VI – iii) Anti-biofouling techniques for more information). Thus, the experiment was pursued in a different marine environment.

The probes were deployed, from the 23rd of May to the 9th of July 2022, in the dock of the Marine Biological station of the University of Vigo, located at Toralla Island, Ria of Vigo, Spain (42°12′07.1″ N 8°47′54.6″ W). The Ria of Vigo is a highly productive coastal ecosystem (primary production rates of up to 3 g cm^{-2} d^{-1} [213]), characterized by clean waters and low sedimentary dynamics, which makes it ideal for shellfish farming and consequently for biological formation.

The instrument was moored attached to a post of a floating dock, at 1.5 m depth from the surface, with the opening of the probes facing the sea bottom to reduce the influence of daylight in the measurements. The location of the installation presents a depth variability of 3 to 5 m during tides.

The probes were connected by an electric cable, that shared power and RS485 communications, to a data logger that recorded the measurements of the six anti-biofouling techniques with a sampling period of one hour. The whole system was supplied by the electrical grid available on the dock and a 230 V AC – 9 V DC converter was used to supply the system. The data logger was composed of an Arduino Mega, microSD card (physical data storage), DS1307 RTC (to keep date and time), LTC1480 (RS485 bus) and SIM7000E Arduino NB-IOT/GSM Module (to send data, in real-time, to a website similar to the one developed for Esposende). The scheme diagram of the data logger is presented in Figure 100.
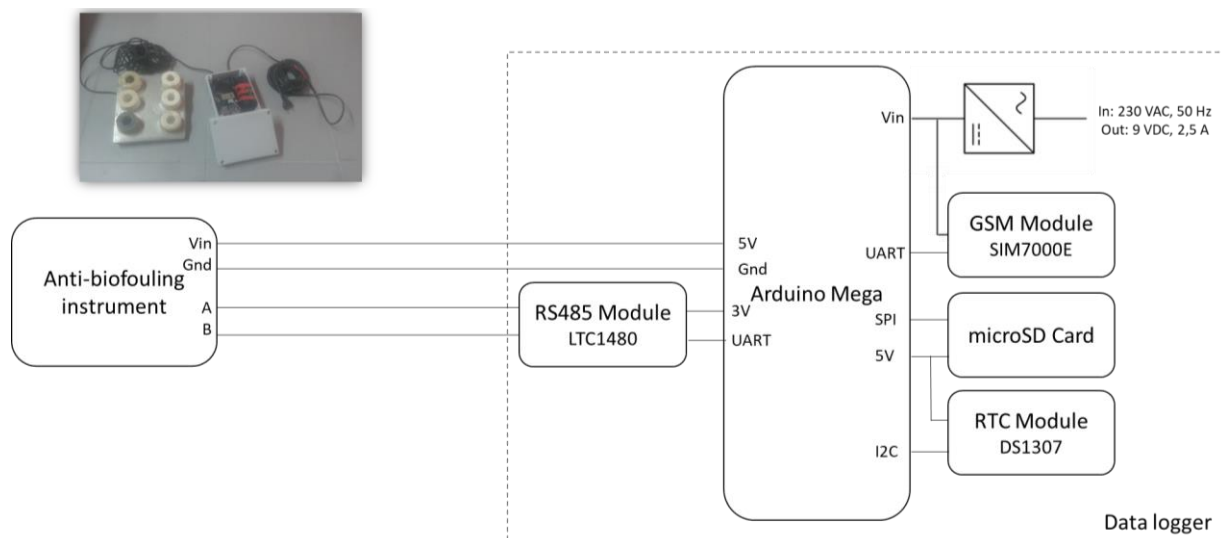
Figure 100. Illustration of the scheme diagram of the data logger used for the anti-biofouling experiment and photograph of the system.

Two days before the end of the experiment, the probes were taken out of the water for soft cleaning. This cleaning process, referred to as *in situ* cleaning hereafter, consisted of the manual removal of the macro biofouling attached to the sensors and the cleaning of the inside of the probes with fresh water and a soft cloth. After the *in situ* cleaning, the probes were deployed again for two more days to confirm the results.

After the experiment, the sensors were taken to the laboratory for hard cleaning. The probes were submerged for five days in a water tank with a high concentration of chlorine. This process killed and detached the algae from the instrument, leaving just cirripeds which were then removed. Finally, and with the probes clean of macro biofouling, the inside of the probes was cleaned with fresh water and a soft cloth.

The efficiency of the developed techniques was evaluated by three different metrics: the analysis of the turbidity measurements of the probes during the *in situ* experiment; visual inspections of the probes; and the comparison of calibrations before and after the test.

4.7.1 Monitoring data validation

Figure 101 shows the measured turbidity of each probe during the field experiment. The experiment started on the 23rd of May 2022 with all probes measuring turbidity values of 50–60 NTU. It is important to notice that turbidity is not expected to change significantly in this area, so the output of the probes should remain constant except for the biofouling interference. However, since biofouling is certain, during the following weeks, the different anti-biofouling techniques presented a drift in the measurements at different stages of the test. On the 7th of July, the probes were taken out of the water for visual inspection and *in situ* cleaning (red vertical line on the graphs of Figure 101) and deployed again for two more days.

The ABS and PLA, which were not expected to provide biofouling protection, took about five days to present a significant drift in the measured turbidity. The turbidity measurement delivered by the PLA probe increased during the experiment, a signal of biofouling interference. For the ABS, the turbidity increased till the 28th of July and then the values decreased to about 100 NTU.

This suggests that macro-fouling had attached to the sensor (e.g., algae) and blocked the passage of light in the sensing area of the sensor. The measurement returned to normal values after the detachment of the algae (in this case slightly above the values at the beginning of the experiment because of micro-biofouling that was still present on the surface of the optical transducers).

Previous field tests conducted in Esposende with the SPM and TVP sensors lead to interpret this high variability in turbidity derived from the attachment and unattachment of macro-fouling. However, the possibility that in some situations the organotin compounds released by the materials could also produce an antifouling effect cannot be excluded.
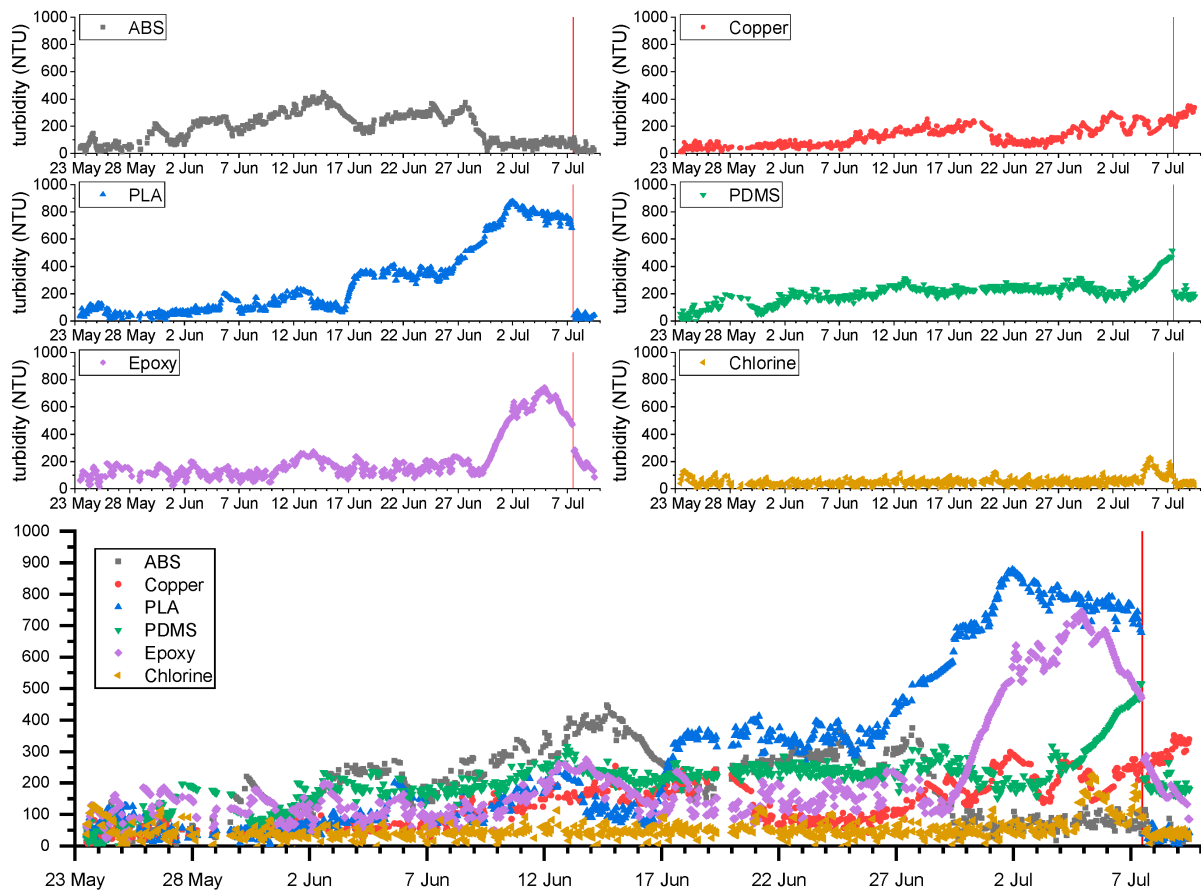
Figure 101. Monitoring results of turbidity produced by the six anti-biofouling techniques during the experiment in Ria of Vigo. The vertical red line marks the date when the probes were taken out of water for the *in situ* cleaning.

The PLA with copper filament presented a significant drift from the 8th of June. Compared with the ABS and PLA probes, which also have optical transducers in contact with water, the releasing of copper biocide into the water seems to increase the operation time of the sensor with minor biofouling interferences. While this technique was also affected by biofouling, the measurements are more constant when compared to the other material techniques.

The probes with epoxy and PDMS coatings did not demonstrate effectiveness against biofouling. The epoxy measurements started with values of 56 NTU and, during the first 3 days of the experiment, it increased to values around 100 NTU. From the beginning of the experiment to the 29th of June, this probe produced measurements of around 100 NTU but showed a high variability (about 40 NTU in amplitude). From this day to the *in situ* cleaning, the sensor registered an increase in the turbidity values, probably caused by macro fouling.

The PDMS probe produced similar results. In the first 3 days of the experiments, the turbidity measurements increased from 50 NTU to 150 NTU. This value slowly increased to around 200 NTU on the 30th of June. As for the epoxy technique, the recorded turbidity measurements increased gradually till the day of *in situ* cleaning.

The last technique, chlorine production, produced the best results among the six probes. Since the first day of the experiment, the probe presented values of 50 NTU with a maximum 5 NTU variation in its measurements. On the 5th of July, an increase in the turbidity measurements was observed, probably associated with the beginning of the drift. The measurements produced by this probe are the expected without biofouling interference.

On the 7th of July, the probes were cleaned and deployed again on the water to check if the *in situ* cleaning process was sufficient to eliminate the biofouling interference. Good results were obtained for the PLA, ABS, and chlorine probes since the turbidity measurements after the cleaning dropped to similar values at the beginning of the experiment.

For the epoxy and PDMS techniques, the cleaning also produced positive effects decreasing the recorded turbidity values. However, these values were still higher than the 50 NTU at the beginning of the tests, which indicates that the micro-biofouling was not eliminated.

Finally, the cleaning did not produce any effect on the copper probe and the turbidity values of the measurements kept increasing till the end of the experiment.

4.7.2 Visual inspections

The objective of the visual inspections was to provide qualitative comparisons between the probes concerning the quantity of biofouling at different stages of the experiment (mostly macro-biofouling).

Photographs of each probe were taken before the experiment, before and after the *in situ* cleaning on the 7th of July, and after the hard cleaning when the experiment ended. Figure 102 shows the state of each probe at these four different moments.

When the instrument was taken out of the water on the 7th of July for the *in situ* cleaning, the external housing of all probes was covered with macro-fouling, namely algae, barnacles, and some small mussels. However, there was a visible difference in the amount of macro-biofouling between the outside and the inside (sensing area) of the probes. The inside of the probes had fewer traces of biofouling, even for the

PLA and ABS substrates. A possible explanation for this event is that the instrument was deployed facing the seafloor and the inside of the probes was protected from direct sunlight, which contributes to the biological growth.
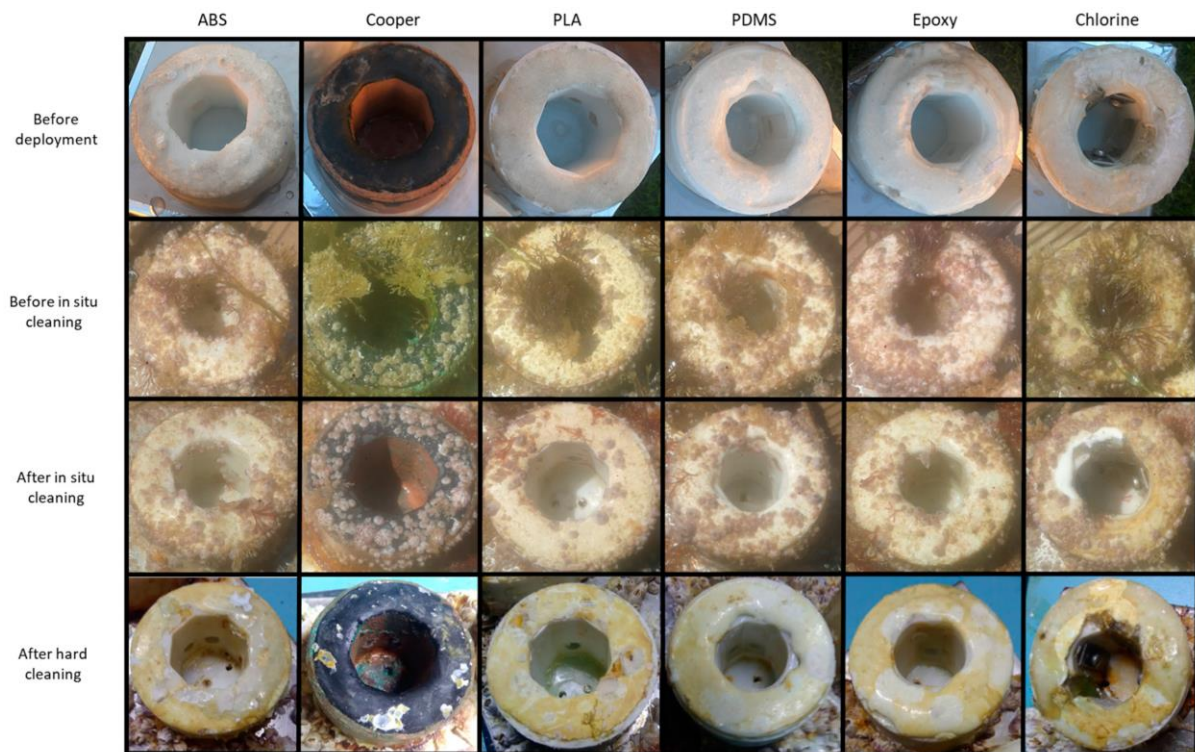
Figure 102. Photographs of the six probes at different stages of the experiment: before deployment, after 46 days of deployment, after the *in situ* cleaning on the 7th of July, and after the hard cleaning at the end of the experiment.

The *in situ* cleaning procedure removed the algae, and the interior of the probes was cleaned with fresh water and a soft cloth. The observation of the probes after the *in situ* cleaning (third row of Figure 102) shows that while the external housing had some barnacles, the sensing area was clean.

At the end of the experiment, the instrument was submerged for five days in water with high chlorine concentration to remove the macro-biofouling and the micro-biofouling from the surfaces. After this process, the barnacles and mussels attached to the sensors weakened and were manually removed. Other ones had to be removed using a chisel. The inside of the probes was cleaned with fresh water and a soft cloth. The state of the probes after this cleaning procedure is shown in the fourth row of Figure 102.

The comparison of the photographs before the field test and after the hard cleaning shows that the housing of the probes was damaged (as expected given they were built using cheap materials). However,

the sensing areas were clean and in good condition. After the hard cleaning, all probes had similar inside conditions as before the experiment, except for the PDMS coating, which was not as transparent as before, presenting a dark blur.

It is important to notice that both coating techniques (PDMS and epoxy) and the chlorine production probe did not have any trace of macro-fouling in their surfaces at any stage of the visual inspection. Additionally, the copper technique was the probe that visually had fewer biofouling traces on its inside. However, during the hard cleaning, it was noticed that a barnacle was growing on the surface of the LED of the copper probe, which was probably the reason why the technique did not produce lower turbidity values after the *in situ* cleaning.

4.7.3 Calibration signal loss

After the hard cleaning, the probes were calibrated again to check if they kept the same output as before the experiment. Figure 103 shows the relative performance after the second calibration in comparison to the first calibration presented in Figure 68. A value of 100 % represents that the sensor kept the same performance as before.

	Average (%)
ABS	96
Copper	98
PLA	99
PDMS	59
Epoxy	93
Chlorine	99
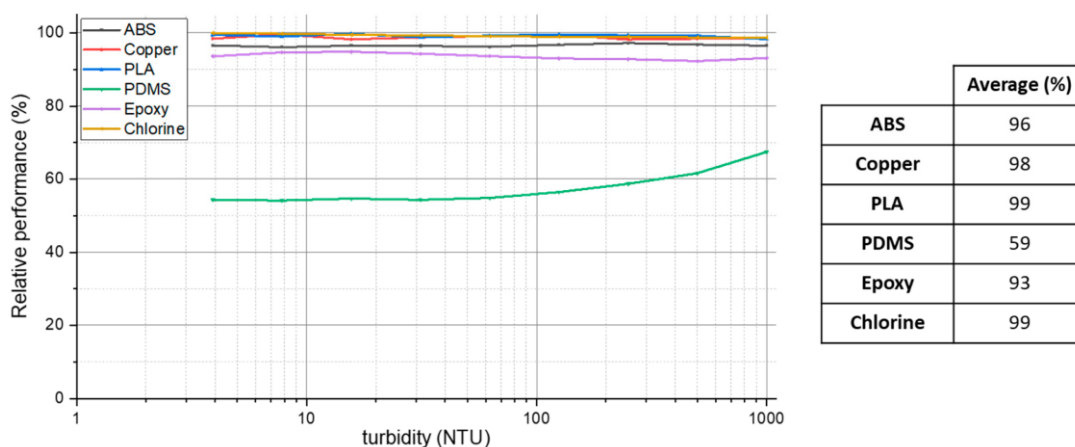
Figure 103. Results of the relative performance between the first and the second calibration of the six anti-biofouling probes. The first calibration was performed before the field experiment and the second calibration afterwards.

The PLA, chlorine, and copper probes presented the lowest performance loss from the first to the second calibration. The turbidity measurements in the second calibration were practically the same as for the first one. The ABS probe presented an average relative performance of 96 %, which is lower than the previous techniques, but still acceptable.

The coating materials are the techniques that presented lower performance, displaying the PDMS with the worst results with a relative performance of only 59 %. This result is consistent with the visual inspections after the hard cleaning when it was noticed that the coating had a dark blur on its surface.

Even with the cleaning process, all techniques presented different calibration results as before the field test, which means that the sensing integrity of the probes was affected.

4.7.4 Discussion

Considering the three metrics used to evaluate the operation of the six anti-biofouling techniques, it can be inferred that chlorine production outperformed the other tested techniques. The measurements carried out during the field test presented a signal without drift and the interference of biofouling was only detected after 41 days of testing. During the visual inspections, the inside of the probe always appeared clean, and the calibration of the probe did not show significant changes after the deployment.

The PLA with copper filament also produced satisfactory results during the field experiment. Compared with the other techniques (except the chlorine), the drift originated by biofouling interference was detected later, and the probe provided 15 days of reliable data. This was the only technique in which the *in situ* cleaning did not produce positive effects, possibly due to the growth of barnacles on the LED surface, which was only detected during the hard cleaning. Although the copper biocide satisfactorily protected the probe housing (during the visual inspections this technique was highlighted as the less susceptible to biofouling growth on its surface), it failed to protect the transducer surface that is in contact with the water.

The results for the other four probes did not provide insights into good protection against biofouling. During the field tests the epoxy and PDMS presented biofouling interference from the day of deployment. However, both stabilized on 100 NTU and 150 NTU, respectively, till almost the end of the experiment. Even the *in situ* cleaning was not sufficient to obtain turbidity measurements similar to the first deployment day. In the second calibration, these techniques presented the worst results, with the PDMS having a significant signal loss resulting from the blur of its coatings. All these factors suggest that these coatings are susceptible to micro-biofouling, even to an irreversible state.

Finally, the PLA and ABS substrates, which were used for comparison with the other techniques and not as effective anti-biofouling protection, presented the worst results during the field tests. The PLA probe produced satisfactory measurements till the 5th of June, but after that day the drift in the measurements

increased significantly. For the ABS probe, the drift was visible since the day of deployment, and contrary to the epoxy and PDMS that suffered mostly from micro-biofouling, macro-biofouling interference was constant throughout the experiment. On the positive side, the *in situ* cleaning provided good results and the hard cleaning left the probes in the same conditions as before the experiment.

The results obtained in this experiment are consistent with those theoretically expected. Chlorine is a strong oxidant that destroys primary biofilms and microbes, and propagules of macro-fouling. The anti-fouling efficiency against the primary film is crucial for a long-term operation without biofouling interference in the measurements. The other tested techniques, based on the release of organotin and toxic compounds into the water, may also be harmful to macro-fouling organisms but are not as effective as chlorine biocide against biofilm formation. The anti-fouling efficiency of copper biocide has been previously validated, as shown in the scientific literature and, consequently, satisfactory results would be expected from this experiment.

5 OTHER APPLICATIONS

This dissertation focused on the coastal environmental monitoring of sedimentary processes. However, the resulting equipment has a wide range of possible applications, even outside the scope of oceanography.

The developed technology was used and tested as standalone devices or integrated with monitoring systems in other Scientific Projects. The technological overview and results of said applications are presented in this chapter.

5.1 Project SAIL – Space-Atmosphere-Ocean Interactions in the Marine Boundary Layer

The Project SAIL was promoted by Marinha Portuguesa and INESC TEC and intended to perform earth monitoring during the circumnavigation trip of the Sagres sail-ship in 2020. The main objective of the Project was to use the world trip navigation of the sail-ship to collect data about the marine boundary layer. To do so, a set of instruments was used to monitor the space/atmosphere component (atmospheric electric field, gamma radiation, ion counter, visibility, solar radiation and kinematic GNSS) and the oceanic component (conductivity, temperature, depth, pH, dissolved oxygen, chlorophyll, spectral radiance and acoustic noise).

The SPM Sensor was used in the project to monitor oceanic chlorophyll. The sensor measures turbidity, which is not relevant in the open sea due to the non-existence of suspended sediment at the surface. However, the capability to distinguish organic from inorganic matter makes it useful to quantify chlorophyll using the UV channel. The sensor was hosted by an STM32L496ZG datalogger which also computed the digital processing of the analogue readings of a hydrophone to measure the acoustic noise.

The instrumentation set (datalogger + SPM Sensor + hydrophone) was integrated with the central processing unit of a monitoring system developed by INESCTEC: the "tow-fish" (Figure 104). The tow-fish was the equipment where all the oceanic sensors were assembled. This device was intended to be towed by the sail-ship and dragged by the ocean along the course of the vessel.

Due to the COVID-19 pandemic situation, the trip of the Sail ship was cancelled at the beginning of its journey and the monitoring information about the oceanic parameters was not recovered.
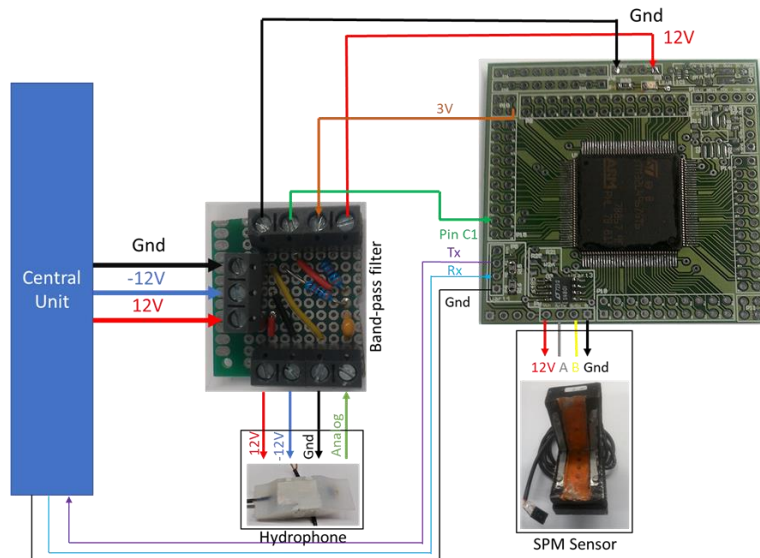
Figure 104. The top image shows a photograph of the tow-fish where the oceanographic instruments were integrated. The bottom image shows the scheme connections of the STM32L496ZG datalogger, SPM Sensor and hydrophone to the central unit of the tow-fish.

5.2 Project SONDA – Synchronous Oceanic and Atmospheric Data Acquisition

Project SONDA (https://sonda.uac.pt/) aims to contribute to better atmospheric and oceanic monitoring by proposing the development of a complementary system to the existing observation means. It intends to use High-Altitude Balloons (HAB) to perform atmospheric monitoring and to release oceanographic probes into regions of interest in the ocean.

The system is two-fold and brings innovation in the respective vectors: (i) the probes and (ii) the probes' carrier. Regarding the probes, the innovation is relative to their ability to continuously monitor parameters of interest from near space to the deep sea. The probes are customizable allowing the integration of atmospheric sensors, motion sensors and marine sensors. When the probe is released into the ocean, it will sink, reaching the sea floor where will remain for a predefined period. Then, the probe will return to

the surface and transmit the data collected during the dive to a ground control station through a satellite or other available communication link. The probe will stay afloat in the ocean, operating as a drifter until it stops functioning due to material degradation.

Regarding the carrier of the probes, a High-Altitude Balloon (HAB) will be used. This low-cost solution with high cargo capability travels passively through the atmosphere to reach targeted areas but with low positional accuracy. In the scope of this project, it is intended to develop a control solution to endow the aerostat with some positioning capability, by controlling its altitude in agreement with the available wind currents. Limiting the HAB rise will also allow to keep it aloft for longer periods, making it not only an excellent atmospheric monitor but also a communications relay between the probes launched in desired locations and a ground control station, reducing the usual satellite communication costs.

The proposed SONDA system, composed of HAB + swarm of probes, will allow the acquisition of data otherwise unreachable in a cost-effective and integrated manner, from near-space to deep-sea (Figure 105). The HAB platform will be capable of deploying disposable probes over hundreds of kilometers, at significant altitudes, something unachievable by other technologies, such as the commonly named drones. This solution also bridges the existing gap between space and surface instrumentation, adding to the available satellite information the detailed long-term analysis of targeted areas.
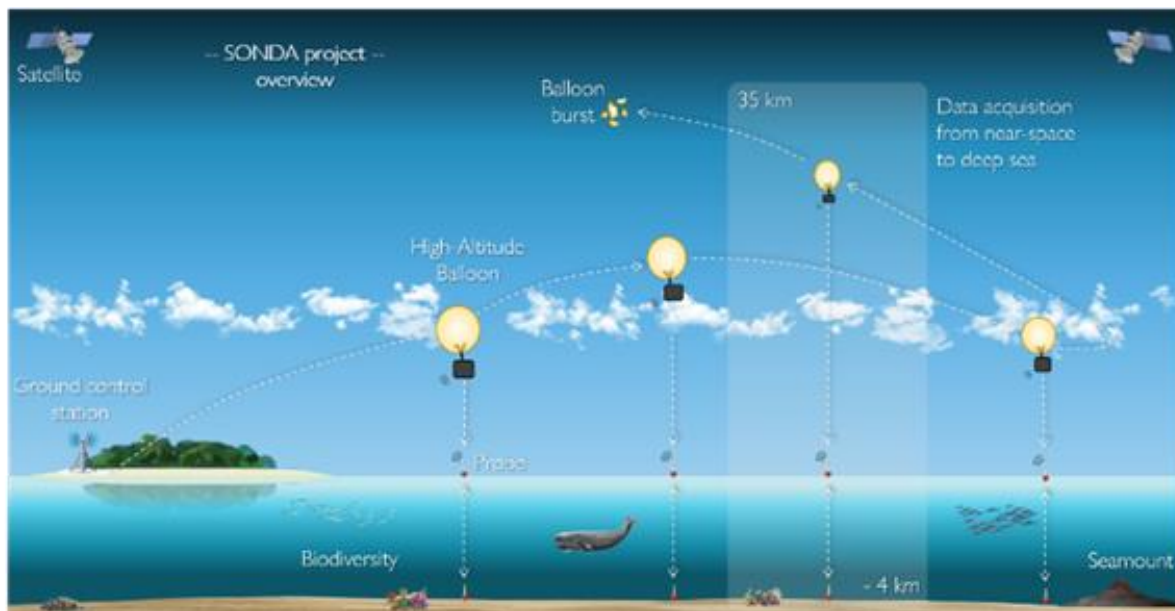
Figure 105. Illustration of the Project SONDA concept overview.

5.2.1 Campaign in Azores Islands 2021

This subsection was published in "Synchronous Oceanic and Atmospheric Data Acquisition: field test release and validation of atmospheric, oceanographic, and deep-sea probes in the Azores", MTS/IEEE OCEANS Limerick 2023 [214]. It reports the test and validation of three probes deployed in São Miguel, Azores, in 2021. The probes are intended to measure atmospheric, coastal/oceanographic and deep-sea parameters.

- Atmospheric probe

The atmospheric probe was developed with APRS communications to transmit the Global Position System (GPS) coordinates and atmospheric data from the HAB to a ground control station during the atmospheric monitoring phase.

From the HAB launch to its bursting up to 35 km high, the atmospheric probe measures the vertical profile of the atmosphere. After the burst of the balloon, the probe falls with a parachute into the ocean and is not recovered. To collect the data, real-time communications between the ground station and the balloon are crucial. The use of APRS communications for HAB flights was validated in previous launches and it is worldwide used [215].

The probe uses a WiMo PicoAPRS-Lite APRS Transceiver Module that provides wireless long-range communications, pressure and air temperature sensors and GPS. A 250 mW solar panel and super-capacitor were used to supply the electronic system (it does not have a battery and works merely on solar energy).

The probe was built in a spherical form, with a 200 mm diameter, in polyurethane material (HB R 16/25—HBQUIMICA) and weighs 1.8 kg. The solar panel was coated with epoxy resin (HB EPOSURF2—HBQUIMICA) to protect it from the environment while keeping transparency.

The atmospheric probe is presented in the left photograph of Figure 107.

- Oceanographic probe

The oceanographic probe was developed to test mainstream sensors for water monitoring. For this probe, the concerns about depth and high-pressure needs were not considered. The main purpose was to test sensors in underwater conditions, validating their acquisition and the watertight of the probe.

The electronics of the probe were designed with a power circuit, STM32L496ZG data logger and sensors to measure the water parameters. The power module uses a 3.7 V 2500 mA LiPo battery and a LiPo Rider V1.3 power manager to supply the electronic system. The data logger uses its integrated RTC to keep date and time and the microSD card to store the monitoring information.

The probe measures water temperature and water depth using the MS5837-30BA sensor and uses the IR-transmitted light detection technology developed for the SPM Sensor to measure daylight luminosity and turbidity. The measured parameters are saved with the date and time on the microSD card. The probe has autonomy for three months of continuous monitoring taking measurements with a sampling period of 2 seconds.

The probe was built in polyurethane material with a watertight capsule that can be opened to access the microSD card to download the data, plug and charge the battery, and update the firmware of the instrument. The oceanographic probe is presented in the middle photograph of Figure 107.

- Deep-sea probe

The deep-sea probe is expected to measure the vertical profile of the ocean, from the surface to the seafloor, in areas up to 4000 m depth. One of the challenges for the dive of the probe is to make it sink when released into the water and be able to return to the surface, after a predefined period, without the use of a propeller.

To accomplish the intended course of action during the dive, the probe was designed with positive buoyancy. Before the launch of the HAB, a salt ballast is added to the instrument. Thus, the buoyancy of the set becomes negative due to the incremental weight. With this configuration, when the probe is submerged it will sink while the salt dissolves in the seawater. Once the buoyancy turns positive again, the probe returns to the surface. At this stage the probe becomes a drifter, sending the acquired data during its dive using satellite communications, as shown in Figure 106.

The electronics of the probe were designed with a 3.7 V 6000 mA LiPo battery and solar panel (to keep power for an indeterminate time during the drifter phase), an LQFP-32 data-logger with an STM32L412K8T processor, an L76X GPS module, and RockBlock 9603 IRIDIUM communications. The instrument measures water depth, water temperature and luminosity.
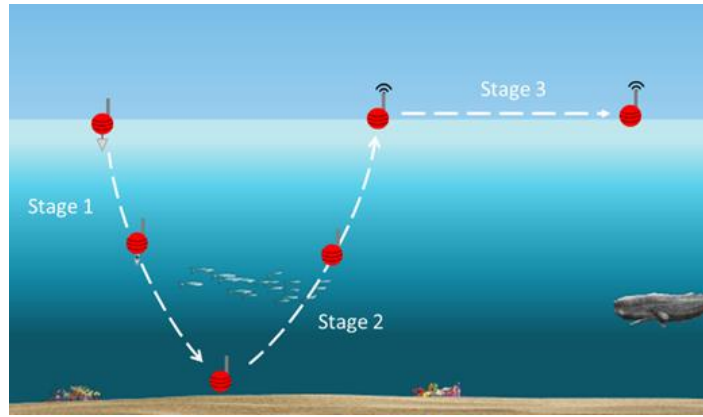
Figure 106. Illustration of the intended dive of the deep-sea probe. Stage 1: when the probe is released in open waters, the salt ballast will make it sink to the ocean floor; Stage 2: once the salt dissolves in the seawater, the probe will return to the surface due to its positive buoyancy; Stage 3: at the surface, the probe will act as a drifter and transmit, by satellite communications, the GPS position and the measurements recorded during Stages 1 and 2.

A 400 bar Sensata Technologies PTE7100 sensor was used to estimate depth, a TMP235AEDCKRQ1 integrated circuit enclosed in epoxy resin to measure water temperature, and a Vishay TEPT5700 photodiode to measure luminosity (same photodetector used to measure the UV transmitted light in the developed optical turbidity sensors). In this prototype, and for testing purposes, a SEACON underwater connector was used to plug the power and program the firmware of the probe.

The probe was built with a mixture of polyurethane and borosilicate glass microspheres (<10 μm diameter) in a proportion of 3:1. The borosilicate spheres were used to reduce the density of the probe. Its final form weighs 1.6 kg and has 27 % positive buoyancy. The deep-sea probe is presented in the right photograph of Figure 107.

Figure 107. Photographs of the three probes deployed during the campaign in São Miguel, Açores. The left image shows the atmospheric probe, the middle image the oceanographic probe and the right image the deep-sea probe.

5.2.1.1 Preliminary tests in a semi-controlled environment

On the 6th of September 2021, preliminary tests were conducted for the three probes in Douro River, Portugal (41°03'59.2'' N 8°24'20.8'' W). The experiments were made to test the watertight of the three probes and their operations.

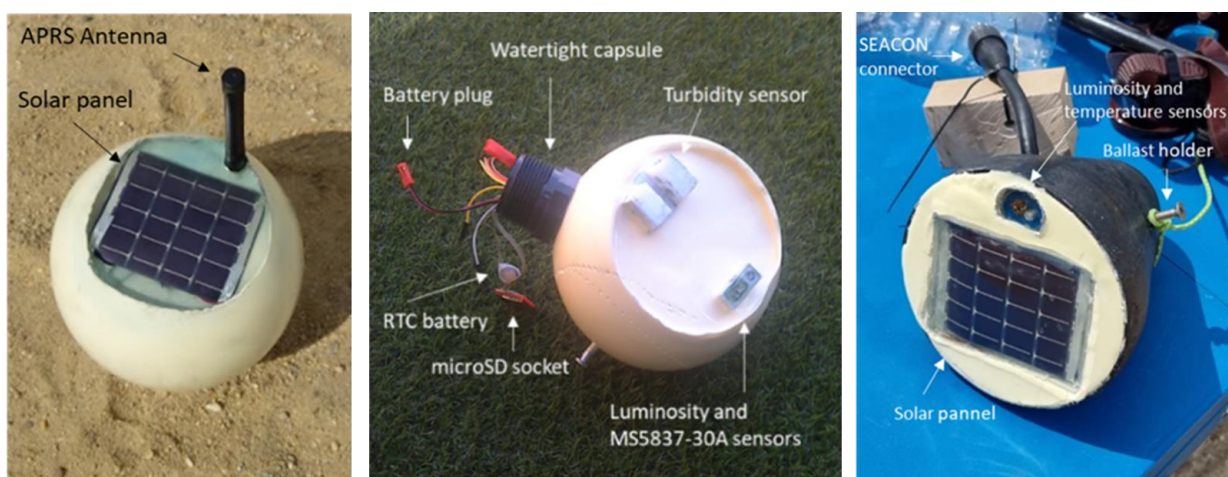The short-range communications of the Atmospheric probe were tested using a KENWOOD TH-D74 as the receiver APRS station. The probe was not launched by balloon. During this experiment, the tests were only conducted on the ground. The communication tests were performed during cloudy weather, which did not present a problem for the operation of the probe (this is an important factor since the probe does not have a battery and works on solar energy). The APRS probe was tested successfully, with communications received by the mobile station.

The oceanographic probe was set with a sampling period of 1 minute and deployed on the river at 2 m and 5 m depth. The battery was plugged at 11h30 with the probe outside the water for five minutes. At 11h35 the probe was submerged up to 2 m depth and remained submerged for ten minutes. At 11h46, the probe was taken to 5 m depth for three minutes and then returned to the surface. Figure 108 shows the measurements recorded.

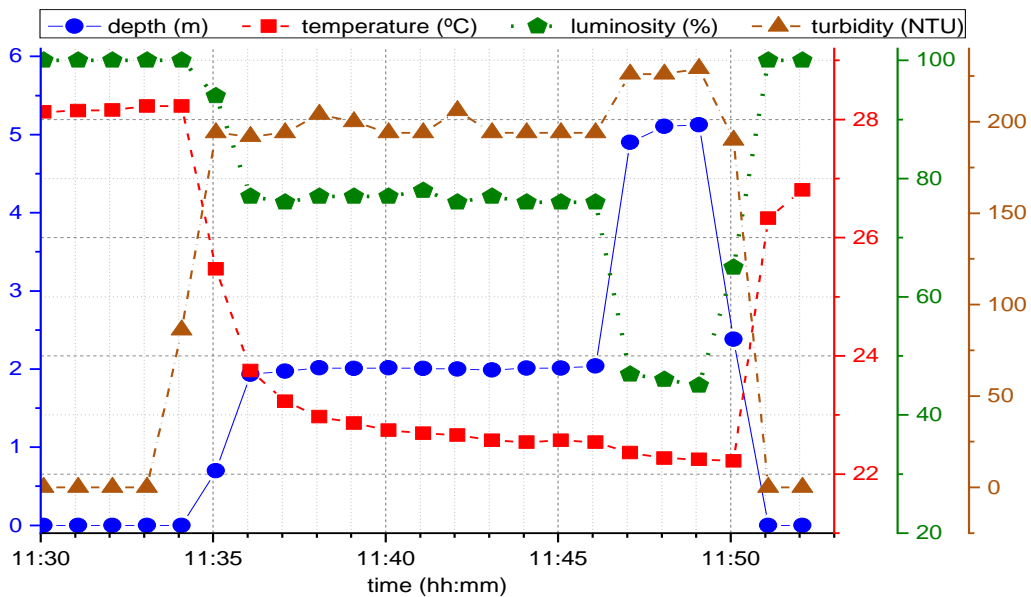Figure 108. Measurements of the oceanographic probe during the river deployment. The records of depth are shown in blue circles and blue line (principal blue Y-axis), the water temperature in red squares and red line (secondary red Y-axis), the relative luminosity in green pentagons and green line (secondary green Y-axis) and the turbidity in brown triangles and brown line (secondary brown Y-axis).

The temperature recorded in the initial minutes of the experiment was 28.2 °C (at this stage, the sensor was measuring the air temperature). After submersion, the temperature gradually decreased to 22.3 °C at 2 m depth and then to 22.1 °C at 5 m depth. When the probe returned to the surface, the temperature increased again to values close to 28 °C (there is a delay in reaching the initial air temperature values because of the thermal capacity of the probe).

The recorded measurements of luminosity were converted to a scale of 0 - 100 %, with 100 % corresponding to the maximum luminosity measured during the experiment (when the probe was outside the water) and 0 % the luminosity with the probe on the dark. The values measured at the beginning and end of the experiment, when the probe was outside the water, were 100%. The luminosity values decreased to 76 % at 2 m depth and 47 % at 5 m depth. This behaviour is compliant with the principle of attenuation of light when travelling through the water.

The turbidity measured with the probe outside the water was 0 NTU, as expected, decreased to 190 NTU at 2 m depth and to 250 NTU at 5 m depth. When the probe was deployed at 5 m depth, it was already on the streambed, so this turbidity difference from 2 m to 5 m can be explained due to streambed turbulence and re-suspension of streambed solids that increase turbidity.

The oceanographic probe was successfully validated in this experiment. The systems acquisition and electronics worked as designed, the watertight capabilities were verified and the results for depth, temperature, luminosity and turbidity were compliant with the theoretical expected.

The deep-sea probe was set to take measurements with a sample period of 30 seconds. The battery was plugged with the probe outside the water and then it was left floating for five minutes at the surface of the river. During this phase, the probe was recording measurements and the satellite communications were disabled. The probe was submerged at 8 m depth for three minutes and returned to the surface. For this experiment, the software of the probe was set to detect its return to the surface, take another three minutes of measurements, and enable the GPS and satellite communications to send the recorded data (drifter mode, stage 3 of Figure 106).

Figure 109 shows the measurements recorded by the deep-sea probe and received by IRIDIUM communications. The results are similar to the experiment using the oceanographic probe: when the probe sunk into the river stream, there was a decrease in the water temperature and luminosity and an increase in depth. The GPS module measured an accurate position of 41°04'00.1'' N 8°24'24.57'' W when the probe returned to the surface.
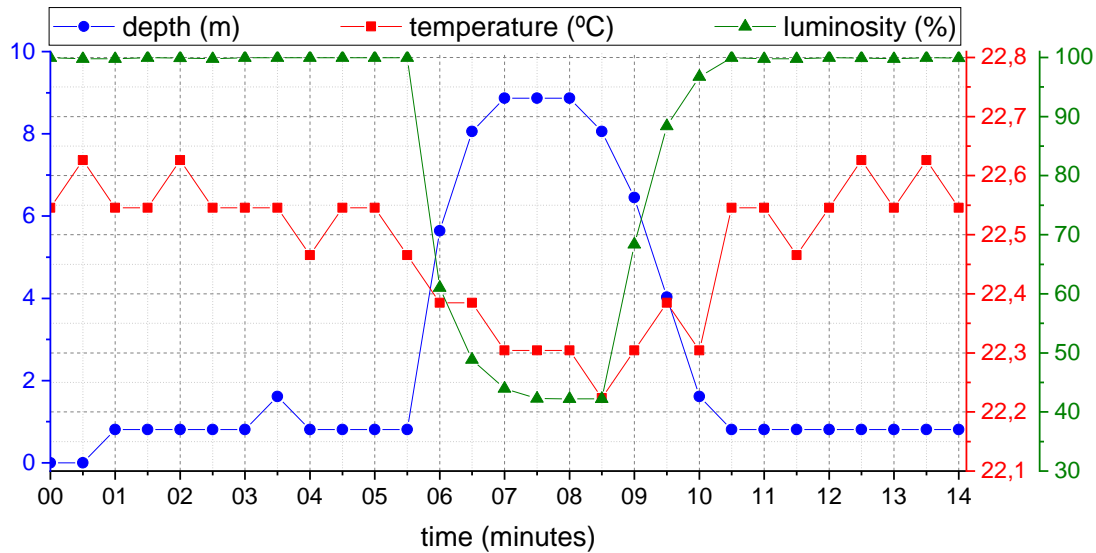
Figure 109. Measurements of the deep-sea probe during the river deployment. The depth is shown in blue circles and blue line (principal blue Y-axis), the water temperature in red squares and red line (secondary red Y-axis) and the relative luminosity in green triangles and green line (secondary green Y-axis).

Besides the operation of the sensors, this experiment also tested the algorithm developed for the different dive stages (detect when the probe is on the surface, the dive, and the returning to the surface to enable the communications) and the efficiency of IRIDIUM communications. The firmware and sensors were successfully validated, but the IRIDIUM presented problems.

When the probe returned to the surface and started to communicate, only 5 messages out of 20 were successfully transmitted. The test was conducted during a cloudy day, which is a concern for satellite communications that need a clear view of the sky for a good performance. However, it was noticed that the transmission rate success with the probe outside the water increased to 16/20. This means that the mass of water around the probe affects the data transmission. In open seawaters, the transmission rate success is expected to be even lower [216].

5.2.1.2 Test and validation in São Miguel, Azores

The field tests in São Miguel Island, Azores, from the 11th to the 20th of September 2021, allowed to test the three probes in realistic scenarios: launch of the atmospheric probe by HAB, deployment of the oceanographic probe on the island coast and release of the deep-sea probe in the Atlantic Ocean. Figure 110 shows the deployment locations of the probes across the island.

Figure 110. Illustration of the locations of the deployments of the oceanographic and deep-sea probes, the launch of the atmospheric probe by HAB and the installation of the APRS ground station.

- <u>Atmospheric probe</u>

On the 16th of September, the atmospheric probe was launched by HAB in Lagoa, São Miguel (37°44'27.9" N 25°34'56.6" W, Atmospheric probe launch in Figure 110). The APRS communications were tested both to a mobile and a fixed ground control station. The mobile station was the KENWOOD TH-D74 receiver used during the fluvial tests. The fixed ground station was installed in Pico da Barrosa, the second highest point of the island with 947 m height (37°45'37.1" N 25°29'29.3" W, APRS Ground Station in Figure 110) and used an FM VHF/UHF and APRS transceiver and a LoRa Gateway LtAP LR8 LTE kit from Mikrotik.

Figure 111 shows the flight simulation of the HAB. The atmospheric probe transmitted successfully to the portable station but lost communications when the HAB was at a 10 km horizontal distance, which was not expected. The APRS transceiver was set to an automatic frequency. When the HAB was launched, the probe was communicating with the portable station using a Portuguese frequency. A possibility raised for the communication failure was the change to an international frequency when the HAB moved away from the island radius.

Contrary to the mobile station, the fixed ground station did not receive any transmission from the probe. Tests with a frequency analyser after the HAB launch showed that other radio amateur signals in the area were producing significant noise on the station, which did not allow to receive the transmissions of the atmospheric probe.

Figure 111. The left image presents the flight simulation of the HAB. The right image presents a photograph of the atmospheric probe with a parachute before the launch.

■ Oceanographic probe

The oceanographic probe was deployed from the 17th to the 20th of September in the coastal area of Ferraria, São Miguel (37°51'29.96'' N 25°51'8.23'' W, Oceanographic probe deployment in Figure 110). The probe was installed at 2-4 m depth, close to a geothermal spring (see Figure 112). The instrument was set to record measurements of depth, water temperature, turbidity and luminosity with a sampling period of 2 seconds.
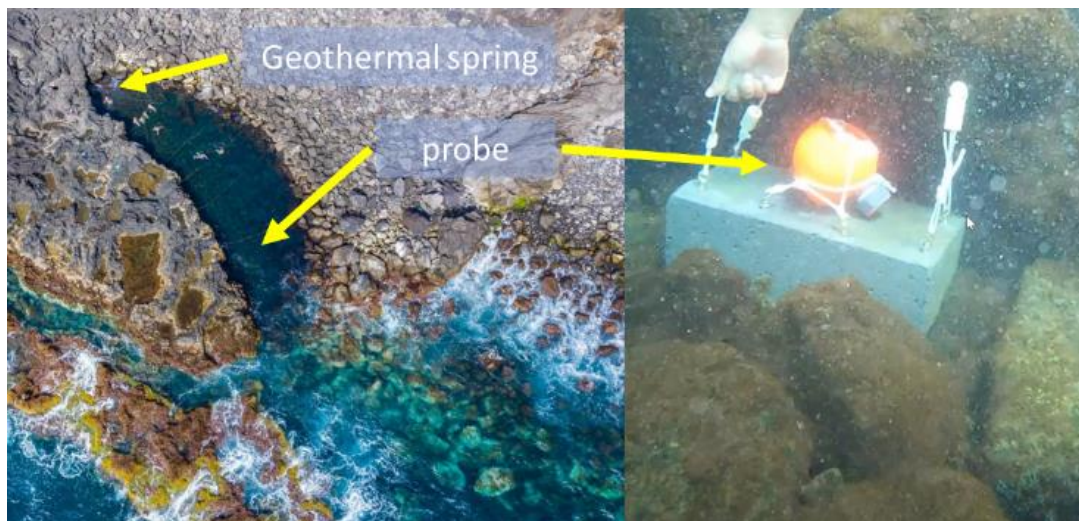
Figure 112. Deployment of the oceanographic probe in Ferraria, Azores, close to a thermal spring. The left image shows an aerial view of the location. The right image shows an underwater photograph of the installation of the probe.

The top graph of Figure 113 shows the depth and water temperature recorded by the probe. The depth is presented in blue circles and discloses the tidal cycles with a tidal amplitude of almost 2 meters

156

between the low and the high tide (low-frequency signal with a period of 12 hours). The data of depth also presents a signal in high frequency. This signal was caused by the small sampling period that was sufficient to measure the height of the sea waves.
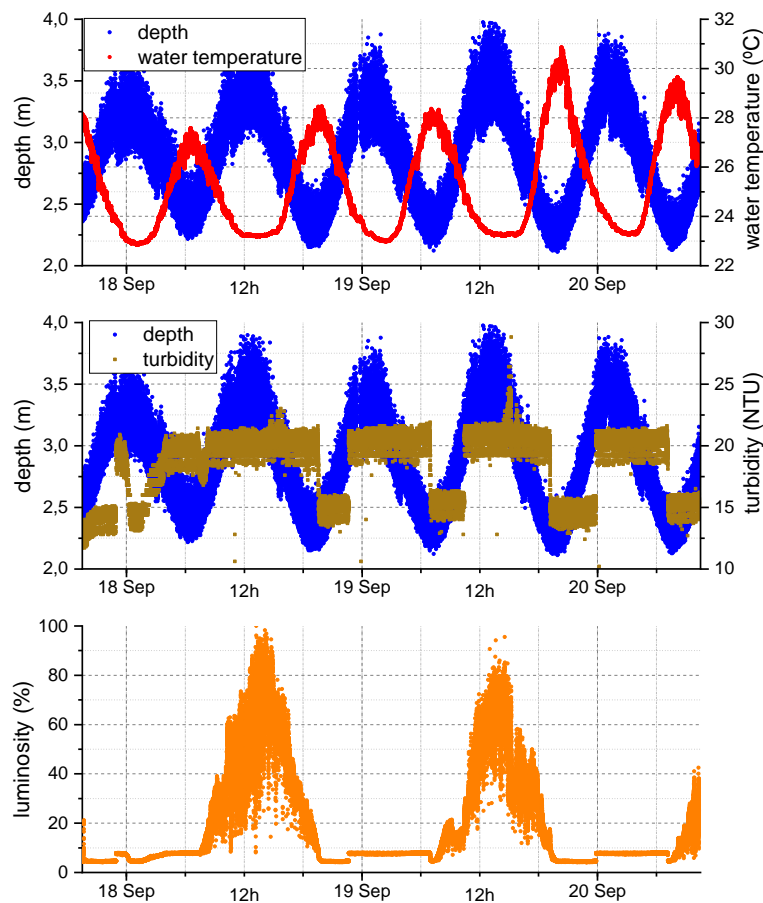
Figure 113. Monitoring results of the oceanographic probe during the *in situ* test in the Azores. The top graph shows the water depth (blue circles) and the water temperature (red circles). The middle graph shows the water depth (blue circles) and turbidity (brown circles). The bottom graph shows luminosity.

The water temperature is presented in red circles and, correlated with the depth, shows an increase in the temperature during the low tides and a decrease during the high tides. The probe recorded minimum water temperatures of 21 °C and maximum of 31 °C. These high values are caused by the hot water coming from the thermal spring.

The temperature amplitude between low and high tides is caused by the mixture of geothermal water with seawater. Since the sea water is colder than the geothermal spring fluid, during the high tide there is a higher volume of cold water, so the water temperature in the area decreases. The opposite happens during the low tide when the hot water coming from the spring warms the surroundings.

As Figure 112 shows, the location where the probe was installed is characterized by clean water and rocky seabed. The absence of fine sediment resulted in low turbidity values recorded by the probe. The middle graph of Figure 113 shows turbidity values of 20 NTU during most time of the experiment and 15 NTU during the increase of the tide (except for the first low-to-high tide on the 18th of September). One explanation for this periodical decrease in turbidity is the difference in water transparency between the water from the ocean and the hot spring. As explained for the water temperature, during the low tide the geothermal water has a higher influence in the area. However, the presented data is not sufficient to draw significant conclusions.

The bottom graph of Figure 113 presents the luminosity data, which follows the daylight behaviour. For all the days of the experiment, the luminosity level started to increase around 6h50 (sunrise), reached its peak at 14h (time of the day when the sun was in direct line to the probe) and decreased till 20h30 (sunset). At night, the luminosity was always above 0 % because of the lunar light (full moon on the 20th of September).

- **Deep-sea probe**

Before the release of the deep-sea probe in open waters, the satellite communications were tested at the sea. As demonstrated during the tests in Douro River, the transmission rate success decreases when the probe is on the water. As expected, this rate decreased even more with the sea waves. Nevertheless, the designed experiment was carried on.

The deep-sea probe was released on the 18th of September, in the Atlantic Ocean, in a location with 1700 m depth (37°28'36.00'' N 25°32'1.00'' W, Deep-sea probe release in Figure 110). A ballast with 2 kg of coarse salt was used and the probe was seen sinking into the deep. During the following days of the release, no satellite transmission was received and there was no feedback from the probe.

As an outcome of the test, several hypotheses were raised to explain the failure in receiving data from the probe: the probe was stuck under the surface (e.g., fishing nets or flora); malfunction of the ballast; materials did not resist to high pressures causing the collapse of the probe; change in the buoyancy level or position of the probe due to the high pressures; water infiltrated into the electronics; malfunction of the software or electronics; problems with the satellite communications.

5.2.2 Campaign during the Cumbre Vieja volcanic eruption, La Palma 2021

The Cumbre Vieja is an active volcanic ridge on the island of La Palma in the Canary Islands, Spain. The latest eruption began on the 19th of September 2021 in the forested area of Las Manchas known as Cabeza de Vaca. Voluminous lava flows quickly reached populated areas downslope, fanning out across settlements and banana plantations, destroying thousands of buildings and ultimately pouring over steep cliffs into the ocean to enlarge the island at several locations. The volcano went quiet on the 13th of December 2021, and on the 25th of December 2021, the local government declared the eruption to be over.

During the eruption of the volcano, several governmental and scientific entities acted on the island for crisis management, risk evaluation and scientific assessment. Project SONDA formed a task force to study the air and water quality on the island during the eruption and executed field tests from the 6th to the 11th of December 2021.

The water quality monitoring relied on the development of a buoy, to be installed in the line coast where the lava was flowing to the ocean, and to understand if the lava was producing anomalies in the sea. Due to the critical situation, a fast response was needed, and the buoy had to be developed in a short period of time.

The buoy was designed with an MKR WAN 1300 LoRa microcontroller, RTC, microSD card module, solar panel, GPS, MSB8537-30BA (pressure and water temperature), Gravity™ Analog pH sensor from Atlas Scientific, conductivity K 10 sensor from Atlas Scientific and own developed hydrophone (similar piezoelectric receiver used for the acoustic ToF current meter but to listen the soundscape).

The buoy was deployed the closest possible to the lava, as Figure 114 shows. Due to safety and bureaucratic issues, the installation was only possible on the 10th of December, one day before the group left the island.

A LoRa Gateway was installed in Porto de Tazacorte to communicate with the buoy and collect the monitoring data. However, the buoy was outside the coverage range of the gateway and the communications were not established. It was impossible to move the gateway closer to the buoy to receive the monitoring data. Since there was no way to collect the data using LoRa communications, the buoy was recovered on the 11th of December to download the data from the SD card.
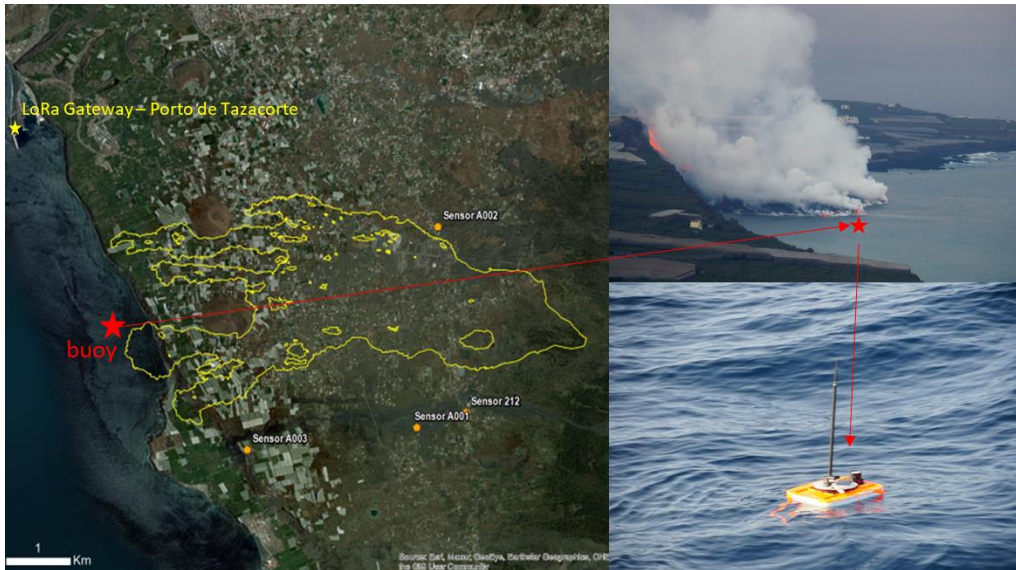
Figure 114. Illustration and photographs of the deployment of the buoy, close to the volcanic lava flowing into the ocean. The left image is an aerial view of the area affected by the volcanic scoria and the positions of the buoy and LoRa Gateway (it is also possible to see the location of some of the air quality systems installed, market with orange circles). The right images are photographs of the deployment of the buoy.

Figure 115 shows the measurements recorded by the buoy. The time of the experiment was short and made it difficult to draw significant conclusions. The measurements of pressure have little relevance since the buoy was floating. The water temperature values show an average value of 20.5 $^\circ$C. The normal water temperature in La Palma during winter is 17–19 $^\circ$C, so the increase in water temperature due to the volcanic lava is a possibility. There is a water temperature variation in the experiments but seems related to the gradient of temperature from day and night.
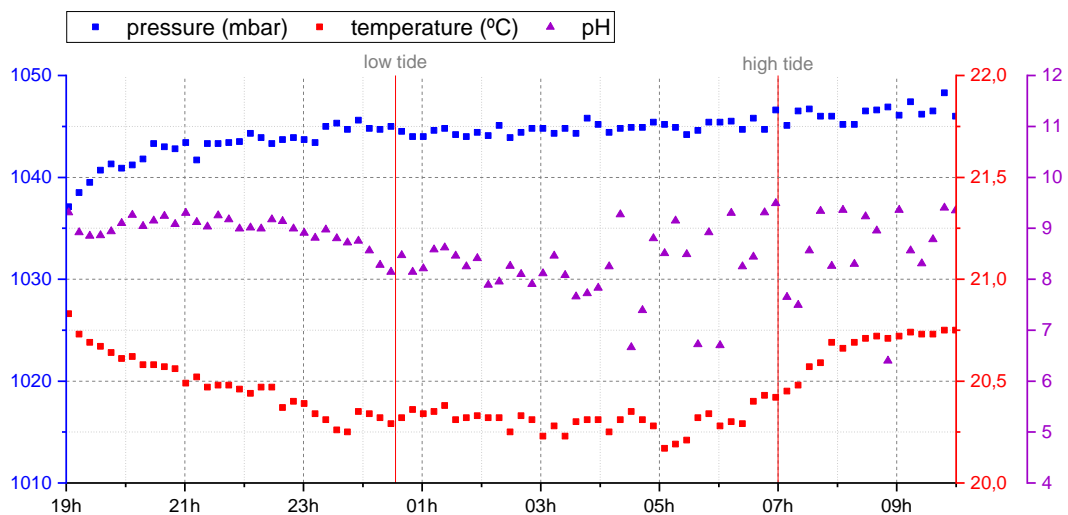

Figure 115. Monitoring results of the buoy deployment in La Palma from the 10th to the 11th of December 2021. The pressure data is presented in blue circles (principal y-axis), the water temperature in red squares (secondary y-axis) and the pH in pink triangles (secondary yy-axis).

The pH measurements show values slightly above the typical 7,9 to 8,3 pH of the Atlantic Ocean. The volcanic eruption that occurred in La Palma was primarily characterized by the emission of basic lava (mafic) which complies with the increase of the water pH. The data from the conductivity probe would help to strengthen this statement, however, it was damaged during the travel to the island and did not produce measurements. When the buoy was recovered, the pH probe was also broken. In the data of Figure 115, it is possible to see a difference in the accuracy of the measurements after and before 4h00 of the 11ᵗʰ of December that was probably caused by this event.

The hydrophone produced 17h hours of soundscape. The measurements were processed using a Fast Fourier Transform (FFT) to be analyzed in the frequency domain. The turbulence of the sea and the strong wind produced noise with high amplitude in the low frequencies and the data did not produce a significant outcome. Figure 116 shows an example of the FFT applied to the hydrophone data and the noise in the low frequencies.
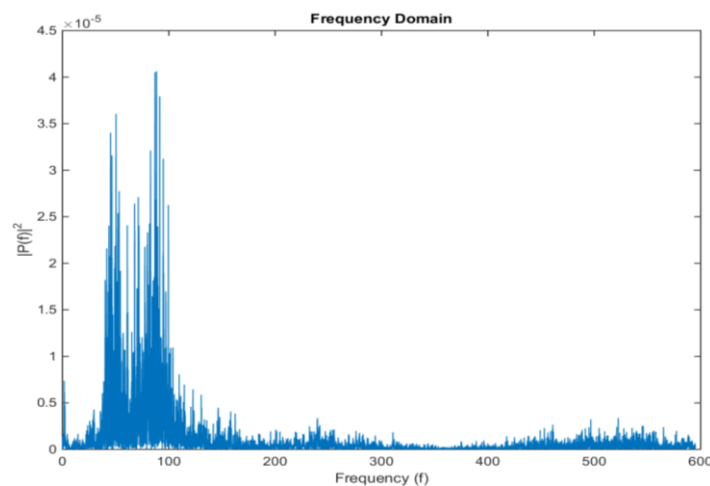

Figure 116. Example of the FFT applied to the hydrophone measurements.

5.3 Project K2D – Knowledge and Data from the Deep to Space

The deep-sea environment is the most challenging in terms of *in situ* data acquisition and presents a large information gap. Project K2D addresses this gap by proposing to take advantage of the already existing (and future) large and widespread infrastructure of telecommunications subsea cables to produce a network of real-time continuous monitoring of oceanographic variables. The underlying concept takes advantage of the signal repeaters distributed along communication cables to establish data and power access points. Therefore, it aims for the development of a global-scale monitoring system for oceans, able to tackle the entire water column in all existing depths, from the deep sea to coastal areas.

Project K2D is a collaboration between dstelecom, the University of Minho, INESC TEC and the University of Algarve. The main goal of the project was to use the standard fibre-optical cables and re-design them with repeater nodes where would be possible to plug other systems such as monitoring stations, AUV control and management systems, sonars, acoustic communications, etc.

A first prototype of 60 meters of fibre-optical cable was installed in Ponto de Apoio Naval de Tróia (38°28'30.3'' N, 8°52'15.1'' W). The cable was terminated with a repeater node with a hydrophone, camera and sensor station (Figure 117).

The sensor station was designed with an LQFP-32 STM data logger, MSB5837-30BA sensor for measurements of depth and water temperature, UART – ETH converter and power over ethernet (POE) cable. The station was used to test and validate the acquisition of water parameters. However, a malfunction in the housing of the monitoring station resulted in infiltration of water after submersion and the system did not produce data.
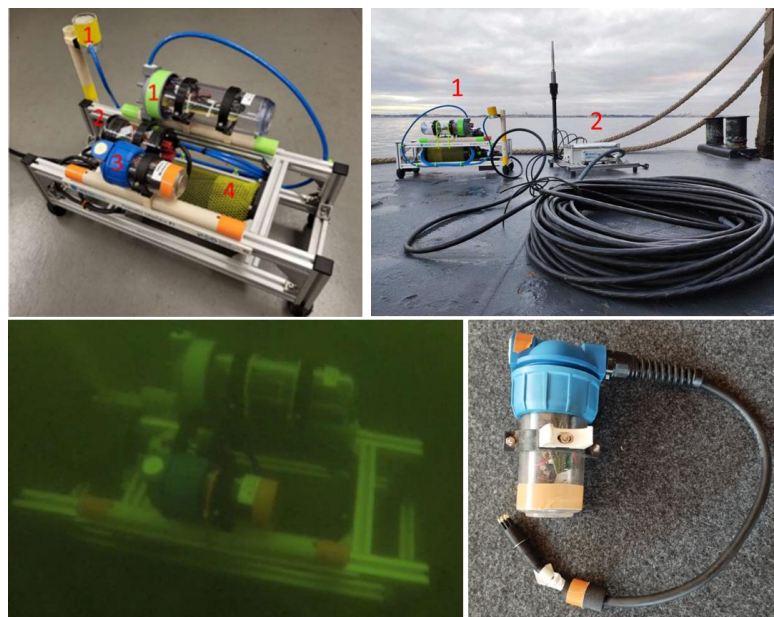

Figure 117. Photographs of the fibre-optical cable, node repeater and monitoring station. The top left image shows the repeater node with system add-ons (1 – hydrophone system; 2 – IP camera; 3 – sensor station). The top right image shows the terminator repeater node (1), 60-meter fibre-optical cable and land-based terminator (2). The bottom left image shows an underwater photograph of the repeater after installed. The bottom right image shows the sensor station.

A second fibre-optical cable of 2000 meters with 3 repeaters was installed in Sesimbra, Setubal – Portugal. The same typology of repeater nodes and add-ons was implemented. The nodes were deployed at the bottom of the sea and displaced 500 meters from each other (node 1 at 1000 meters from the

shore, node 2 at 500 meters from node 1 and node 3 at 500 meters from node 2). Figure 118 shows the installation scheme of the system.
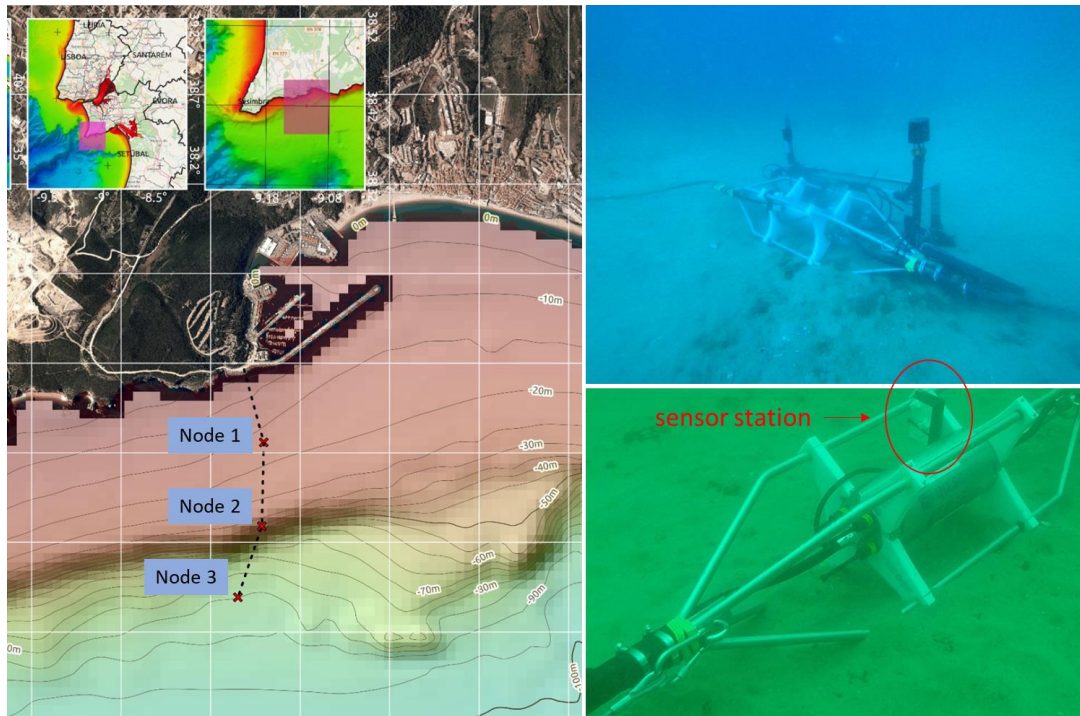

Figure 118. The left image shows the installation scheme of the fibre-optical cable with the developed repeater nodes (38°26'03.2" N 9°06'57.5" W). The top right image shows an underwater photograph of the repeater node 2 with the sensor station and hydrophones. The bottom left image shows an underwater photograph of the repeater node 1 with the sensor station.

A sensor station was built for each one of the repeaters. For standardization, a PCB was designed with a microcontroller based on LQFP-32 STM processors with UART – ETH converter to host commercial and own-developed sensors (electronic schematic available in Supplementary Material I 20 and PCB in Supplementary Material II 20).

The sensor station of node 1 was designed with a turbidity sensor based on the transmitted light detection of the SPM sensor, and MS5837-30BA to measure water temperature and depth. The stations for nodes 2 and 3 were designed with the MS5837-30BA.

The developed microcontroller with STM processor and UART – ETH converter was also used in the core of the repeaters nodes to host Inertial measurement units (IMU), electric current sensor modules, relay drivers and water leak modules.

While the main purpose of the sensor station was the engineering validation of an ethernet system to act as a monitoring station, it provided monitoring information on the tidal cycles and sea wave conditions.

Figure 119 shows an example of the monitoring information from the sensor stations of nodes 1, 2 and 3, on the 10th of September 2023.
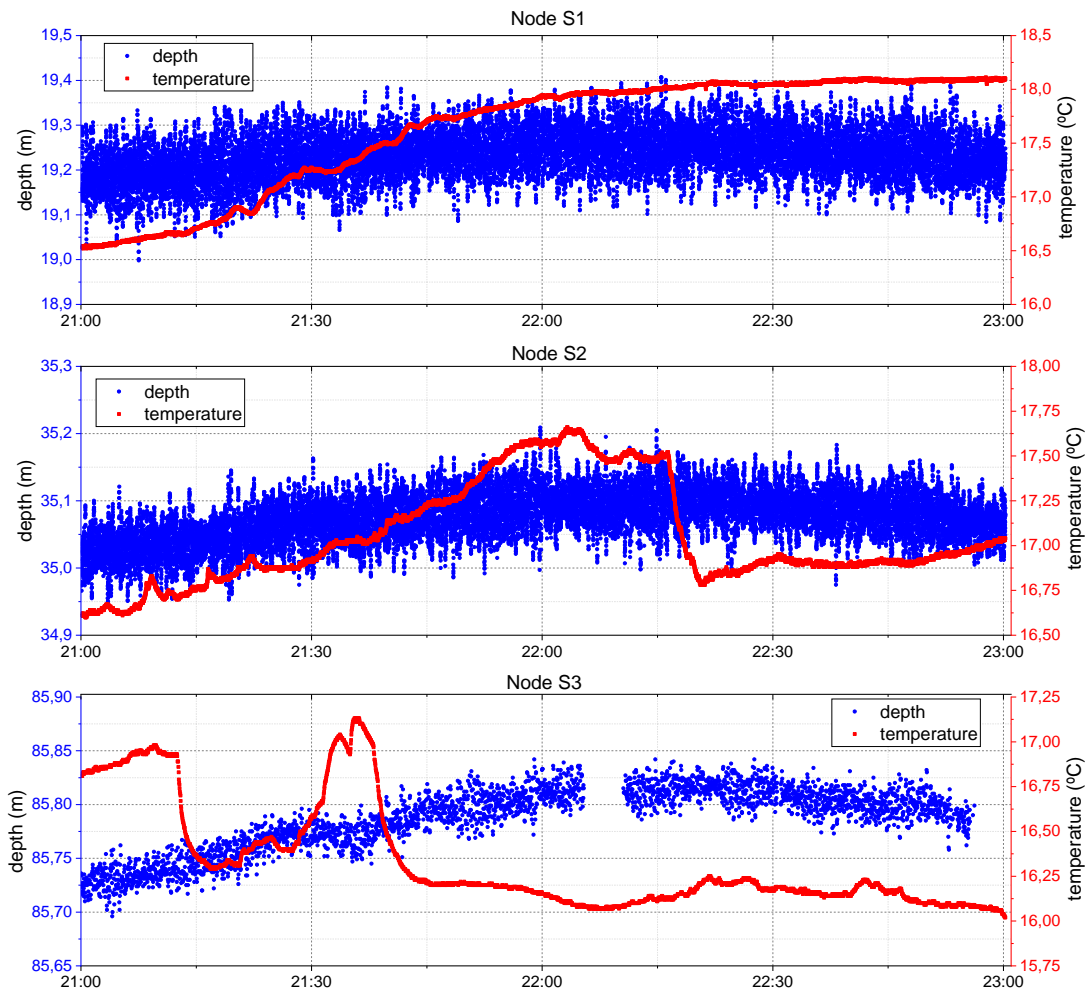

Figure 119. Monitoring results of water temperature and depth from the sensor stations of repeater nodes 1, 2 and 3, on the 10th of September 2023. The depth measurements are shown in blue circles and the water temperature in red squares.

The data shows that the stations were installed at different depths: node 1 at 19 m, node 2 at 35 m and node 3 at 85 m. The measurements show a high-frequency variation that is related to the sea waves and a low-frequency variation related to the tidal cycles (the period of the measurements matches with the peak of the high tide).

The measurements of water temperature show that the region of node 1 is the warmest and node 3 is the coldest. This matches with the gradient of temperature in the ocean since the water temperature decreases with depth. It is also possible to observe abrupt temperature variations in nodes 2 and 3 that can be explained by seashore currents (note that these variations have a small amplitude, less than 0.5° C).

The measurements of depth, when recorded at a high frequency, can be used to monitor sea waves and for beach and seashore management. The top graph of Figure 120 shows the complete tidal cycle, with a tide amplitude of 2.5 m, and an inset of depth records for a period of 5 minutes. The measurements were taken with a sampling period of 300 ms and the data shows that the wave signal is consistently captured. It is possible no analyse the characteristics of the sea waves by applying an FFT to the depth data.

The bottom graph of Figure 120 shows an example of the application of an FFT to the depth data (the depth from 05h00 to 06h00 on the 14th of September 2023 was used for the presented computation). The results show that during the represented time the period of waves had its strongest component on 0.0916 HZ (wave period of 10.91 seconds). The size of the wave can also be calculated if the depth sensor is calibrated in depth for different wave amplitudes as presented by J. L. Rocha *et al.* [217].
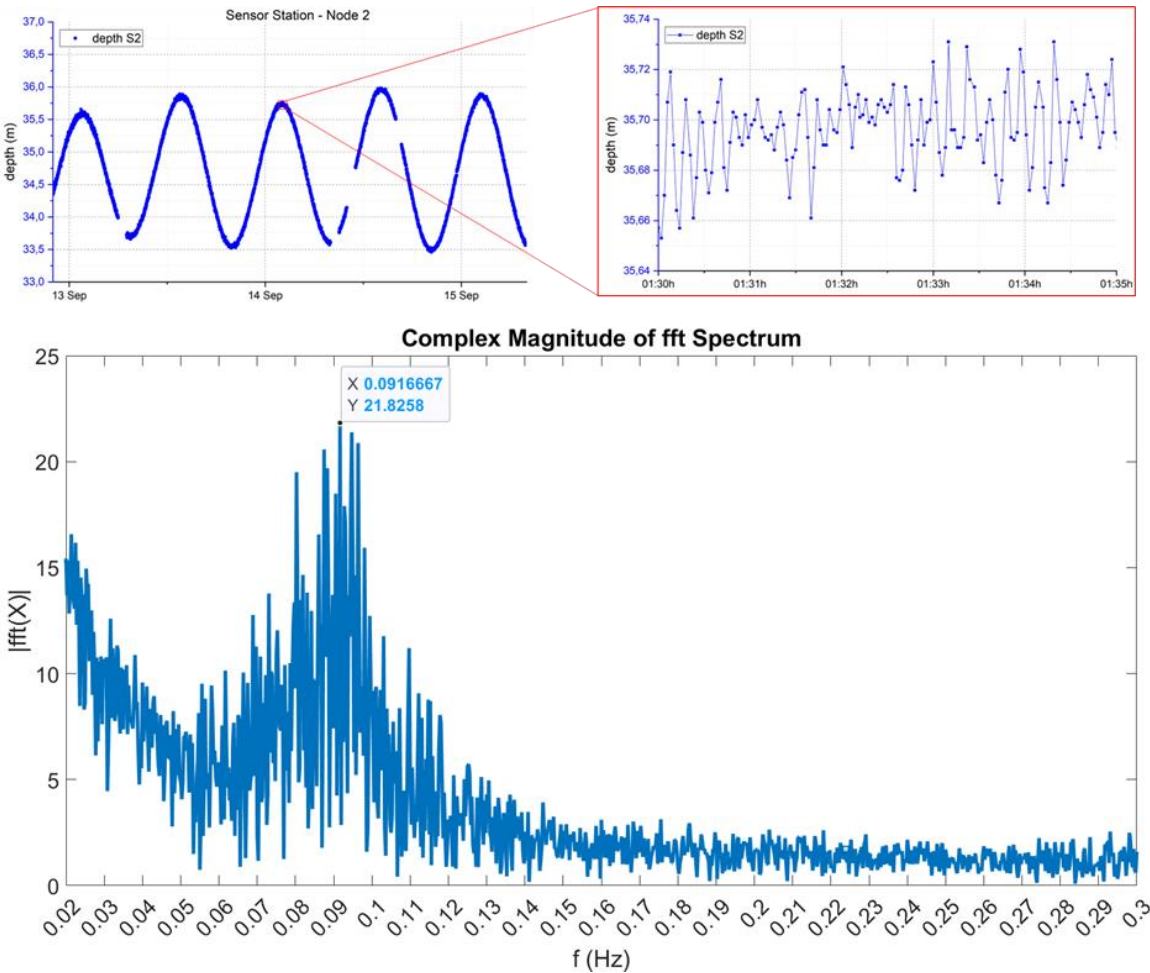

Figure 120. Computation process of the wave period. The top graph shows measurements of water depth, presenting the tidal cycles in low frequency and the sea undulation in high frequency. The bottom graph shows the application of an FFT to calculate the wave period.

On the 13ᵗʰ of September, around 7h29, the terminal node repeater of the fibre-optical cable was lifted from the bottom of the ocean to the surface. This event was not planned and was triggered by an unknown party. It was assumed to be caused by the anchor of a vessel that lifted the fibre-optical structure.

Figure 121 shows the measurements of depth and water temperature of the sensor station and the accelerometer records of the repeater node 3. The data of depth shows that the repeater was submerged at 85 meters and, at 7h30, it was lifted from the streambed up to the surface and then released again into the ocean. The depth information is compliant with the measurements of the accelerometer.

During the lift of the repeater to the surface, the sensor station was able to measure the temperature gradient along the water column. This incident showed the potential of using the MBS5837-30BA to measure the vertical profile of the ocean. This is one of the most important techniques in oceanography to study oceanic currents that uses expensive conductivity-temperature-depth (CTD) sensors [218-219]. The MSB5837-30BA offers two of the three parameters needed.
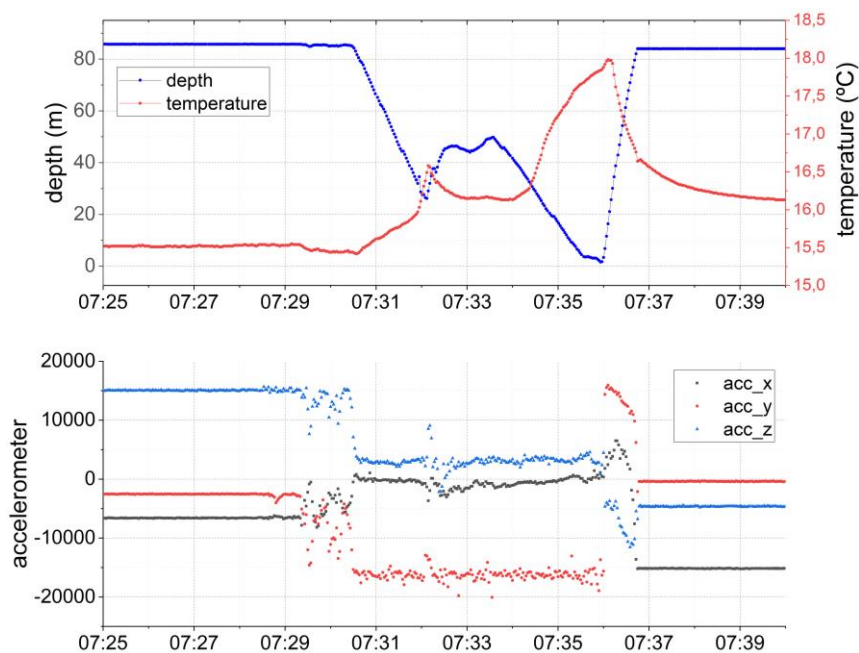

Figure 121. Measurements of water temperature, depth and accelerometer produced by node repeater 3 during its lift to the surface. The top graph shows the depth in blue circles and blue line and the water temperature in red circles and red line. The bottom graph shows the measurements of the 3-axis accelerometer.

6 CONCLUSION

The presented work intended to develop automatic tools to continuously monitor sedimentary processes in marine environments. These processes were decomposed into two branches: sediment transport and sediment deposition and erosion. Different instruments were developed from scratch to monitor water variables associated with these processes. The electric, mechanical and fabrication design and the methodologies of calibration and preparation for *in situ* deployments of each developed sensor were presented so they can be replicated by the scientific community.

The developed technology was built considering important factors to allow replication, scalability and massive deployments (reduced costs); ease of use, transport and installation (reduced size and weight); long-term operation without maintenance (high energy efficiency); and the necessary watertight capabilities for continuous monitoring. Table 5 resumes the main characteristics of the developed sensors.

Table 5. Main characteristics of the developed sensors.

Sensor	Measured variable	Measuring range	Resolution	Power consumption	Materials cost
MS5837-30BA	water temperature depth	-20 to 85 °C 0 to 290 m	0.008 °C 0.2 cm	1.8 µW	8 €
SPM	turbidity sediment concentration organic/inorganic ratio	0 – 4000 NTU 0 – 140 g/L [1] – [2]	– [3] – [3] – [2,3]	400 mW (5 ms) 60 µW (sleep)	20 €
TVP	turbidity sediment concentration organic/inorganic ratio	10 – 4000 NTU – [4] – [2]	– [3] – [3,4] – [2,3]	500 mW (25 ms) 150 µW (sleep)	100 - 150 €
SDE	streambed height	160 mm	5 mm	150 mW (35 ms) 60 µW (sleep)	32 €
Acoustic ToF	water velocity	|v| > 0.1 m/s	0.1 m/s	50 mW (10 ms) 60 µW (sleep)	53 €
SeT	water velocity sediment concentration[5]	-1 – 1 m/s [6] 0 – 4 g/L	≈0.05 m/s [6] ≈0.01 g/L	325 mW (3 ms) 60 µW (sleep)	70 €

[1] Values adopted for the calibration of the sensor
[2] Dependent on the organic matter used for the calibration
[3] Dependent on the light path length and light detection technique adopted
[4] The sensor was not calibrated with seashore sand
[5] Can also measure turbidity if a calibration is established
[6] Dependent on the gain of the instrument amplifier

The first instrument developed was the SPM sensor which was based on the existing technology of optical turbidimeters. The commercial devices available on the market to measure turbidity already provide the necessary measuring ranges and resolution for environmental monitoring, and there is no need for better

performance. However, the prices of said instruments (thousands of euros) are an obstacle to massive use and it was one of the main focuses during the development of the SPM sensor (production cost of 20 € in raw materials). Even if it is not fair to compare commercial prices, which include research, labour work, marketing, etc., with production costs that only include raw materials, it is reasonable to say that the SPM Sensor successfully achieved its objective. It did not outperform the capabilities of the existing commercial instruments, but it was able to deliver data with good quality to be used in environmental monitoring. It is important to notice that the underperformance of the sensor was related to its resolution and ability to measure low turbidity values. This deficit can be overcome by increasing the light path of optical channels (that in turn will reduce the maximum measuring range).

Besides the standard calibration with formazin, the SPM sensor was calibrated with seashore sand. Different particle sizes were used to understand the difficulty of standardizing the suspended concentration units and the interchange of measurements between different instruments. This was an important step to achieve the final goal of estimating sediment transportation and it is a calibration methodology not commonly seen in the literature, that gives preference to turbidity calibrations using formazin solutions.

The SPM sensor was also designed to provide information about the suspended matter compounds using an organic/inorganic (IR/UV) ratio. This technology can be seen as a merge of the particularities of turbidity sensors with chlorophyll sensors but was non-existent as a single sensor in the literature or commercial offer. The methodology for calibration with organic matter was presented so it could be replicated by others.

The TVP sensor was designed to replicate the SPM Sensor, using 8 monitoring nodes to perform the sediment evaluation along the water column. The main objective was to make the instrument scalable so other TVP sensors could be assembled on top of each other to increase the measured length of the vertical profile. After the *in situ* experiments it was realized that the use of multiple TVP sensors was impractical without the existence of a structure to support them. Even if it is an instrument with the potential to be used in fluvial or marine infrastructures (harbours, dams, offshore infrastructures, etc.), it was discarded for simpler environmental studies.

Another disadvantage of the TVP sensor was the price of the underwater cables needed to assemble multiple devices. While the total cost of the instrument is still considered low-cost, the price of the cables is higher than the cost of fabrication of the rest of the sensor. Even if the TVP sensor did not produce a

clear practical improvement, it was the origin of an instrument to measure sediment deposition and erosion.

The SDE sensor was developed to evaluate the process of sediment displacement of the streambed. The sensor measures the sediment deposition and erosion along 160 mm length with 5 mm resolution. The *in situ* experiments confirmed the potential of the instrument that recorded patterns of sediment deposition and resuspension in the bed of the estuary during the low and high tides, abnormal events of streambed erosion during high precipitation days and abnormal sediment deposition during algae bloom phenomena.

The SDE sensor is a fully automated instrument capable of continuously monitoring the sediment height in the streambed of a waterway. While it does not provide qualitative information about the characteristics of the sediment as the mechanical samplers do, it can provide real-time information about the bedform changes. When compared to other automated technologies from the state of the art, the developed instrument was able not only to measure sediment deposition but also streambed erosion. This is an important improvement since previous sensors based on deposition plates are not able to measure events of sediment resuspension. The presented sensor also offers minimal disturbance in the streamflow, is independent of external ambient light and can properly work in high turbidity waters, which is not the case of the PEEP [133] and SED [134] sensors, or the commercial SediMeter from Lincon, Inc., that are considered the current edging automated tools to measure sediment accumulation in field.

The SDE sensor does not require calibration. This is a great advantage compared to the typical oceanographic sensors, which normally require complex and time-consuming laboratory calibrations. The developed instrument is ready to be installed without any prior laboratory analysis. Also, the binary output of the array of optical channels makes the instrument less susceptible to biofouling interference.

The instrument was designed for a maximum measuring length of 160 mm. This range was not sufficient, and the sensor had to be repositioned during the field experiment. The design of the sensor is scalable and setups with different combinations of length and resolution can be built. Considering this, further optimizations should rethink the use of more optical channels to increase the range of the sensor. It is recommended to maintain the 5 mm resolution since it provided good results.

During the tests, the sensor was set to take measurements every 30 minutes. Even though the results are satisfactory, in some periods consecutive measurements presented a difference of 10 mm to 20 mm (higher than the 5 mm resolution), so it is recommended to increase the sampling frequency in future

deployments. Another recommendation is to assemble the sensor into a fixed structure whenever possible (easiest to do when monitoring in infrastructures), to be sure that the sensor is not lifted due to high stream flows.

The reported automated instrument is an improvement of the current state of the art and can be used to deliver real-time data of the bedform changes, providing significant impact in broad applications such as sedimentary studies or managing and planning of fluvial and marine infrastructures affected by silting like dams, harbours or navigation channels, or by scour and other erosion problems in bridges or offshore infrastructures.

The other sedimentary process to measure was sediment transport. With the SPM sensor developed and validated, it was in need the development of an instrument to monitor the water velocity. The initial idea was the development of a 2-axes MEMS biomimetic sensor based on the cupula of blind cavefish. The principle of operation of the device was validated in COMSOL software but its fabrication presented several obstacles. The final design of the sensor did not have the necessary robustness to perform reliable measurements *in situ* and it was discarded.

An acoustic sensor using time-of-flight principles was successfully developed and tested in a real scenario. The instrument showed its potential to measure water velocity in two directions. However, concerns arose about its structure layout that was propitious to the attachment of macro fouling. This characteristic, together with the fact that the sensor itself did not result in an improvement of the state of the art, led to the pursuit of new approaches.

The final instrument to measure sediment transport was achieved with the SeT Sensor that combined in a single instrument a piezoresistive cantilever to measure water velocity, an IR optical channel to measure suspended sediment concentration and the MSB5837-30BA to measure water depth. This instrument is the first of a kind found in the scientific literature that combines these parameters to evaluate sediment transport. The methodologies to calibrate the instrument to both water velocity and suspended sediment concentration were presented.

The instrument was successfully validated *in situ*, measuring the water velocity in two directions during the different phases of tides and the suspended sediment concentration of the estuary. The methodology to use the combination of water velocity, suspended sediment concentration and depth was presented to estimate the water discharge, total volume of water, sediment transport rate and total amount of

sediment. These are the types of data that are missing for environmental studies of watersheds and are needed to support and validate the existing sedimentary computing models.

Finally, biofouling is a problem that affects mostly the performance of optical instruments and has been obstructing long-term monitoring studies with fully automated systems, without the need for pauses in the tests for cleaning, new calibrations, or other maintenance purposes. The scientific community has been focusing attention on this problem and new and innovative technologies have been emerging. However, most of these technologies are still confined to the laboratories and have not been truly applied in real sensors and tested in the field.

Since the monitoring of suspended sediment concentration relies on optical technology, biofouling needed to be addressed. Different anti-biofouling techniques based on materials, coatings and biocides were developed and tested in Vigo, Spain (the high sediment dynamics and mud of the Cávado estuary made it impossible to conduct the experiment in this area). The techniques using copper biocide and chlorine production by the electrolyse of salty water showed the potential to increase the lifetime of the sensor without maintenance. The chlorine probe was designed to produce seawater electrolysis using 1050 μW of electric power, but similar results might be achieved with lower power. Since energy efficiency is a concern for long-term monitoring, the optimal power to protect the instrument against biofouling must be addressed and other energy consumptions must be tested. In addition, even presenting less efficiency than chlorine production, the copper technique should not be discarded, and other structural housings based on copper materials can be tested.

6.1 Future Work

The objective of developing technology to continuously monitor sediment transport and deposition *in situ* was accomplished. The developed instruments showed the necessary measuring range and accuracy to deliver good-quality data about these processes. However, the validation of a sensor is always a concern. How can the user be sure that the delivered data represents the measured variable and is not influenced by any failure of the instrument?

The mistrust about the reliability of sensors, and in particular oceanographic instruments, is not uncommon. Sensors need proper calibration and regular maintenance to ensure accurate data. Oceanographic instruments are exposed to harsh environmental conditions, such as saltwater, extreme temperatures and pressure, which can lead to degradation over time. Biofouling is an even bigger

problem. The environmental processes are open systems and sudden spikes or drops in the data can be easily mistaken by errors produced by the sensor. All these factors combined contribute to a certain degree of uncertainty when using sensors *in situ*.

The developed technologies are low-cost prototypes that by themselves are already an incremental source of uncertainty. The calibrations of the sensors give some confidence about the variables they measure and their accuracy. Even if the real scenarios present additional challenges compared to controlled laboratory environments, it is fair to say that in the first hours, or even days, of monitoring it is not expected a significant drift in the data. During the conducted experiments, the analysis of the measurements was made using environmental information (tides, moon phase, precipitation, temperature, etc.) whenever necessary to explain patterns and events. While this is a needed exercise to fit the data with the external occurrences, it can also lead to wishful thinking. During the installation, maintenance and recovery of the sensors, validation measurements such as photographic records, visual inspections and analysis of the environmental surroundings were used whenever possible. While this is not an optimal scientific approach, it was useful to analyse some events.

The validation of sensors must be discussed and improved so that environmental monitoring can achieve its potential. For the case of the technology presented in this work, the standardization of the fabrication and production, which assures the needed quality control, is the next step to elevate the instruments from simple prototypes assembled by hand to consistent and commercial products. This would increase the reliability and robustness of the instruments, and optimize the methodologies for calibration, installation and maintenance.

The overload of *in situ* experiments, in new locations and different conditions, will also show the real potential of the instruments and increase the trust in their measurements. The redundancy and cross-verification with replicas or "ground-truth" instruments must also be applied (similar experiments as the one conducted in TRATAVE with the SPM and Hatch sensors).

The objective of the conducted field experiments relied solely upon the validation of the instruments. However, the data loggers were developed considering future environmental case studies. The estuary of Cávado is an area in focus and a plan for its monitoring is already on-going. A multiparameter sensor is under development to consolidate in a single instrument the measurements of streambed height (based on the SDE sensor), suspended sediment concentration and organic/inorganic distinguish (using IR and

UV transmitted light channels as in the SPM sensor), depth and water temperature (MS5837-30BA), and salinity and conductivity (based on the sensor of J. L. Rocha, *et al.* [220]).

Figure 122 shows the design of the multiparametric instrument (the electronic schematic is available in Supplementary Material I 18, the printed circuit board in Supplementary Material II 18 and the mechanical drawings in Supplementary Material III 6). The piezoresistive cantilever of the SeT sensor is intended to be assembled in the sensor in the next version of the prototype.
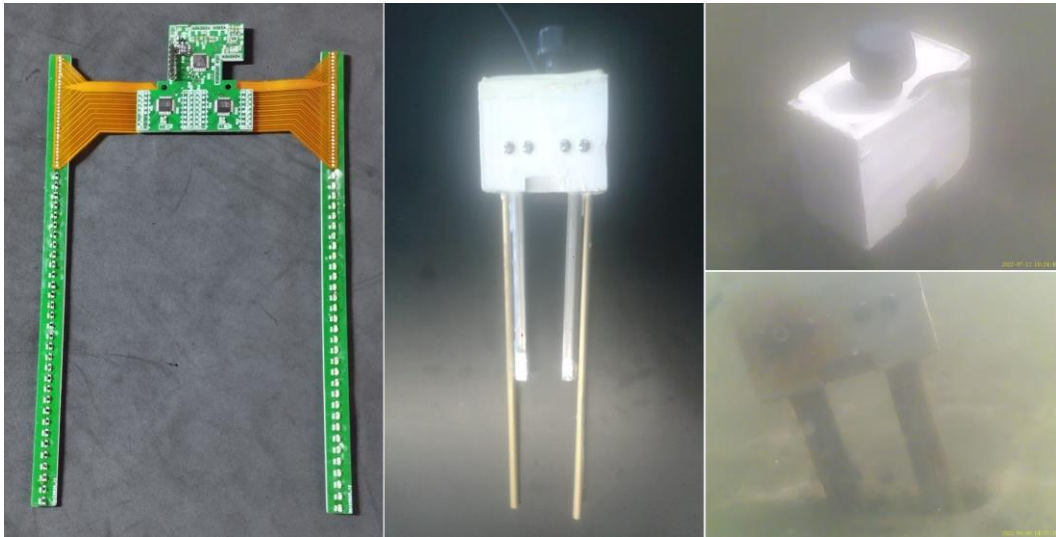
Figure 122. Photographs of the multiparametric instrument. The left image shows the electronics of the device with the PCBs of the optical arrays, instrumentation and processor circuits, and flexible PCBs for the connections. The middle image shows the sensor after fabrication. The right images show the instrument deployed in the estuary of Cávado.

The multiparametric sensor will be installed in 6 locations along 6 km upstream of the Cávado River mouth and connected to data loggers with STM microprocessor, XBee module (RF communications), RTC and SDcard (electronic schematic available in Supplementary Material I 19 and printed circuit board in Supplementary Material II 19). The XBee will provide a synchronized network mesh with the already existing monitoring station acting as a central node (Figure 123). All sensors will wake up at the same time, take the measurements and send it by RF XBee to the central unit which will send the data to the website using the Wi-Fi module of the station. The coverage of the XBee network was already successfully validated (orange arrows of Figure 123).

The network will allow the analysis of the hydraulics dynamics of the estuary in different locations and the synchronism of data will infer the latency of the tidal dynamics along the river to understand how the ocean influences those areas and how far can it reach.

The monitoring network will be installed with the legal consent of Delegação Marítima de Esposende da Capitania do Porto de Viana do Castelo (Supplementary Material IV 3), Instituto da Conservação da Natureza e das Florestas – ICNF (Supplementary Material IV 4), Câmara Municipal de Esposende and remaining institutions and associations (DOCAPESCA, node 2; Clube Náutico de Fão, node 3; Clube Náutico de Gemeses, node 5).

Figure 123. The image at left shows the location of the monitoring station, the 5 new locations of the XBee nodes and in orange arrows the test of XBee network coverage. The image at right shows the data logger housing with an IPV6 waterproof housing, solar panel and RF antenna.

6.2 Scientific Outputs

This Doctoral dissertation contributed to the publishing of 4 manuscripts in Scientific Journals (one more under revision), as the first author:

- **T. Matos**, M.S. Martins, Renato Henriques, L.M. Goncalves, "Design of a sensor to estimate sediment transport in situ using the measurements of water velocity, suspended sediment concentration and depth", Journal of Environmental Management, Elsevier (under revision)

- **T. Matos**, Vânia Pinto, Paulo Sousa, Marcos Martins, Emilio Fernández, Renato Henriques, Luis Miguel Gonçalves, "Design and *In situ* Validation of Low-Cost and Easy to Apply Anti-Biofouling Techniques for Oceanographic Continuous Monitoring with Optical Instruments", Sensors "Marine Sensors: Recent Advances and Challenges, Volume II" 2023, MDPI, DOI: 10.3390/s23020605

- **T. Matos**, J. L. Rocha, C. L. Faria, M. S. Martins, Renato Henriques and L. M. Goncalves, "Development of an automated sensor for in-situ continuous monitoring of streambed sediment height of a waterway", Science of The Total Environment 2021, Elsevier, DOI: 10.1016/j.scitotenv.2021.152164

- **T. Matos**, C. L. Faria, M. S. Martins, Renato Henriques, P. A. Gomes and L. M. Goncalves, "Design of a Multipoint Cost-Effective Optical Instrument for Continuous In-Situ Monitoring of Turbidity and Sediment", Sensors "Physical Sensors" 2020, MDPI, DOI: 10.3390/s20113194

- **T. Matos**, C. L. Faria, M. S. Martins, Renato Henriques, P. A. Gomes and L. M. Goncalves, "Development of a Cost-Effective Optical Sensor for Continuous Monitoring of Turbidity and Suspended Particulate Matter

in Marine Environment", Sensors "Marine Sensors: Recent Advances and Challenges" 2019, MDPI, DOI: 10.3390/s19204439

and 3 articles with oral presentation in Conference Proceedings (one more under revision):

- **T. Matos**, Paulo Sousa, M.S. Martins, Renato Henriques, L.M. Goncalves, "Design, simulation and fabrication of a MEMS biomimetic current meter inspired by the lateral line of the blind cavefish to measure flow in 2 axes", MTS / IEEE OCEANS SINGAPORE 2024 (under revision)

- **Tiago Matos**, Marcos Martins, Alexandra Moutinho, et all., "Synchronous Oceanic and Atmospheric Data Acquisition: field test release and validation of atmospheric, oceanographic, and deep-sea probes in the Azores", MTS / IEEE OCEANS LIMERICK 2023, DOI: 10.1109/OCEANSLimerick52467.2023.10244259

- **T. Matos**, J.L. Rocha, H. Dinis, C. Faria, M.S. Martins, R. Henriques, L.M. Gonçalves, "A low-cost, low-power and low-size multi-parameter station for real-time and online monitoring of the coastal area", MTS / IEEE OCEANS HAMPTON ROADS 2022, DOI: 10.1109/OCEANS47191.2022.9977347

- **T. Matos**, C. Faria, M.S. Martins, R. Henriques, L.M. Gonçalves, "Optical sensor for *in situ* monitoring of suspended particle matter and organic/inorganic distinguish", MTS / IEEE OCEANS MARSEILLE 2019, DOI: 10.1109/OCEANSE.2019.8867080

This work also led to participation in other related publications, where T. Matos is not the first author:

- J.L. Rocha, **Tiago Matos**, C.L. Faria, C.M. Penso, M.S. Martins, P.A. Gomes, L.M. Gonçalves, "Wave Profile and Tide Monitoring System for Scalable Implementation", 2023 IEEE SENSORS, DOI: 10.1109/SENSORS56945.2023.10325051

- Hugo Dinis, João Rocha, **Tiago Matos**, Luís M. Gonçalves, Marcos Martins, "The Challenge of Long-Distance Over-the-Air Wireless Links in the Ocean: A Survey on Water-to-Water and Water-to-Land MIoT Communication", Applied Sciences "Advances in Wireless Communication Technologies" 2022, MDPI, DOI: 10.3390/app12136439

- C. L. Faria, Marcos Martins, **T. Matos**, João Miranda, Rui A. Lima, Luís Gonçalves, "Underwater Energy Harvesting to Extend Operation Time of Submersible Sensors", Sensors "Marine Sensors: Recent Advances and Challenges" 2022, MDPI, DOI: 10.3390/s22041341

- M. S. Martins; Nuno A. Cruz; A. Silva; Bruno Ferreira; Fred Zabel; **Tiago Matos**, et all., "Network nodes for ocean data exchange through submarine fiber optic cable repeaters", MTS / IEEE OCEANS HAMPTON ROADS 2022, DOI: 10.1109/OCEANS47191.2022.9977361

- Luís Araujo, **Tiago Matos**, Jorge Cabral, M. S. Martins, "4-FSK High-Speed Underwater Acoustic Communication System", MTS / IEEE OCEANS LIMERICK 2022, DOI: 10.1109/OCEANSLimerick52467.2023.10244623

- Viveiros, F, **et all.**, "Air quality real-time monitoring during volcanic crises with low-cost sensors: the Cumbre Vieja volcano study case", EGU22 General Assembly, Viena, 2022, DOI: 10.5194/egusphere-egu22-3253

- Pacheco, J, **et all.**, "Low-cost, fast deployment multi-sensor observations of the 2021 Cumbre Vieja eruption", EGU22 General Assembly, Viena, 2022, DOI: 10.5194/egusphere-egu22-8830

- C. Faria, **T. Matos**, M.S. Martins, R.M. Lima, L.M. Miranda, L.M. Gonçalves, "Ocean energy harvesting device for long-term monitoring applications", INEGI 2022

- J.L. Rocha; **T. Matos**; M.S. Martins; S.F. Lopes; P.A. Gomes; R. Henriques; L.M. Gonçalves, "Cost Effective CTD for Long Term Deployments in Water Columns", MTS / IEEE OCEANS SAN DIEGO - PORTO 2021, DOI: 10.23919/OCEANS44145.2021.9705844

- C.L. Faria; M.S. Martins; R. Lima; **T. Matos**; J.M. Miranda; L.M. Gonçalves, "Underwater generator for submersible sensors", MTS / IEEE OCEANS SAN DIEGO - PORTO 2021, DOI: 10.23919/OCEANS44145.2021.9706019

- M. S. Martins, C. L. Faria, **T. Matos**, L. M. Goncalves, J. Cabral, A. Silva, S. M. Jesus, "Wideband and Wide Beam Polyvinylidene Difluoride (PVDF) Acoustic Transducer for Broadband Underwater Communications", Sensors "Marine Sensors: Recent Advances and Challenges" 2019, MDPI, DOI: 10.3390/s19183991

- C.L. Faria, M.S. Martins, **T. Matos**, Rui M. Lima, L.M. Gonçalves, "Optimization of an Electromagnetic Generator for Underwater Energy Harvester", MTS / IEEE OCEANS MARSEILLE 2019, DOI: 10.1109/OCEANSE.2019.8867185

- J.P. Baptista, C.L. Faria, **T. Matos**, Eliana M. F. Vieira, Sérgio F. Lopes, L.M. Gonçalves, "A four-probe salinity sensor optimized for long-term autonomous marine deployments", MTS / IEEE OCEANS MARSEILLE 2019, DOI: 10.1109/OCEANSE.2019.8867544

BIBLIOGRAPHY

[1]   B. J. Boruff, C. Emrich, and S. L. Cutter, "Erosion Hazard Vulnerability of US Coastal Counties," *J. Coast. Res.*, 2005, doi: 10.2112/04-0172.1.

[2]   L. C. Van Rijn, "Coastal erosion and control," *Ocean Coast. Manag.*, vol. 54, no. 12, pp. 867–887, Dec. 2011, doi: 10.1016/j.ocecoaman.2011.05.004.

[3]   A. Aslan, "Sediments," in *Encyclopedia of Quaternary Science: Second Edition*, 2013.

[4]   M. . Langland and T. Cronin, "A summary report of sediment processes in Chesapeake Bay and watershed," *Water-Resources Investig. Rep.*, 2003, doi: 10.1038/130149a0.

[5]   R. G. Wetzel, *Limnology: Lake and River Ecosystems*. 2001.

[6]   R. A. Duller *et al.*, "From grain size to tectonics," *J. Geophys. Res. Earth Surf.*, 2010, doi: 10.1029/2009JF001495.

[7]   J. M. Galloway, D. A. Evans, and W. R. Green, "Comparability of suspended-sediment concentration and total suspended-solids data for two sites on the L'Anguille River, Arkansas, 2001 to 2003," 2005.

[8]   K. Furukawa, E. Wolanski, and H. Mueller, "Currents and sediment transport in mangrove forests," *Estuar. Coast. Shelf Sci.*, 1997, doi: 10.1006/ecss.1996.0120.

[9]   E. J. Hickin, "River geomorphology," *River Geomorphol.*, 1995.

[10]   B. Sellwood, "Applied sedimentology," *Mar. Pet. Geol.*, 2003, doi: 10.1016/0264-8172(90)90042-f.

[11]   W. L. Balsam and J. P. Beeson, "Sea-floor sediment distribution in the Gulf of Mexico," *Deep. Res. Part I Oceanogr. Res. Pap.*, 2003, doi: 10.1016/j.dsr.2003.06.001.

[12]   D. E. Walling and B. W. Webb, "Erosion and sediment yield: a global overview," *Eros. Sediment Yield Glob. Reg. Perspect. Proceeedings Exet. Symp.*, 1996.

[13]   P. G. Griffiths, R. Hereford, and R. H. Webb, "Sediment yield and runoff frequency of small drainage basins in the Mojave Desert, U.S.A," *Geomorphology*, 2006, doi: 10.1016/j.geomorph.2005.07.017.

[14]   P. Wang, Q. Li, and C. F. Li, "Sedimentology," in *Developments in Marine Geology*, 2014.

[15]   K. R. Dyer, "Sediment transport processes in estuaries," *Dev. Sedimentol.*, vol. 53, no. C, pp. 423–449, Jan. 1995, doi: 10.1016/S0070-4571(05)80034-2.

[16]   F. Hjulström, "Studies of the morphological activity of rivers as illustrated by the River Fyris," *Bull. Geol. Inst. Univ. Upsala*, vol. 25, pp. 221–527, 1935.

[17]   S. Dey, "Bed-Load Transport," Springer, Berlin, Heidelberg, 2014, pp. 261–326.

[18]   C. P. Holliday, T. C. Rasmussen, and W. P. Miller, "Establishing the Relationship Between Turbidity and Total Suspended Sediment Concentration," 2003.

[19]   M. Alber, "Settleable and non-settleable suspended sediments in the Ogeechee River Estuary, Georgia, U.S.A.," *Estuar. Coast. Shelf Sci.*, vol. 50, no. 6, pp. 805–816, Jun. 2000, doi: 10.1006/ecss.1999.0610.

[20]   L. Håkanson, "The relationship between salinity, suspended particulate matter and water clarity in aquatic systems," in *Ecological Research*, Jan. 2006, vol. 21, no. 1, pp. 75–90, doi: 10.1007/s11284-005-0098-x.

[21]   A. D. Knighton, "Downstream variation in stream power," *Geomorphology*, 1999, doi: 10.1016/S0169-555X(99)00015-X.

[22]   C. D. Guzman, S. A. Tilahun, A. D. Zegeye, and T. S. Steenhuis, "Suspended sediment concentration-

discharge relationships in the (sub-) humid Ethiopian highlands," *Hydrol. Earth Syst. Sci.*, 2013, doi: 10.5194/hess-17-1067-2013.

[23]   M. A. Allison, C. A. Nittrouer, and G. C. Kineke, "Seasonal sediment storage on mudflats adjacent to the Amazon River," *Mar. Geol.*, 1995, doi: 10.1016/0025-3227(95)00017-S.

[24]   J. P. Michaud, "Citizens' guide to Understanding and Monitoring Lakes and Streams," *Washington State Department of Ecology - Department of Ecology Publications Office*, 1991.

[25]   G. M. Kondolf *et al.*, "Sustainable sediment management in reservoirs and regulated rivers: Experiences from five continents," *Earth's Futur.*, 2014, doi: 10.1002/2013ef000184.

[26]   E. H. Stanley, M. A. Luebke, M. W. Doyle, and D. W. Marshall, "Short-Term Changes in Channel Form and Macroinvertebrate Communities Following Low-Head Dam Removal," *J. North Am. Benthol. Soc.*, 2002, doi: 10.2307/1468307.

[27]   P. Ruggiero and W. G. McDougal, "An analytic model for the prediction on wave setup, longshore currents and sediment transport on beaches with seawalls," *Coast. Eng.*, 2001, doi: 10.1016/S0378-3839(01)00012-6.

[28]   W. M. R. Wan Hussin, K. M. Cooper, C. R. S. B. Froján, E. C. Defew, and D. M. Paterson, "Impacts of physical disturbance on the recovery of a macrofaunal community: A comparative analysis using traditional and novel approaches," *Ecol. Indic.*, 2012, doi: 10.1016/j.ecolind.2011.03.016.

[29]   V. Rachold *et al.*, "Coastal erosion vs riverline sediment discharge in the Arctic shelfx seas," *Int. J. Earth Sci.*, vol. 89, no. 3, pp. 450–460, 2000, doi: 10.1007/s005310000113.

[30]   V. Chazottes, J. J. G. Reijmer, and E. Cordier, "Sediment characteristics in reef areas influenced by eutrophication-related alterations of benthic communities and bioerosion processes," *Mar. Geol.*, vol. 250, no. 1–2, pp. 114–127, Apr. 2008, doi: 10.1016/j.margeo.2008.01.002.

[31]   M. R. Palermo, P. R. Schroeder, T. J. Estes, N. R. Francingues, and N. R. F. September, "Technical Guidelines for Environmental Dredging of Contaminated Sediments," 2008.

[32]   S. Hess, A. S. Wenger, T. D. Ainsworth, and J. L. Rummer, "Exposure of clownfish larvae to suspended sediment levels found on the Great Barrier Reef: Impacts on gill structure and microbiome," *Sci. Rep.*, 2015, doi: 10.1038/srep10561.

[33]   D. S. Marszalek, "Impact of dredging on a subtropical reef community, Southeast Florida, USA," 1981.

[34]   ADEM, "Nutrient Total Maximum Daily Loads (TMDLs) for the Cahaba River Watershed," *Development*, 2006.

[35]   D. W. Meals, J. B. Harcum, and S. A. Dressing, "Monitoring for Microbial Pathogens and Indicators," *TechNotes*, 2013.

[36]   A. Shirmohammadi *et al.*, "Uncertainty in TMDL models," *Transactions of the ASABE*. 2006.

[37]   J. W. Barko, D. Gunnison, and S. R. Carpenter, "Sediment interactions with submersed macrophyte growth and community dynamics," *Aquat. Bot.*, vol. 41, no. 1–3, pp. 41–65, Jan. 1991, doi: 10.1016/0304-3770(91)90038-7.

[38]   S. Tuckerman and B. Zawiski, "Case Studies of Dam Removal and TMDLs: Process and Results," *J. Great Lakes Res.*, vol. 33, pp. 103–116, Jan. 2007, doi: 10.3394/0380-1330(2007)33[103:CSODRA]2.0.CO;2.

[39]   C. A. Omuombo, D. O. Olago, and E. O. Odada, "Coastal Erosion," in *Developments in Earth Surface Processes*, 2013.

[40]   U.S. Environmental Protection Agency, "Contaminated sediment remediation guidance for hazardous waste sites," 2005.

[41]   M. R. Palermo, P. R. Schroeder, T. J. Estes, N. R. Francingues, and N. R. F. September, "tabla de

contenidos del Technical Guidelines for Environmental Dredging of Contaminated Sediments," 2008.

[42] P. F. Lagasse, J. D. Schall, and E. V. Richardson, "Stream Stability at Highway Structures," *Hydraulic Engineering*. 2001.

[43] L. a. Arneson, L. W. Zevenbergen, P. F. Lagasse, and P. E. Clopper, "Evaluating Scour at Bridges Fifth Edition," 2012.

[44] M. W. Schmeeckle and M. W. Schmeeckle, "Numerical simulation of turbulence and sediment transport of medium sand," *J. Geophys. Res. Earth Surf.*, vol. 119, no. 6, pp. 1240–1262, Jun. 2014, doi: 10.1002/2013JF002911.

[45] C. C. Kiat, A. A. Ghani, R. Abdullah, and N. A. Zakaria, "Sediment transport modeling for Kulim River – A case study," *J. Hydro-environment Res.*, vol. 2, no. 1, pp. 47–59, Sep. 2008, doi: 10.1016/J.JHER.2008.04.002.

[46] J. G. Duan and S. K. Nanda, "Two-dimensional depth-averaged model simulation of suspended sediment concentration distribution in a groyne field," *J. Hydrol.*, vol. 327, no. 3–4, pp. 426–437, Aug. 2006, doi: 10.1016/J.JHYDROL.2005.11.055.

[47] Yanto and M. Dimyati, "Development, implementation and validation of Sediment Transport and Erosion Prediction (STEP) model," *Environ. Model. Softw.*, vol. 164, p. 105686, Jun. 2023, doi: 10.1016/J.ENVSOFT.2023.105686.

[48] P. Zheng *et al.*, "Development, calibration and validation of a phase-averaged model for cross-shore sediment transport and morphodynamics on a barred beach," *Cont. Shelf Res.*, vol. 258, p. 104989, Apr. 2023, doi: 10.1016/J.CSR.2023.104989.

[49] A. (Thanos) N. Papanicolaou, M. Elhakeem, G. Krallis, S. Prakash, and J. Edinger, "Sediment Transport Modeling Review—Current and Future Developments," *J. Hydraul. Eng.*, vol. 134, no. 1, pp. 1–14, Jan. 2008, doi: 10.1061/(ASCE)0733-9429(2008)134:1(1)/ASSET/36E9167D-03E8-40BF-A4C9-304F21B4BD37/ASSETS/(ASCE)0733-9429(2008)134:1(1).FP.PNG.

[50] J. Southard, "Threshold of Movement," *Spec. Top. An Introd. to Fluid Motions, Sediment Transp. Curr. Sediment. Struct.*, 2006.

[51] T. Crone, "The Basic Sediment Transport Equations Made Ridiculously Simple," 2004.

[52] S. a Shearer, "Fluid Mechanics : Stokes ' Law and Viscosity," *Biosyst. Agric. Eng.*, 2011.

[53] N. D. Pope, J. Widdows, and M. D. Brinsley, "Estimation of bed shear stress using the turbulent kinetic energy approach-A comparison of annular flume and field data," *Cont. Shelf Res.*, 2006, doi: 10.1016/j.csr.2006.02.010.

[54] T. von Karman, "Progress in the Statistical Theory of Turbulence," *Proc. Natl. Acad. Sci.*, 1948, doi: 10.1073/pnas.34.11.530.

[55] C. M. Weaver and G. F. S. Wiggs, "Field measurements of mean and turbulent airflow over a barchan sand dune," *Geomorphology*, 2011, doi: 10.1016/j.geomorph.2010.12.020.

[56] L. C. van Rijn, "Sediment transport, part I: Bed load transport," *J. Hydraul. Eng.*, 1984, doi: 10.1061/(ASCE)0733-9429(1984)110:10(1431).

[57] L. C. van Rijn, "Sediment transport, part II: Suspended load transport," *J. Hydraul. Eng.*, 1984, doi: 10.1061/(ASCE)0733-9429(1984)110:11(1613).

[58] Breu, Fx, Guggenbichler, S, Wollmann, and Jc, "Total Suspended Solids," *Vasa*, 2008.

[59] "Turbidity Measurement." http://www.tuner.tw/OMEGA CD/zsection/TURBIDIT.PDF (accessed Jan. 17, 2017).

[60] G. Johnson *et al.*, "Turbidity TMDL Protocols and Submittal Requirements," no. January, 2006.

[61]   R. W. Preisendorfer, "Secchi disk science: Visual optics of natural waters," *Limnol. Oceanogr.*, 1986, doi: 10.4319/lo.1986.31.5.0909.

[62]   T. J. B. Carruthers, B. J. Longstaff, W. C. Dennison, E. G. Abal, and K. Aioi, "Measurement of light penetration in relation to seagrass," *Glob. Seagrass Res. Methods*, pp. 369–392, Jan. 2001, doi: 10.1016/B978-044450891-1/50020-7.

[63]   R. W. Holmes, "The Secchi disk in turbid coastal waters," *Limnol. Oceanogr.*, vol. 15, no. 2, pp. 688–694, 1970, doi: 10.4319/lo.1970.15.5.0688.

[64]   USEPA, "Method 180.1: Determination of Turbidity by Nephelometry," 1993.

[65]   "Measuring Turbidity, TSS, and Water Clarity - Environmental Measurement Systems." http://www.fondriest.com/environmental-measurements/equipment/measuring-water-quality/turbidity-sensors-meters-and-methods/ (accessed Jan. 15, 2017).

[66]   A. Public Health Association, "APHA Method 2130: Standard Methods for the Examination of Water and Wastewater."

[67]   Standard Methods for Examination of Water and Wastewater, "Standard Methods for Examination of Water and Wastewater." .

[68]   International Organization for Standardization, *WATER QUALITY – DETERMINATION OF TURBIDITY – PART 1: QUANTITATIVE METHODS*. 2016.

[69]   Great Lakes Instruments, "Turbidity Gli Method 2," 1992, [Online]. Available: https://law.resource.org/pub/us/cfr/ibr/004/gli.method.2.2009.pdf.

[70]   Hach Company, "Hach Method 10133 - Determination of Turbidty by Laser Nephelometry."

[71]   P. L. Mitchell and L. Mitchell, "Determination of Turbidity by Laser Nephelometry - Mitchell Method M5271," 2009.

[72]   Thermo Fisher Scientific, "Determination of Turbidity by LED Nephelometry - Thermo Scientific Orion Method AQ4500," 2009.

[73]   SWAN Analytische Instrumente AG, "Continuous Measurement of Turbidity Using a SWAN AMI Turbiwell Turbidimeter," 2009.

[74]   G. Xu, W. Shen, and X. Wang, "Applications of Wireless Sensor Networks in Marine Environment Monitoring: A Survey," *Sensors 2014, Vol. 14, Pages 16932-16954*, vol. 14, no. 9, pp. 16932–16954, Sep. 2014, doi: 10.3390/S140916932.

[75]   T. Duckey, M. Lewis, and G. Chang, "Optical oceanography: Recent advances and future directions using global remote sensing and in situ observations," *Rev. Geophys.*, vol. 44, no. 1, Mar. 2006, doi: 10.1029/2003RG000148.

[76]   Y. Wang, S. M. S. M. Rajib, C. Collins, and B. Grieve, "Low-Cost Turbidity Sensor for Low-Power Wireless Monitoring of Fresh-Water Courses," *IEEE Sens. J.*, vol. 18, no. 11, pp. 4689–4696, Jun. 2018, doi: 10.1109/JSEN.2018.2826778.

[77]   C. D. Fay and A. Nattestad, "Advances in Optical Based Turbidity Sensing Using LED Photometry (PEDD)," *Sensors 2022, Vol. 22, Page 254*, vol. 22, no. 1, p. 254, Dec. 2021, doi: 10.3390/S22010254.

[78]   D. Gillett and A. Marchiori, "A Low-Cost Continuous Turbidity Monitor," *Sensors 2019, Vol. 19, Page 3039*, vol. 19, no. 14, p. 3039, Jul. 2019, doi: 10.3390/S19143039.

[79]   M. Metzger *et al.*, "Low-Cost GRIN-Lens-Based Nephelometric Turbidity Sensing in the Range of 0.1–1000 NTU," *Sensors 2018, Vol. 18, Page 1115*, vol. 18, no. 4, p. 1115, Apr. 2018, doi: 10.3390/S18041115.

[80]   W. D. Kirkey, J. S. Bonner, and C. B. Fuller, "Low-Cost Submersible Turbidity Sensors Using Low-Frequency Source Light Modulation," *IEEE Sens. J.*, vol. 18, no. 22, pp. 9151–9162, Nov. 2018, doi:

10.1109/JSEN.2018.2869368.

[81]   J. Droujko and P. Molnar, "Open-source, low-cost, in-situ turbidity sensor for river network monitoring," *Sci. Reports I*, vol. 12, p. 10341, 123AD, doi: 10.1038/s41598-022-14228-4.

[82]   A. A. Azman, M. H. F. Rahiman, M. N. Taib, N. H. Sidek, I. A. Abu Bakar, and M. F. Ali, "A low cost nephelometric turbidity sensor for continual domestic water quality monitoring system," *Proc. - 2016 IEEE Int. Conf. Autom. Control Intell. Syst. I2CACIS 2016*, pp. 202–207, Mar. 2017, doi: 10.1109/I2CACIS.2016.7885315.

[83]   L. Parra, J. Rocher, J. Escrivá, and J. Lloret, "Design and development of low cost smart turbidity sensor for water quality monitoring in fish farms," *Aquac. Eng.*, vol. 81, pp. 10–18, May 2018, doi: 10.1016/j.aquaeng.2018.01.004.

[84]   a Lohrmann and a Calibration, "Monitoring sediment concentration with acoustic backscattering instruments," *Nortek AS*, vol. 3, no. I, pp. 1–5, 2001, [Online]. Available: http://scholar.google.com/scholar?hl=en&btnG=Search&q=intitle:Monitoring+Sediment+Concentration+with+acoustic+backscattering+instruments#0.

[85]   A. M. Crawford and A. E. Hay, "Determining suspended sand size and concentration from multifrequency acoustic backscatter," *J. Acoust. Soc. Am.*, 1993, doi: 10.1121/1.407237.

[86]   Y. H. Kim and G. Voulgaris, "Estimation of supsended sediment concentration in estuarine environmetns using Acoustic Backscatter from an ADCP," *Proc. Coast. Sediment 03*, 2003, doi: 10.1121/1.397061.

[87]   H. M. Manik, "Measuring acoustic backscattering strength of underwater target using high frequency sonar," *Proc. 2013 3rd Int. Conf. Instrumentation, Commun. Inf. Technol., Biomed. Eng. Sci. Technol. Improv. Heal. Safety, Environ., ICICI-BME 2013*, pp. 381–384, 2013, doi: 10.1109/ICICI-BME.2013.6698529.

[88]   A. Tonge, J. Bux, D. Cowell, J. Peakall, S. Freear, and T. Hunter, "Concentration profiling using a novel acoustic backscatter system with single transducers pulsed at multiple frequencies," *IEEE Int. Ultrason. Symp. IUS*, Oct. 2017, doi: 10.1109/ULTSYM.2017.8092880.

[89]   P. D. Thorne, C. E. Vincent, P. J. Hardcastle, S. Rehman, and N. Pearson, "Measuring suspended sediment concentrations using acoustic backscatter devices," *Mar. Geol.*, vol. 98, no. 1, pp. 7–16, 1991, doi: 10.1016/0025-3227(91)90031-X.

[90]   T. K. Chereskin, "ADCP measurement techniques." http://tryfan.ucsd.edu/adcp/adcp.htm (accessed Jan. 10, 2017).

[91]   A. N. Gorban', A. M. Gorlov, and V. M. Silantyev, "Limits of the Turbine Efficiency for Free Fluid Flow," *J. Energy Resour. Technol.*, vol. 123, no. 4, pp. 311–317, Dec. 2001, doi: 10.1115/1.1414137.

[92]   L. C. Lynnworth and Y. Liu, "Ultrasonic flowmeters: Half-century progress report, 1955–2005," *Ultrasonics*, vol. 44, no. SUPPL., pp. e1371–e1378, Dec. 2006, doi: 10.1016/J.ULTRAS.2006.05.046.

[93]   F. Suñol, D. A. Ochoa, and J. E. Garcia, "High-Precision Time-of-Flight Determination Algorithm for Ultrasonic Flow Measurement," *IEEE Trans. Instrum. Meas.*, vol. 68, no. 8, pp. 2724–2732, Aug. 2019, doi: 10.1109/TIM.2018.2869263.

[94]   G. Rajita and N. Mandal, "Review on transit time ultrasonic flowmeter," *2016 2nd Int. Conf. Control. Instrumentation, Energy Commun. CIEC 2016*, pp. 88–92, Jul. 2016, doi: 10.1109/CIEC.2016.7513740.

[95]   F. Ejeian *et al.*, "Design and applications of MEMS flow sensors: A review," *Sensors Actuators A Phys.*, vol. 295, pp. 483–502, Aug. 2019, doi: 10.1016/J.SNA.2019.06.020.

[96]   J. T. W. Kuo, L. Yu, and E. Meng, "Micromachined Thermal Flow Sensors—A Review," *Micromachines 2012, Vol. 3, Pages 550-573*, vol. 3, no. 3, pp. 550–573, Jul. 2012, doi: 10.3390/MI3030550.

[97]   C. H. Wu, D. Kang, P. H. Chen, and Y. C. Tai, "MEMS thermal flow sensors," *Sensors Actuators A Phys.*,

vol. 241, pp. 135–144, Apr. 2016, doi: 10.1016/J.SNA.2016.02.018.

[98] W. Xu, X. Wang, Y. Chiu, and Y. K. Lee, "High Sensitivity and Wide Dynamic Range Thermoresistive Micro Calorimetric Flow Sensor with CMOS MEMS Technology," *IEEE Sens. J.*, vol. 20, no. 8, pp. 4104–4111, Apr. 2020, doi: 10.1109/JSEN.2019.2961948.

[99] W. Xu, B. Wang, M. Duan, M. Ahmed, A. Bermak, and Y. K. Lee, "A Three-Dimensional Integrated Micro Calorimetric Flow Sensor in CMOS MEMS Technology," *IEEE Sensors Lett.*, vol. 3, no. 2, Feb. 2019, doi: 10.1109/LSENS.2019.2893151.

[100] L. Huang, "Micromachined Thermal Time-of-Flight Flow Sensors and Their Applications," *Micromachines 2022, Vol. 13, Page 1729*, vol. 13, no. 10, p. 1729, Oct. 2022, doi: 10.3390/MI13101729.

[101] A. S. Fiorillo, C. D. Critello, and A. S. Pullano, "Theory, technology and applications of piezoresistive sensors: A review," *Sensors Actuators A Phys.*, vol. 281, pp. 156–175, Oct. 2018, doi: 10.1016/J.SNA.2018.07.006.

[102] P. Sharma, J. F. Motte, F. Fournel, B. Cross, E. Charlaix, and C. Picard, "A Direct Sensor to Measure Minute Liquid Flow Rates," *Nano Lett.*, vol. 18, no. 9, pp. 5726–5730, Sep. 2018, doi: 10.1021/ACS.NANOLETT.8B02332/SUPPL_FILE/NL8B02332_SI_001.PDF.

[103] Q. Zhang, W. Ruan, H. Wang, Y. Zhou, Z. Wang, and L. Liu, "A self-bended piezoresistive microcantilever flow sensor for low flow rate measurement," *Sensors Actuators A Phys.*, vol. 158, no. 2, pp. 273–279, Mar. 2010, doi: 10.1016/J.SNA.2010.02.002.

[104] Y. H. Wang, C. Y. Lee, and C. M. Chiang, "A MEMS-based Air Flow Sensor with a Free-standing Micro-cantilever Structure," *Sensors 2007, Vol. 7, Pages 2389-2401*, vol. 7, no. 10, pp. 2389–2401, Oct. 2007, doi: 10.3390/S7102389.

[105] J. E. Dusek, M. S. Triantafyllou, and J. H. Lang, "Piezoresistive foam sensor arrays for marine applications," *Sensors Actuators A Phys.*, vol. 248, pp. 173–183, Sep. 2016, doi: 10.1016/J.SNA.2016.07.025.

[106] H. Devaraj *et al.*, "Bio-inspired flow sensor from printed PEDOT:PSS micro-hairs," *Bioinspir. Biomim.*, vol. 10, no. 1, p. 016017, Feb. 2015, doi: 10.1088/1748-3190/10/1/016017.

[107] A. G. P. Kottapalli, M. Bora, M. Asadnia, J. Miao, S. S. Venkatraman, and M. Triantafyllou, "Nanofibril scaffold assisted MEMS artificial hydrogel neuromasts for enhanced sensitivity flow sensing," *Sci. Reports 2016 61*, vol. 6, no. 1, pp. 1–12, Jan. 2016, doi: 10.1038/srep19336.

[108] E. Kanhere *et al.*, "Crocodile-inspired dome-shaped pressure receptors for passive hydrodynamic sensing," *Bioinspir. Biomim.*, vol. 11, no. 5, p. 056007, Aug. 2016, doi: 10.1088/1748-3190/11/5/056007.

[109] H. Bleckmann and R. Zelick, "Lateral line system of fish," *Integr. Zool.*, vol. 4, no. 1, pp. 13–25, Mar. 2009, doi: 10.1111/J.1749-4877.2008.00131.X.

[110] J. F. Webb, J. C. Montgomery, and J. Mogdans, "Bioacoustics and the Lateral Line System of Fishes," *Fish Bioacoustics*, pp. 145–182, Apr. 2008, doi: 10.1007/978-0-387-73029-5_5.

[111] H. Hu, C. Liu, and N. Chen, "A robust tactile shear stress sensor derived from a bio-inspired artificial haircell sensor," *Proc. IEEE Sensors*, pp. 1517–1519, 2008, doi: 10.1109/ICSENS.2008.4716735.

[112] N. Chen, C. Tucker, J. M. Engel, Y. Yang, S. Pandya, and C. Liu, "Design and characterization of artificial haircell sensor for flow sensing with ultrahigh velocity and angular sensitivity," *J. Microelectromechanical Syst.*, vol. 16, no. 5, pp. 999–1014, Oct. 2007, doi: 10.1109/JMEMS.2007.902436.

[113] Y. Yang, N. Chen, C. Tucker, J. Engel, S. Pandya, and C. Liu, "From artificial hair cell sensor to artificial lateral line system: Development and application," *Proc. IEEE Int. Conf. Micro Electro Mech. Syst.*, pp. 577–580, 2007, doi: 10.1109/MEMSYS.2007.4432986.

[114] A. G. P. Kottapalli, M. Asadnia, J. M. Miao, G. Barbastathis, and M. S. Triantafyllou, "A flexible liquid crystal polymer MEMS pressure sensor array for fish-like underwater sensing," *Smart Mater. Struct.*, vol. 21, no.

11, p. 115030, Oct. 2012, doi: 10.1088/0964-1726/21/11/115030.

[115]   A. G. P. Kottapalli, M. Asadnia, J. Miao, and M. Triantafyllou, "Soft polymer membrane micro-sensor arrays inspired by the mechanosensory lateral line on the blind cavefish," *http://dx.doi.org/10.1177/1045389X14521702*, vol. 26, no. 1, pp. 38–46, Feb. 2014, doi: 10.1177/1045389X14521702.

[116]   V. I. Fernandez, S. M. Hou, F. S. Hover, J. H. Lang, and M. S. Triantafyllou, "Lateral-Line Inspired MEMS-Array Pressure Sensing for Passive Underwater Navigation," 2007, Accessed: Feb. 12, 2023. [Online]. Available: https://dspace.mit.edu/handle/1721.1/97026.

[117]   M. Asadnia *et al.*, "From Biological Cilia to Artificial Flow Sensors: Biomimetic Soft Polymer Nanosensors with High Sensing Performance," *Sci. Reports 2016 61*, vol. 6, no. 1, pp. 1–13, Sep. 2016, doi: 10.1038/srep32955.

[118]   A. G. P. Kottapalli *et al.*, "Engineering biomimetic hair bundle sensors for underwater sensing applications," *AIP Conf. Proc.*, vol. 1965, no. 1, p. 160003, May 2018, doi: 10.1063/1.5038533.

[119]   M. Olfatnia, T. Xu, J. M. Miao, L. S. Ong, X. M. Jing, and L. Norford, "Piezoelectric circular microdiaphragm based pressure sensors," *Sensors Actuators A Phys.*, vol. 163, no. 1, pp. 32–36, Sep. 2010, doi: 10.1016/J.SNA.2010.06.016.

[120]   X. Guo, B. Yang, Q. H. Wang, C. F. Lu, and D. Hu, "Design and Characterization of a Novel Bio-inspired Hair Flow Sensor Based on Resonant Sensing," *J. Phys. Conf. Ser.*, vol. 986, no. 1, p. 012005, Mar. 2018, doi: 10.1088/1742-6596/986/1/012005.

[121]   W. Y. Chang, C. H. Chu, and Y. C. Lin, "A flexible piezoelectric sensor for microfluidic applications using polyvinylidene fluoride," *IEEE Sens. J.*, vol. 8, no. 5, pp. 495–500, May 2008, doi: 10.1109/JSEN.2008.918749.

[122]   D. Sengupta *et al.*, "Characterization of single polyvinylidene fluoride (PVDF) nanofiber for flow sensing applications," *AIP Adv.*, vol. 7, no. 10, p. 105205, Oct. 2017, doi: 10.1063/1.4994968.

[123]   S. R. Anton and H. A. Sodano, "A review of power harvesting using piezoelectric materials (2003–2006)," *Smart Mater. Struct.*, vol. 16, no. 3, p. R1, May 2007, doi: 10.1088/0964-1726/16/3/R01.

[124]   O. Aminoroayaie Yamini, S. H. Mousavi, M. R. Kavianpour, and A. Movahedi, "Numerical modeling of sediment scouring phenomenon around the offshore wind turbine pile in marine environment," *Environ. Earth Sci. 2018 7723*, vol. 77, no. 23, pp. 1–15, Nov. 2018, doi: 10.1007/S12665-018-7967-4.

[125]   L. Håkanson, S. Floderus, and M. Wallin, "Sediment trap assemblages - a methodological description," *Hydrobiologia*, vol. 176–177, no. 1, pp. 481–490, Jul. 1989, doi: 10.1007/BF00026583.

[126]   C. D. Storlazzi, M. E. Field, and M. H. Bothner, "The use (and misuse) of sediment traps in coral reef environments: Theory, observations, and suggested protocols," *Coral Reefs*, vol. 30, no. 1, pp. 23–38, Mar. 2011, doi: 10.1007/s00338-010-0705-3.

[127]   P. V. Ridd, "A sediment level sensor for erosion and siltation detection," *Estuar. Coast. Shelf Sci.*, vol. 35, no. 4, pp. 353–362, Oct. 1992, doi: 10.1016/S0272-7714(05)80032-0.

[128]   F. De Rooij, S. B. Dalziel, and P. F. Linden, "Electrical measurement of sediment layer thickness under suspension flows," *Exp. Fluids*, vol. 26, no. 5, pp. 470–474, 1999, doi: 10.1007/s003480050311.

[129]   G. Arnaud, M. Mory, S. Abadie, and M. Cassen, "Use of a resistive rods network to monitor bathymetric evolution in the surf/swash zone.," in *Journal of Coastal Research*, 2009, no. SPEC. ISSUE 56, pp. 1781–1785.

[130]   S. Thomas and P. Ridd, "Field assessment of innovative sensor for monitoring of sediment accumulation at inshore coral reefs," in *Marine Pollution Bulletin*, Jan. 2005, vol. 51, no. 1–4, pp. 470–480, doi: 10.1016/j.marpolbul.2004.10.026.

[131]   P. Ridd *et al.*, "Measurement of sediment deposition rates using an optical backscatter sensor," *Estuar. Coast. Shelf Sci.*, vol. 52, no. 2, pp. 155–163, Feb. 2001, doi: 10.1006/ecss.2000.0635.

[132]   J. Whinney, R. Jones, A. Duckworth, and P. Ridd, "Continuous in situ monitoring of sediment deposition in shallow benthic environments," *Coral Reefs*, vol. 36, no. 2, pp. 521–533, Jun. 2017, doi: 10.1007/s00338-016-1536-7.

[133]   D. M. Lawler, "A New Technique for the Automatic Monitoring of Erosion and Deposition Rates," *Water Resour. Res.*, vol. 27, no. 8, pp. 2125–2128, 1991, doi: 10.1029/91WR01191.

[134]   Z. Hu, W. Lenting, D. van der Wal, and T. J. Bouma, "Continuous monitoring bed-level dynamics on an intertidal flat: Introducing novel, stand-alone high-resolution SED-sensors," *Geomorphology*, vol. 245, pp. 223–230, Sep. 2015, doi: 10.1016/j.geomorph.2015.05.027.

[135]   D. M. Lawler, "Advances in the continuous monitoring of erosion and deposition dynamics: Developments and applications of the new PEEP-3T system," *Geomorphology*, vol. 93, no. 1–2, pp. 17–39, Jan. 2008, doi: 10.1016/J.GEOMORPH.2006.12.016.

[136]   D. M. Lawler, "Defining the moment of erosion: the principle of thermal consonance timing," *Earth Surf. Process. Landforms*, vol. 30, no. 13, pp. 1597–1615, Dec. 2005, doi: 10.1002/ESP.1234.

[137]   E. L. Gallagher, W. Boyd, S. Elgar, R. T. Guza, and B. Woodward, "Performance of a sonar altimeter in the nearshore," *Mar. Geol.*, vol. 133, no. 3–4, pp. 241–248, Aug. 1996, doi: 10.1016/0025-3227(96)00018-7.

[138]   H. Jestin, P. Bassoullet, P. Le Hir, J. L'Yavanc, and Y. Degres, "Development of ALTUS, a high frequency acoustic submersible recording altimeter to accurately monitor bed elevation and quantify deposition or erosion of sediments," in *Oceans Conference Record (IEEE)*, 1998, vol. 1, pp. 189–194, doi: 10.1109/oceans.1998.725734.

[139]   E. L. Gallagher, W. Boyd, S. Elgar, R. T. Guza, and B. Woodward, "Performance of a sonar altimeter in the nearshore," *Mar. Geol.*, vol. 133, no. 3–4, pp. 241–248, Aug. 1996, doi: 10.1016/0025-3227(96)00018-7.

[140]   H. Jestin, P. Bassoullet, P. Le Hir, J. L'Yavanc, and Y. Degres, "Development of ALTUS, a high frequency acoustic submersible recording altimeter to accurately monitor bed elevation and quantify deposition or erosion of sediments," *Ocean. Conf. Rec.*, vol. 1, pp. 189–194, 1998, doi: 10.1109/OCEANS.1998.725734.

[141]   A. Laenen, "Measuring water surface and streambed elevation changes with the acoustic velocity metering system," *Water Resour. Res.*, vol. 19, no. 5, pp. 1317–1322, Oct. 1983, doi: 10.1029/WR019I005P01317.

[142]   T. Matos *et al.*, "Design and In Situ Validation of Low-Cost and Easy to Apply Anti-Biofouling Techniques for Oceanographic Continuous Monitoring with Optical Instruments," *Sensors 2023, Vol. 23, Page 605*, vol. 23, no. 2, p. 605, Jan. 2023, doi: 10.3390/S23020605.

[143]   D. Rittschof, A. S. Clare, D. J. Gerhart, S. A. Mary, and J. Bonaventura, "Barnacle in vitro assays for biologically active substances: Toxicity and settlement inhibition assays using mass cultured balanus amphitrite amphitrite darwin," *Biofouling*, vol. 6, no. 2, pp. 115–122, Nov. 1992, doi: 10.1080/08927019209386217.

[144]   X. Liu, J. L. Yang, D. Rittschof, J. S. Maki, and J. D. Gu, "Redirecting marine antibiofouling innovations from sustainable horizons," *Trends Ecol. Evol.*, vol. 37, no. 6, pp. 469–472, Jun. 2022, doi: 10.1016/j.tree.2022.02.009.

[145]   L. Delauney, C. Compare, and M. Lehaitre, "Biofouling protection for marine environmental sensors," *Ocean Sci.*, vol. 6, no. 2, pp. 503–511, May 2010, doi: 10.5194/OS-6-503-2010.

[146] L. F. Melo and T. R. Bott, "Biofouling in water systems," *Exp. Therm. Fluid Sci.*, vol. 14, no. 4, pp. 375–381, May 1997, doi: 10.1016/S0894-1777(96)00139-2.

[147] R. Venkatesan, P. Senthilkumar, N. Vedachalam, and P. Murugesh, "Biofouling and its effects in sensor mounted moored observatory system in Northern Indian Ocean," *Int. Biodeterior. Biodegradation*, vol. 116, pp. 198–204, Jan. 2017, doi: 10.1016/J.IBIOD.2016.10.034.

[148] Y. Sun, Y. Fang, P. Liang, and X. Huang, "Effects of online chemical cleaning on removing biofouling and resilient microbes in a pilot membrane bioreactor," *Int. Biodeterior. Biodegradation*, vol. 112, pp. 119–127, Aug. 2016, doi: 10.1016/J.IBIOD.2016.05.010.

[149] A. Y. Alexandrovskaya, P. V. Melnikov, A. V. Safonov, A. O. Naumova, and N. K. Zaytsev, "A comprehensive study of the resistance to biofouling of different polymers for optical oxygen sensors. The advantage of the novel fluorinated composite based on core-dye-shell structure," *Mater. Today Commun.*, vol. 23, p. 100916, Jun. 2020, doi: 10.1016/J.MTCOMM.2020.100916.

[150] A. Kerr *et al.*, "The early stages of marine biofouling and its effect on two types of optical sensors," *Environ. Int.*, vol. 24, no. 3, pp. 331–343, Apr. 1998, doi: 10.1016/S0160-4120(98)00011-7.

[151] S. Bhatia *et al.*, "Biofouling of an All-Optical Sensor for Seafloor Monitoring of Marine Carbon Capture and Storage Sites," *Energy Procedia*, vol. 63, pp. 3848–3852, Jan. 2014, doi: 10.1016/J.EGYPRO.2014.11.414.

[152] Y. Boukazia *et al.*, "Metrological performances of fouling sensors based on steady thermal excitation applied to bioprocess," *Food Bioprod. Process.*, vol. 119, pp. 226–237, Jan. 2020, doi: 10.1016/J.FBP.2019.11.007.

[153] Y. T. Chen and J. Crossman, "The impacts of biofouling on automated phosphorus analysers during long-term deployment," *Sci. Total Environ.*, vol. 784, p. 147188, Aug. 2021, doi: 10.1016/J.SCITOTENV.2021.147188.

[154] A. Delgado, C. Briciu-Burghina, and F. Regan, "Antifouling Strategies for Sensors Used in Water Monitoring: Review and Future Perspectives," *Sensors (Basel).*, vol. 21, no. 2, pp. 1–25, Jan. 2021, doi: 10.3390/S21020389.

[155] H. Gueuné, G. Thouand, and M. J. Durand, "A new bioassay for the inspection and identification of TBT-containing antifouling paint," *Mar. Pollut. Bull.*, vol. 58, no. 11, pp. 1734–1738, Nov. 2009, doi: 10.1016/J.MARPOLBUL.2009.09.012.

[156] I. Amara, W. Miled, R. Ben Slama, and N. Ladhari, "Antifouling processes and toxicity effects of antifouling paints on marine environment. A review," *Environ. Toxicol. Pharmacol.*, vol. 57, pp. 115–130, Jan. 2018, doi: 10.1016/J.ETAP.2017.12.001.

[157] D. V Manov, G. C. Chang, and T. D. Dickey, "Methods for Reducing Biofouling of Moored Optical Sensors," *J. Atmos. Ocean. Technol.*, vol. 21, no. 6, 2004, doi: https://doi.org/10.1175/1520-0426(2004)021<0958:MFRBOM>2.0.CO;2.

[158] F. P.Chavez, D. Wright, R. Herlien, M. Kelley, F. Shane, and P. Strutton, "A Device for Protecting Moored Spectroradiometers from Biofouling," *J. Atmos. Ocean. Technol.*, vol. 17, no. 2, 2000, doi: https://doi.org/10.1175/1520-0426(2000)017<0215:ADFPMS>2.0.CO;2.

[159] L. McBride, M. Brown, M. Kelley, and M. Risi, "MBARI new anti-biofouling shutter," *Ocean. 2003 Celebr. Past... Teaming Towar. Futur.*, vol. 3, pp. 1602–1605, 2003, doi: 10.1109/OCEANS.2003.178111.

[160] K. N. Richard, K. Z. Hunsucker, H. Gardner, K. Hickman, and G. Swain, "The Application of UVC Used in Synergy with Surface Material to Prevent Marine Biofouling," *J. Mar. Sci. Eng. 2021, Vol. 9, Page 662*, vol. 9, no. 6, p. 662, Jun. 2021, doi: 10.3390/JMSE9060662.

[161] J. S. Patil, H. Kimoto, T. Kimoto, and T. Saino, "Ultraviolet radiation (UV-C): a potential tool for the control

of biofouling on marine optical instruments," *http://dx.doi.org/10.1080/08927010701275598*, vol. 23, no. 4, pp. 215–230, Jul. 2007, doi: 10.1080/08927010701275598.

[162] A. Lakretz, E. Z. Ron, and H. Mamane, "Biofouling control in water by various UVC wavelengths and doses," *https://doi.org/10.1080/08927010903484154*, vol. 26, no. 3, pp. 257–267, Apr. 2009, doi: 10.1080/08927010903484154.

[163] Y. Lu, Y. Ding, M. L. Wang, L. J. Yang, and Y. Wang, "An environmentally friendly laser cleaning method to remove oceanic micro-biofoulings from AH36 steel substrate and corrosion protection," *J. Clean. Prod.*, vol. 314, p. 127961, Sep. 2021, doi: 10.1016/J.JCLEPRO.2021.127961.

[164] S. Zimbelmann, B. Emde, T. H. von Waldegge, D. Stübing, M. Baumann, and J. Hermsdorf, "Interaction between laser radiation and biofouling for ship hull cleaning," *Procedia CIRP*, vol. 111, pp. 705–710, Jan. 2022, doi: 10.1016/J.PROCIR.2022.08.013.

[165] N. Zhang, H. J. Lee, Y. Wu, M. A. Ganzoury, and C. F. de Lannoy, "Integrating biofouling sensing with fouling mitigation in a two-electrode electrically conductive membrane filtration system," *Sep. Purif. Technol.*, vol. 288, p. 120679, May 2022, doi: 10.1016/J.SEPPUR.2022.120679.

[166] L. Jiang, L. Chen, and L. Zhu, "Electrically conductive membranes for anti-biofouling in membrane distillation with two novel operation modes: Capacitor mode and resistor mode," *Water Res.*, vol. 161, pp. 297–307, Sep. 2019, doi: 10.1016/J.WATRES.2019.06.015.

[167] J. H. Lee, E. T. Yun, S. Y. Ham, H. S. Kim, P. F. Sun, and H. D. Park, "Electrically conductive carbon nanotube/graphene composite membrane for self-cleaning of biofouling via bubble generation," *Desalination*, vol. 535, p. 115841, Aug. 2022, doi: 10.1016/J.DESAL.2022.115841.

[168] M. Legg, M. K. Yücel, I. Garcia De Carellan, V. Kappatos, C. Selcuk, and T. H. Gan, "Acoustic methods for biofouling control: A review," *Ocean Eng.*, vol. 103, pp. 237–247, Jul. 2015, doi: 10.1016/J.OCEANENG.2015.04.070.

[169] L. Grilli *et al.*, "Development, Optimization, Biological Assays, and In Situ Field Immersion of a Transparent Piezoelectric Vibrating System for Antifouling Applications," *Actuators 2022, Vol. 11, Page 47*, vol. 11, no. 2, p. 47, Feb. 2022, doi: 10.3390/ACT11020047.

[170] X. She *et al.*, "Miniature sono-electrochemical platform enabling effective and gentle electrode biofouling removal for continuous sweat measurements," *Chem. Eng. J.*, vol. 431, p. 133354, Mar. 2022, doi: 10.1016/J.CEJ.2021.133354.

[171] R. E. Wilson, I. Stoianov, and D. O'Hare, "Biofouling and in situ electrochemical cleaning of a boron-doped diamond free chlorine sensor," *Electrochem. commun.*, vol. 71, pp. 79–83, Oct. 2016, doi: 10.1016/J.ELECOM.2016.08.015.

[172] S. Lou, P. Wang, B. Ma, J. Wu, and D. Zhang, "Biofouling protection for marine optical windows by electrolysis of seawater to generate chlorine using a novel Co-based catalyst electrode," *Colloids Surfaces A Physicochem. Eng. Asp.*, vol. 638, p. 128270, Apr. 2022, doi: 10.1016/J.COLSURFA.2022.128270.

[173] P. Woerther and A. Grouhel, "MAREL: Automated measurement network for the coastal environment," *Ocean. Conf. Rec.*, vol. 2, pp. 1149–1154, 1998, doi: 10.1109/OCEANS.1998.724415.

[174] D. Laurent *et al.*, "Biofouling protection by electro-chlorination on optical windows for oceanographic sensors and imaging devices," *Ocean. 2015-Genova. ITALY*, doi: 10.1109/OCEANS-Genova.2015.7271715.

[175] F. Sousa-Cardoso, R. Teixeira-Santos, and F. J. M. Mergulhão, "Antifouling Performance of Carbon-Based Coatings for Marine Applications: A Systematic Review," *Antibiot. 2022, Vol. 11, Page 1102*, vol. 11, no. 8, p. 1102, Aug. 2022, doi: 10.3390/ANTIBIOTICS11081102.

[176] P. Yi *et al.*, "Anti-biofouling properties of TiO2 coating with coupled effect of photocatalysis and

microstructure," *Colloids Surfaces A Physicochem. Eng. Asp.*, vol. 656, p. 130357, Jan. 2023, doi: 10.1016/J.COLSURFA.2022.130357.

[177] S. Sfameni *et al.*, "Design and Development of Fluorinated and Biocide-Free Sol–Gel Based Hybrid Functional Coatings for Anti-Biofouling/Foul-Release Activity," *Gels 2022, Vol. 8, Page 538*, vol. 8, no. 9, p. 538, Aug. 2022, doi: 10.3390/GELS8090538.

[178] A. R. Neves *et al.*, "Antifouling Marine Coatings with a Potentially Safer and Sustainable Synthetic Polyphenolic Derivative," *Mar. Drugs 2022, Vol. 20, Page 507*, vol. 20, no. 8, p. 507, Aug. 2022, doi: 10.3390/MD20080507.

[179] C. M. Magin, S. P. Cooper, and A. B. Brennan, "Non-toxic antifouling strategies," *Mater. Today*, vol. 13, no. 4, pp. 36–44, Apr. 2010, doi: 10.1016/S1369-7021(10)70058-4.

[180] T. Matos, C. L. Faria, M. S. Martins, R. Henriques, P. A. Gomes, and L. M. Goncalves, "Development of a Cost-Effective Optical Sensor for Continuous Monitoring of Turbidity and Suspended Particulate Matter in Marine Environment," *Sensors*, vol. 19, no. 20, p. 4439, Oct. 2019, doi: 10.3390/s19204439.

[181] T. Matos, C. L. Faria, M. Martins, R. Henriques, and L. Goncalves, "Optical device for in situ monitoring of suspended particulate matter and organic/inorganic distinguish," in *OCEANS 2019 - Marseille, OCEANS Marseille 2019*, Jun. 2019, vol. 2019-June, doi: 10.1109/OCEANSE.2019.8867080.

[182] L. van Rijn, "Principles of Sediment Transport in Rivers, Estuaries and Coastal Seas," *Princ. Sediment Transp. Rivers , Estuaries Coast. Seas*, pp. 1–17, 1993, doi: 10.1002/9781444308785.

[183] H. Khouja, "Turbidimetry & Nephelometry," *Cell Biochem. Funct.*, vol. 11, no. 1, pp. 1–3, 2010.

[184] R. T. Balch, "Measurement of Turbidity with a Spectrophotometer: With Especial Reference to Sugarhouse Products," *Ind. Eng. Chem. - Anal. Ed.*, vol. 3, no. 2, pp. 124–127, 1931, doi: 10.1021/ac50074a003.

[185] J. L. Weishaar, G. R. Aiken, B. A. Bergamaschi, M. S. Fram, R. Fujii, and K. Mopper, "Evaluation of Specific Ultraviolet Absorbance as an Indicator of the Chemical Composition and Reactivity of Dissolved Organic Carbon," *Environ. Sci. Technol.*, vol. 37, no. 20, pp. 4702–4708, Oct. 2003, doi: 10.1021/ES030360X.

[186] H. M. Kalaji *et al.*, "Frequently asked questions about in vivo chlorophyll fluorescence: Practical issues," *Photosynth. Res.*, vol. 122, no. 2, pp. 121–158, Aug. 2014, doi: 10.1007/S11120-014-0024-6/FIGURES/8.

[187] R. J. Gibbs, "Principles of Studying Suspended Materials in Water," *Suspended Solids in Water*, pp. 3–15, 1974, doi: 10.1007/978-1-4684-8529-5_1.

[188] J. Downing, "Twenty-five years with OBS sensors: The good, the bad, and the ugly," *Cont. Shelf Res.*, vol. 26, no. 17–18, pp. 2299–2318, Nov. 2006, doi: 10.1016/J.CSR.2006.07.018.

[189] E. Boss *et al.*, "Comparison of inherent optical properties as a surrogate for particulate matter concentration in coastal waters.," 2009, doi: 10.25607/OBP-358.

[190] Hach, "Water Analysis Guide 09/2013," 2013.

[191] T. Matos, C. L. Faria, M. S. Martins, R. Henriques, P. A. Gomes, and L. M. Goncalves, "Design of a Multipoint Cost-Effective Optical Instrument for Continuous In-Situ Monitoring of Turbidity and Sediment," *Sensors*, vol. 20, no. 11, p. 3194, Jun. 2020, doi: 10.3390/s20113194.

[192] T. Matos, J. L. Rocha, C. L. Faria, M. S. Martins, R. Henriques, and L. M. Goncalves, "Development of an automated sensor for in-situ continuous monitoring of streambed sediment height of a waterway," *Sci. Total Environ.*, vol. 808, p. 152164, Feb. 2022, doi: 10.1016/J.SCITOTENV.2021.152164.

[193] S. M. van Netten and M. J. McHenry, "The Biophysics of the Fish Lateral Line," pp. 99–119, 2013, doi: 10.1007/2506_2013_14.

[194] S. M. van Netten, "Hydrodynamics of the excitation of the cupula in the fish canal lateral line," *J. Acoust.*

Soc. Am., vol. 89, no. 1, p. 310, Jun. 1998, doi: 10.1121/1.400512.

[195] Y. Xu, X. Xia, and K. Mohseni, "Modeling and simulation of a fish-like swimmer in an ideal flow with lateral-line flow sensors," *AIAA Guid. Navig. Control Conf. 2013*, 2015, doi: 10.2514/6.2015-1082.

[196] S. Vlassov *et al.*, "Adhesion and mechanical properties of PDMS-based materials probed with AFM: A review," *Rev. Adv. Mater. Sci.*, vol. 56, no. 1, pp. 62–78, May 2018, doi: 10.1515/RAMS-2018-0038/MACHINEREADABLECITATION/RIS.

[197] A. Borók, K. Laboda, and A. Bonyár, "PDMS Bonding Technologies for Microfluidic Applications: A Review," *Biosens. 2021, Vol. 11, Page 292*, vol. 11, no. 8, p. 292, Aug. 2021, doi: 10.3390/BIOS11080292.

[198] B. Oh *et al.*, "Evaluation of bonding between oxygen plasma treated polydimethyl siloxane and passivated silicon," *J. Phys. Conf. Ser.*, vol. 34, no. 1, p. 155, Apr. 2006, doi: 10.1088/1742-6596/34/1/026.

[199] M. S. Martins, J. V. G. Rocha, J. M. Tavares, V. Cabral, and S. Lanceros-Mendez, "Ultrasonic wireless broadband communication system for underwater applications," 2013.

[200] M. Tiboni, A. Filippini, C. Amici, and D. Vetturi, "Test-Bench for the Characterization of Flexion Sensors Used in Biomechanics," *Electron. 2021, Vol. 10, Page 2994*, vol. 10, no. 23, p. 2994, Dec. 2021, doi: 10.3390/ELECTRONICS10232994.

[201] S. Jung, T. Van Chau, M. Kim, and W. B. Na, "Artificial Seaweed Reefs That Support the Establishment of Submerged Aquatic Vegetation Beds and Facilitate Ocean Macroalgal Afforestation: A Review," *J. Mar. Sci. Eng. 2022, Vol. 10, Page 1184*, vol. 10, no. 9, p. 1184, Aug. 2022, doi: 10.3390/JMSE10091184.

[202] W. T. Piver, "Organotin compounds: industrial applications and biological investigation.," *Environ. Health Perspect.*, vol. 4, p. 61, 1973, doi: 10.1289/EHP.730461.

[203] M. Niaounakis, "Economic Evaluation and Environmental Impacts," *Biopolym. Reuse, Recycl. Dispos.*, pp. 275–290, Jan. 2013, doi: 10.1016/B978-1-4557-3145-9.00010-5.

[204] G. W. Swain, W. G. Nelson, and S. Preedeekanit, "The influence of biofouling adhesion and biotic disturbance on the development of fouling communities on non-toxic surfaces," *https://doi.org/10.1080/08927019809378358*, vol. 12, no. 1–3, pp. 257–269, 2009, doi: 10.1080/08927019809378358.

[205] J. S. Puh, P. A. Wagner, B. J. Little, and W. L. Bradley, "The Effect of Biofouling on Graphite/Epoxy Composites," *J. Compos. Technol. Res.*, vol. 20, no. 1, pp. 59–67, 1998, doi: 10.1520/CTR10501J.

[206] Š. Petronis, K. Berntsson, J. Gold, and P. Gatenholm, "Design and microstructuring of PDMS surfaces for improved marine biofouling resistance," *http://dx.doi.org/10.1163/156856200743571*, vol. 11, no. 10, pp. 1051–1072, 2012, doi: 10.1163/156856200743571.

[207] E. Seo *et al.*, "Eco-friendly erucamide–polydimethylsiloxane coatings for marine anti-biofouling," *Colloids Surfaces B Biointerfaces*, vol. 207, p. 112003, Nov. 2021, doi: 10.1016/J.COLSURFB.2021.112003.

[208] E. Seo *et al.*, "Anti-Biofouling Features of Eco-Friendly Oleamide-PDMS Copolymers," *ACS Omega*, vol. 5, no. 20, pp. 11515–11521, May 2020, doi: 10.1021/ACSOMEGA.0C00633/SUPPL_FILE/AO0C00633_SI_001.PDF.

[209] G. Minas, L. Gonçalves, V. Pinto, and P. Sousa, "Antibiofouling device for optical sensors, methods and uses thereof," WO 2021/149024 A1, 2021.

[210] V. C. Pinto, P. J. Sousa, E. M. F. Vieira, L. M. Gonçalves, and G. Minas, "Antibiofouling strategy for optical sensors by chlorine generation using low-cost, transparent and highly efficient electrodes based on platinum nanoparticles coated oxide," *Chem. Eng. J.*, vol. 404, p. 126479, Jan. 2021, doi: 10.1016/J.CEJ.2020.126479.

[211] T. Matos *et al.*, "A low-cost, low-power and low-size multi-parameter station for real-time and online

monitoring of the coastal area," *Ocean. Conf. Rec.*, vol. 2022-October, 2022, doi: 10.1109/OCEANS47191.2022.9977347.

[212] E. Loureiro, H. M. Granja, and J. L. S. Pinho, "Morphodynamics of the Cávado estuary inlet (NW Portugal)," 2005, Accessed: Mar. 18, 2023. [Online]. Available: https://repositorium.sdum.uminho.pt/handle/1822/4637.

[213] E. Fernández, X. A. Álvarez-Salgado, R. Beiras, A. Ovejero, and G. Méndez, "Coexistence of urban uses and shellfish production in an upwelling-driven, highly productive marine environment: The case of the Ría de Vigo (Galicia, Spain)," *Reg. Stud. Mar. Sci.*, vol. 8, pp. 362–370, Nov. 2016, doi: 10.1016/J.RSMA.2016.04.002.

[214] T. Matos *et al.*, "Synchronous Oceanic and Atmospheric Data Acquisition: field test release and validation of atmospheric, oceanographic, and deep-sea probes in the Azores Islands," *Ocean. 2023 - Limerick*, pp. 1–7, Jun. 2023, doi: 10.1109/OCEANSLIMERICK52467.2023.10244259.

[215] C. A. K. Singam, "Implementation of a Low-Cost Flight Tracking System for High-Altitude Ballooning," *https://doi.org/10.2514/1.I010679*, vol. 17, no. 6, pp. 278–284, Feb. 2020, doi: 10.2514/1.I010679.

[216] W. Chen, C. Li, J. Yu, J. Zhang, and F. Chang, "A survey of maritime communications: From the wireless channel measurements and modeling perspective," *Reg. Stud. Mar. Sci.*, vol. 48, p. 102031, Nov. 2021, doi: 10.1016/J.RSMA.2021.102031.

[217] J. L. Rocha *et al.*, "Wave Profile and Tide Monitoring System for Scalable Implementation," *Proc. IEEE Sensors*, 2023, doi: 10.1109/SENSORS56945.2023.10325051.

[218] K. A. Orvik, Ø. Skagseth, and M. Mork, "Atlantic inflow to the Nordic Seas: current structure and volume fluxes from moored current meters, VM-ADCP and SeaSoar-CTD observations, 1995–1999," *Deep Sea Res. Part I Oceanogr. Res. Pap.*, vol. 48, no. 4, pp. 937–957, Apr. 2001, doi: 10.1016/S0967-0637(00)00038-8.

[219] O. M. Johannessen, "Brief Overview of the Physical Oceanography," *Nord. Seas*, pp. 103–128, 1986, doi: 10.1007/978-1-4615-8035-5_4.

[220] J. L. Rocha *et al.*, "Cost Effective CTD for Long Term Deployments in Water Columns," *Ocean. Conf. Rec.*, vol. 2021-September, 2021, doi: 10.23919/OCEANS44145.2021.9705844.

SUPPLEMENTARY MATERIAL I – ELECTRONIC SCHEMATICS
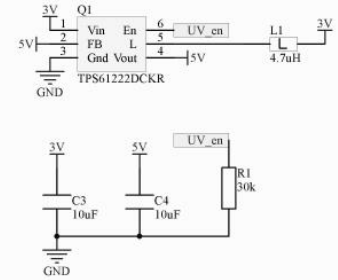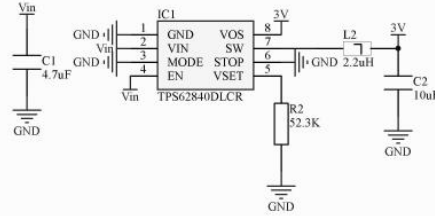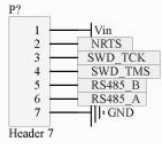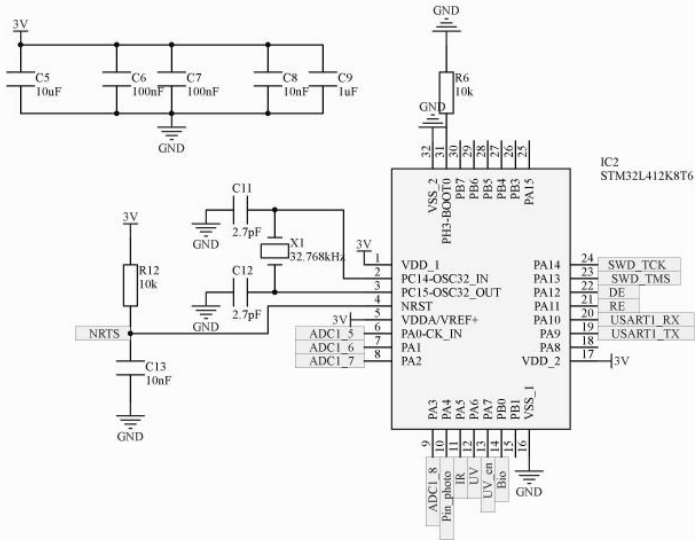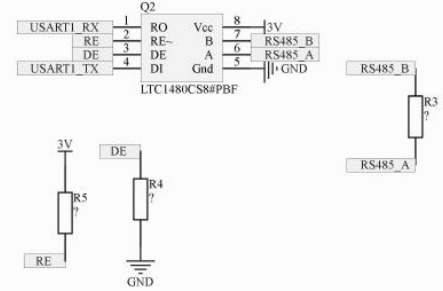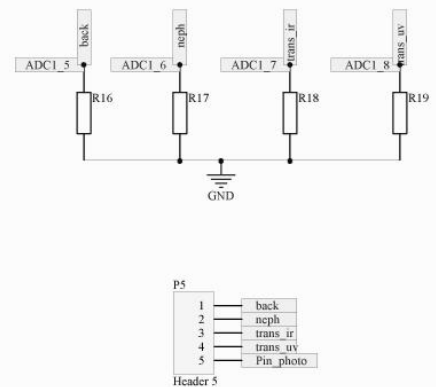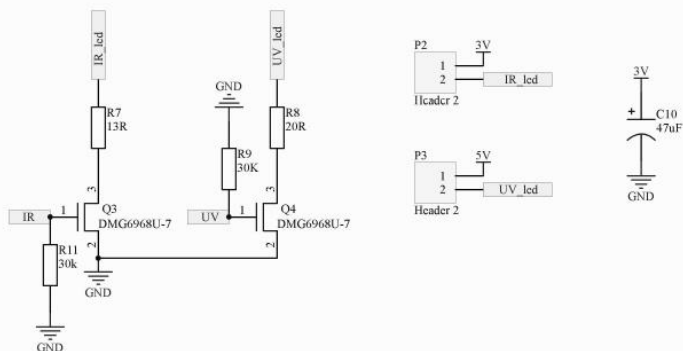
Supplementary Material I 1. Electronic schematic of the SPM Sensor.
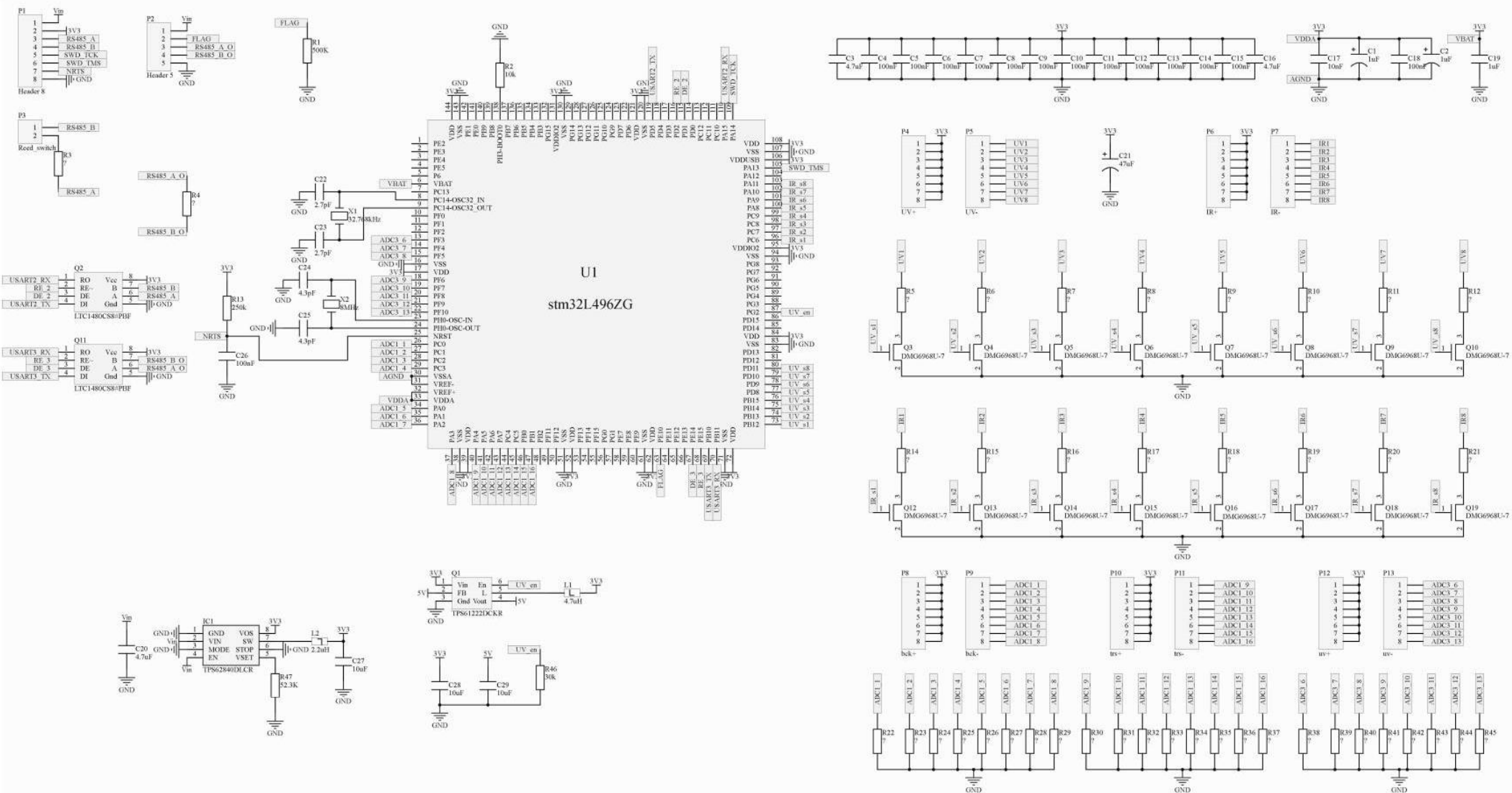
Supplementary Material I 2. Electronic schematic of the TVP Sensor.
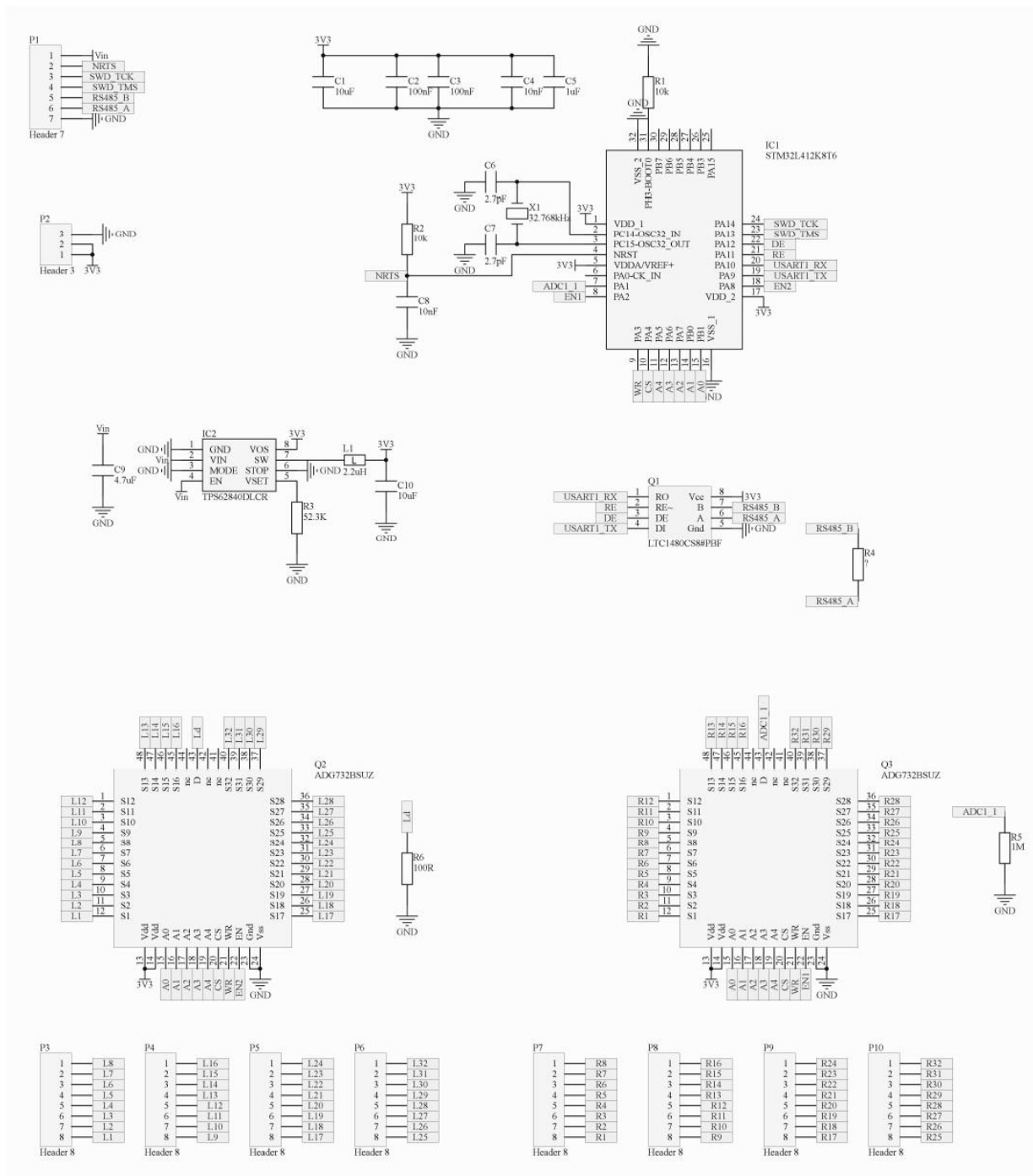
Supplementary Material I 3. Electronic schematic of the management PCB of the SDE Sensor.
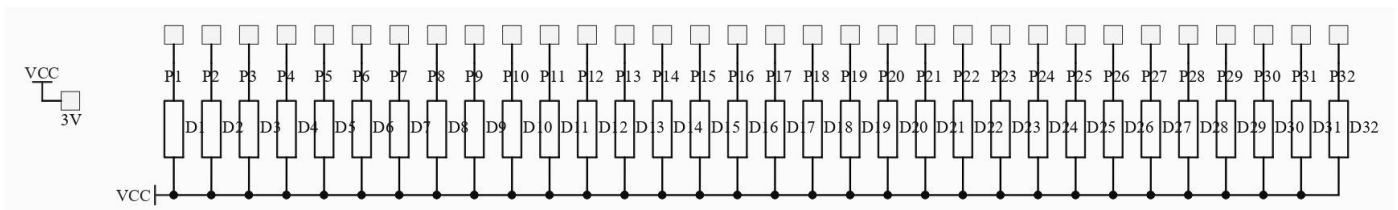
Supplementary Material I 4. Electronic schematic of the array PCB of the SDE Sensor.
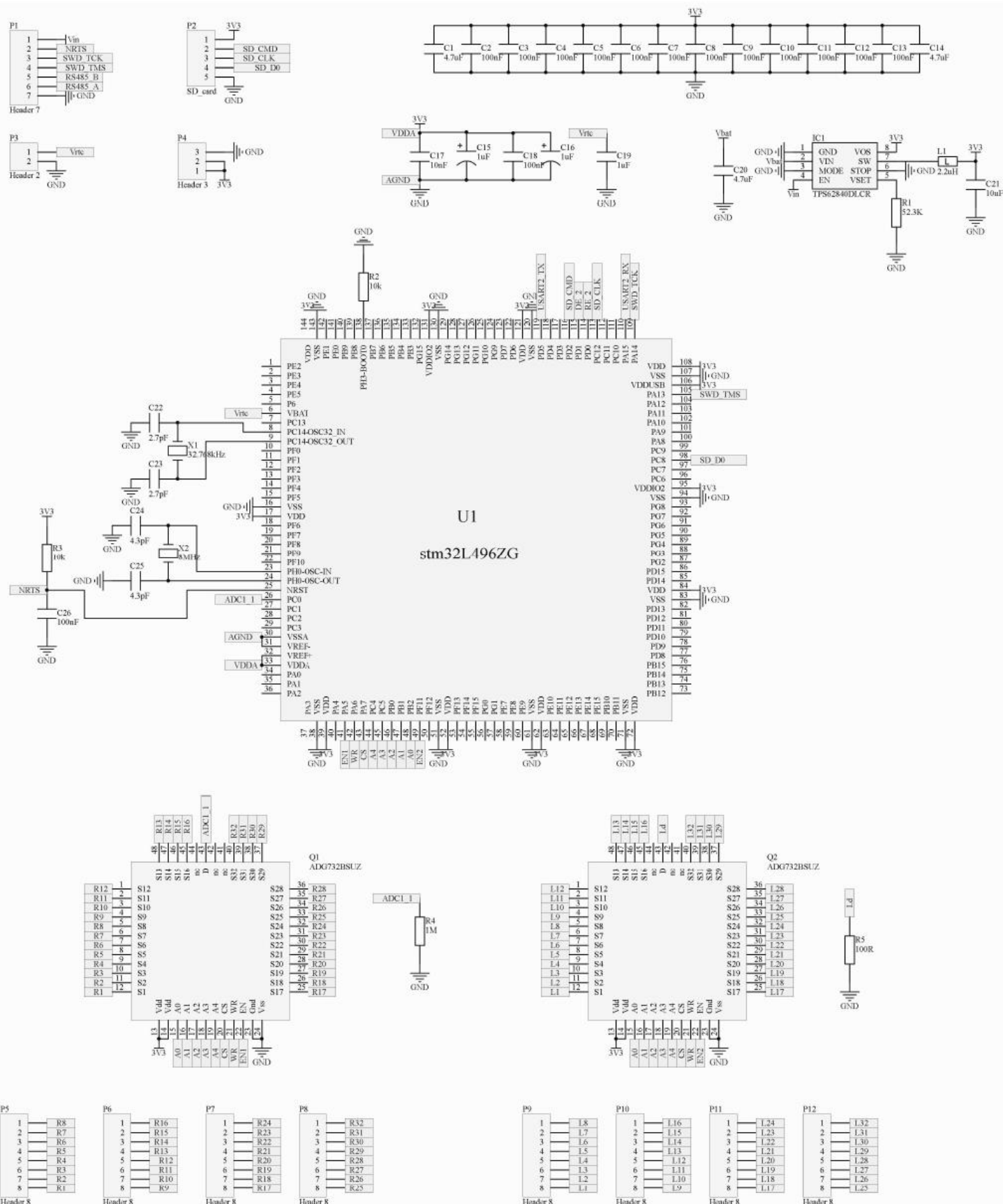
Supplementary Material I 5. Electronic schematic of the management PCB of the SDE Sensor – portable.
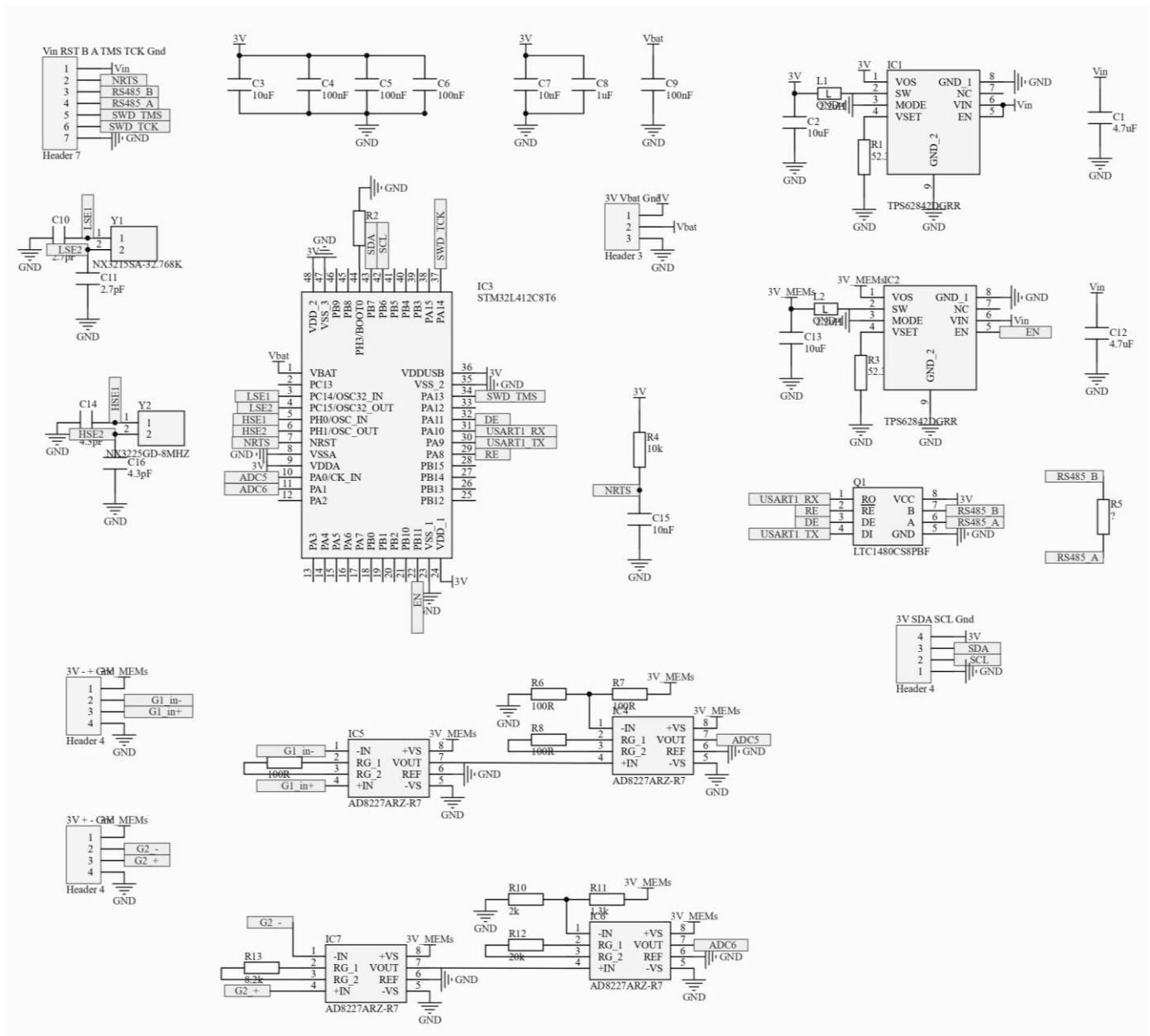
Supplementary Material I 6. Electronic schematic of the MEMS biomimetic current meter.
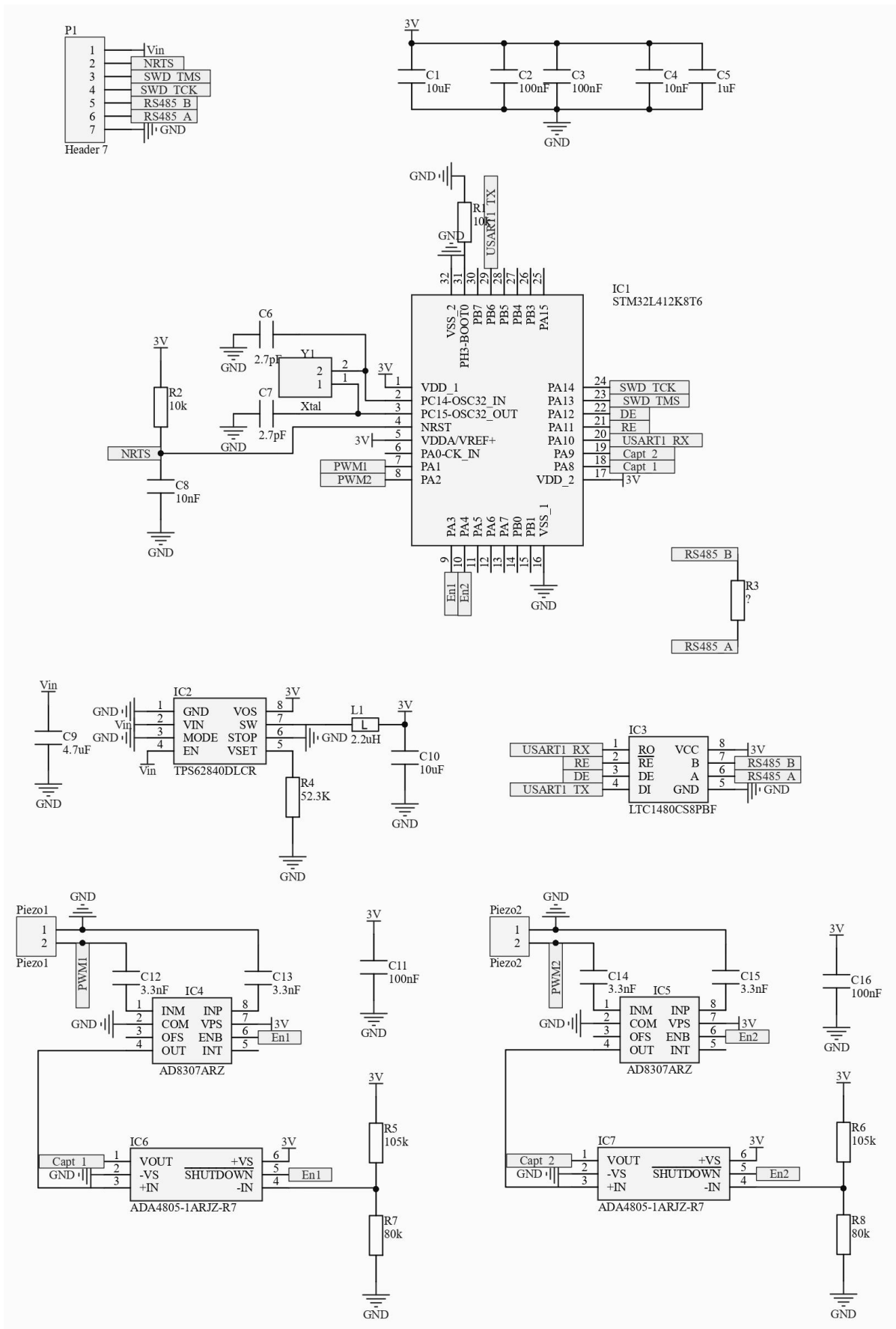
Supplementary Material I 7. Electronic schematic of the acoustic ToF current meter.
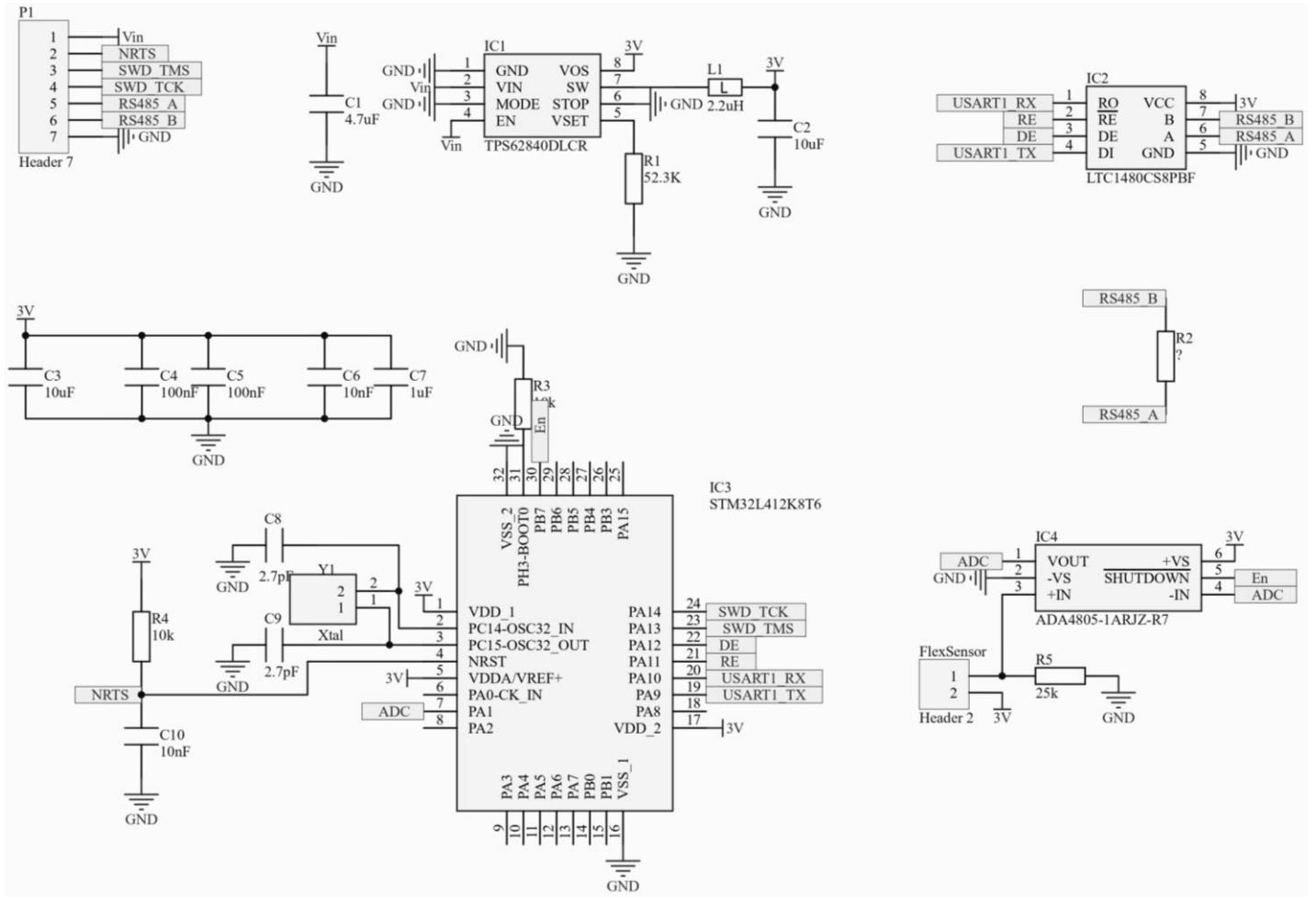
Supplementary Material I 8. Electronic schematic of the first prototype of the SeT sensor using the Flex Sensor.
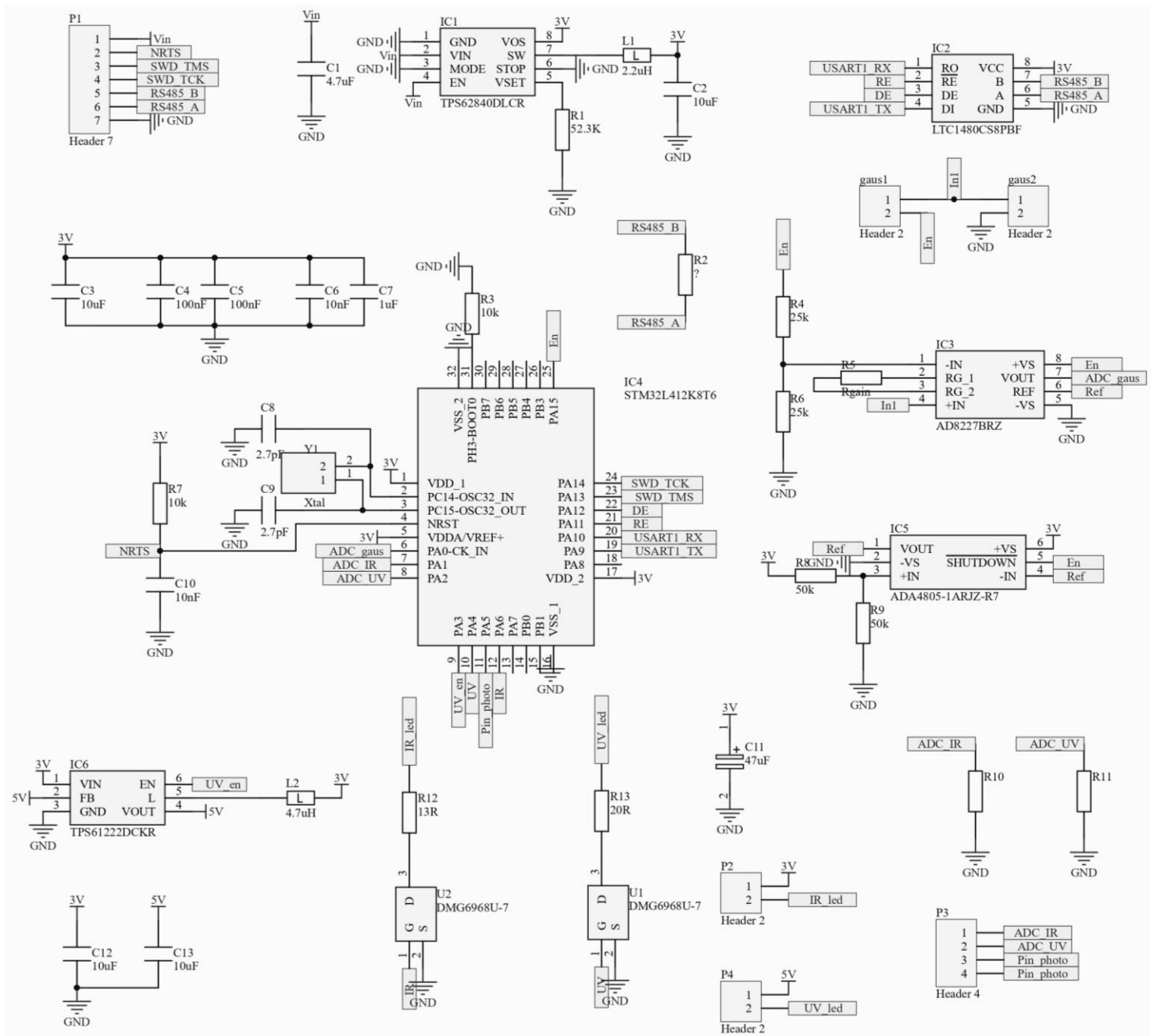
Supplementary Material I 9. Electronic schematic of the second prototype of the SeT sensor using the Flex Sensor.
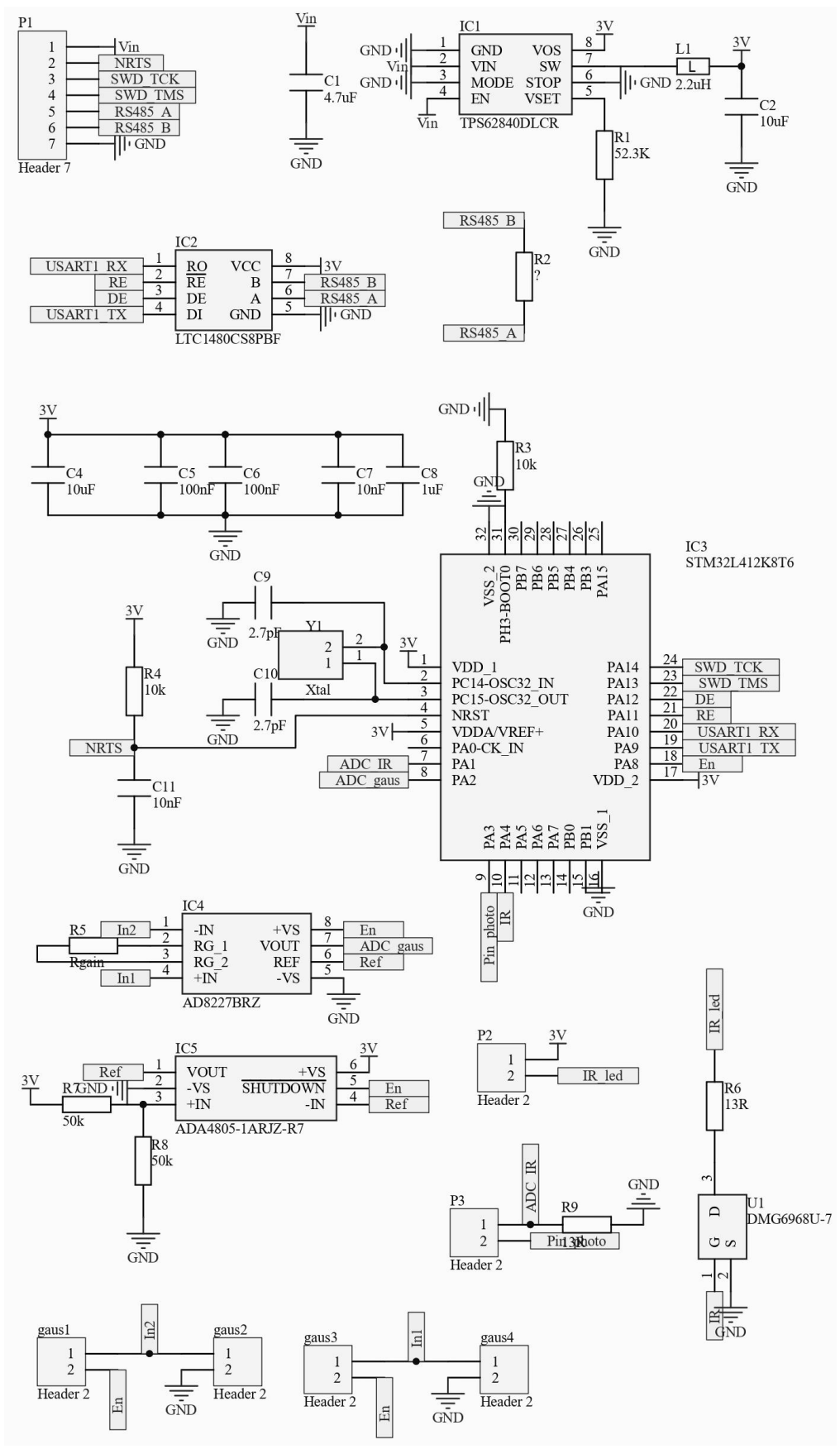
Supplementary Material I 10. Electronic schematic of the SeT sensor.
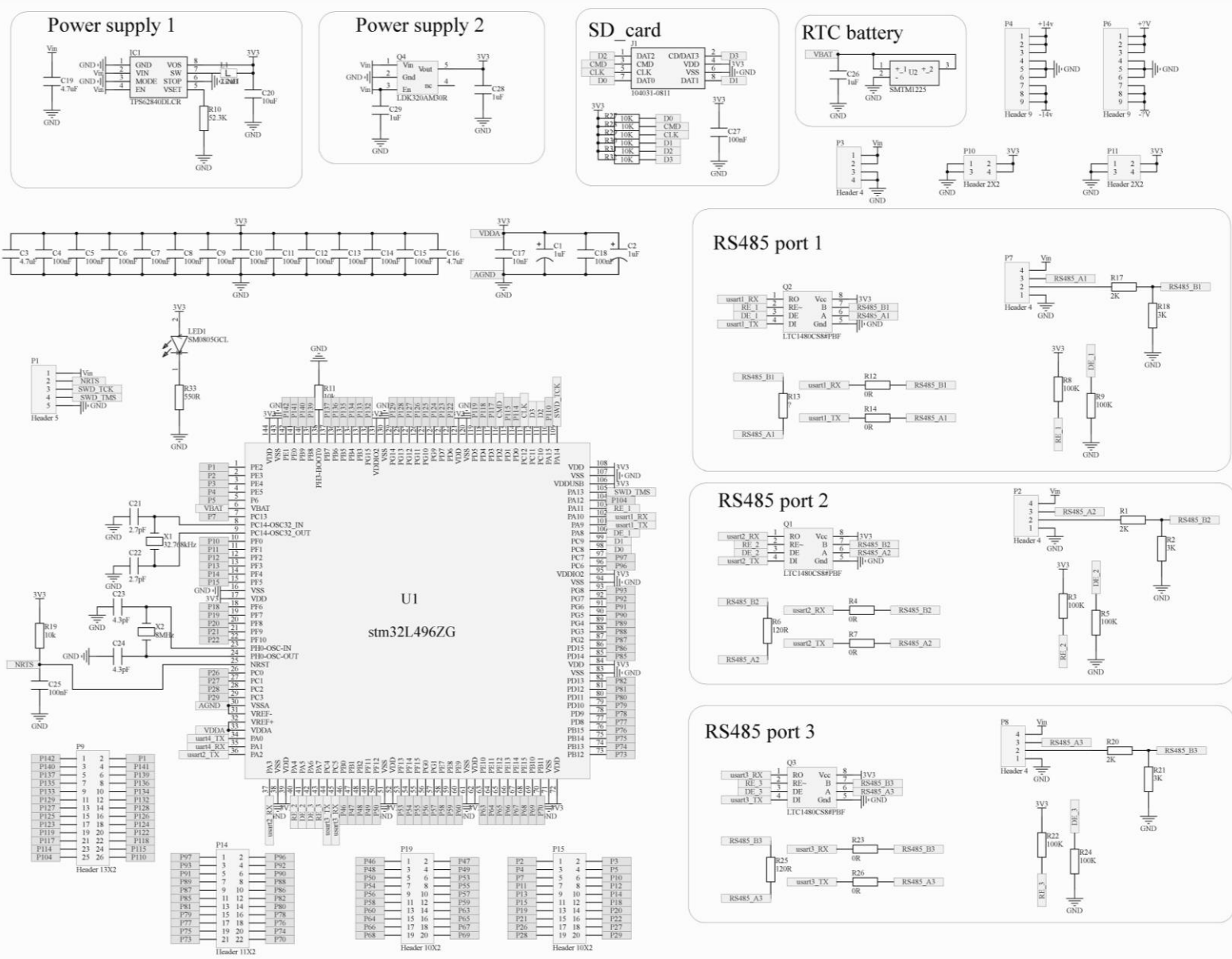
Supplementary Material I 11. Electronic schematic of the data logger with the STM32L496ZG microprocessor. This version includes two different options for the power supply and three RS485 buses.
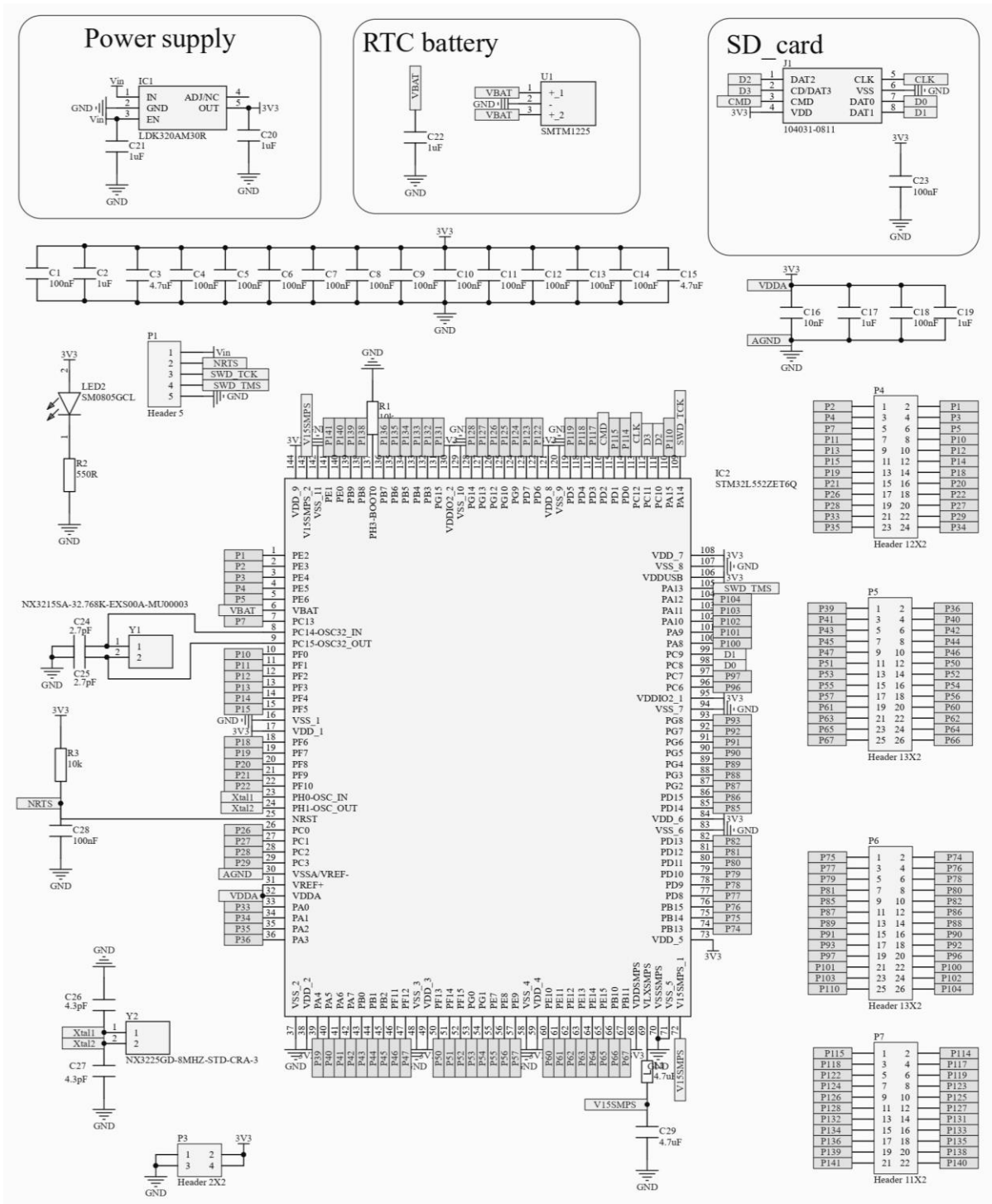
Supplementary Material I 12. Electronic schematic of the data logger with the STM32L552ZET6Q microprocessor.
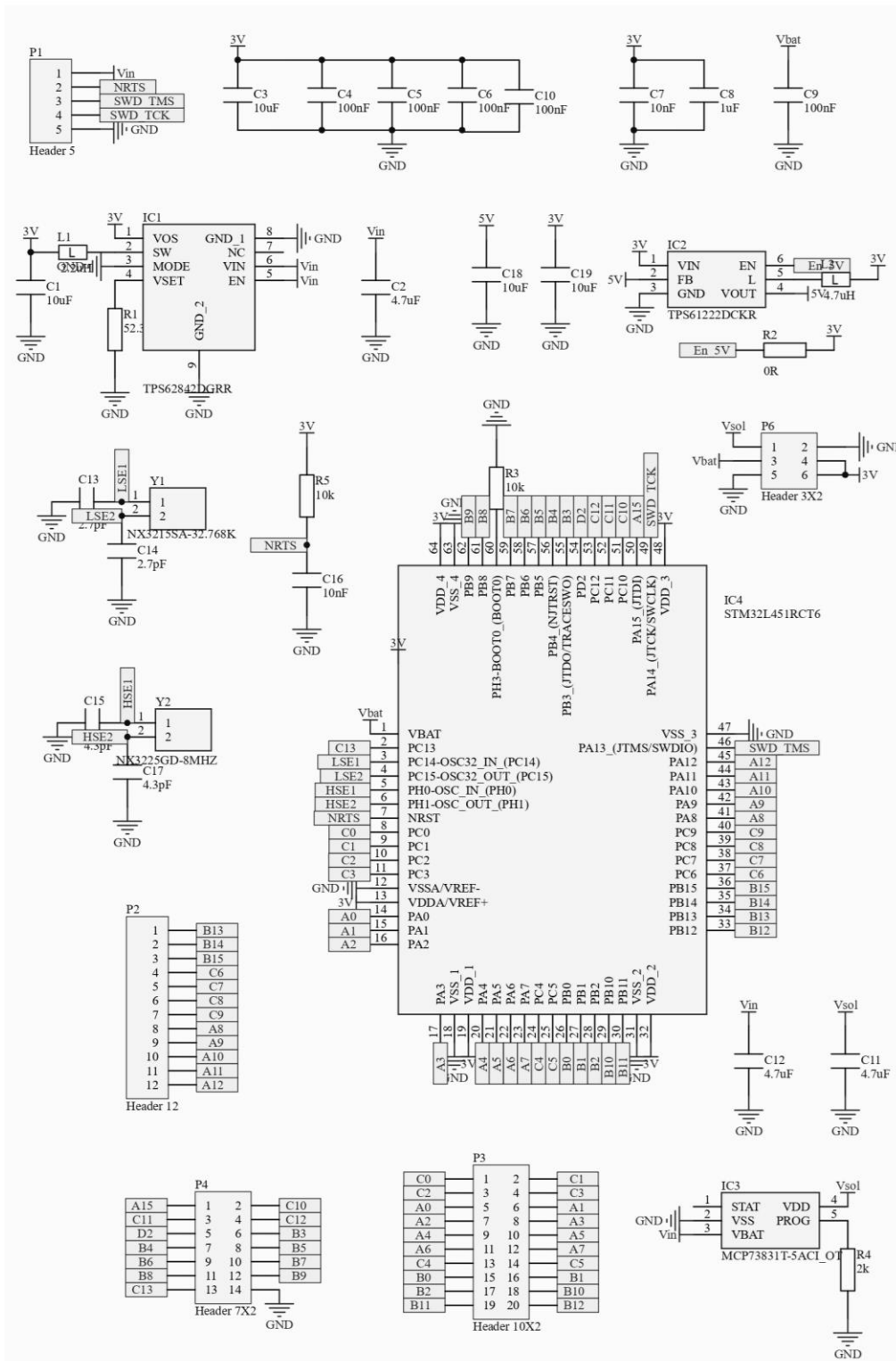
Supplementary Material I 13. Electronic schematic of the data logger for the LQFP-64 package.
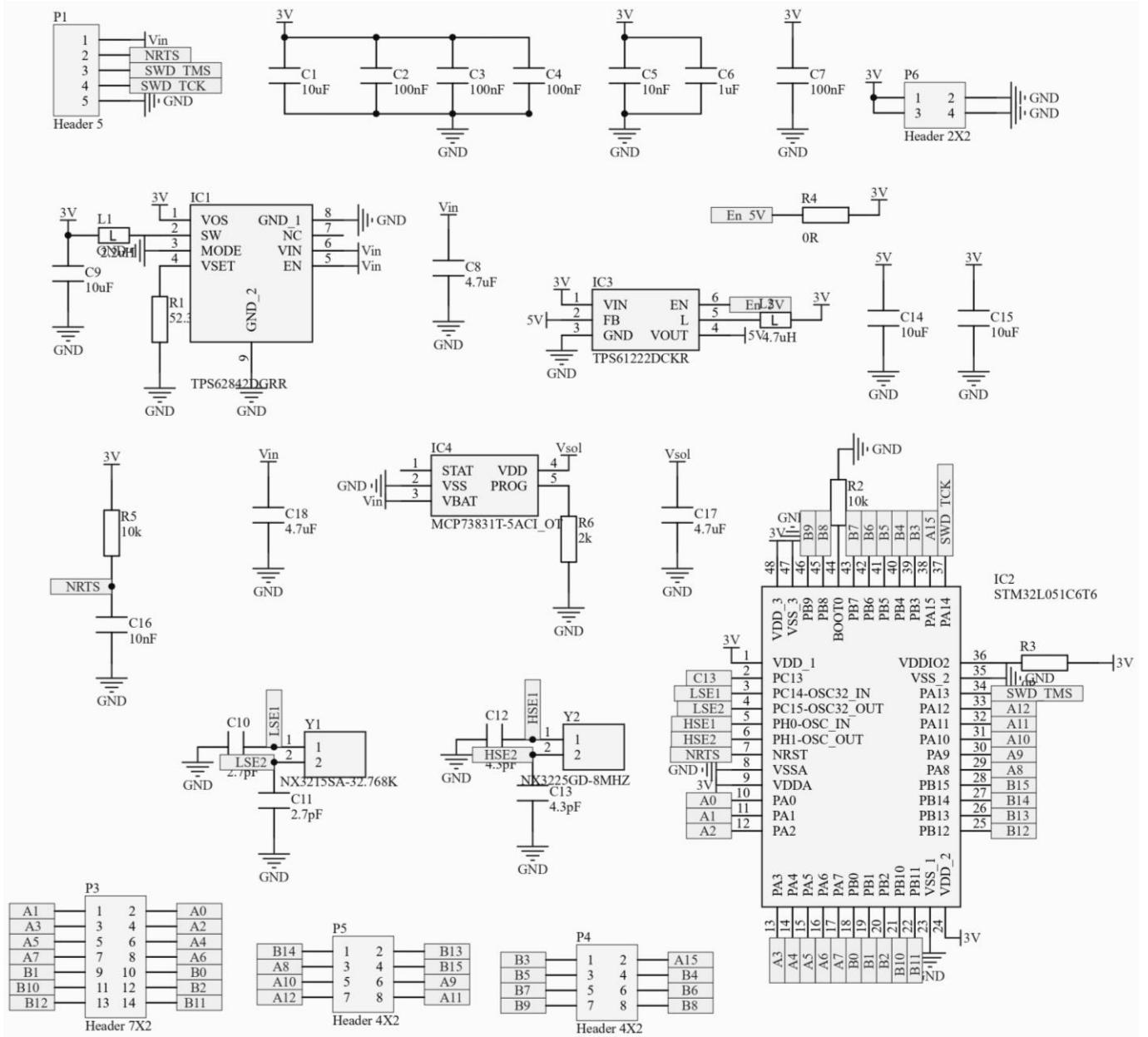
Supplementary Material I 14. Electronic schematic of the data logger for the LQFP-48 package.
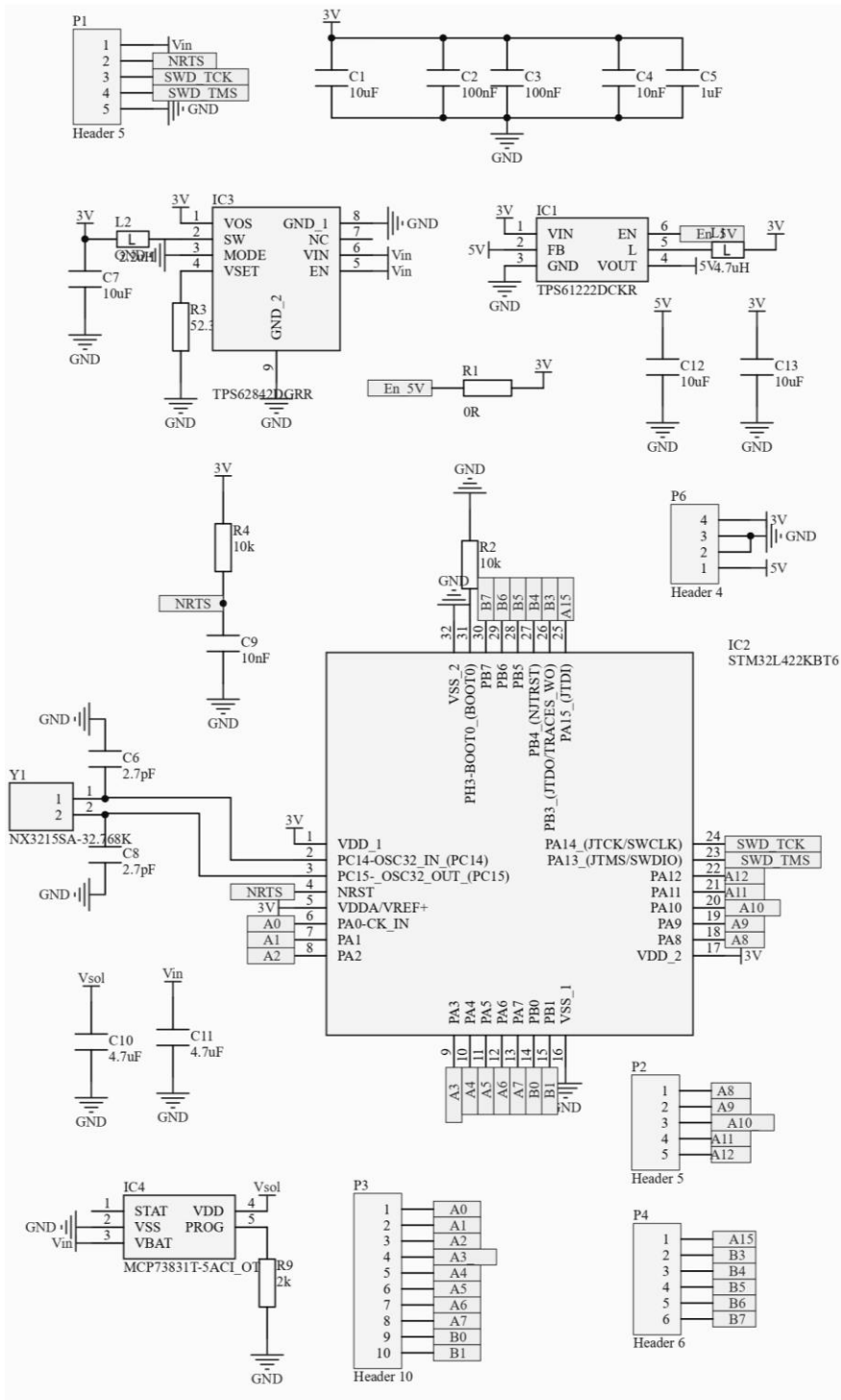
Supplementary Material I 15. Electronic schematic of the data logger for the LQFP-32 package.
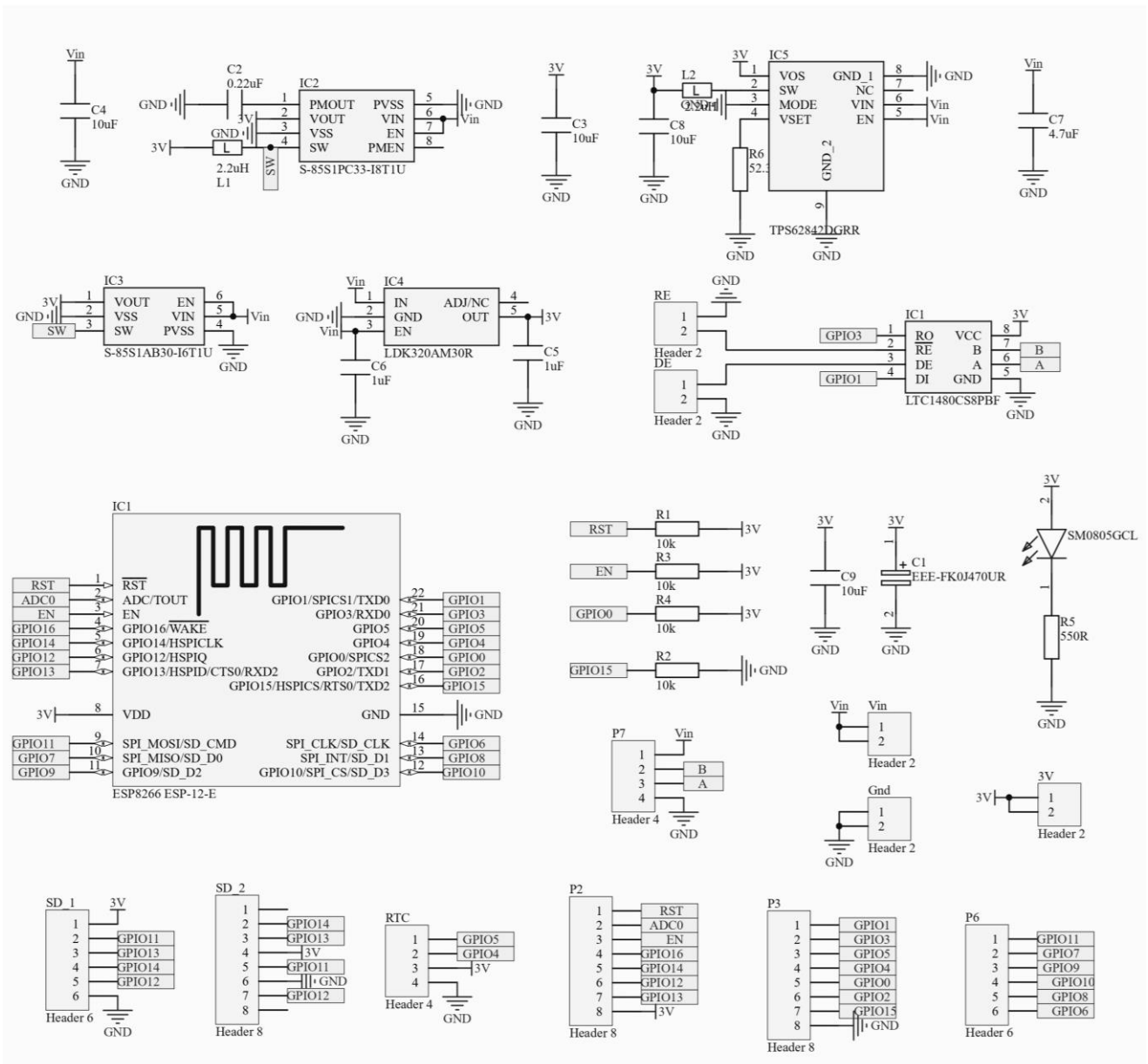
Supplementary Material I 16. Electronic schematic of the data logger with the ESP8266 microcontroller.
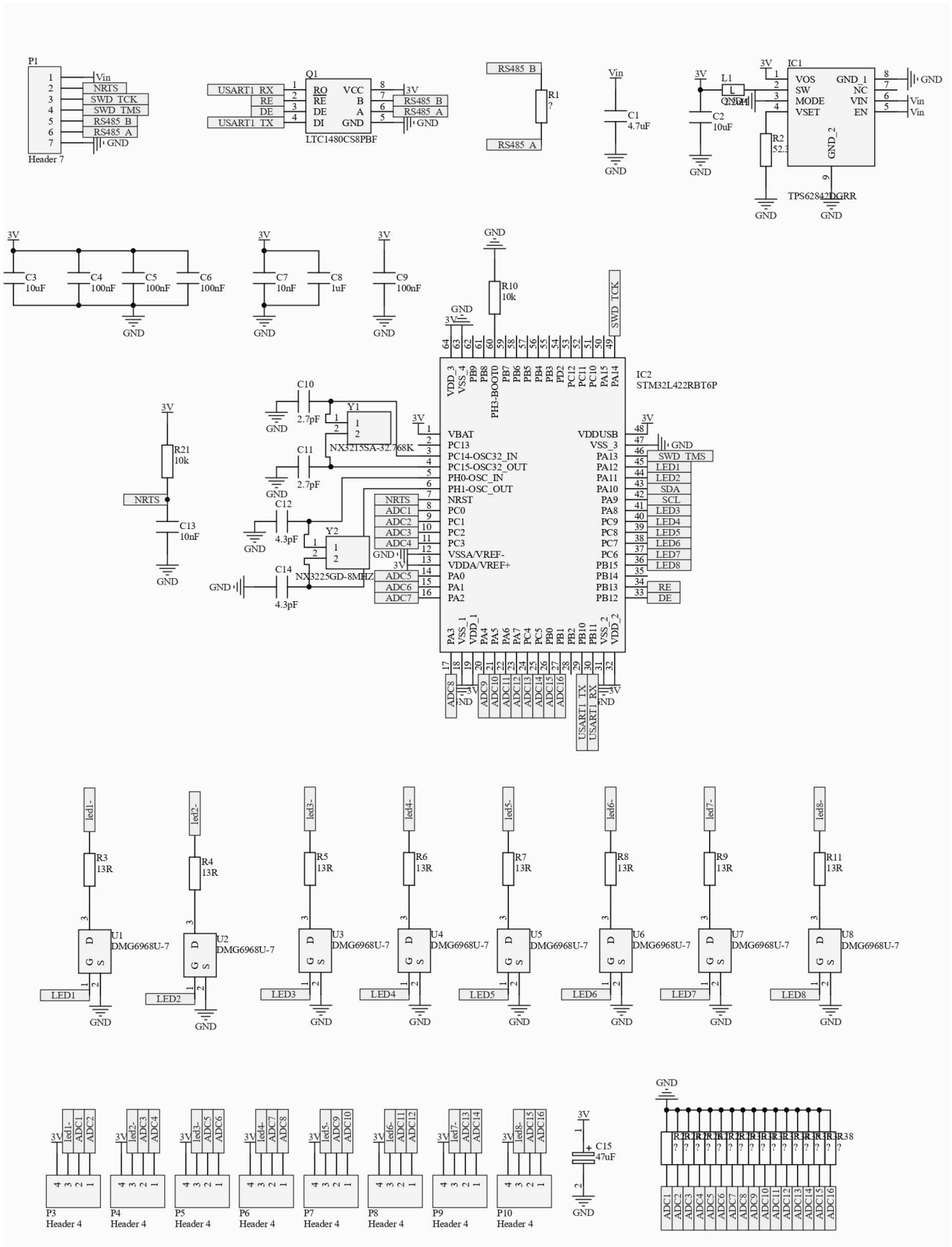
Supplementary Material I 17. Electronic schematic of the anti-biofouling probes.
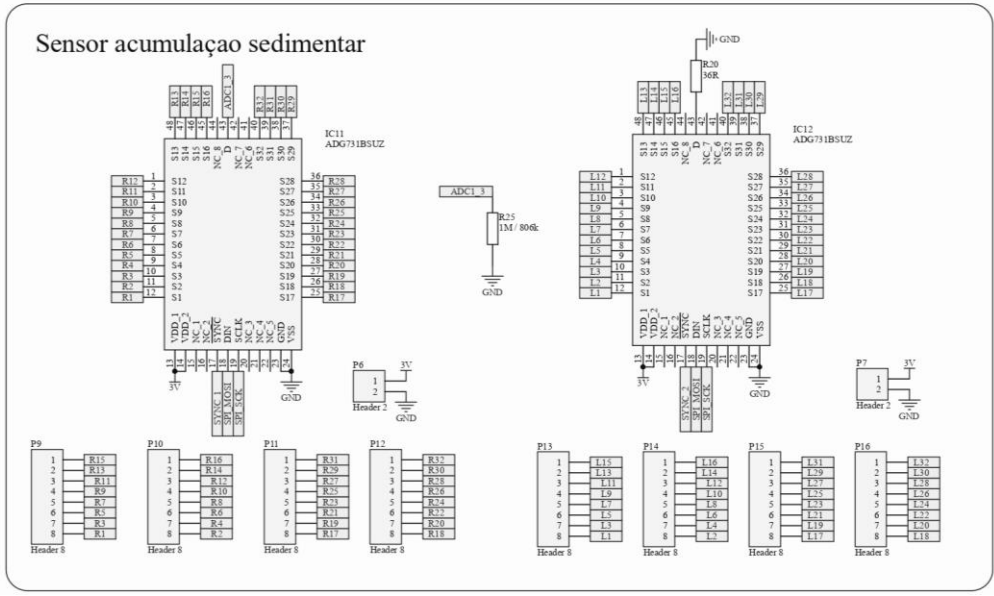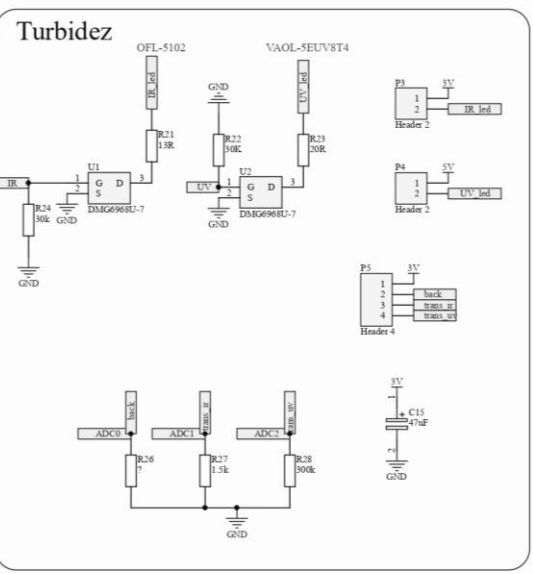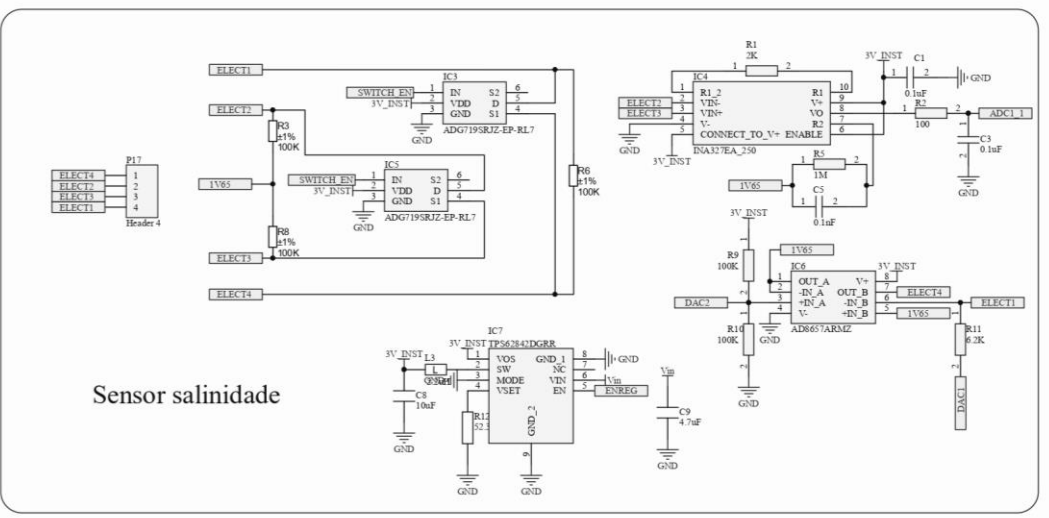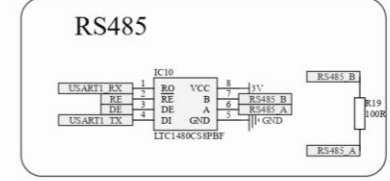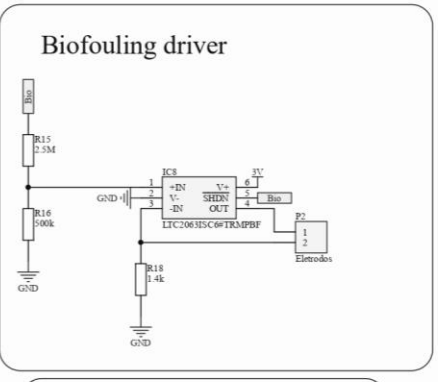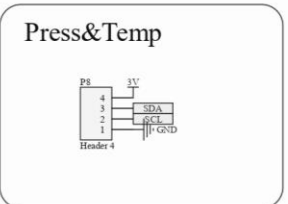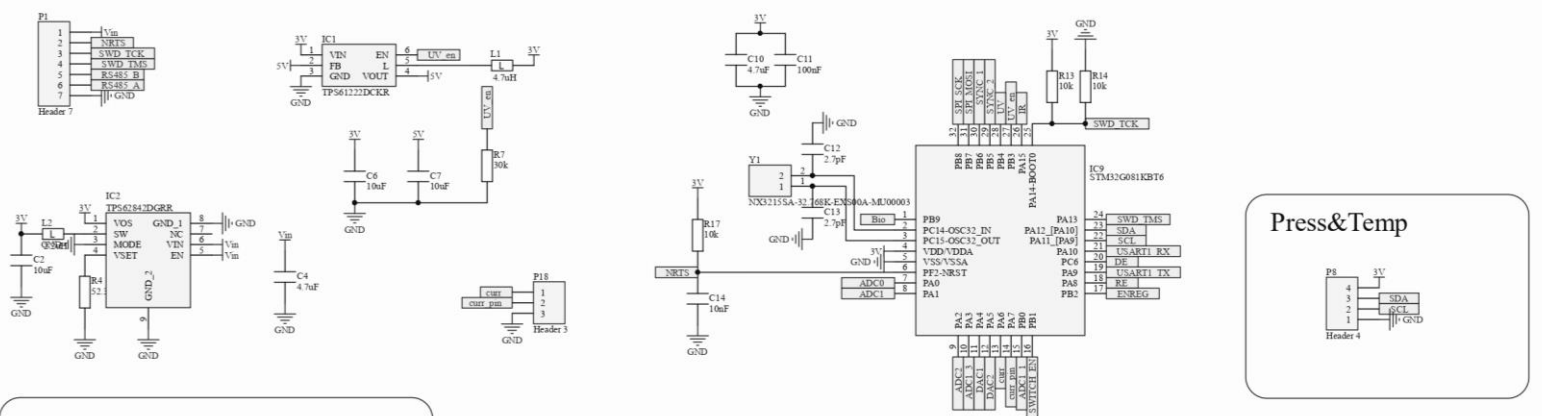
Supplementary Material I 18. Electronic schematic of the multiparameter sensor.
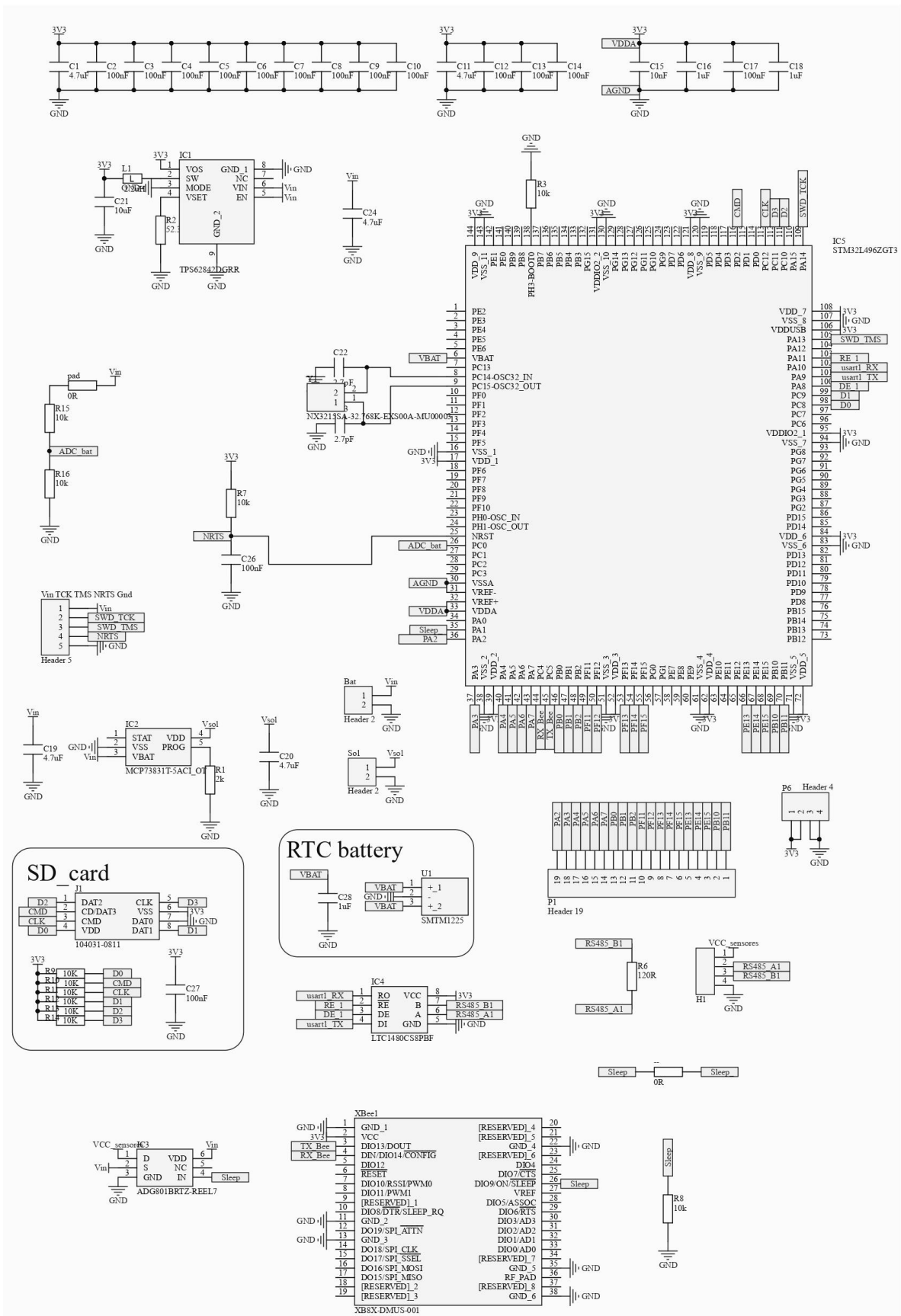
Supplementary Material I 19. Electronic schematic of the data logger with the XBee SX 868.
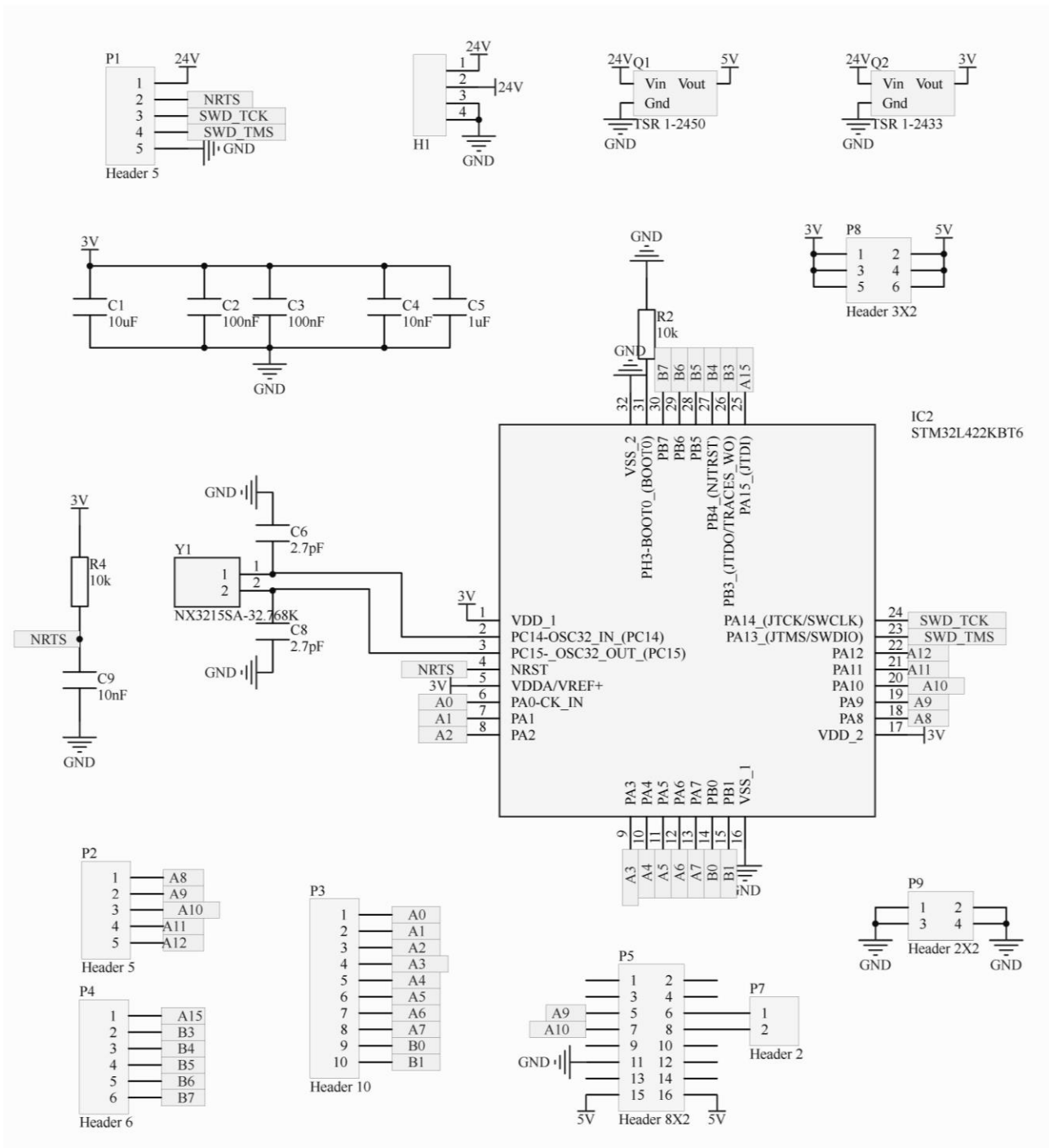
Supplementary Material I 20. Electronic schematic of the microcontroller based on STM processors with UART – ETH converter for K2D project.

SUPPLEMENTARY MATERIAL II – PRINTED CIRCUIT BOARDS
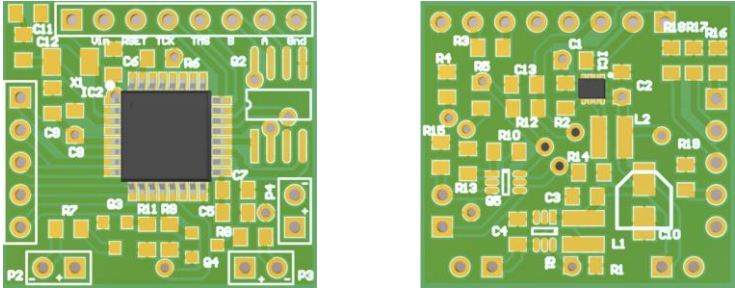
Supplementary Material II 1. Printed circuit board of the SPM Sensor (size: 20 x 25 mm).
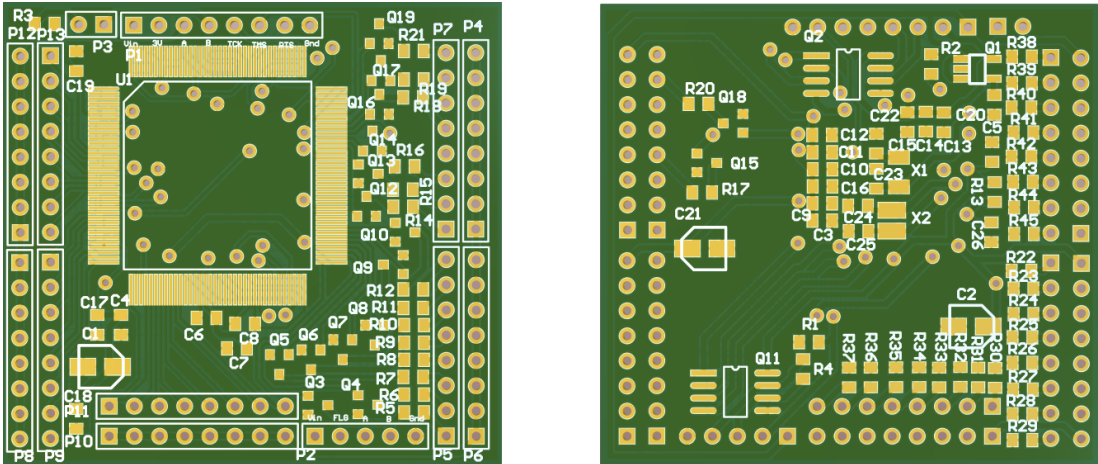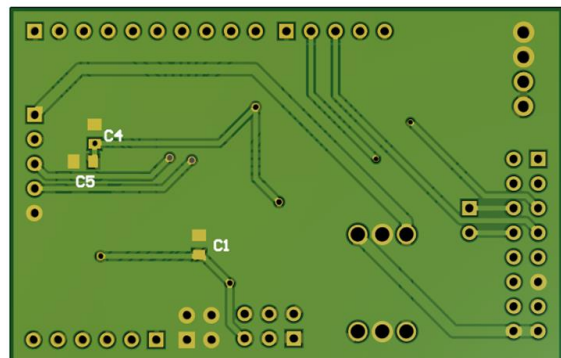

Supplementary Material II 2. Printed circuit board of the TVL Sensor (size: 50 x 47 mm).
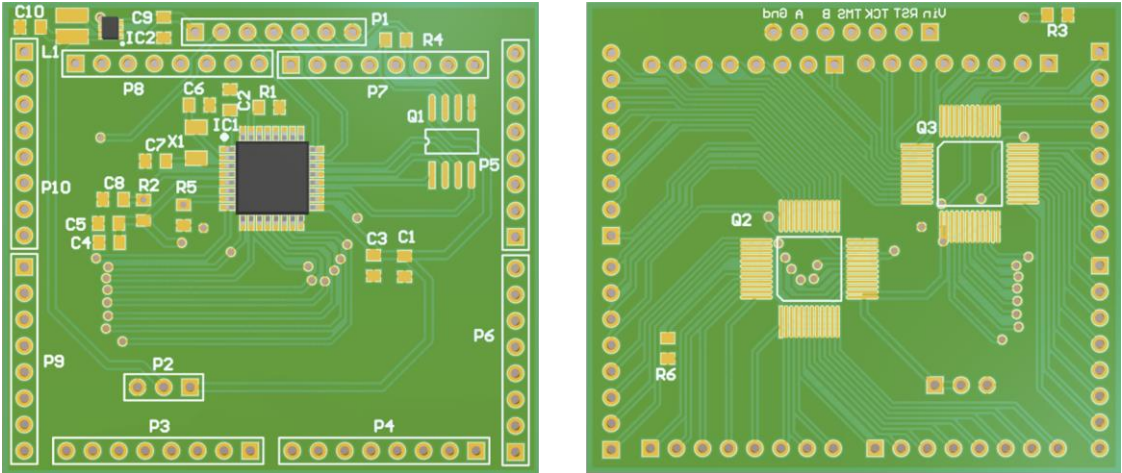
Supplementary Material II 3. Management printed circuit board of the SDE Sensor (size: 52 x 46 mm).
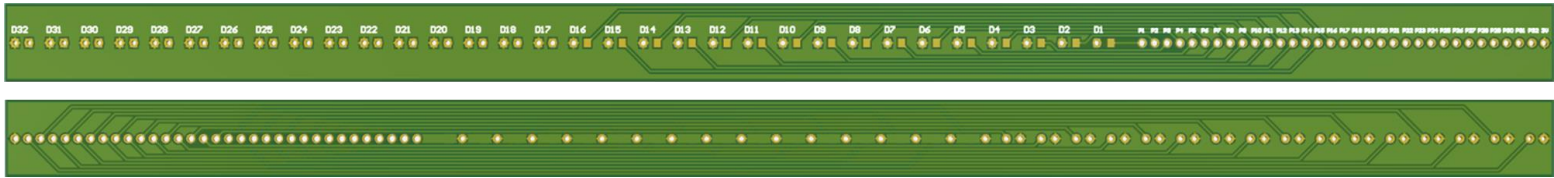
Supplementary Material II 4. Array printed circuit board of the SDE Sensor (size: 222 x 11 mm).
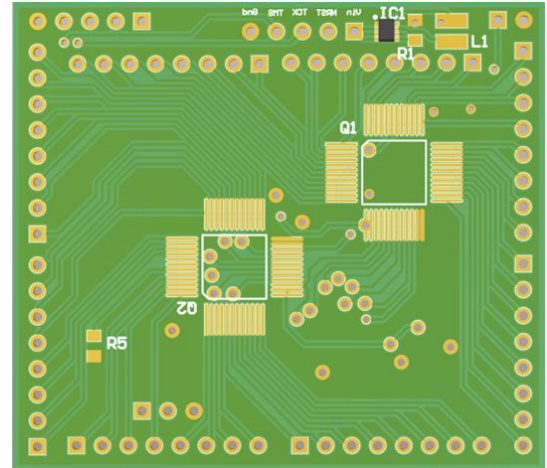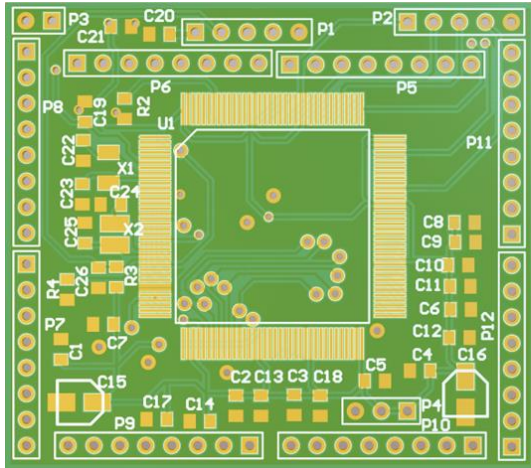
Supplementary Material II 5. Management printed circuit board of the SDE Sensor – portable (size: 52 x 46 mm).
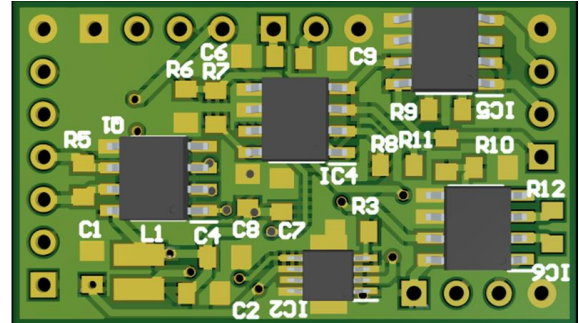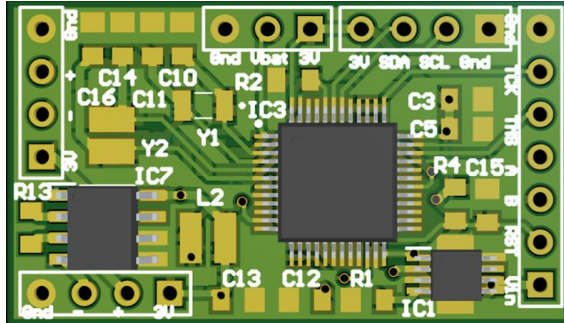
Supplementary Material II 6. Printed circuit board of the MEMS biomimetic current meter (size: 34 x 20 mm).
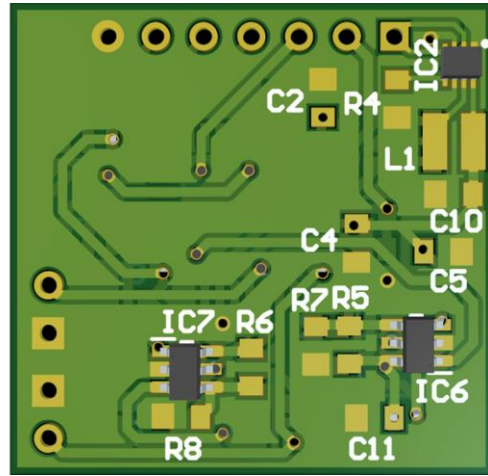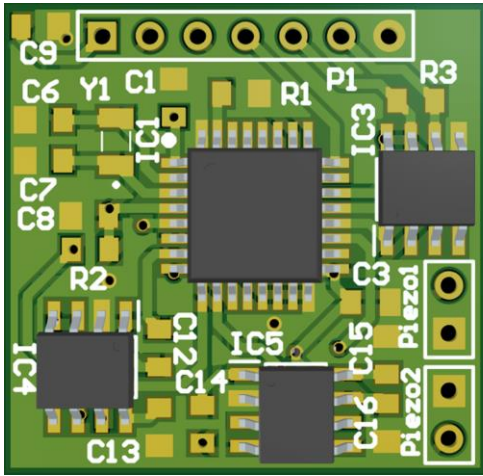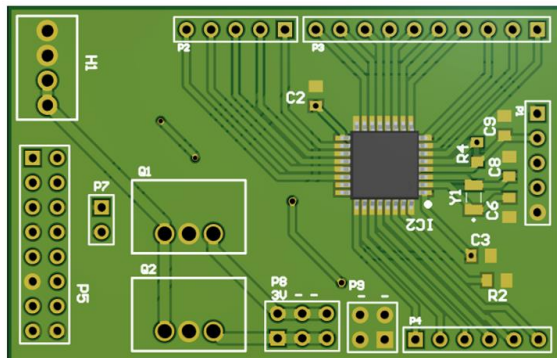
Supplementary Material II 7. Printed circuit board of the acoustic ToF current meter (size: 26 x 25 mm).
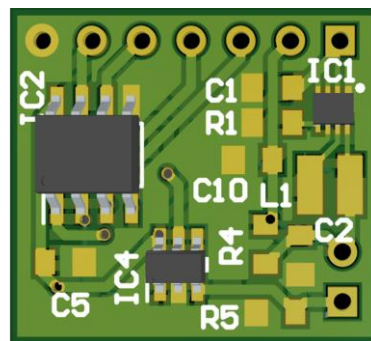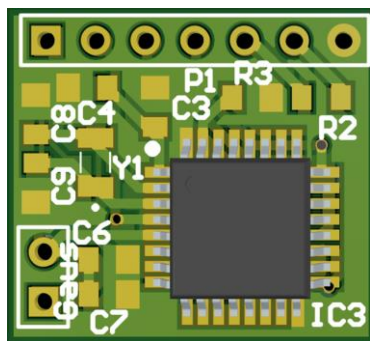
Supplementary Material II 8. Printed circuit board of the first prototype of the SeT sensor using the Flex Sensor (size: 19 x 17 mm).
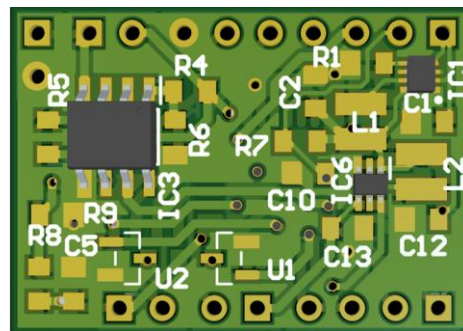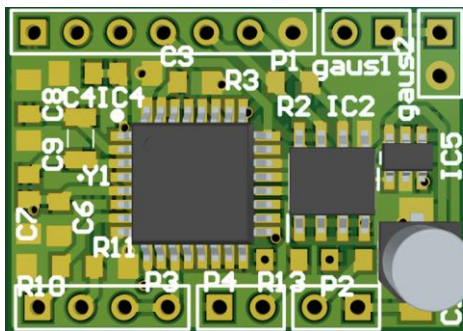
Supplementary Material II 9. Printed circuit board of the second prototype of the SeT sensor using the Flex Sensor (size: 27 x 19 mm).
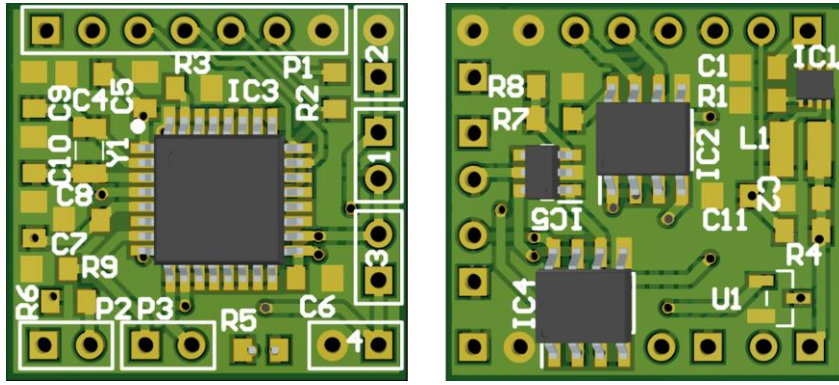
Supplementary Material II 10. Printed circuit board of the SeT sensor (size: 22 x 21 mm).
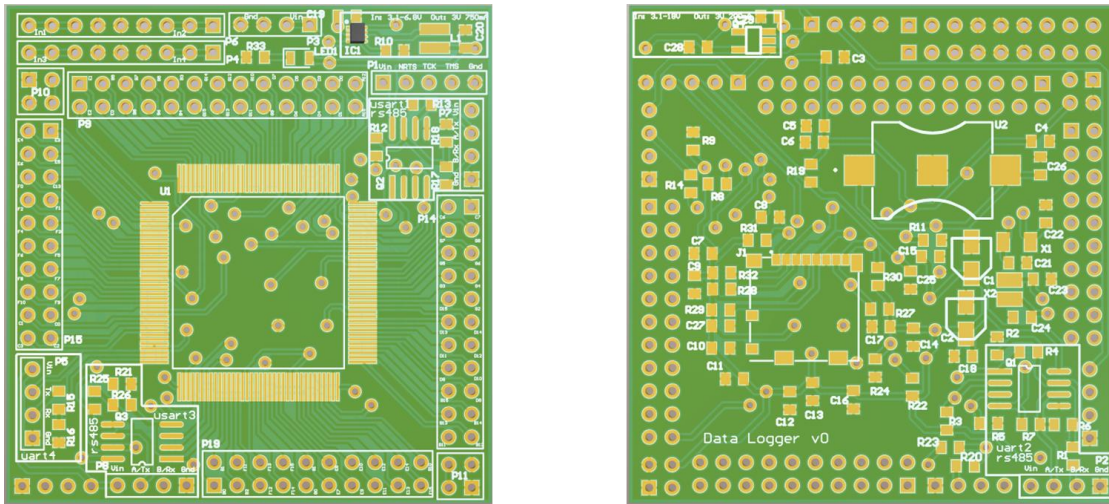
Supplementary Material II 11. Printed circuit board of the data logger with the STM32L496ZG microprocessor (size: 54 x 55 mm).
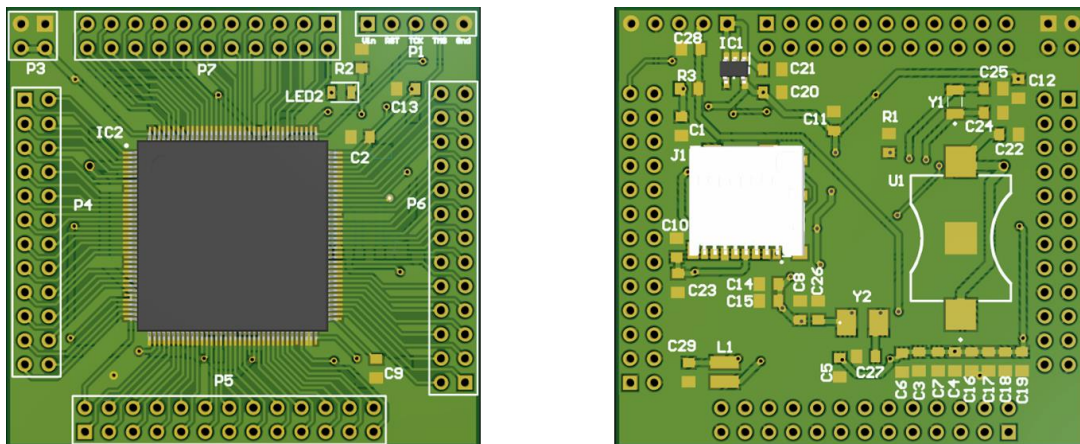
Supplementary Material II 12. Printed circuit board of the data logger with the STM32L552ZET6Q microprocessor (size: 50 x 46 mm).
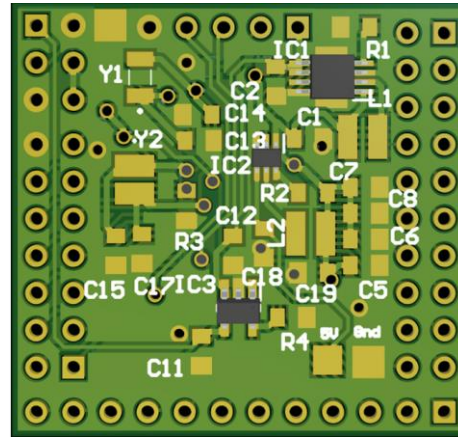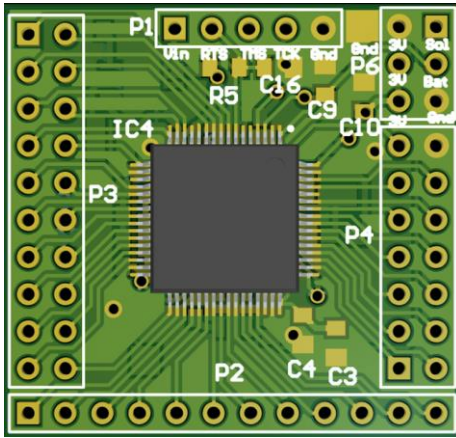
Supplementary Material II 13. Printed circuit board of the data logger with the LQFP-64 package (size: 30 x 31 mm).
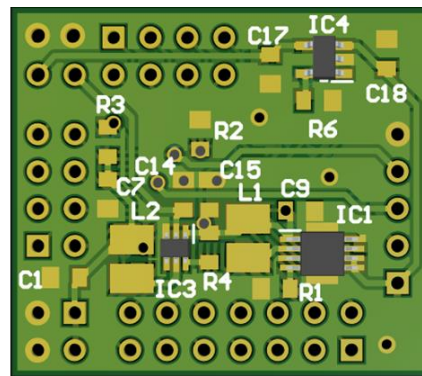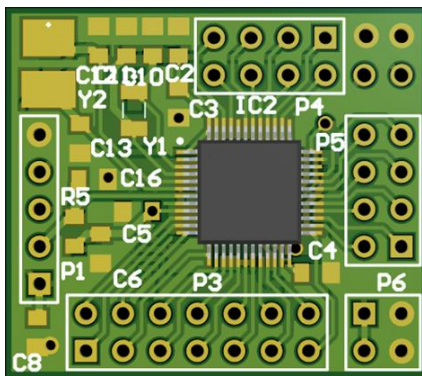
Supplementary Material II 14. Printed circuit board of the data logger with the LQFP-48 package (size: 25 x 29 mm).
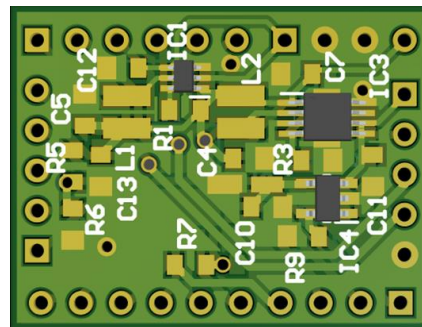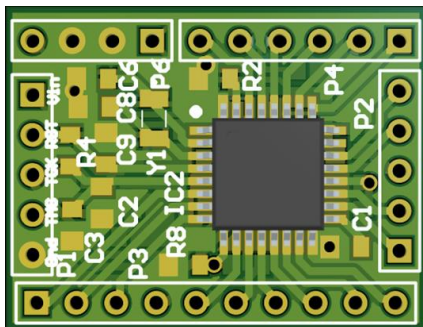
Supplementary Material II 15. Printed circuit board of the data logger with the LQFP-32 package (size: 26 x 20 mm).
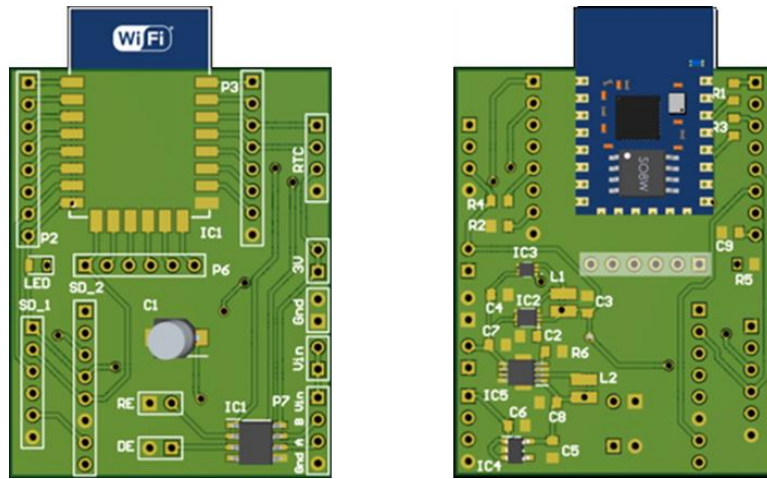
Supplementary Material II 16. Printed circuit board of the data logger with the ESP8266 (size: 37 x 47 mm).
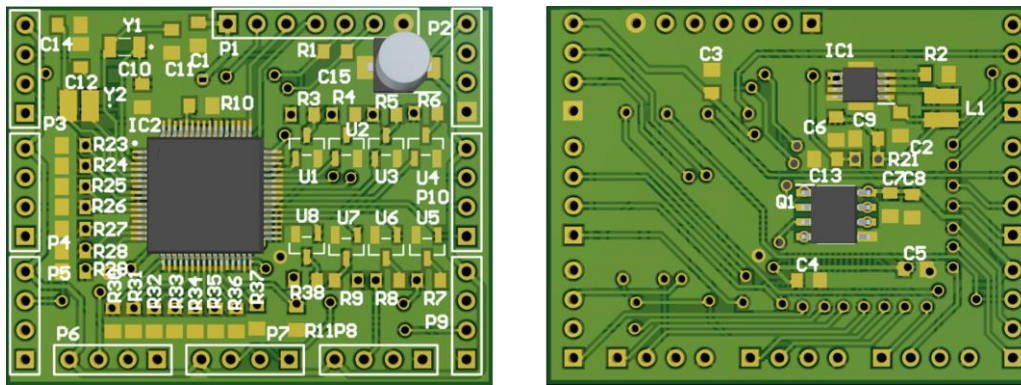
Supplementary Material II 17. Printed circuit board of the anti-biofouling probes (size: 42 x 33 mm).
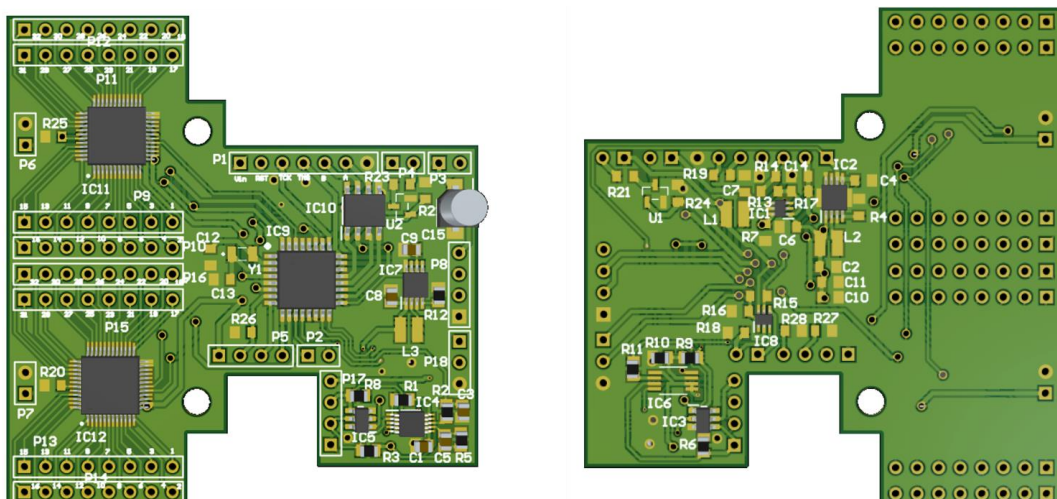
Supplementary Material II 18. Printed circuit board of the multiparameter sensor (size: 56 x 59 mm).
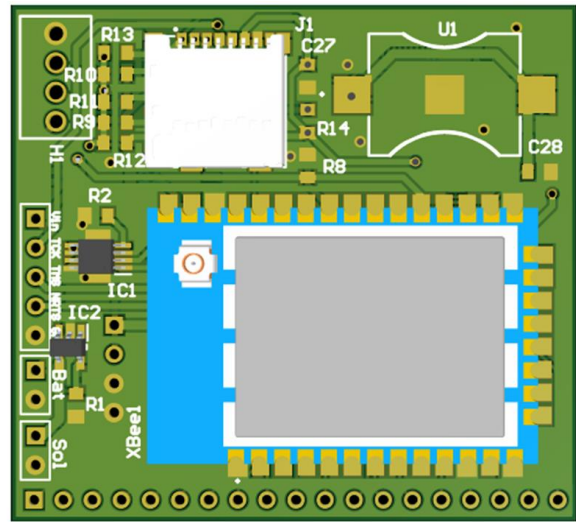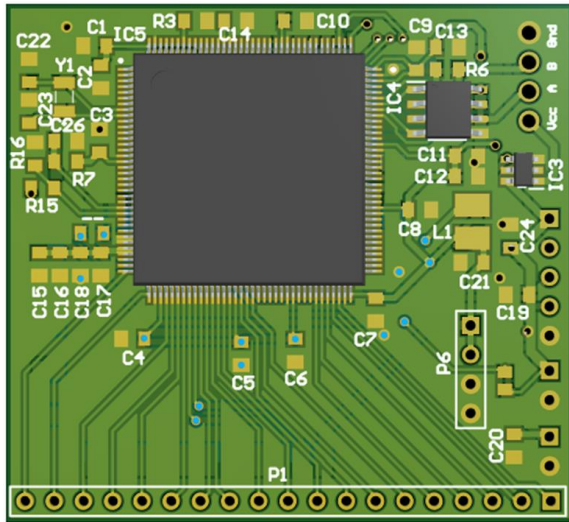
Supplementary Material II 19. Printed circuit board of the data logger with the XBee SX 868 (size: 50 x 45 mm).

Supplementary Material II 20. Printed circuit board of the microcontroller based on STM processors with UART – ETH converter for K2D project.
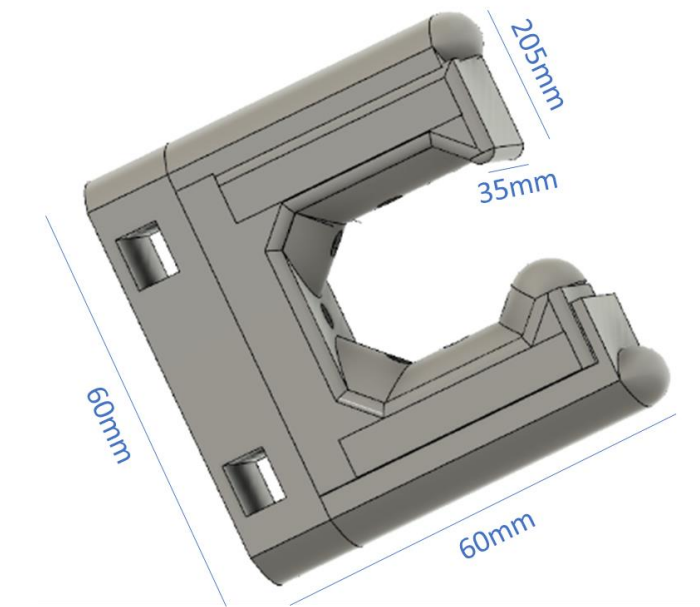
Supplementary Material III 1. SPM Sensor housing in U-shape.
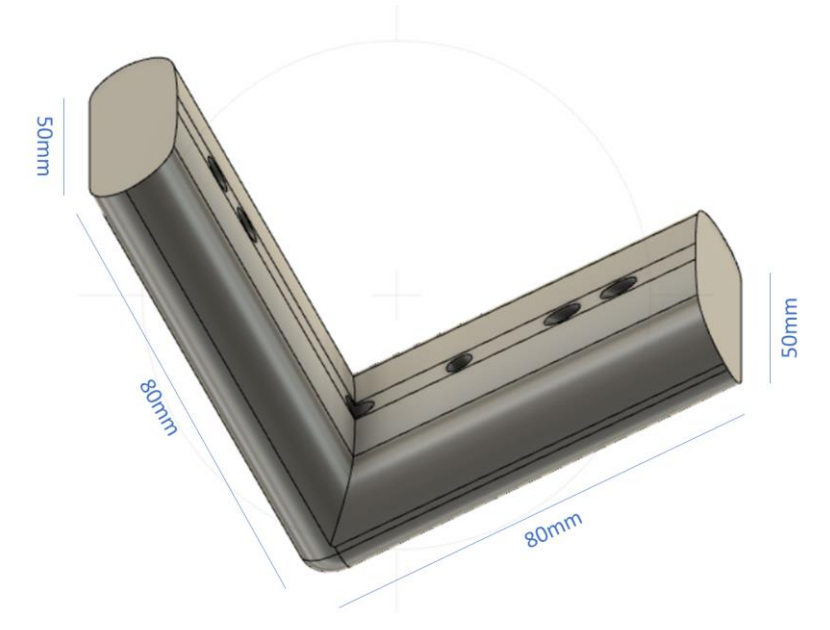
Supplementary Material III 2. SPM Sensor housing in L-shape.
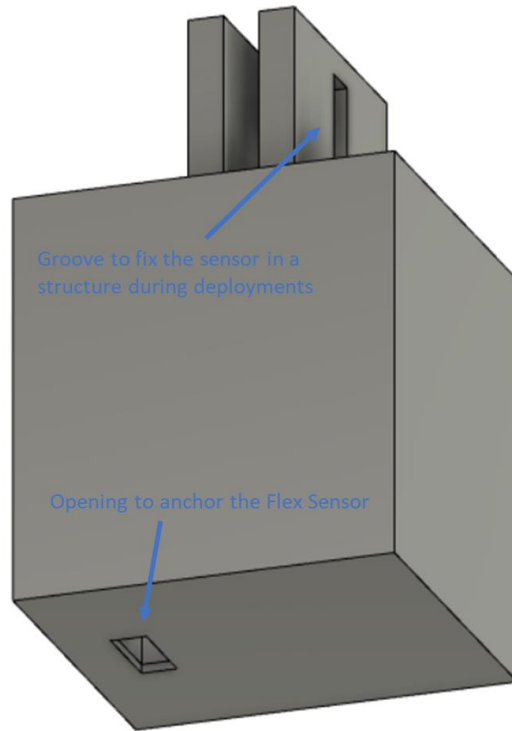
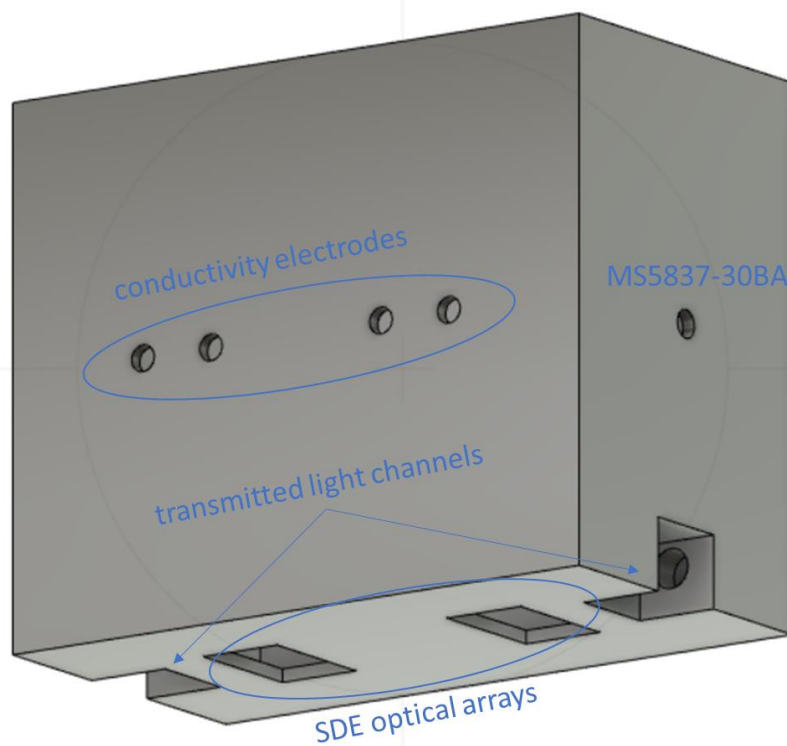Supplementary Material III 3. Sensor housing of the first prototype with the Flex Sensor (box housing size: 40 x 46 x 43 mm).
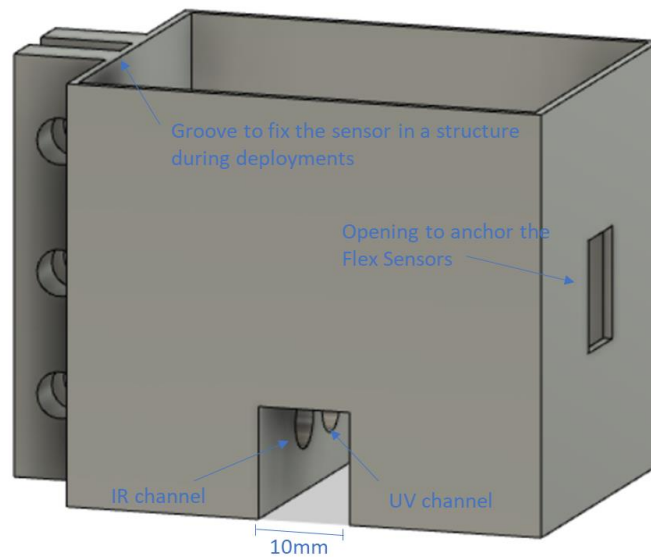
Supplementary Material III 4. Sensor housing of the first second prototype with the Flex Sensor (box housing size: 40 x 45 x 52 mm).
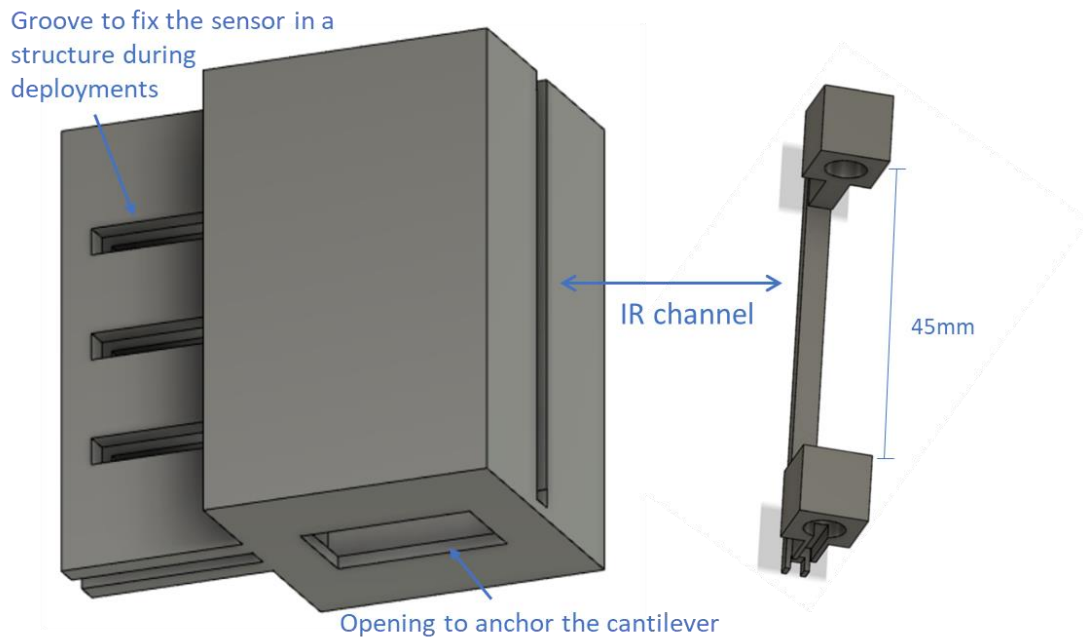
Supplementary Material III 5. Sensor housing of the SeT sensor (box housing size: 72 x 47 x 47 mm).

Supplementary Material III 6. Sensor housing of the multiparameter sensor (box housing size: 82 x 100 x 54 mm).

SUPPLEMENTARY MATERIAL IV — PERMITS, LICENCES AND AUTHORIZATIONS

S. R.

MINISTERIO DA DEFESA NACIONAL
AUTORIDADE MARÍTIMA NACIONAL
CAPITANIA DO PORTO DE VIANA DO CASTELO
DELEGAÇÃO MARITIMA DE ESPOSENDE

DESPACHO Nº 052/2020 DME

Assunto: INSTALAÇÃO DE SENSORES NA FOZ DO CAVADO
Referência: Email de Tiago Matos, de 17AGO 2020 12:04.

1. Em resposta ao Email em referência, **autorizo**, ao abrigo das competências conferidas pelo Decreto-Lei n.º 44/2002, de 2 de março, por um período a contar da data emissão da licença até final do ano de 2020, a montagem de um conjunto de sensores no leito do estuário utilizando um sistema de ancoragem "wombat", para fins de investigação e desenvolvimento que permitem fazer medição de parâmetros da água (salinidade e condutividade, temperatura, pressão e nível de água, turdidez e acumulação sedimentar) na localização requerida e indicada em anexo, mediante o cumprimento dos seguintes condicionalismos.

    a. Para além de condições meteo-oceanográficas favoráveis, designadamente a inexistência de avisos de mau tempo e avisos meteorológicos, a instalação e remoção do sistema apenas poderá ser realizada no arco diurno e com boas condições de visibilidade;

    b. É responsabilidade do requerente garantir a segurança dos intervenientes e a existência dos seguros exigíveis para o equipamento a utilizar;

    c. Que na execução da instalação, operação e remoção do dispositivo seja acautelada a segurança da navegação e a não interferência com as demais atividades em curso;

    d. Que o sistema de ancoragem do dispositivo fique posicionado no leito do rio, conforme preconizado, por debaixo da ponte de acesso ao pontão flutuante, a cerca de 3,5 m da muralha e a uma profundidade de 1,5 m com a maré vazia, submerso a cerca de 1 m da superfície, e seja monitorizado com regularidade a evolução, devendo por questões de segurança ser sinalizado por boia à superfície, que não interfira com as manobras das embarcações que utilizam a parte interior do pontão;

    e. Que a cablagem que liga ao poste para alimentação e comunicação seja revestida por tubo com resistência mecânica adequada, que acautele a segurança de pessoas;

    f. Que seja informado o Parque Natural do Litoral Norte (PNLN) e obtido autorização por parte da Câmara Municipal de Esposende (CME) para o acesso ao pontão flutuante, ligação ao poste de alimentação e instalação do equipamento wi-fi.

2. O requerente deverá fornecer um ponto de contacto (identificação e contacto telefónico), da pessoa que ficará responsável por monitorizar os trabalhos, para que possa ser contactado em caso de necessidade.

Despacho n.º 052/2020 DME
Av. Eng.º Arantes e Oliveira   Página 1 de 2   Nº Telefone 253 961 222
4740-204 ESPOSENDE   delmaresposende.geral@amn.pt

220

3. No início e no fim dos trabalhos de instalação dos sensores deverá ser estabelecido contacto com o Comando Local da Polícia Marítima de Viana do Castelo através do n.º telemóvel 916352353, bem como deverá ser prontamente comunicado qualquer incidente.

4. A não observância das determinações constantes neste despacho, além de constituir infração contraordenacional, prevista e sancionada na alínea j), do n.º 1, do art. 4.º, do Decreto-Lei n.º 45/2002, de 2 de março, pode tipificar contraordenação nos termos do regime sancionatório aplicável.

5. À Repartição Marítima para as subsequentes diligências, sendo os custos suportados pelo requerente nos termos da Portaria n.º 506/2018, de 2 de outubro.

6. Dê-se conhecimento do presente despacho ao PNLN e à CME.

7. A ESV de Esposende para conhecimento.

8. À Polícia Marítima para conhecimento, emissão de correspondente aviso à navegação e ação fiscalizadora.

9. Informe-se o requerente do teor do despacho.

Esposende, 15 de setembro de 2020

O Capitão do Porto,

Luís José Sameiro Matias
Capitão-de-fragata

Supplementary Material IV 1. Legal permit by Delegação Marítima de Esposende da Capitania do Porto de Viana do Castelo for the installation of the monitoring station in the estuary of Cávado River.

Enviado por correio eletrónico para:
matos.tiagoandre@cmems.uminho.pt

À
Universidade do Minho
A/c Dr. Tiago Matos

SUA REFERÊNCIA	SUA COMUNICAÇÃO DE	NOSSA REFERÊNCIA
S/ ref.	07-09-2020 e 24-09-2020	42209/2020/DR-N/DRCNB/DAC

ASSUNTO   AUTORIZAÇÃO PARA INSTALAÇÃO DE SENSORES NO ESTUÁRIO DO RIO CÁVADO
PARQUE NATURAL DO LITORAL NORTE
ANCORADOURO JUNTO AO MUSEU MARÍTIMO DE ESPOSENDE

Em resposta ao pedido de autorização relativo ao assunto em epígrafe (N/ Entrada n.º 71848/2020), e depois de analisado os elementos instrutórios fornecidos, ao abrigo da alínea b) do n.º 1 do artigo 39.º do Regulamento do Plano de Ordenamento do Parque Natural do Litoral Norte, aprovado pela Resolução do Conselho de Ministros n.º 175/2008, **o ICNF autoriza a instalação dos sensores nos termos propostos.**

Mais se informa V. Ex.ª que a presente autorização não dispensa a consulta de outras entidades competentes em razão da matéria, nem substitui as demais licenças, autorizações ou aprovações exigíveis nos termos da lei, bem como caduca decorridos dois anos após a data da sua emissão.

Com os melhores cumprimentos,

O Diretor do Departamento Regional de Conservação da Natureza e da Biodiversidade

Assinado por : **DUARTE JOSÉ FARIA VILAR DE FIGUEIREDO**
Num. de Identificação: BI081074700
Data: 2020.10.16 16:55:55+01'00'

CARTÃO DE CIDADÃO

Duarte Figueiredo

1/1

Supplementary Material IV 2. Authorization by ICNF for the installation of the monitoring station in the estuary of Cávado River.

MINISTERIO DA DEFESA NACIONAL
AUTORIDADE MARÍTIMA NACIONAL
CAPITANIA DO PORTO DE VIANA DO CASTELO
DELEGAÇÃO MARITIMA DE ESPOSENDE

DESPACHO Nº 030/2022 DME

Assunto: INSTALAÇÃO REDE DE SENSORES PARA MONITORIZAÇÃO DO ESTUÁRIO DO CÁVADO

Referência: Email de Tiago Matos (matos.tiagoandre@gmail.pt), de 22JUN2020 13:23.

1. Em resposta ao Email em referência, **autorizo**, ao abrigo das competências conferidas pelo Decreto-Lei n.º 44/2002, de 2 de março, por um período a contar da data emissão da licença até final do ano de 2022, a montagem de uma rede de monitorização no Estuário do Cávado, constituída por 6 conjuntos de sensores que serão instalados no leito do estuário do Cávado, conforme plano em anexo, os quais permitirão registar temporalmente as várias variáveis hidrográficas e perceber a influência do mar no estuário durante os ciclos de marés, mediante o cumprimento dos seguintes condicionalismos.

    a. Para além de condições meteo-oceanográficas favoráveis, designadamente a inexistência de avisos de mau tempo e avisos meteorológicos, a instalação e remoção da rede apenas poderá ser realizada no arco diurno e com boas condições de visibilidade;

    b. É responsabilidade do requerente garantir a segurança dos intervenientes e a existência dos seguros exigíveis para o equipamento a utilizar;

    c. Que na execução da instalação, operação e remoção dos dispositivos seja acautelada a segurança da navegação e a não interferência com as demais atividades em curso;

    d. Que a rede de sensores e restante equipamento de apoio fiquem posicionados conforme informação constante no documento de suporte enviado, e sejam monitorizados com regularidade, devendo por questões de segurança ser sinalizados por boia à superfície (identificada como sendo equipamento científico), que não interfira com as manobras de embarcações;

    e. Que seja informado o Parque Natural do Litoral Norte (PNLN) e obtidas as autorizações das entidades públicas competentes (CM de Esposende e DOCAPESCA - estações 2 e 3, respetivamente) e privadas (Clube Náutico de Fão e Clube Náutico de Gemeses – estações 4 e 6, respetivamente).

Despacho n.º 030/2022 DME
Av. Eng.º Arantes e Oliveira
4740-204 ESPOSENDE

Página 1 de 3

Nº Telefone 253 961 222
delmaresposende.geral@amn.pt

223

2. O requerente deverá fornecer um ponto de contacto (identificação e contacto telefónico), da pessoa que ficará responsável por monitorizar os trabalhos, para que possa ser contactado em caso de necessidade.

3. No início e no fim dos trabalhos de instalação da rede deverá ser estabelecido contacto com o Comando Local da Polícia Marítima de Viana do Castelo (CLPM-VC), através do número permanente 916 352 353, bem como deverá ser prontamente comunicado qualquer incidente.

4. A não observância das determinações constantes neste despacho, além de constituir infração contraordenacional, prevista e sancionada na alínea j), do n.º 1, do art. 4.º, do Decreto-Lei n.º 45/2002, de 2 de março, pode tipificar contraordenação nos termos do regime sancionatório aplicável.

5. À Repartição Marítima para as subsequentes diligências, sendo os custos suportados pelo requerente nos termos da Portaria n.º 506/2018, de 2 de outubro.

6. Dê-se conhecimento do presente despacho ao PNLN, à CM Esposende e à DOCAPESCA.

7. A ESV de Esposende para conhecimento.

8. À Policia Marítima para conhecimento e emissão de correspondente aviso à navegação.

9. Informe-se o requerente do teor do despacho.

Esposende, 23 de junho de 2020

O Capitão do Porto,

Assinado por: **RUI PEDRO GOMES FERNANDO DA SILVA LAMPREIA**
Num. de Identificação: 09134663
Data: 2022.06.23 14:25:56+01'00'

CARTÃO DE CIDADÃO

Rui Pedro Gomes Fernando da Silva Lampreia
Capitão de fragata

ANEXO: Rede de monitorização do estuário do Cávado

2

ANEXO

Rede de monitorização do estuário do Cávado

Despacho n.º 030/2022 DME
Av. Eng.º Arantes e Oliveira
4740-204 ESPOSENDE

Página 3 de 3

Nº Telefone 253 961 222
delmaresposende.geral@amn.pt

Supplementary Material IV 3. Legal permit by Delegação Marítima de Esposende da Capitania do Porto de Viana do Castelo for the installation of the monitoring network in the estuary of Cávado River.

REPÚBLICA
PORTUGUESA
AMBIENTE E
AÇÃO CLIMÁTICA

ICNF
Instituto da Conservação
da Natureza e das Florestas

Enviado por correio eletrónico para:
matos.tiagoandre@cmems.uminho.pt

À
Universidade do Minho
A/c Dr. Tiago Matos

SUA REFERÊNCIA	SUA COMUNICAÇÃO DE	NOSSA REFERÊNCIA
S/ ref.	07-09-2020 e 24-09-2020	42209/2020/DR-N/DRCNB/DAC

ASSUNTO   AUTORIZAÇÃO PARA INSTALAÇÃO DE SENSORES NO ESTUÁRIO DO RIO CÁVADO
PARQUE NATURAL DO LITORAL NORTE
ANCORADOURO JUNTO AO MUSEU MARÍTIMO DE ESPOSENDE

Em resposta ao pedido de autorização relativo ao assunto em epígrafe (N/ Entrada n.º 71848/2020), e depois de analisado os elementos instrutórios fornecidos, ao abrigo da alínea b) do n.º 1 do artigo 39.º do Regulamento do Plano de Ordenamento do Parque Natural do Litoral Norte, aprovado pela Resolução do Conselho de Ministros n.º 175/2008, **o ICNF autoriza a instalação dos sensores nos termos propostos.**

Mais se informa V. Ex.ª que a presente autorização não dispensa a consulta de outras entidades competentes em razão da matéria, nem substitui as demais licenças, autorizações ou aprovações exigíveis nos termos da lei, bem como caduca decorridos dois anos após a data da sua emissão.

Com os melhores cumprimentos,

O Diretor do Departamento Regional de Conservação da Natureza e da Biodiversidade

Assinado por : **DUARTE JOSÉ FARIA VILAR DE FIGUEIREDO**
Num. de Identificação: BI081074700
Data: 2020.10.16 16:55:55+01'00'

CARTÃO DE CIDADÃO
• • • •

Duarte Figueiredo

1/1

Supplementary Material IV 4. Authorization by ICNF for the installation of the monitoring network in the estuary of Cávado River.

Sediment Deposition and Erosion
Sensor

USER MANUAL

matos.tiagoandre@gmail.com

Universidade do Minho · CMEMS UMINHO CENTER FOR MICROELECTROMECHANICAL SYSTEMS · nextsea

Index

2

Parts of the Sensor
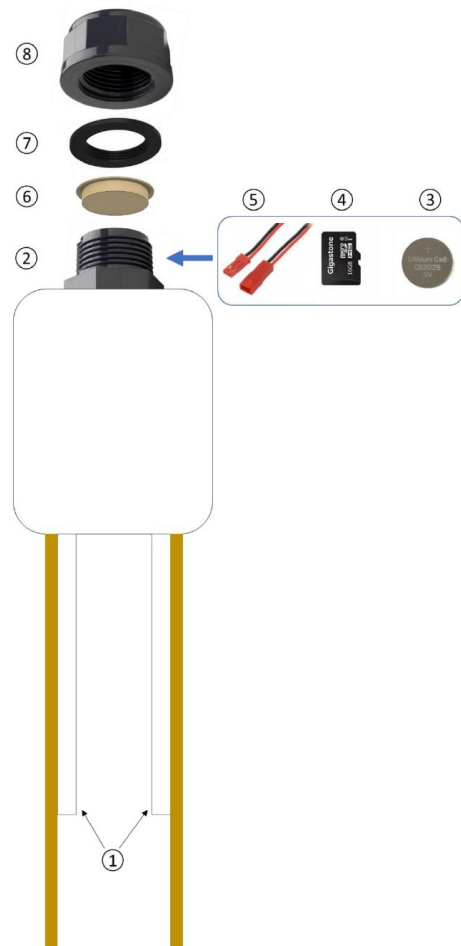
1) **Sensor's optical nodes**

An array of 32 LEDs and 32 photodetectors to measure sediment accumulation and erosion.

To be buried in the streambed. Please see *How to deploy the sensor* for more considerations.

2) **Watertight capsule**

Watertight capsule that comprises the electronics: coin battery for the clock (3), microSD card (4) and battery connectors (5).

3) **Coin battery**

This is a standard 3V coin battery normally used in watches. It keeps the date and time when the sensor is not supplied.

This battery is expected to last for years. See *How to replace the clock battery* if you need to change the battery.

4) **MicroSD card**

Standard microSD card to record the monitoring data. The sensor only works with 8Gb, 16Gb and 32Gb cards. See *How to replace the microSD card* for more considerations.

When the sensor is recording measurements, it will save one txt file per day with the file name: *month_day*.txt. See *How to process the monitoring data* for more considerations.

5) **Battery connector**

When this connector is plugged the sensor is supplied and takes measurements. Unplug the connector when the sensor is not being used to save the battery.

This connector is also used to charge the sensor. See *How to charge the sensor* for more considerations.

6) **Silicone cover**

When preparing the sensor to be deployed, insert all the electronics (3-5) in the capsule (2) and close it with this silicone cover. Its function is only to be sure that everything fits inside the capsule before closing it with the cap (8) and that the electronics are not damaged during this procedure.

7) **Sealant o'ring**

This sealant is the most important part to prevent water to enter the capsule. Put it in the bottom of the cap (8) before closing the sensor.

Never deploy the sensor without this sealant or the sensor can be damaged if water enters the capsule.

8) **Sensor cap**

Close the cap to the end of the capsule (2) before submerging the sensor into the water.

## How to set a new date and time

You can set a new date and time anytime you need before deploying the sensor. For that, you need to create a *date.txt* file on the microSD card with the desired date and time in this format: "*day/month/year hours:minutes:seconds*".

After creating the file, remove the microSD card from the computer and put it back on the sensor. Plug the battery connector, wait 1 or 2 seconds, and unplug the connector.

To make sure that the process worked, insert the microSD card again into your computer and you should have one txt file with one measurement and the new date and time.

Example step by step:

1) Remove the microSD card from the sensor and insert it into your computer.
2) Open the microSD card directory (My computer -> SDHC (E:)).
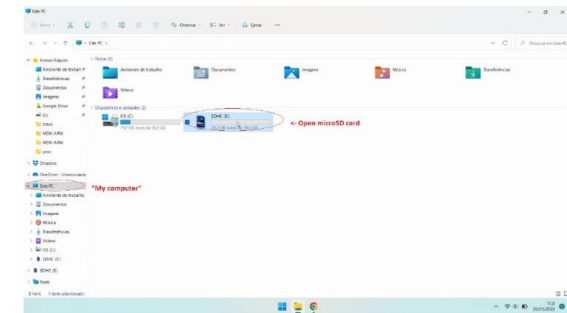
3) Create e new *txt file* named *date* (new->text document; date.txt)
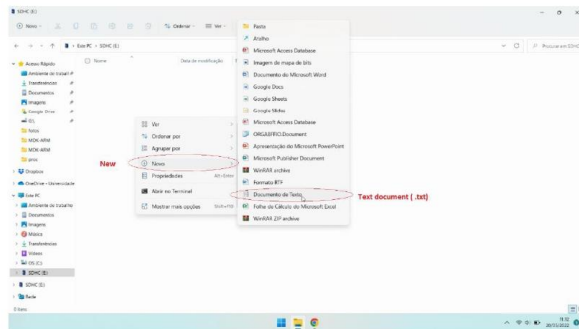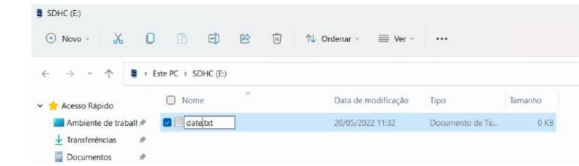
4) Open the date.txt file and write the date and time in the format:

day/month/year hour:minutes:seconds
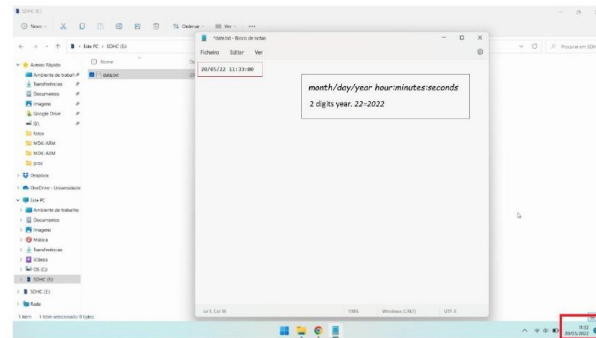
5) Close the date.txt file and save it.

6) Remove the SD card from the computer and put it in the sensor.

7) Plug the battery connector.

8) Wait for 2 seconds and unplug the battery connector.

9) To check if the operation worked, remove the SD card from the sensor and insert it into the computer again. You should have a file in the format *month_day.txt* with the new date and time and one measurement. The date.txt is automatically deleted during the operation.
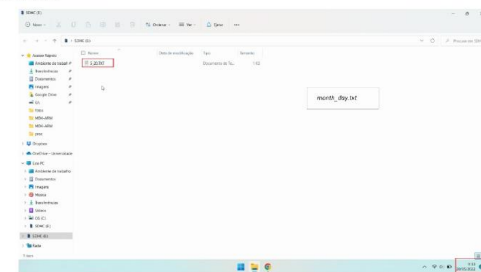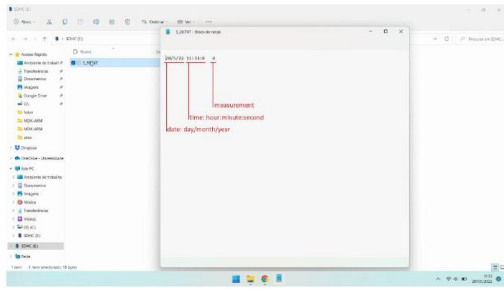
How to change the sampling frequency

By default, the sensor is taking measurements every 15 minutes. To change the sampling frequency you need to create a *time.txt* file in the microSD card with the desired sampling period (in minutes).

Example step by step:

1) Remove the microSD card from the sensor and insert it into your computer.
2) Open the microSD card directory (My computer -> SDHC (E:)).
3) Create e new *txt file* named *time* (new->text document; time.txt)
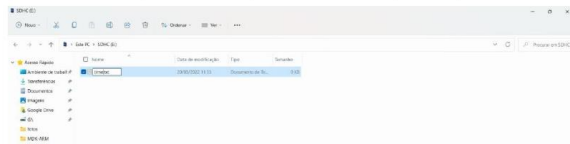
4) Open the time.txt file and write the desired sampling period.
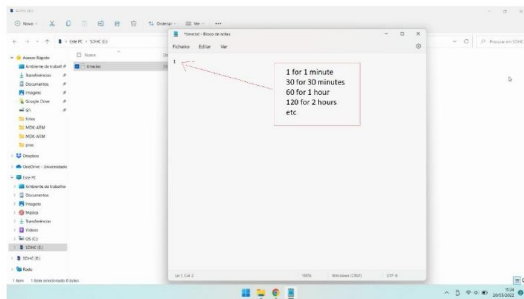
5) Save the file, remove the SD card and insert it into the sensor.

If the time.txt is not changed, the sensor will take measurements at the defined sampling period.

If the time.txt does not exist, the sensor will take measurements at each 15 minutes.

Example for a sampling period of 1 minute:
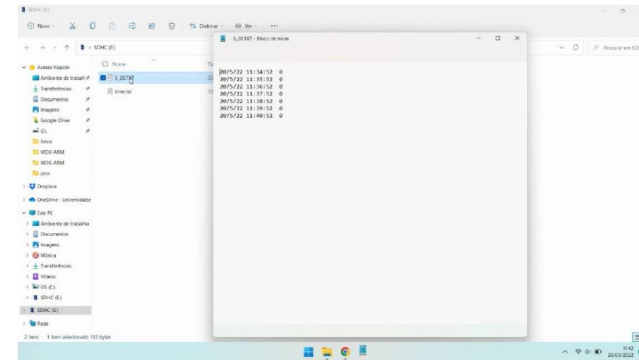
With a sampling period of 1 minute, the sensor is fully charged and is expected to take continuous measurements for 290 days.

Estimation of the battery life for different sampling periods:
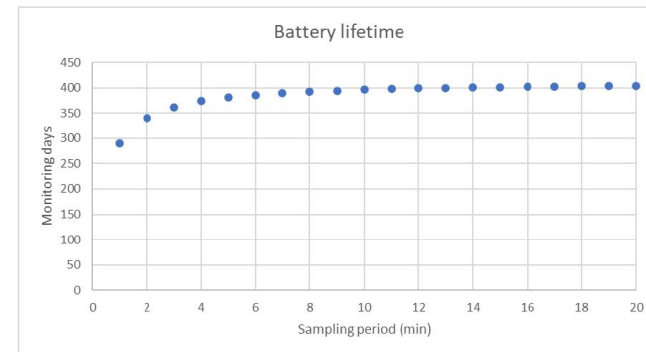
How to deploy the sensor

1) Make sure you have the microSD card in the sensor.

2) Plug the battery connector (the sensor will start to record measurements at this time).

3) Put the microSD and connector inside the capsule and close it with the silicone cover.

4) Put the sealant o'ring inside the cap. <u>Never submerge the sensor without the sealant!</u>

5) Grease the capsule, cap and sealant with vaseline (this step is optional, but it makes it easier to close and open the cap).

6) Close the sensor with the cap till the end (the use of a spanner or a pipe wrench is advisable).

7) Use a security rope on the hook if you want to. If the sensor becomes loose from the stream floor, it will be secured by this rope, and you can recover it.


8) Burry the sensor in the streambed with half of the optical nodes covered with sand. This way it can measure sediment deposition (more nodes covered) and erosion (nodes uncovered).
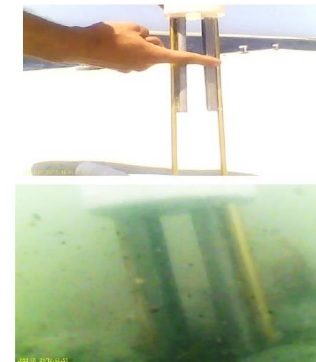
How to process the monitoring data

Once the sensor is recovered from the field tests the microSD card will contain the record of the measurements. During the tests, the sensor will be taking the measurements and saving them in a .txt file per day with the filename format: *month_day.txt*.
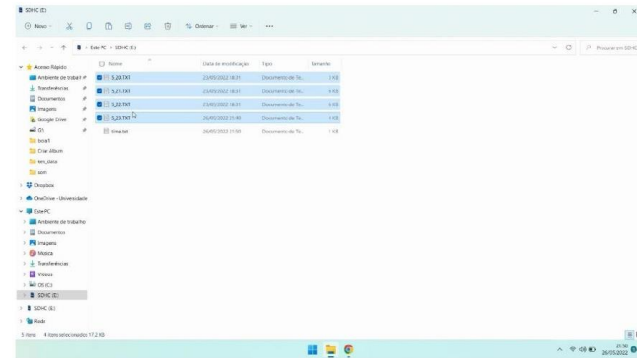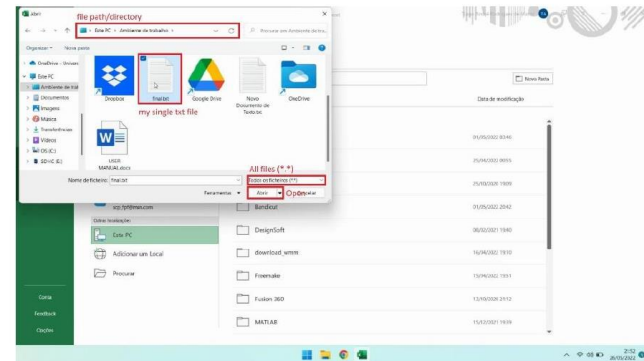

The first thing to do is to merge all the files into one. You can do it manually by copying and pasting all the files into a new .txt file.
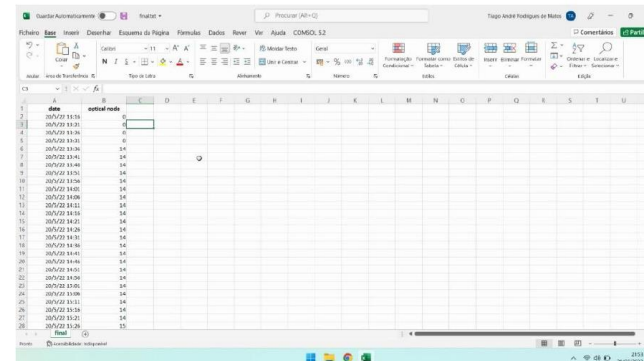
With all data in one single file, open it using Excel (Excel-> Open).
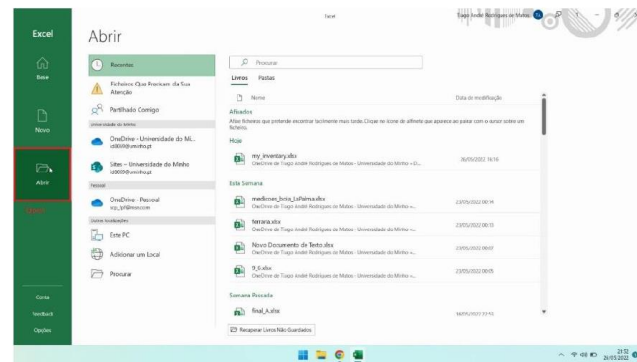
Go to the single txt file directory, select **All files (*.*)**, and open.


You will have a sheet with the date and time in column A and the measurement in column B.

After this point, you can process the data as you want. It is recommended to zero the sensor to the initial point, so it is easier to see when there is sediment deposition in the streambed (positive values) or erosion (negative values).

In the example of the image above, the first 4 measurements are 0 (at this time the sensor was outside the water) so I'll just delete it. The next value is 14 (which means that the bottom 14 nodes are covered with sand) and I'll use it as my zero for this experiment.
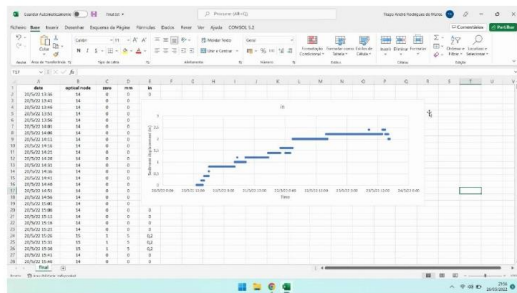
Column C is Column B-14.
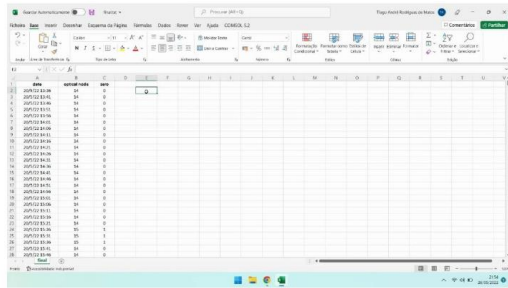
After the sensor is zeroed, convert the node number to a measuring unit. Each node is displaced 5milimeters (≈0.19 in). Multiply your length unit by the node measurement.

Column D is Column C * 5mm. Column E is Column C*0.2 in.
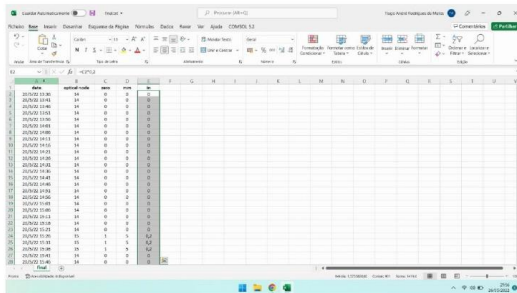

Data Plot:

How to clean the sensor

There are no major precautions to have when it is time to clean the sensor.

After recovering the sensor from the in-situ deployment, clean the optical arrays with fresh water and use a soft cleaning cloth if needed.

After a long time or consecutive deployments, there is a chance for the surface of the optical array to become a white colour. To clean it, apply water and scratch the surface with water sandpaper (the white material will be removed).

How to charge the sensor

1) Connect the battery charger to the sensor connector.
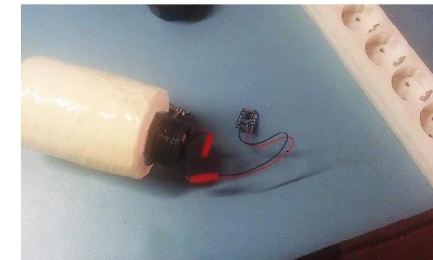
2) Use a micro-USB cable to connect the battery charger to any USB 5V Power supply (you can use a computer USB Port, Phone charger, power bank, etc).

A red light will turn on while the sensor is charging.

A blue light will turn on when the sensor is fully charged. This process can take some hours to more than a day, depending on the remaining charge of the sensor.
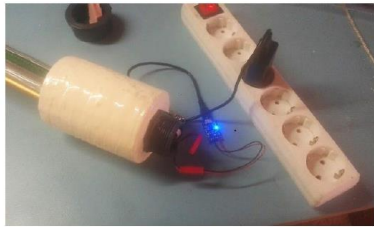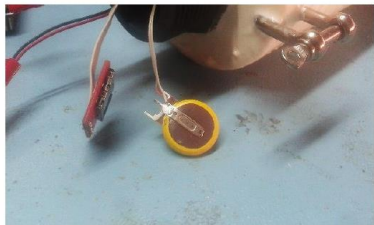
How to replace the clock battery

The sensor has a 3V coin battery inside the capsule that is used to keep the date and time when the sensor is not supplied. This clock battery is like the ones that we use in our watches so after some time (years) it must be changed.

You'll need to change the clock battery when the sensor stops to have a date and time. The sensor will keep taking measurements as before, but the date and time will be frozen as *00/00/00 00:00:00*.

When this happens, just buy another 3V coin battery and connect it to the clock wires (red for +, white for -). You can solder if the new battery has a holder or use duct tape to make the contacts.

Cover all the metal parts of the coin battery with duct tape and put it at the bottom of the capsule. You'll not need it for another 2/3 years.
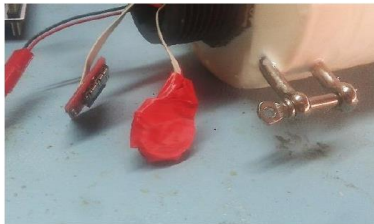
How to replace the microSD card

Any 8Gb, 16Gb or 32Gb can be used in the sensor. You can replace the microSD card with another one anytime.

If you replace the microSD card but the sensor is not working, that's because the microSD card is not formatted as FAT32.

How to format the microSD card in FAT32:

1) Insert the microSD card into your computer.
2) Go to *my computer*, right-click on the *SD card directory* and select *format*.
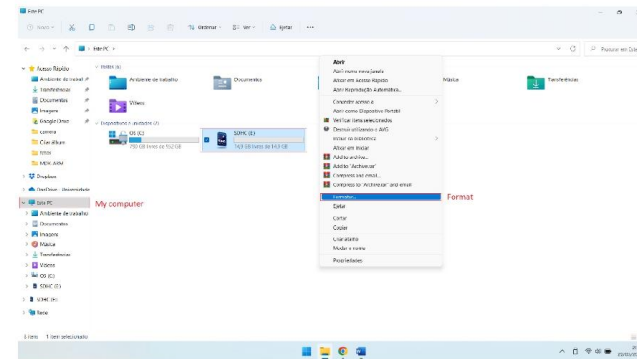
3) Select FAT32 and click Ok/Start.

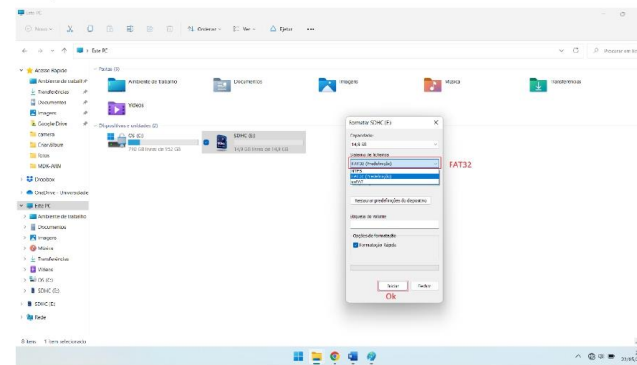# SUPPLEMENTARY MATERIAL VI – FAILED EXPERIMENTS

i) SeT Sensor – prototype I

The prototype I of the SeT Sensor was installed in the estuary of Cávado from the 31st of January to the 24th of February 2022. The instrument was fixed in an inox structure, buried in the streambed using an Archimedes screw to keep the sensor at 150 cm from the riverbed, as Supplementary Material VI 1 shows. The cantilever structure was positioned perpendicular to the estuary margin, so it could measure the water velocity in the upstream and downstream directions of the normal river flow. The depth sensor was used to record water depth and temperature. Both sensors were set to take measurements with a sampling period of 10 minutes.


Supplementary Material VI 1. Illustration and underwater photograph of the installation setup of the prototype I of the SeT sensor. The right image shows the sensor during the installation.

Supplementary Material VI 2 shows the electric output of the sensor and the depth and water temperature from the MS5837-30BA sensor. The data shows that the electric output increases during the low tide (cantilever bending in the downstream direction) and decreases during the high tide (cantilever bending in the upstream direction). This variation matches the expected behaviour based on the installation setup of the sensor.

However, it would be expected that the variation from the low-to-high tides always crossed a reference value, that would correspond to null flow. In other words, for the proper operation of the sensor, it was expected to see a reference value corresponding to 0 m/s which would increase during the low tide ("positive" velocity, meaning downstream direction) and decrease during the high tide ("negative" velocity, meaning upstream

direction). In the data provided by the current meter, this reference line does not exist, or its value is always changing.
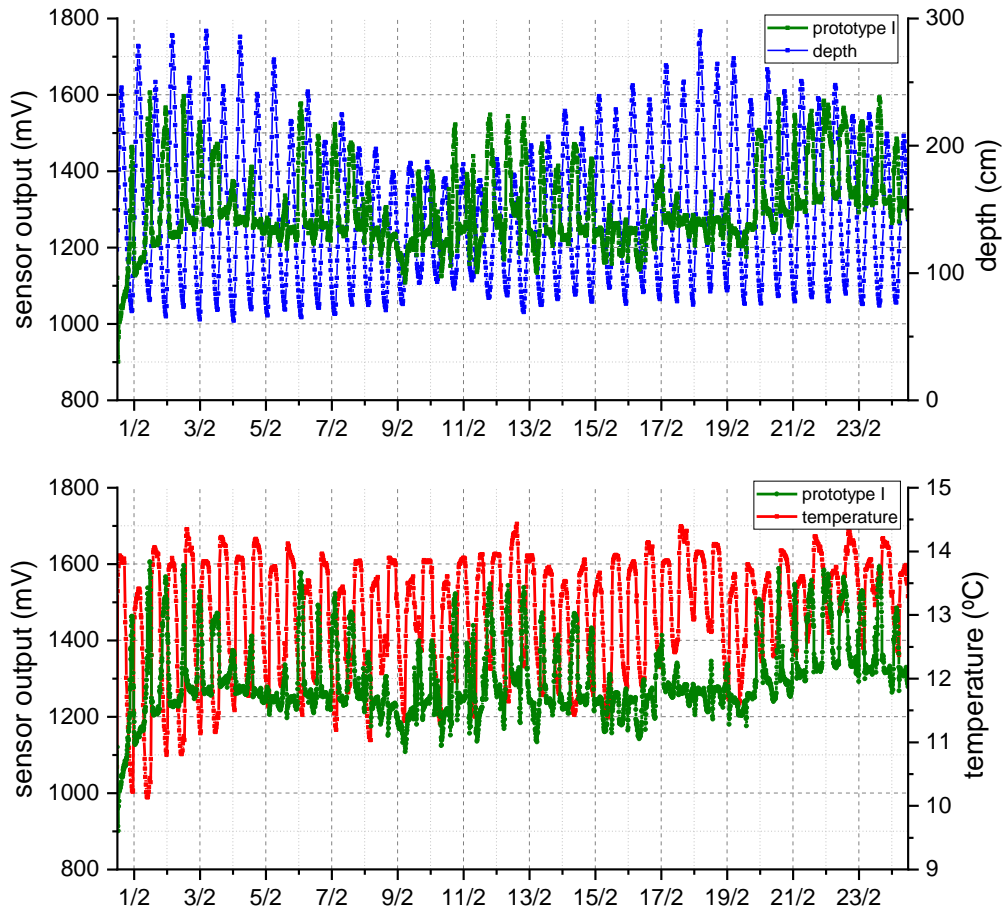
Supplementary Material VI 2. Monitoring results of the prototype I of the SeT Sensor from the 31st of January the 24th of February 2022. The top graph shows in green circles and green line the sensor output of prototype I (left y-axis) and in blue circles and blue line the water level produced by the MS5837-30BA sensor (right y-axis). The bottom graph presents in green circles and green line the same sensor output of prototype I (left y-axis) and in red circles and red line the water temperature from the MS5837-30BA sensor (right y-axis).

This prototype I was built using a piezoresistive structure, and the problem with this kind of material is that its nominal resistance changes with the temperature. That was the cause for the absence of the reference value of 0 m/s, which was constantly changing due to the variation of the water temperature in the estuary. The data on water temperature shown in the bottom graph of Supplementary Material VI 2 supports this conclusion.

During the first hours of the experiment, it is possible to observe that the average value of the sensor output is increasing. This happened because of the difference in temperature between the air and water. The sensor was outside the water before the installation. When it was submerged, the cantilever started to cool down, as did the piezoresistive material. The nominal resistance of the sensor decreases with the decrease in temperature, which increases its electric output.

During the whole experiment, it is possible to observe that the average value of the sensor output changes with the average value of temperature in the estuary. While the maximum temperature during the high tide does not change much, the temperature amplitude during the low tides is higher. It is possible to see that the average values of the sensor output present a similar signal tendency as the minimum temperature values during the low tides (see for example 31st of January to 9th of February or 19th to 24th of February).

When the sensor was recovered, it was noticed that the cantilever structure was damaged and the piezoresistive material was in contact with the water. The data presented in Supplementary Material VI 2 do not provide a clear insight about when it happened, but it cannot be discarded the interference that this event produced in the records.
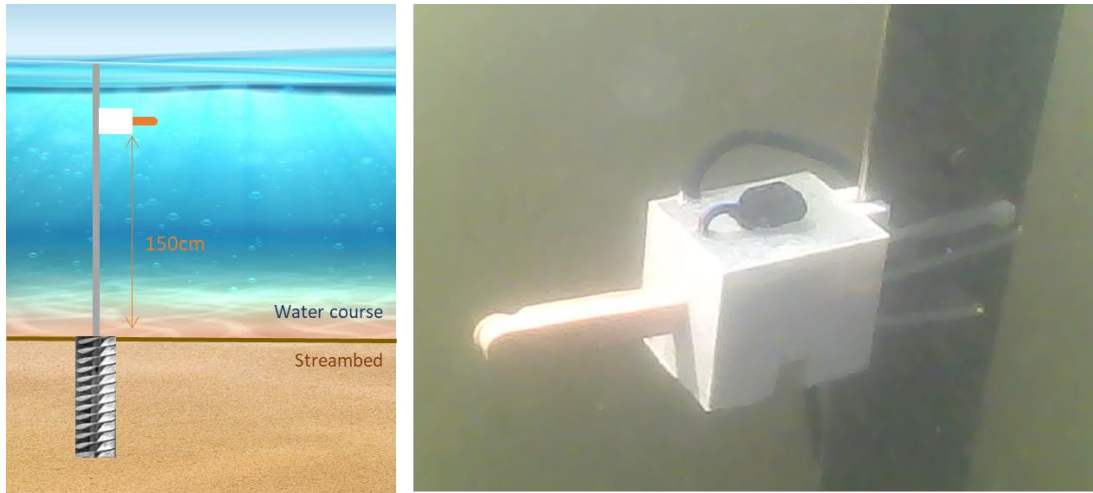
Supplementary Material VI 3 shows a photograph of the damaged cantilever and an underwater photograph of the sensor on the recovery day. It is possible to observe that the sensor did not suffer from biofouling, but it was covered in mud which is also a problem from long-time monitoring. The mud in the cantilever changes its weight and flexibility which causes errors in the measurements due to the less flexibility of the structure.

Supplementary Material VI 3. Photographs of the prototype I of the SeT Sensor after and at the end of the experiment. The right image shows a photograph of the damaged cantilever. The left image shows an underwater photograph of the sensor at the recovery day.
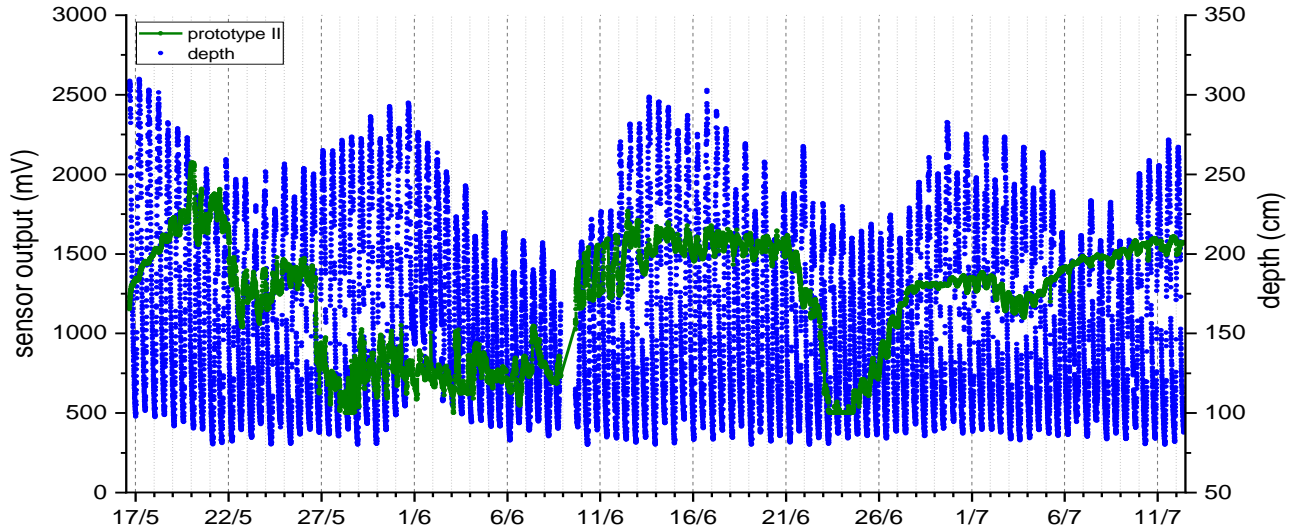
ii)   SeT Sensor – prototype II

The prototype II of the SeT Sensor was also developed based on the use of the Flex Sensor as the piezoresistive material for the cantilever. The major problem pointed to the prototype I was its susceptibility to temperature. The new version used two Flex Sensors, placed back-to-back in a half Wheatstone bridge to mitigate this difficulty. The second prototype was installed in the estuary of Cávado, from the 17th of May to the 12th of Jully 2022, in a similar setup as prototype I (Supplementary Material VI 4).

Supplementary Material VI 4. Illustration and underwater photograph of the installation setup of prototype II of the SeT sensor. The right image shows the sensor during the installation.
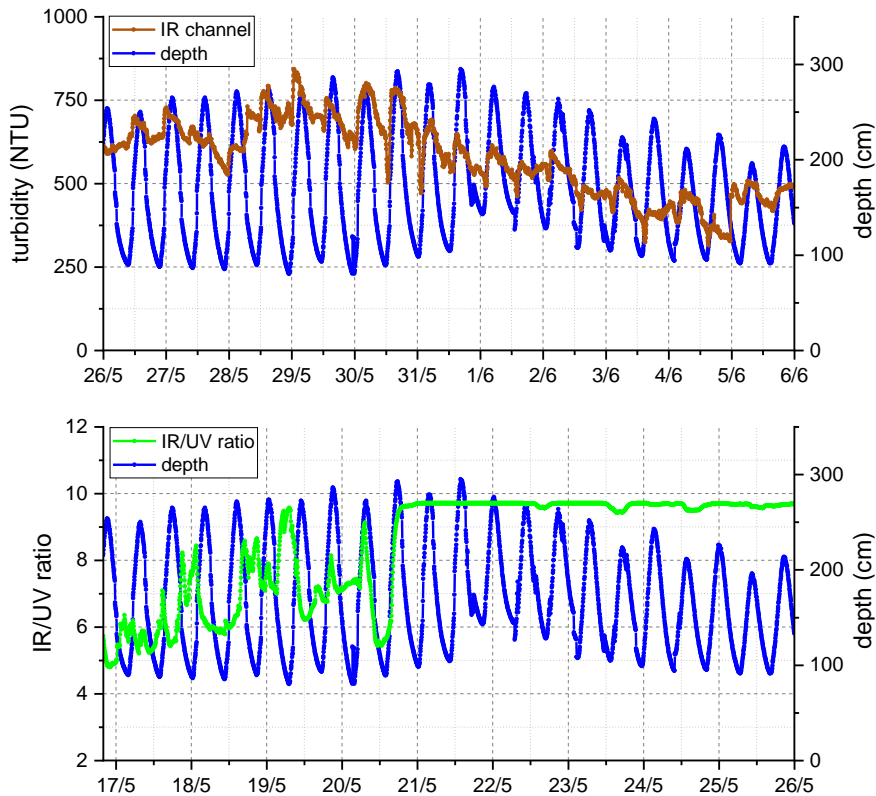
Supplementary Material VI 5 shows the monitoring records of prototype II and the depth data. The results are similar to the ones presented by prototype I: the sensor output increases during the low tide (downstream direction) and decreases during the high tide (upstream direction). However, the reference value of 0 m/s is floating once again. Compared to the data in Supplementary Material VI 2, the new version presents an even higher variation on the reference line. The prototype II also failed to measure water velocity in the field.

Supplementary Material VI 5. Monitoring results of the prototype II of the SeT Sensor from the 17th of May to the 12th of Jully 2022. The graph shows in green circles and green line the sensor output of prototype II (left y-axis) and in blue circles and blue line the water depth recorded by the MS5837-30BA sensor (right y-axis).

The device was built with IR and UV transmitted light optical channels to evaluate the suspended sediment. The top graph of Supplementary Material VI 6 presents the turbidity measurements using the IR optical channel. It shows the same patterns detected by the SPM and SDE Sensors during their experiments, showing

an increase of turbidity during the high tide and decrease during the low tide. The average value of turbidity also decreased from the spring to the neap tide.

Supplementary Material VI 6. Monitoring results of the prototype II from the 17th of May to the 12th of Jully 2022. The top graph shows in brown circles and brown line the turbidity produced by prototype II (left y-axis) and in blue circles and blue line the water depth recorded by the MS5837-30BA sensor (right y-axis). The bottom graph shows in green circles and green line the IR/UV ratio produced by prototype II (left y-axis) and in blue circles and blue line the water depth recorded by the MS5837-30BA sensor (right y-axis).

The UV channel, used to evaluate the organic load, also presented similar patterns detected before. The peaks of organic load were detected during the low tides (exceptions for the second high tide on the 19th of May and the high tides on the 20th of May).

After four days of deployment, the UV channel became obstructed by fouling. This behaviour can be observed at the end of the 20th of May, with the IR/UV ratio saturating close to the value of 10.

The experiment with prototype II was marked by a period of extreme algae blooms in the estuary that was reflected in the records (compare for example the turbidity and IR/UV ratio average values with the experiment conducted with the SPM Sensor). The attachment of macro biofouling to the instruments can be observed in the underwater photographs in Supplementary Material VI 7. When the sensor was recovered, it was covered with algae that was blocking the optical channels. Inversely, the cantilever structure was clean and without traces of biofouling or mud.

Supplementary Material VI 7. Photographs of the prototype II of the SeT Sensor during and after the experiment.
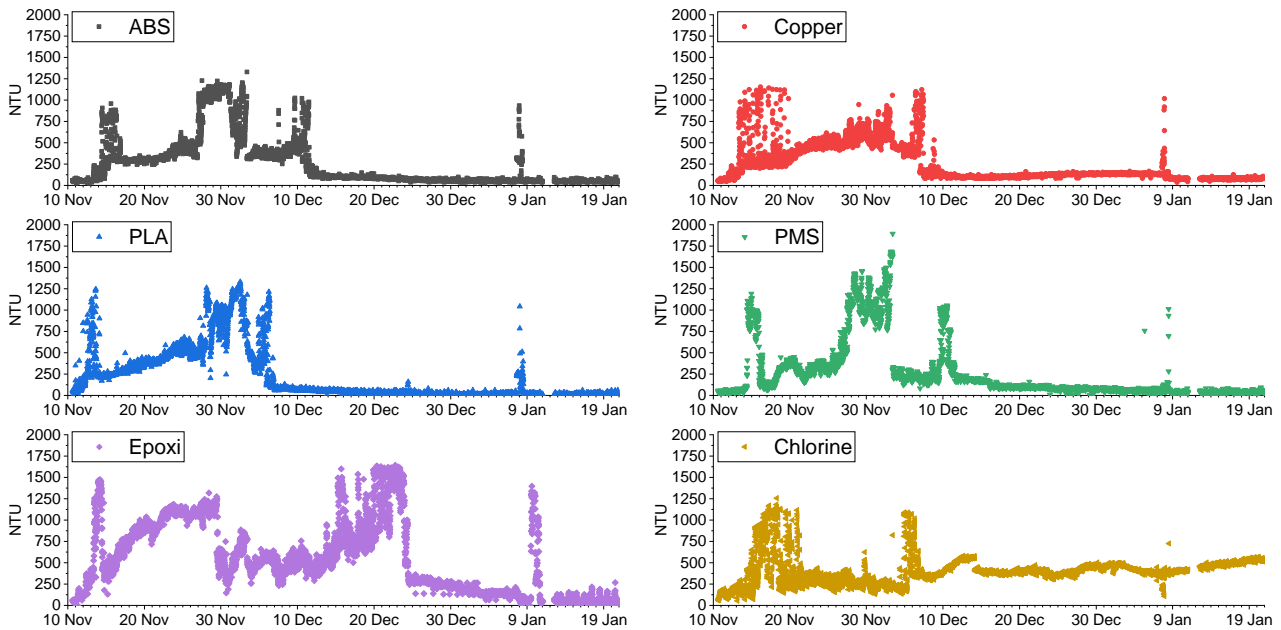
iii)   Anti-biofouling techniques

The six turbidity probes to test anti-biofouling techniques were installed in the monitoring station of Cávado River, from the 10th of November 2021 to the 21st of January 2022. The instrument was fixed, at 1 meter distance from the watercourse bed, in a structure buried with an Archimedes' screw (Supplementary Material VI 8). The probes were placed facing the streambed to avoid daylight interference in the measurements.
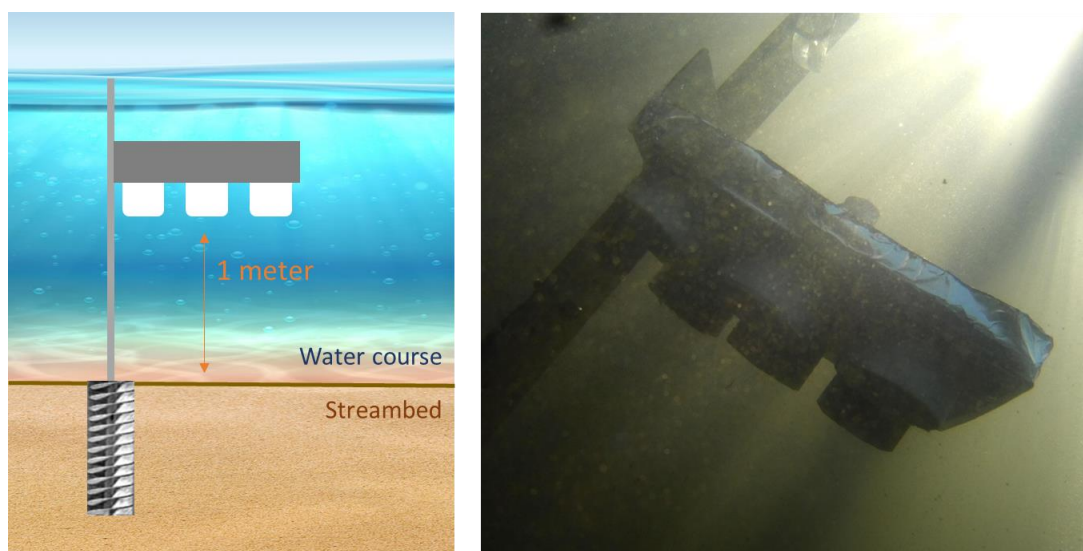
Supplementary Material VI 8. Illustration and underwater photograph of the installation setup of the anti-biofouling probes. The right image the instrument during the installation.

Supplementary Material VI 9 shows the measurements of the six probes during the field experiment. Since the day of installation of the instrument, all six probes reported an abrupt increase in the measurement of turbidity. However, this event was not caused by the existence of biofouling in the surfaces of the probes. Instead, during multiple inspections of the instrument, it was noticed that it was covered in mud (inorganic matter originated by the sediment load of the estuary).

Supplementary Material VI 9. Monitoring results of the anti-biofouling techniques during the experiment in the estuary of Cávado from the 10th of November 2021 to the 21st of January 2022. The graphs show the turbidity measurements of the six anti-biofouling probes.

Other occurrence was observed that overlapped the intended objectives of the experiment. Around the 10th of December, all probes sensed a decrease in the turbidity measurements. Inspection of the instrument showed that the probes were filled with air. The light transmission on air is higher comparing with on water, increasing the electric voltage reading from the phototransistor that correspond to a decrease of turbidity.

The air inside the probes was originated by biogeochemical processes. These processes, such as the anaerobic decomposition of organic material, releases gases like carbon dioxide and methane. These gases forms air pockets under the mud of the streambed and eventually are released in form of bubbles. Since the probes were facing the streambed, the air that entered in the cylindrical shape of the apparatus could not escape.

Due to these two phenomena, the testing with the anti-biofouling techniques was not suited to be conducted in the estuary of Cávado. A cleaner, and less dynamic environment in terms of sediment, was needed to test the instrument, where variables other than biofouling formation could be mitigate.